

Pulsed laser heating in the diamond anvil cell: applications in geo- and material sciences

DISSERTATION

zur Erlangung des akademischen Grades eines

Doktors der Naturwissenschaften (Dr. rer. nat.)

in der Bayreuther Graduiertenschule für Mathematik und Naturwissenschaften
(BayNAT)

der Universität Bayreuth

vorgelegt von

Georgios Aprilis

aus Thessaloniki (Griechenland)

Bayreuth, 2020

This doctoral thesis was prepared at the department of Laboratory of Crystallography and the Bavarian Research Institute of Experimental Geochemistry and Geophysics (BGI) at the University of Bayreuth from 05/2014 until 12/2019 and was supervised by Prof. Dr. Natalia Dubrovinskaia and Prof. Dr. Leonid Dubrovinsky.

This is a full reprint of the thesis submitted to obtain the academic degree of Doctor of Natural Sciences (Dr. rer. nat.) and approved by the Bayreuth Graduate School of Mathematical and Natural Sciences (BayNAT) of the University of Bayreuth.

Date of submission: 14.01.2020

Date of defense: 20.05.2020

Acting director: Prof. Dr. Markus Lippitz

Doctoral committee:

Prof. Dr. Natalia Dubrovinskaia	(reviewer)
PD. Dr. Gerd Steinle-Neumann	(reviewer)
Prof. Dr. Daniel Frost	(chairman)
Prof. Dr. Leonid Dubrovinsky	

(additional reviewer: Prof. Dr. Carmen Sanchez-Valle)

蝸
牛
そ
ろ
そ
ろ
登
れ
富
士
の
山

O snail
climb Mount Fuji,
but slowly, slowly!

Kobayashi Issa

1763 – 1828

Zusammenfassung

Moderne Hochdruckforschung erfordert die Untersuchung verschiedener Materialeigenschaften *in situ* in Diamantstempelzellen (DACs, von englisch *diamond anvil cells*) bei gleichzeitig hoher Temperatur und hohem Druck. Die zwei Hauptmethoden zum Heizen von Proben in DACs sind Laser- und Widerstandsheizung. Die Laserheizung wird bereits seit mehr als fünf Jahrzehnten eingesetzt und findet zahlreiche Anwendungen in den Bereichen Mineralphysik und Hochdruckchemie, Physik, Geowissenschaften und Materialwissenschaften.

Neben der üblichen Methode der Dauerstrich-Laserheizung (CW-Laserheizung, von englisch *continuous-wave laser*) wurden seit den ersten Versuchen der Laserheizung in einer DAC auch gepulste Laser verwendet, die den Vorteil haben, dass aufgrund der Konzentration hoher Laserleistung in kurzen Impulsen signifikant höhere Temperaturen erzielt werden können. So wird bei der gepulsten Laserheizung durch das wiederholte Heizen und Abkühlen der Probe die Zeit zu einer weiteren Variablen neben Druck und Temperatur. Damit wurde ein neues Forschungsfeld eingeführt, in dem wichtige Materialeigenschaften wie Wärmeleitfähigkeit und Diffusionsvermögen bestimmt und komplexe Prozesse in der Probe, insbesondere das Schmelzen, untersucht werden können. Als weiterer möglicher Vorteil wird angenommen, dass die gepulste Laserheizung die chemische Stabilität der geheizten Probe durch Minimierung der Diffusion verbessert. Dies wurde jedoch bisher nicht experimentell untersucht. Das Hauptziel dieser Dissertation ist es, die Möglichkeiten der experimentellen Technik der gepulsten Laserheizung in der DAC in Anwendungen der Mineral- und Materialphysik zu untersuchen.

Im Rahmen dieser Arbeit wurde ein tragbares doppelseitiges gepulstes Laserheizsystem entwickelt, das problemlos mit Geräten für zeitaufgelöste Messungen wie Röntgenbeugung (XRD), Nuclear Inelastic Scattering (NIS), Synchrotron-Mössbauer-Spektroskopie (SMS) und Röntgenabsorptions-Nahkantenstruktur-Spektroskopie (XANES) an Synchrotronanlagen wie der Europäischen Synchrotron-Strahlungsanlage (ESRF) und PETRA III am DESY gekoppelt werden kann.

Die Auswirkungen der gepulsten Lasererheizung auf die chemische Stabilität von Proben innerhalb der Diamantstempelzelle wurden in zwei separaten, für die Hochdruckgeowissenschaften wichtigen experimentellen Fällen untersucht:

In der ersten Studie wurde die chemische Wechselwirkung zwischen einer Probe aus Eisen und dem Kohlenstoff der Diamantstempel während kontinuierlicher (CW) und gepulster Laserheizung untersucht. Es ist ein bekanntes Problem, dass das Laserheizen von Eisen in einer DAC durch eine chemische Reaktion mit dem diffundierenden Kohlenstoff zur Bildung von

Eisenkarbiden oder der Lösung von Kohlenstoff in Eisen führen kann. Dies kann die geschätzte Schmelztemperatur in Eisenschmelzexperimenten erheblich beeinflussen und die Analyse der Phasengrenzen zwischen verschiedenen Eisenphasen erschweren. In einer Reihe von Experimenten, bei denen verschiedene Punkte auf Eisenproben entweder mit einem gepulsten Laser oder einem CW-Laser erhitzt wurden und außerdem die Dauer des Erhitzens variierte, wurde die Eisen-Kohlenstoff-Wechselwirkung mit Hilfe von XANES verfolgt. Die Zusammensetzungen der erhitzten Proben wurden anschließend unter Verwendung von SMS und XRD an verschiedenen Strahllinien der ESRF und PETRA III untersucht. Die Ergebnisse dieser Studie zeigen keinen offensichtlichen Vorteil des Erhitzens im gepulsten Modus und beweisen so im Wesentlichen, dass die chemische Wechselwirkung zwischen Eisen (oder, allgemeiner, allen Materialien in einer DAC) und dem Kohlenstoff der Diamantstempel kaum vermeidbar ist.

Die zweite Studie untersuchte den Einfluss von gepulster Laserheizung auf die Stabilität von Ferroperiklas mit der geochemisch bedeutsamen Zusammensetzung von $(\text{Fe}_{0,25}\text{Mg}_{0,75})\text{O}$ (Fp25) in einem weiten Temperaturbereich unter Drücken, die dem oberen Teil des unteren Erdmantels entsprechen. Es wurde über die Zersetzung von Fp25 unter Bildung einer Hochdruck- $(\text{Mg,Fe})_3\text{O}_4$ -Phase mit CaTi_2O_4 -Struktur sowie über die durch Erhitzen induzierte Dissoziation von Fp25 in eine Fe-reiche und eine Mg-reiche Phase berichtet. Die Ergebnisse unterstützen außerdem den Schluss, dass gepulste Lasererwärmung chemische Prozesse möglicherweise beschleunigt, anstatt sie zu unterdrücken.

Die Dissertation beinhaltet auch die Entwicklung von zwei weiteren experimentellen Systemen, die die Möglichkeiten von Laserheizungsstudien und deren Kopplung mit verschiedenen experimentellen Techniken erweitern:

Das erste System ist ein Einkristall-XRD-Laserheizsystem, das aus einem Einkristall-Röntgendiffraktometer und einem doppelseitigen Laserheizsystem besteht. Der Aufbau wurde für die Beamline P02.2 bei PETRA III entwickelt. Die Leistung des Systems wurde am Beispiel der Einkristall-XRD-Untersuchung von FeN und CrN unter Hochdruck- und Hochtemperaturbedingungen veranschaulicht.

Das zweite System wird verwendet, um vollständig zeitaufgelöste SMS bei hohem Drücken in Kombination mit gepulster Laserheizung in DACs durchzuführen. Das System ist in der Lage, die Mössbauer-Absorption der Probe über die Dauer des Laserpulses zu verfolgen, Änderungen der Probenoberflächentemperatur beidseitig zeitaufgelöst spektrometrisch zu messen und die Probenoberflächentemperatur durch die zentrale Verschiebung der Mössbauer-Spektren zu bestimmen. Das System wurde getestet, indem Eisen in KCl bei 32 GPa, Eisen in Argon bei 36 GPa und $\text{Fe}_{25}\text{O}_{32}$ in Ne bei 77 GPa erhitzt wurden.

Zusammenfassend trägt diese Arbeit bei zur Weiterentwicklung der Laserheizungstechnik für die Hochdruckforschung und zum besseren Verständnis komplexer chemischer und physikalischer Prozesse in der Probenkammer der DAC unter Laserbestrahlung.

Summary

Modern high-pressure research demands studying various properties of materials *in situ*, inside diamond anvil cells (DACs), simultaneously at high temperature and high pressure. Among the two major methods of heating in DACs, are laser and resistive heating; laser heating has been already used for more than five decades and found numerous applications in mineral physics and high-pressure chemistry, physics, Earth, and materials sciences.

In addition to the common method of continuous-wave (CW) laser heating, pulsed lasers have been used from the first attempts of laser heating in a DAC, having the advantage of achieving significantly higher temperatures due to the concentration of high laser power in a short impulse. The repetitive heating and cooling of the sample makes time an extra variable, additionally to pressure and temperature, something that is not possible with CW laser heating. A new field of research has been introduced, allowing the determination of important material properties, such as thermal conductivity and diffusivity, and studies of complex processes within the sample, particularly melting. As another possible advantage, pulsed laser heating is thought to improve the chemical stability of the heated sample by minimizing diffusion. However, this was not investigated experimentally. The main goal of this thesis is to investigate the capabilities of the experimental technique of pulsed laser heating inside the DAC in applications of mineral and material physics studies.

As part of the thesis, a portable double-sided pulsed laser heating system has been developed, that can be easily coupled with equipment at synchrotron facilities for time-resolved measurements, such as X-ray diffraction (XRD), Nuclear Inelastic Scattering (NIS), Synchrotron Mössbauer Source (SMS), and X-ray Absorption Near Edge Structure spectroscopy (XANES) both at the European Synchrotron Radiation Facility (ESRF) and PETRA III at DESY.

The effects of pulsed laser heating on the chemical stability of samples inside the DAC were investigated in two separate experimental cases that are important in high-pressure geoscience:

In the first study, the chemical interaction between iron and carbon of the diamond anvils during CW and pulsed laser heating was examined. It is a known problem that laser heating of iron in a DAC may lead to formation of iron carbides or a solution of carbon in iron, as a result of a chemical reaction between the sample and carbon diffusing from a diamond anvil into the sample chamber. This can significantly affect the estimated melting temperature in iron melting experiments and complicate the analysis of phase boundaries between different iron phases. In a series of experiments, in which different spots of iron samples were heated by either a pulsed laser or a CW laser and by varying the duration of heating, the iron-carbon interaction was tracked using XANES. The compositions of the heated samples were examined

afterwards using SMS and XRD at different beamlines of the ESRF and PETRA III. The results of this study show no obvious advantage due to heating in pulsed mode and essentially prove that the chemical interaction between iron (or generally any materials in a DAC) and carbon from the anvils is hardly avoidable.

The second study investigated the effect of pulsed laser heating on the stability of ferropericlasite with a geochemically relevant composition of $(\text{Fe}_{0.25}\text{Mg}_{0.75})\text{O}$ (Fp25) at pressure conditions corresponding to the upper part of the lower mantle and at wide temperature range. The decomposition of Fp25 with formation of a high-pressure $(\text{Mg,Fe})_3\text{O}_4$ phase with CaTi_2O_4 -type structure was reported, as well as the dissociation of Fp25 into an Fe-rich and a Mg-rich phases induced by heating. The results further support that pulsed laser heating can possibly accelerate, rather than suppress, chemical processes.

The thesis includes the development of two more experimental systems that further extend the capabilities of laser heating studies and its coupling with different experimental techniques:

The first system is a single-crystal XRD/laser-heating setup consisting of a single-crystal X-ray diffractometer and a double-sided laser heating system. The setup was developed for beamline P02.2 at PETRA III. The system's performance was illustrated with the example of the single-crystal XRD study of FeN and CrN at high-pressure and high-temperature conditions.

The second system is used to perform fully time-resolved SMS at high pressures in combination with pulsed laser heating in DACs. The system is capable to track the Mössbauer absorption of the sample along the duration of the laser pulse, follow changes of the sample surface temperature from both heating directions using spectroradiometry, and bulk sample temperature by means of central shift of the Mössbauer spectra. The system was tested by heating iron in KCl at 32 GPa, iron in argon at 36 GPa, and $\text{Fe}_{25}\text{O}_{32}$ in Ne at 77 GPa.

To summarize, this work contributes to the development of the laser heating technique for high-pressure research and to a better understanding of complex chemical and physical processes in the sample chamber of a DAC under laser irradiation.

Acknowledgements

The five and a half years of my dissertation studies were a period with many achievements in the scientific and personal aspect of my life but also with difficulties. The people in my environment played a very important role during this time, by supporting me in the difficult moments and by providing the necessary solid foundation that would help me advance my experience and knowledge in a field that was completely new to me before arriving to Bayreuth. The least I can do to show my gratitude is to acknowledge their -either direct or indirect- contribution to this thesis.

I would firstly like to thank my supervisors Prof. Dr. Natalia Dubrovinskaia and Prof. Dr. Leonid Dubrovinsky for their support, guidance, patience and understanding but most importantly, for being true “mentors” during my studies, rather than only “supervisors”.

I was lucky to be working in the warm and friendly environment of the Laboratory of Crystallography, so I would like to thank all the members of the laboratory for this. Special thanks to Prof. Dr. Sander van Smaalen and PD Dr. Andreas Schönleber for their support and helpful discussions, Denis Kelk-Huth, the secretary, for being very helpful and supportive in all my administrative questions and problems, and my office-mates Kerstin Kuspert, Leyla Ismailova and Somnath Dey for the good times we shared.

A big part of my working time was in BGI, so I would like to thank everyone there for being welcoming and helpful, providing a friendly and collaborative working atmosphere that is rarely found elsewhere. Especially Prof. Hans Keppler, Prof. Tomoo Katsura, Prof. Dan Frost, Dr. Catherine McCammon and Dr. Tiziana Boffa-Ballaran, who, through either their lectures or helpful scientific discussions and corrections, introduced me to the field of geoscience and helped me to develop my skills.

I spent the last year of my studies in Hamburg, where I was lucky to collaborate with the staff of the Extreme Conditions Beamline of PETRA III, Hanns-Peter Liermann, Konstantin Glazyrin, Mario Wendt, Sergej Wenz, and Jan Torben Roeh that were always willing to help me with the technical and scientific issues.

I am particularly thankful to Georg Spiekermann, who, apart from being a good collaborator and friend, also kindly agreed to translate the Summary of this thesis into German.

I would like to especially thank the friends that I made during my studies: Elena Bykova, Maxim Bykov, Egor Koemets, Iuliia Koemets, Timofey Fedotenko, Saiana Khandarkhaeva, Denis Vasiukov, Dariia Simonova, Leyla Ismailova, Irina Chuvashova, Ilya Kupenko, Alexander Kurnosov, Stella Chariton, Serena Dominijanni, Valerio Cerantola, Sylvain Petitgirard, Ines

Collings, Robert Arato, Ingrid Blanchard, Esther Posner and Caterina Melai. Thank you all for the things you taught me, the times you helped me, the long beamtimes we shared and your priceless friendship. I might regretfully forget someone this moment, but I consider it a bliss to have so many good people surrounding me that it is hard to recall such a long list. I would also like to thank my flat-mates, Dominik Hanft and Alina Simet for the two years we shared together and their support and understanding during some difficult times for me.

A short paragraph is definitely not enough to express my gratitude to my parents, Dimitra Aprili and Ioannis Aprilis, for their endless love and compassion and for being there at every important moment of my life -happy or sad-, supporting all my decisions.

The last person I am grateful to, is no one else than the person that at some point during my studies accepted to be my wife, Anna Pakhomova, who was always there, even when she could not be there.

Table of Contents

Zusammenfassung	1
Summary	3
Acknowledgements	5
1. Introduction	11
References	15
2. Motivation	17
2.1 Portable pulsed laser heating system	18
2.2 Chemical reaction(s) of laser-heated materials, iron particularly, with carbon from the diamond anvils	19
2.3 Stability of ferropicicase at high pressures	20
2.4 Fully time-resolved Synchrotron Mössbauer Source spectroscopy	21
2.5 Single-crystal diffraction in the LHDAC	22
References	24
3. Experimental Methods	29
3.1 Pressure Generation	29
3.1.1 Diamond Anvil Cells	30
3.1.2 Pressure transmitting media	31
3.1.3 Pressure determination	32
3.2 Laser Heating in the Diamond Anvils Cell	33
3.3 Temperature Measurement	35
3.4 Mössbauer spectroscopy	37
3.4.1 Basic Principles	37
3.4.2 Synchrotron Mössbauer Source	39
3.4.3 Nuclear Inelastic Scattering	40
3.5 X-ray Absorption Spectroscopy	42
3.6 High Pressure SCXRD	46
References	50

4. Thesis Synopsis	53
4.1 Summary of research studies	53
4.1.1 Portable double-sided pulsed laser heating system for time- resolved geoscience and materials science applications	54
4.1.2 Comparative study of the influence of pulsed and continuous wave laser heating on the mobilization of carbon and its chemical reaction with iron in a diamond anvil cell	58
4.1.3 The effect of pulsed laser heating on the stability of ferropericlase at high pressures	64
4.1.4 Single-crystal diffractometer coupled with double-sided laser heating system at the Extreme Conditions Beamline P02.2 at PETRAIII	69
4.1.5 Fully time-resolved synchrotron Mössbauer spectroscopy for pulsed laser heating experiments in diamond anvil cell	72
4.2 Outlook and perspectives	75
4.3 List of manuscripts and statement of authors' contribution	76
References	79
5. Results	85
5.1 <i>Portable double-sided pulsed laser heating system for time- resolved geoscience and materials science applications</i>	85
5.1.1 Abstract	85
5.1.2 Introduction	86
5.1.3 System overview	87
5.1.4 Examples of application	95
5.1.5 Conclusions	102
5.1.6 Acknowledgements	103
5.1.7 References	103
5.2 <i>Comparative study of the influence of pulsed and continuous wave laser heating on the mobilization of carbon and its chemical reaction with iron in a diamond anvil cell</i>	107
5.2.1 Abstract	107
5.2.2 Introduction	108
5.2.3 Experimental Methods	109
5.2.4 Results and Analysis	113

5.2.5	Discussion	124
5.2.6	Conclusions	126
5.2.7	Acknowledgements	126
5.2.8	References	126
5.3 The effect of pulsed laser heating on the stability of ferropericlase at high pressures		130
5.3.1	Abstract	130
5.3.2	Introduction	130
5.3.3	Experimental	131
5.3.4	Results	134
5.3.5	Discussion	141
5.3.6	Tables	144
5.3.7	Refereces	147
5.4 Single-crystal diffractometer coupled with double-sided laser heating system at the Extreme Conditions Beamline P02.2 at PETRAIII		151
5.4.1	Abstract	151
5.4.2	Introduction	151
5.4.3	Setup overview	152
5.4.4	Setup operation	155
5.4.5	Examples of the setup application	158
5.4.6	Conclusions	162
5.4.7	Acknowledgments	162
5.4.8	References	162
5.5 Fully time-resolved synchrotron Mössbauer spectroscopy for pulsed laser heating experiments in diamond anvil cell		165
5.5.1	Abstract	165
5.5.2	Introduction	165
5.5.3	Experiment	167
5.5.4	Pulsed Laser Heating of Metallic Iron	170
5.5.5	Pulsed Laser Heating of Fe ₂₅ O ₃₂	174

5.5.6	Conclusion and Outlook	177
5.5.7	Acknowledgements	178
5.5.8	References	178
	Abbreviations	181
	(Eidesstattliche) Versicherungen und Erklärungen	182

Chapter 1

Introduction

The progress of modern science relies in the progress of technology. Not only applied but also fundamental research is advancing alongside the improvement of instrumentation and the pursuit of knowledge is pushing the limits of technological capability. By reaching higher energies, shorter timescales, higher measurement precision, more extreme conditions, experimental instruments provide the means to expand the barriers of knowledge to degrees not previously possible.

The beginning of the 20th century was marked by scientific breakthroughs in physics, chemistry and biology that established the foundations of modern science. These achievements were based in the individual brilliance of a number of scientists that are now considered the founding “fathers” and “mothers” of their respective field of research. A century later, milestone discoveries of contemporary science derive mainly from the effort of broad, interdisciplinary scientific groups collaborating at large-scale projects and facilities rather than the novel idea conception of an individually outstanding scientist. Large-scale facilities, such as particle accelerators, synchrotrons, X-ray free-electron lasers, space observatories and laser interferometer gravitational-wave observatories are the places where engineers and scientists of diverse backgrounds expand the boundaries of modern scientific knowledge.

High-pressure science, being heavily experimental, is one such science that relies on the advances of scientific equipment and large-scale facilities. The inception of devices such as the diamond anvil cell (DAC)¹ and the multi-anvil press² and the further improvement of their designs has allowed the investigation of material properties and chemistry at pressure and temperature conditions of the Earth’s core and interiors of extrasolar bodies^{3,4}. This is of great importance for geo- and planetary science, due the lack of actual samples from the deep Earth and other planets interior. Similarly, material science and condensed-matter physics profit from the expansion of the pressure and temperature limits within which matter can be investigated, in topics of research such as high-temperature superconductivity⁵, ultrahard materials⁶ and new materials discovery⁷.

Alongside with the development of high-pressure apparatuses, different techniques have been utilized to heat samples at geologically relevant temperatures. One of the favored methods had been external electrical resistive heating^{8–10}. In this approach, resistive heaters can surround the whole DAC, the diamonds and gasket assemblage, or the supports for the diamonds. Although external resistive heating creates a homogeneous temperature field in the pressure chamber, it suffers from temperature and pressure limitations. Diamond begins to graphitize at temperatures over 1200 °C, metallic gaskets become soft and yield, and the expansion of the body of the DAC at high temperatures can create unwanted changes in the pressure. Alternatively, the resistive heating can be internal^{11–13}, by passing current through a metallic wire inside the sample chamber, often the wire being the sample itself. This method is more efficient and can also produce homogeneous heating, but still has temperature limitations, and is extremely labor consuming.

The highest range of temperatures inside the DAC can be achieved with laser heating. Taking advantage of the transparency of the diamond anvils for a wide range of radiation energies, a laser beam can be focused on the sample through both diamond anvils and heat the pressurized sample up to several thousands of degrees Kelvin. The fact that it is possible to achieve temperatures that exceed the Earth's geotherm for its entire pressure range has established the laser-heated diamond anvil cell (LHDAC) technique as a very important method for mineral physics and high pressure chemistry, Earth and material sciences^{14,15}.

In contrast to resistive heating, the focused laser beam heats only a small area inside the pressure chamber and, depending on the case, not the entire sample. Due to this, the LHDAC technique benefits significantly from synchrotron radiation for *in situ* measurements of the heated sample. The heated part of the sample can be probed by the high-brilliance, focused X-ray beam produced at synchrotron light source facilities, without probing the surrounding, cold part of the pressure chamber. Consequently, over the last years, the LHDAC technique has been coupled with various experimental set-ups at synchrotrons, such as X-ray diffraction^{16,17}, Nuclear Inelastic Scattering (NIS), the Synchrotron Mössbauer Source (SMS)^{18,19}, and X-ray Absorption Near Edge Structure spectroscopy (XANES)^{20,21} and most high-pressure beamlines are equipped with an *in situ* LHDAC system.

The temperature determination during laser heating is much less accurate than the thermocouples that are used to determine the temperature during resistive heating. The most common method employed is spectroradiometry (see Section 3.3) that estimates the surface temperature of the sample from its thermal radiation. The uncertainty of spectroradiometry is in the order of ± 100 K -which is less than 5% for temperatures above 2000 K- and is acceptable for most experimental conditions. The temperature of the heated sample can be also provided from other spectroscopic methods. The spectroradiometric measurement can be combined with that information, which improves the accuracy of the total temperature estimation.

Another drawback for laser heating comparatively to resistive heating is the fact that not all materials absorb laser power in the same way and some samples might not be possible to be heated by a specific type of laser. Different LHDAC systems utilize lasers of different wavelength depending on the materials under investigation. The most commonly used laser types are:

- a) Solid-state lasers with Nd-doped YAG crystals as lasing medium or fiber lasers that both emit in the near-infrared radiation (NIR) range, specifically at around 1064 nm. NIR lasers are used to usually heat metallic samples or samples that contain metals that are usually non-transparent at the visible range.
- b) Gas lasers, more specifically CO₂ lasers, emit infrared radiation (IR) at around 10 μm. These lasers are absorbed by a wider range of materials, including non-metallic and light-element samples that are transparent to the visible light. Although such lasers are also suited for metallic compounds, due to their difficulty to be focused and their easy absorption by intermediate optics, they are mainly utilized only for samples that cannot be easily heated by NIR lasers.
- c) Lasers that emit at the visible spectrum (VIS) range are well suited for heating samples at high pressure, but the intense visible light they produce hinders the *in situ* visual observation of the sample and interferes with the spectroradiometry measurements. Heating lasers at the visible range have, therefore, limited application in LHDAC systems.

Additionally to the common laser heating method of continuous-wave (CW) heating, where the laser power is steadily transferred to the heated sample, pulsed lasers have been used from the very first attempts of laser heating in a DAC^{22,23}. Pulsed laser heating has the advantage of achieving significantly higher temperatures due to the concentration of a high amount of laser power in a short impulse.

In the first decades of laser heating the capabilities of pulsed lasers have not been fully explored. Only in the beginning of the 2000s, pulsed laser heating has been coupled with time-resolved measurements^{24,25}. The repetitive heating and cooling of the sample makes time an extra variable in addition to pressure and temperature, which is not possible with continuous-wave laser heating. An entirely new field of research has been introduced, allowing determination of important material properties such as thermal conductivity and diffusivity, and melting temperatures^{26–29}.

The present thesis focuses in the advancement of the pulse laser heating method. The development of LHDAC setups is presented that are coupled with different X-ray spectroscopy and diffraction methods and are capable of *in situ* time-resolved measurements during pulse heating of the samples. The pulsed laser heating technique is further investigated regarding its effects on the chemical stability of the materials, in comparison to conventional CW

heating. The experiments reported include the chemical interaction of iron with carbon from the diamond anvils as well as the high-pressure chemistry of iron-rich ferropericlase ($\text{Fe}_{0.25}\text{Mg}_{0.75}\text{O}$), a geologically important mineral.

References

1. Weir, C. E., Lippincott, E. R., Van Valkenburg, A. & Bunting, E. N. Infrared studies in the 1- to 15-micron region to 30,000 atmospheres. *J. Res. Natl. Bur. Stand. Sect. A Phys. Chem.* **63A**, 55 (1959).
2. Kawai, N. & Endo, S. The Generation of Ultrahigh Hydrostatic Pressures by a Split Sphere Apparatus. *Rev. Sci. Instrum.* **41**, 1178–1181 (1970).
3. Tateno, S., Hirose, K., Ohishi, Y. & Tatsumi, Y. The Structure of Iron in Earth's Inner Core. *Science (80-.)*. **330**, 359–361 (2010).
4. Dubrovinskaia, N. *et al.* Terapascal static pressure generation with ultrahigh yield strength nanodiamond. *Sci. Adv.* **2**, e1600341 (2016).
5. Drozdov, A. P., Erements, M. I., Troyan, I. A., Ksenofontov, V. & Shylin, S. I. Conventional superconductivity at 203 kelvins at high pressures in the sulfur hydride system. *Nature* **525**, 73–76 (2015).
6. Dubrovinsky, L. S. *et al.* The hardest known oxide. *Nature* **410**, 653–654 (2001).
7. Zhang, L., Wang, Y., Lv, J. & Ma, Y. Materials discovery at high pressures. *Nat. Rev. Mater.* **2**, 17005 (2017).
8. Zha, C.-S. & Boehler, R. Melting of sodium and potassium in a diamond anvil cell. *Phys. Rev. B* **31**, 3199–3201 (1985).
9. Zha, C., Boehler, R., Young, D. A. & Ross, M. The argon melting curve to very high pressures. *J. Chem. Phys.* **85**, 1034–1036 (1986).
10. Dubrovinskaia, N. & Dubrovinsky, L. Whole-cell heater for the diamond anvil cell. *Rev. Sci. Instrum.* **74**, 3433–3437 (2003).
11. Liu, L.-G. & Bassett, W. A. The melting of iron up to 200 kbar. *J. Geophys. Res.* **80**, 3777–3782 (1975).
12. Boehler, R., Nicol, M., Zha, C. S. & Johnson, M. L. Resistance heating of Fe and W in diamond-anvil cells. *Phys. B+C* **139–140**, 916–918 (1986).
13. Zha, C.-S. & Bassett, W. A. Internal resistive heating in diamond anvil cell for in situ x-ray diffraction and Raman scattering. *Rev. Sci. Instrum.* **74**, 1255–1262 (2003).
14. Bassett, W. A. The birth and development of laser heating in diamond anvil cells. *Rev. Sci. Instrum.* **72**, 1270 (2001).
15. Bassett, W. A. Diamond Anvil Cells: Laser heating of samples at high pressure: 50 years. (2016). Available at: <https://www.laserfocusworld.com/test-measurement/test-measurement/article/16547047/diamond-anvil-cells-laser-heating-of-samples-at-high-pressure-50-years>. (Accessed: 8th January 2020)

16. Schultz, E. *et al.* Double-sided laser heating system for in situ high pressure–high temperature monochromatic x-ray diffraction at the esrf. *High Press. Res.* **25**, 71–83 (2005).
17. Meng, Y., Hrubciak, R., Rod, E., Boehler, R. & Shen, G. New developments in laser-heated diamond anvil cell with in situ synchrotron x-ray diffraction at High Pressure Collaborative Access Team. *Rev. Sci. Instrum.* **86**, (2015).
18. Lin, J. F. *et al.* Absolute temperature measurement in a laser-heated diamond anvil cell. *Geophys. Res. Lett.* **31**, 3–6 (2004).
19. Kuppenko, I. *et al.* Portable double-sided laser-heating system for Mössbauer spectroscopy and X-ray diffraction experiments at synchrotron facilities with diamond anvil cells. *Rev. Sci. Instrum.* **83**, 124501 (2012).
20. Aquilanti, G. *et al.* Development of micro-XANES mapping in the diamond anvil cell. *J. Synchrotron Radiat.* **16**, 376–379 (2009).
21. Marini, C., Kantor, I., Mathon, O. & Pascarelli, S. On-line laser heating setup for ED-XAS at ID24: Preliminary optical design and test results. *High Press. Res.* **33**, 108–113 (2013).
22. Bassett, W. A. & Li-Chung Ming. Disproportionation of Fe₂SiO₄ to 2FeO+SiO₂ at pressures up to 250kbar and temperatures up to 3000 °C. *Phys. Earth Planet. Inter.* **6**, 154–160 (1972).
23. Gold, J. S., Bassett, W. A., Weathers, M. S. & Bird, J. M. Melting of Diamond. *Science (80-)*. **225**, 921–922 (1984).
24. Funamori, N. & Sato, T. Heating in a diamond-anvil cell using relaxation oscillations of a Q-switched Nd:YAG laser. *Rev. Sci. Instrum.* **77**, 77–80 (2006).
25. Goncharov, A. F. & Crowhurst, J. C. Pulsed laser Raman spectroscopy in the laser-heated diamond anvil cell. *Rev. Sci. Instrum.* **76**, 063905 (2005).
26. McWilliams, R. S., Dalton, D. A., Konôpková, Z., Mahmood, M. F. & Goncharov, A. F. Opacity and conductivity measurements in noble gases at conditions of planetary and stellar interiors. *Proc. Natl. Acad. Sci.* **112**, 7925–7930 (2015).
27. Yang, L., Karandikar, A. & Boehler, R. Flash heating in the diamond cell: Melting curve of rhenium. *Rev. Sci. Instrum.* **83**, 1–6 (2012).
28. Goncharov, A. F. *et al.* Thermal conductivity of argon at high pressures and high temperatures. *J. Appl. Phys.* **111**, 112609 (2012).
29. Beck, P. *et al.* Measurement of thermal diffusivity at high pressure using a transient heating technique. *Appl. Phys. Lett.* **91**, 10–13 (2007).

Chapter 2

Motivation

Although laser heating inside the diamond anvil cell is a well-established technique that has led to significant advances of high-pressure science, the use of pulsed lasers for time-resolved measurements is relatively recent and only a handful of scientific groups have so far developed systems and established methods for such experiments¹⁻⁴. Pulsed laser heating is considered to have several advantages over CW laser heating, that are often reported in literature:

- a) *Better heating stability over long measurements.* Optical components on the laser beam path as well as the DAC itself progressively heat up due to the partially absorbed laser radiation and their thermal expansion can cause optical misalignment or mechanical failure to the components of the heating system, especially during measurements that require long time of heating. Pulsed heating allows the thermal relaxation between pulses and minimizes the thermal expansion³.
- b) *Higher achievable temperatures.* Diamond is a material with extremely high thermal conductivity and in order for the sample to be heated, the thermal losses through the diamond anvils need to be overcome. This problem is more prominent for experiments at very high pressures, when the pressure chamber is small and the insulation layer between the sample and the diamonds is very thin. In pulsed heating, the laser energy is concentrated in a short duration pulse that can overcome the energy losses more easily than continuous wave heating^{1,5}.
- c) *Possibility of time-resolved measurements.* Pump-probe experiments rely in the excitation of the sample with laser pulses and the observation of its response as a function of time. Such studies allow the investigation of chemical processes and properties of matter^{1,4,5}.
- d) *Improved chemical stability.* As the pulsed laser heating minimizes the heating duration in individual pulses down to microseconds or even shorter, it is considered¹⁻

⁵ to be a technique that suppresses diffusion and thus improves the chemical stability of the system under investigation. However, there have not been studies so far, which could allow a direct comparison of the effects of pulsed laser and continuous wave laser heating.

In the course of the present thesis, a pulsed laser heating system was developed to exploit the aforementioned advantages of the novel technique and utilize it, in combination with different spectroscopic methods, in experiments of geological and material science importance (Sections 5.1, 5.4 and 5.5). Experiments with duration of up to 24 hours of pulsed laser heating are reported (Section 5.1) as well as examples of time-resolved studies (Sections 5.1 and 1.1). Lastly, two studies investigate the effects of pulsed and CW laser heating on the mobilization of carbon and its chemical reaction with iron in a diamond anvil cell (Section 5.2) and the stability of ferropericlase at high pressures (Section 5.3).

2.1 Portable pulsed laser heating system

Laser heating inside the diamond anvil cell is an experimental technique that greatly profits from the analytical capabilities provided by the focused and brilliant X-ray beam of a synchrotron. For this reason, many high-pressure beamlines are equipped with laser heating setups, coupled with different experimental methods⁶⁻¹¹. The versatility of LHDAC and the need of heating samples both at home institutions as well as synchrotrons led to the development of portable setups that can be easily transported to a synchrotron beamline, fit into the limited space provided and, if necessary, allow the movement of the sample during data collection¹¹⁻¹⁴.

One of the goals of this thesis was to develop a pulsed laser heating system that is designed to be easily movable between home institutions and synchrotrons, or between different beamlines and can be combined with different experimental setups. A number of challenges had to be addressed to design a system that is versatile regarding the laser pulses shape and synchronization, depending on the demands of each experiment, and accurately measure the time-resolved temperature of the sample while heating.

Another aspect that is of great importance in a LHDAC experiment is the information about the spatial distribution of temperatures at and around the heated spot. The significance of a surface temperature map has been noted in several studies¹⁵⁻²⁰, being especially relevant to high-pressure melting experiments¹⁷⁻²⁰, but not exclusively^{15,16}. In melting experiments, the temperature distribution map provides information on the maximum and minimum temperature of the heated spot, as well as the temperature at exactly the boundary between the melted and non-melted material, which defines its melting point.

The methods used so far to determine the surface temperature distribution estimate the temperature profile along one line on the sample by leading the thermal emission into a spectrometer through a slit¹⁷⁻¹⁹. Direct two-dimensional temperature mapping techniques

included only computational estimations such as peak scaling¹⁶ or multispectral imaging radiometry approaches, without full spectroradiometry²¹. The portable pulsed laser heating system developed in the course of the present thesis, aimed to provide a solution for both temporally and spatially resolved temperature measurements in a double-sided LHDAC.

2.2 Chemical reaction(s) of laser-heated materials, iron particularly, with carbon from the diamond anvils

The LHDAC method has wide application in experiments that investigate the melting temperature of materials as a function of pressure, i.e. their melting curve^{18–20,22–24}. Knowledge of melting of metals under pressure is of a fundamental importance, but the high-pressure melting curve of iron is of particular interest for geosciences, as it provides crucial constrains for modelling thermal conditions in the Earth's core and at the core-mantle boundary (CMB). Despite extensive research, it still remains uncertain and the data are contradictory^{25–28}.

The results of studies on melting depend on many factors including the heating method, melting criterion, and the temperature measurement technique. Undesirable chemical reactions are among the major experimental obstacles. It is well known by now that laser heating of iron in a DAC may lead to formation of iron carbides or a solution of carbon in iron^{29–32} as a result of a chemical reaction between the sample and carbon diffusing from a diamond anvil into the sample chamber. This is highly unwanted in melting experiments, since the presence of carbides or Fe-C solid solutions can significantly affect the melting temperature¹⁹. The results of a recent study²⁷ on the melting curve of iron appears to have been affected by this carbon contamination^{33,34}. This problem is not limited to iron³⁵ but due to the important geological implications of its melting curve, iron is a widely investigated material.

The detection of the undesirable chemical reactions often presents a separate complex task. Since laser heating affects the surface of the sample, the volume of the laser-heated material may be very small. The amount of products of undesirable chemical reactions can appear to be below the detection limit of the applied analytical method. The question of whether a chemical reaction indeed took place becomes crucial for establishing correct melting curves of metals or, more generally, for any experiments in laser-heated DACs.

Solid state chemical reactions are driven by mutual diffusion of the components, which is promoted by high temperature and prolonged heating. As the pulsed laser heating minimizes the heating duration in short pulses, it is considered as an option that suppresses diffusion and, thus, prevents or minimizes (relatively to CW heating) the reactions between carbon from the diamond anvils and heated matter.

However, the benefits of pulsed laser heating have not been thoroughly studied and there has been no direct comparison of the effects of pulsed and CW laser heating on the mobilization of carbon in a DAC and its chemical reaction with the sample. Such experiments require a

sample in a particular chemical environment to be heated using both a PL and a CW laser, in order to support the argument of increased chemical stability when pulsed heating is used.

In the present thesis, experiments were performed in a structured way, by heating the same sample with different heating methods and investigating the existence of chemical reaction using X-ray diffraction, SMS, and XANES. The dependence of the chemical reaction on the laser heating method used and pressure medium in the DAC was investigated, as well as the influence of the detection method in the characterization of the possible reaction products.

2.3 Stability of ferropericlase at high pressures

The Earth's lower mantle constitutes more than half of the volume of the planet, from the transition zone at the depth of 660 km to the core-mantle boundary (CMB) at 2900 km³⁶. Currently it is widely accepted that the lower mantle consists of mainly three major minerals – ferropericlase, bridgmanite and calcium silicate perovskite^{37–39}. Ferropericlase ((Mg,Fe)O) is a magnesium oxide with iron content and is believed to be the second most abundant of the three, comprising approximately 16-20 wt% of the lower mantle^{36,40,41} (Figure 2.3-1).

The expected percentage of iron (expressed as Fe/(Mg+Fe)) in (Fe,Mg)O in the lower mantle is 10-25%, as follows, particularly, from studies of Mg-Fe partitioning between bridgmanite and ferropericlase.^{42,43} Ferropericlase with such composition is so far considered to be stable in a NaCl-type (B1) structure ($Fm\bar{3}m$) throughout the lower mantle⁴⁴.

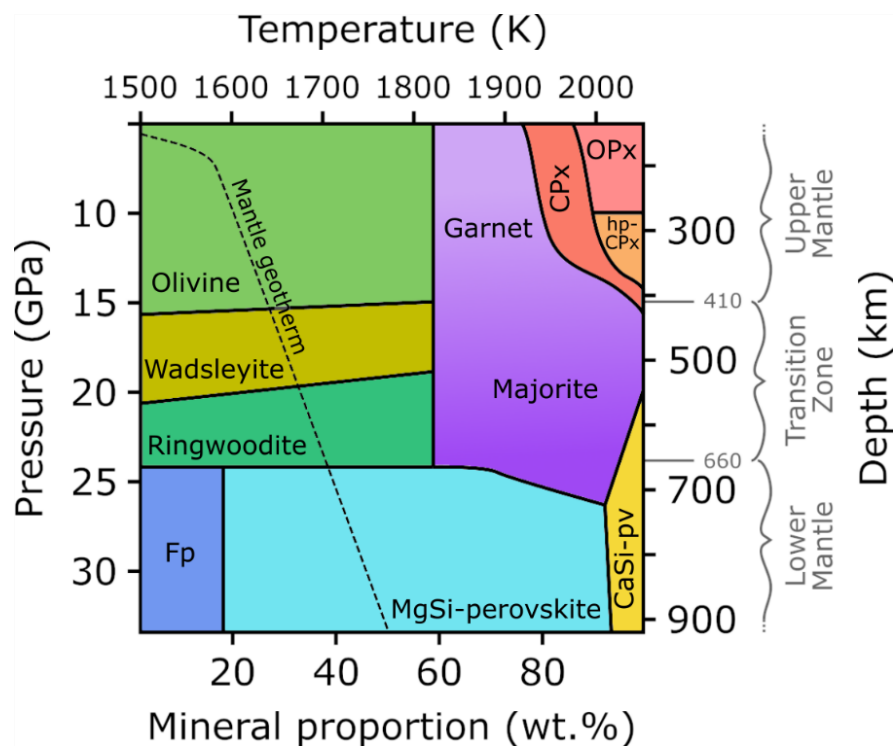


Figure 2.3-1. Experimental data on mineral composition and phase transformations in the mantle within the pressure range 5 – 35 GPa. Fp stands for ferropericlase; CPx stands for clinopyroxenes; OPx stands for orthopyroxenes; hp-CPx stands for high-pressure clinopyroxenes. Modified after ⁴⁵.

There are, however, reports that (Mg,Fe)O with relatively large amount of Fe may decompose at pressure-temperature conditions of the lowermost mantle into an Fe-richer and a Mg-richer phases^{46,47}. In contrast to the earlier reports on decomposition, subsequent studies in laser-heated diamond anvil cells (LHDACs) did not observe any segregation between iron and magnesium^{44,48-50}. Ferropericlasite inclusions in super-deep diamonds show very large variations of Mg/Fe ratio⁴⁵ suggesting that there are natural processes which lead to compositional differentiation in the formation of (Mg,Fe)O. The behavior of ferropericlasite as well as partitioning of iron between minerals co-existing in lower mantle play a crucial role in understanding the dynamics, geophysics, and geochemistry of the Earth.^{51,52}

A possible reason for the contradictory results in the decomposition of ferropericlasite into of Fe- and Mg-rich components upon heating has been suggested to be the short heating duration⁴⁸, signifying the influence of chemical kinetics. A study on the reactivity of iron with the diamond anvils inside a DAC that is part of the present thesis, shows no obvious advantage due to heating in pulse mode, in contrast to the general belief that pulse laser heating in experiments with DACs prevents or minimizes (in comparison with continuous wave, CW) the reactions between diamond anvils (carbon) and heated matter^{1,4}. Considering this, the repetitive cooling and heating of the sample in a short timescale might be a method to accelerate reaction kinetics, due to the high thermal gradients developed during heating.

A series of experiments presented in this thesis, investigate the effect of pulsed laser heating on the stability of ferropericlasite with a geochemically relevant composition of (Fe_{0.25}Mg_{0.75})O at pressure conditions corresponding to the upper part of the lower mantle^{53,54} (Figure 2.3-1) and at a wide temperature range.

2.4 Fully time-resolved Synchrotron Mössbauer Source spectroscopy

Recoilless nuclear resonance fluorescence, namely the Mössbauer effect, is a physical phenomenon that has found many applications in science. Its importance was immediately evident, awarding physicist Rudolf Mössbauer a Nobel Prize in 1961, just four years after its discovery.

While many elements can be suitable sources for the Mössbauer effect, Mössbauer spectroscopy (MS) using the isotope ⁵⁷Fe has found particular use in earth science, emerging as an ideal probe for the coordination, speciation, spin state, magnetic order, and dynamics of earth materials because of its sensitivity and the abundance of iron. Despite the significant utility of the technique for probing materials at high pressures, conventional MS under pressure is difficult due to the lack of efficient focusing schemes and, in particular, its combination with laser heating faces severe challenges, since usually only a small portion of the sample is heated.

Synchrotron radiation sources allow the excitation of Mössbauer transitions with a synchrotron beam and their high brilliance permits focusing down to the micrometer scale.

The experimental technique of MS using synchrotron radiation, namely Synchrotron Mössbauer spectroscopy (SMS)⁵⁵, has yielded important results for Earth science, in experiments conducted in DACs^{56–58}. Another characteristic of SMS is the determination of the temperature of the bulk of the sample via the measure of the second order doppler shift from the Mössbauer spectra⁵⁹. In combination with spectroradiometry, SMS can be a powerful tool for experiments in LHDACs.

The combination of Mössbauer spectroscopy with pulsed laser irradiation for samples at ambient pressure has already been demonstrated along with the possible applications of the method⁶⁰. It was immediately clear that it is necessary to have time-resolved information of the Mössbauer absorption in order to take full advantage of the dynamic nature of pulsed laser heating in the DAC. Previous experimental schemes for high-pressure, high-temperature studies allowed only limited, time-differentiated information⁶¹.

As part of the present thesis, a detection scheme to perform fully time-resolved SMS at high pressures was developed, in combination with pulsed laser heating in DACs. The Mössbauer absorption of the sample can be fully tracked along the duration of the laser pulse, and its temperature can be estimated on both heated surfaces using spectroradiometry as well as in bulk from the central shift (CS) of the Mössbauer spectra. The experimental setup allows to take full advantage of the pulsed laser heating technique and investigate the dynamics of samples at high pressure in high time resolution.

2.5 Single-crystal diffraction in the LHDAC

Very important high-pressure science discoveries were based in results from X-ray diffraction experiments in DACs, such as the synthesis of post-perovskite⁶², iron oxides with unexpected stoichiometries at conditions of the Earth's interior^{63,64}, and exotic chemistry compounds⁶⁵. Single-crystal X-ray diffraction (SCXRD) is a powerful technique that provides significant information about the sample under investigation. While powder X-ray diffraction (PXRD) can determine the symmetry and unit cell parameters of the crystal structure of a novel compound (see Section 5.4), single-crystal X-ray diffraction can provide a full model of atomic positions and bond relations between atoms in the crystal, helping to determine not only the crystal structure of a material, but also to refine its chemical composition even for very complex multi-phase and/or multigrain samples.

Due to significant progress in the field of high-pressure technology, the last decade SCXRD became available at pressures above ~15 GPa. Novel gas-loading systems^{66–71} allow the use of soft pressure transmitting media (helium or neon) in DACs, preserving single crystals to megabar pressures. New types of diamond anvils and DACs with wide X-ray opening up to 90 degrees⁷² enlarge the coverage of the reciprocal space and thus improve the data redundancy which leads to the higher quality of the final structural models.

The achievement of geologically relevant pressures for SCXRD studies combined with the

possibility to reach high temperatures with laser heating allows to conduct experiments *in situ*, which is of great importance for studies dedicated to the modelling of processes in deep Earth's interior. However, combining LHDAC with SCXRD is experimentally challenging. Double-sided laser-heating systems used at synchrotron facilities^{6,12,73,74} are suitable for X-ray diffraction studies combined with laser heating, but only powder diffraction data can be collected while the sample is heated. This is due to the nature of the data collection, since single-crystal analysis requires the rotation of the DAC over a wide angle.

Single-crystal data collection during heating requires the sample to be at a stable temperature during the whole collection as well as at a stable position relative to the X-ray and laser beams. Stationary optics cannot focus the laser beam through the diamond anvils while the diamond anvil rotates. It is, therefore, necessary to be able to rotate the optics in alignment with the DAC during data collection, keeping the laser beam at a constant angle and relative position to the diamond anvils and heated sample. The limited space of beamline facilities is an extra challenge in this task and special care needs to be taken for the placement of the optics and movable parts, while maintaining the stability of the system during rotation.

Until recently, all synchrotron LHDAC setups were stationary and did not allow DAC rotation during simultaneous heating, thus making *in situ* high-pressure high-temperature SCXRD impossible. As part of this thesis, a modification of the portable laser-heating system developed in Bayerisches Geoinstitut (BGI) was mounted directly on a goniometer stage and rotated along with the DAC providing the opportunity to collect SCXRD during laser heating.

References

1. Goncharov, A. F. *et al.* Laser heating in diamond anvil cells: developments in pulsed and continuous techniques. *J. Synchrotron Radiat.* **16**, 769–772 (2009).
2. Rekhi, S., Tempere, J. & Silvera, I. F. Temperature determination for nanosecond pulsed laser heating. *Rev. Sci. Instrum.* **74**, 3820–3825 (2003).
3. Deemyad, S. *et al.* Pulsed laser heating and temperature determination in a diamond anvil cell. *Rev. Sci. Instrum.* **76**, 1–4 (2005).
4. Goncharov, A. F. *et al.* X-ray diffraction in the pulsed laser heated diamond anvil cell. *Rev. Sci. Instrum.* **81**, 113902 (2010).
5. Goncharov, A. F. & Crowhurst, J. C. Pulsed laser Raman spectroscopy in the laser-heated diamond anvil cell. *Rev. Sci. Instrum.* **76**, 063905 (2005).
6. Schultz, E. *et al.* Double-sided laser heating system for in situ high pressure–high temperature monochromatic x-ray diffraction at the esrf. *High Press. Res.* **25**, 71–83 (2005).
7. Meng, Y., Hrubciak, R., Rod, E., Boehler, R. & Shen, G. New developments in laser-heated diamond anvil cell with in situ synchrotron x-ray diffraction at High Pressure Collaborative Access Team. *Rev. Sci. Instrum.* **86**, (2015).
8. Aquilanti, G. *et al.* Development of micro-XANES mapping in the diamond anvil cell. *J. Synchrotron Radiat.* **16**, 376–379 (2009).
9. Marini, C., Kantor, I., Mathon, O. & Pascarelli, S. On-line laser heating setup for ED-XAS at ID24: Preliminary optical design and test results. *High Press. Res.* **33**, 108–113 (2013).
10. Lin, J. F. *et al.* Absolute temperature measurement in a laser-heated diamond anvil cell. *Geophys. Res. Lett.* **31**, 3–6 (2004).
11. Kuppenko, I. *et al.* Portable double-sided laser-heating system for Mössbauer spectroscopy and X-ray diffraction experiments at synchrotron facilities with diamond anvil cells. *Rev. Sci. Instrum.* **83**, 124501 (2012).
12. Boehler, R., Musshoff, H. G., Ditz, R., Aquilanti, G. & Trapananti, A. Portable laser-heating stand for synchrotron applications. *Rev. Sci. Instrum.* **80**, 045103 (2009).
13. Dubrovinsky, L. *et al.* Portable laser-heating system for diamond anvil cells. *J. Synchrotron Radiat.* **16**, 737–741 (2009).
14. Shen, G., Wang, L., Ferry, R., Mao, H. & Hemley, R. J. A portable laser heating microscope for high pressure research. *J. Phys. Conf. Ser.* **215**, 012191 (2010).
15. Sinmyo, R. & Hirose, K. The Soret diffusion in laser-heated diamond-anvil cell. *Phys. Earth Planet. Inter.* **180**, 172–178 (2010).

16. Rainey, E. S. G. & Kavner, A. Peak scaling method to measure temperatures in the laser-heated diamond anvil cell and application to the thermal conductivity of MgO. *J. Geophys. Res. Solid Earth* **119**, 8154–8170 (2014).
17. Thomson, A. R., Walter, M. J., Lord, O. T. & Kohn, S. C. Chemistry and mineralogy of earth's mantle. Experimental determination of melting in the systems enstatite-magnesite and magnesite-calcite from 15 to 80 GPa. *Am. Mineral.* **99**, 1544–1554 (2014).
18. Lord, O. T. *et al.* The NiSi melting curve to 70GPa. *Phys. Earth Planet. Inter.* **233**, 13–23 (2014).
19. Lord, O. T., Walter, M. J., Dasgupta, R., Walker, D. & Clark, S. M. Melting in the Fe–C system to 70 GPa. *Earth Planet. Sci. Lett.* **284**, 157–167 (2009).
20. Lord, O. T. *et al.* The melting curve of Ni to 1 Mbar. *Earth Planet. Sci. Lett.* **408**, 226–236 (2014).
21. Campbell, A. J. Measurement of temperature distributions across laser heated samples by multispectral imaging radiometry. *Rev. Sci. Instrum.* **79**, 015108 (2008).
22. Kavner, A. & Jeanloz, R. High-pressure melting curve of platinum. *J. Appl. Phys.* **83**, 7553 (1998).
23. Du, Z. & Lee, K. K. M. High-pressure melting of MgO from (Mg,Fe)O solid solutions. *Geophys. Res. Lett.* **41**, 8061–8066 (2014).
24. Mashino, I., Miozzi, F., Hirose, K., Morard, G. & Sinmyo, R. Melting experiments on the Fe–C binary system up to 255 GPa: Constraints on the carbon content in the Earth's core. *Earth Planet. Sci. Lett.* **515**, 135–144 (2019).
25. Boehler, R. Temperatures in the Earth's core from melting-point measurements of iron at high static pressures. *Nature* **363**, 534–536 (1993).
26. Anzellini, S., Dewaele, A., Mezouar, M., Loubeyre, P. & Morard, G. Melting of Iron at Earth's Inner Core Boundary Based on Fast X-ray Diffraction. *Science (80-.).* **340**, 464–466 (2013).
27. Aquilanti, G. *et al.* Melting of iron determined by X-ray absorption spectroscopy to 100 GPa. *Proc. Natl. Acad. Sci.* **112**, 12042–12045 (2015).
28. Sinmyo, R., Hirose, K. & Ohishi, Y. Melting curve of iron to 290 GPa determined in a resistance-heated diamond-anvil cell. *Earth Planet. Sci. Lett.* **510**, 45–52 (2019).
29. Prakapenka, V. B., Shen, G. & Dubrovinsky, L. S. Carbon transport in diamond anvil cells. *High Temp. - High Press.* **35–36**, 237–249 (2003).
30. Rouquette, J. *et al.* Iron-carbon interactions at high temperatures and pressures. *Appl. Phys. Lett.* **92**, 121912 (2008).

31. Frost, D. J. *et al.* Partitioning of oxygen between the Earth's mantle and core. *J. Geophys. Res.* **115**, B02202 (2010).
32. Tateno, S., Hirose, K., Ohishi, Y. & Tatsumi, Y. The Structure of Iron in Earth's Inner Core. *Science (80-.)*. **330**, 359–361 (2010).
33. Boccato, S. *et al.* The Melting Curve of Nickel Up to 100 GPa Explored by XAS. *J. Geophys. Res. Solid Earth* **122**, 9921–9930 (2017).
34. Morard, G. *et al.* Solving Controversies on the Iron Phase Diagram Under High Pressure. *Geophys. Res. Lett.* **45**, 11074–11082 (2018).
35. Dewaele, A., Mezouar, M., Guignot, N. & Loubeyre, P. High Melting Points of Tantalum in a Laser-Heated Diamond Anvil Cell. *Phys. Rev. Lett.* **104**, 255701 (2010).
36. Kaminsky, F. V. *The Earth's Lower Mantle*. (Springer International Publishing, 2017). doi:10.1007/978-3-319-55684-0
37. Lee, K. K. M. *et al.* Equations of state of the high-pressure phases of a natural peridotite and implications for the Earth's lower mantle. *Earth Planet. Sci. Lett.* **223**, 381–393 (2004).
38. Tschauner, O. *et al.* Discovery of bridgmanite, the most abundant mineral in Earth, in a shocked meteorite. *Science (80-.)*. **346**, 1100–1102 (2014).
39. Xu, W., Lithgow-Bertelloni, C., Stixrude, L. & Ritsema, J. The effect of bulk composition and temperature on mantle seismic structure. *Earth Planet. Sci. Lett.* **275**, 70–79 (2008).
40. Irifune, T. Absence of an aluminous phase in the upper part of the Earth's lower mantle. *Nature* **370**, 131–133 (1994).
41. Wood, B. J. Phase transformations and partitioning relations in peridotite under lower mantle conditions. *Earth Planet. Sci. Lett.* **174**, 341–354 (2000).
42. Mao, H., Guoyin, S. & Hemley, R. J. Multivariable Dependence of Fe-Mg Partitioning in the Lower Mantle. *Science (80-.)*. **278**, 2098–2100 (1997).
43. Katsura, T. & Ito, E. Determination of Fe-Mg partitioning between perovskite and magnesiowüstite. *Geophys. Res. Lett.* **23**, 2005–2008 (1996).
44. Lin, J.-F. *et al.* Stability of magnesiowüstite in Earth's lower mantle. *Proc. Natl. Acad. Sci.* **100**, 4405–4408 (2003).
45. Kaminsky, F. Mineralogy of the lower mantle: A review of 'super-deep' mineral inclusions in diamond. *Earth-Science Rev.* **110**, 127–147 (2012).
46. Dubrovinsky, L. S. Stability of Ferropericlase in the Lower Mantle. *Science (80-.)*. **289**, 430–432 (2000).
47. Dubrovinsky, L., Dubrovinskaia, N., Annersten, H., Hålenius, E. & Harryson, H. Stability

- of $(\text{Mg}_{0.5}\text{Fe}_{0.5})\text{O}$ and $(\text{Mg}_{0.8}\text{Fe}_{0.2})\text{O}$ magnesiowustites in the lower mantle. *Eur. J. Mineral.* **13**, 857–861 (2001).
48. Kondo, T., Ohtani, E., Hirao, N., Yagi, T. & Kikegawa, T. Phase transitions of $(\text{Mg,Fe})\text{O}$ at megabar pressures. *Phys. Earth Planet. Inter.* **143–144**, 201–213 (2004).
 49. Lin, J.-F. *et al.* Electrical conductivity of the lower-mantle ferropericlase across the electronic spin transition. *Geophys. Res. Lett.* **34**, 2–5 (2007).
 50. Fei, Y. *et al.* Spin transition and equations of state of $(\text{Mg, Fe})\text{O}$ solid solutions. *Geophys. Res. Lett.* **34**, L17307 (2007).
 51. Badro, J. *et al.* Iron Partitioning in Earth’s Mantle: Toward a Deep Lower Mantle Discontinuity. *Science (80-.)*. **300**, 789–791 (2003).
 52. Deng, J. & Lee, K. K. M. Viscosity jump in the lower mantle inferred from melting curves of ferropericlase. *Nat. Commun.* **8**, 1997 (2017).
 53. Katsura, T., Yoneda, A., Yamazaki, D., Yoshino, T. & Ito, E. Adiabatic temperature profile in the mantle. *Phys. Earth Planet. Inter.* **183**, 212–218 (2010).
 54. Trubitsyn, V. P. & Trubitsyna, A. P. Effects of compressibility in the mantle convection Equations. *Izv. Phys. Solid Earth* **51**, 801–813 (2015).
 55. Smirnov, G. V. Synchrotron Mössbauer source of ^{57}Fe radiation. *HYPERFINE Interact.* **125**, 91–112 (2000).
 56. McCammon, C. *et al.* Stable intermediate-spin ferrous iron in lower-mantle perovskite. *Nat. Geosci.* **1**, 684–687 (2008).
 57. Kuppenko, I. *et al.* Magnetism in cold subducting slabs at mantle transition zone depths. *Nature* **570**, 102–106 (2019).
 58. Prescher, C. *et al.* High Poisson’s ratio of Earth’s inner core explained by carbon alloying. *Nat. Geosci.* **8**, 220–223 (2015).
 59. Maradudin, A. A., Flinn, P. A. & Ruby, S. Velocity Shift of the Mössbauer Resonance. *Phys. Rev.* **126**, 9–23 (1962).
 60. Vagizov, F., Kolesov, R., Olariu, S., Rostovtsev, Y. & Kocharovskaya, O. Experimental observation of vibrations produced by pulsed laser beam in $\text{MgO}:\text{Fe}$. *Hyperfine Interact.* **167**, 917–921 (2006).
 61. Kuppenko, I. *et al.* Time differentiated nuclear resonance spectroscopy coupled with pulsed laser heating in diamond anvil cells. *Rev. Sci. Instrum.* **86**, 114501 (2015).
 62. Murakami, M., Hirose, K., Kawamura, K., Sata, N. & Ohishi, Y. Post-Perovskite Phase Transition in MgSiO_3 . *Science (80-.)*. **304**, 855–858 (2004).
 63. Bykova, E. *et al.* Structural complexity of simple Fe_2O_3 at high pressures and

- temperatures. *Nat. Commun.* **7**, 10661 (2016).
64. Hu, Q. *et al.* FeO₂ and FeOOH under deep lower-mantle conditions and Earth's oxygen–hydrogen cycles. *Nature* **534**, 241–244 (2016).
 65. Zhang, W. *et al.* Unexpected Stable Stoichiometries of Sodium Chlorides. *Science (80-.)*. **342**, 1502–1505 (2013).
 66. Mills, R. L., Liebenberg, D. H., Bronson, J. C. & Schmidt, L. C. Procedure for loading diamond cells with high-pressure gas. *Rev. Sci. Instrum.* **51**, 891–895 (1980).
 67. Yagi, T., Yusa, H. & Yamakata, M. An apparatus to load gaseous materials to the diamond-anvil cell. *Rev. Sci. Instrum.* **67**, 2981–2984 (1996).
 68. Kenichi, T., Sahu, P. C., Yoshiyasu, K. & Yasuo, T. Versatile gas-loading system for diamond-anvil cells. *Rev. Sci. Instrum.* **72**, 3873–3876 (2001).
 69. Couzinet, B., Dahan, N., Hamel, G. & Chervin, J.-C. Optically monitored high-pressure gas loading apparatus for diamond anvil cells. *High Press. Res.* **23**, 409–415 (2003).
 70. Rivers, M. *et al.* The COMPRES/GSECARS gas-loading system for diamond anvil cells at the Advanced Photon Source. *High Press. Res.* **28**, 273–292 (2008).
 71. Kurnosov, A. *et al.* A novel gas-loading system for mechanically closing of various types of diamond anvil cells. *Rev. Sci. Instrum.* **79**, 045110 (2008).
 72. Boehler, R. New diamond cell for single-crystal x-ray diffraction. *Rev. Sci. Instrum.* **77**, 115103 (2006).
 73. Shen, G., Rivers, M. L., Wang, Y. & Sutton, S. R. Laser heated diamond cell system at the advanced photon source for in situ x-ray measurements at high pressure and temperature. *Rev. Sci. Instrum.* **72**, 1273–1282 (2001).
 74. Prakapenka, V. B. *et al.* Advanced flat top laser heating system for high pressure research at GSECARS: application to the melting behavior of germanium. *High Press. Res.* **28**, 225–235 (2008).

Chapter 3

Experimental Methods

This chapter provides a description of all the methods utilized to implement the experiments of this thesis. They consist of techniques applied to achieve the necessary temperature and pressure conditions of the sample under investigation, as well as different spectroscopic methods used to probe the sample properties.

3.1 Pressure Generation

The study of the properties and chemical behavior of materials at pressures higher than the atmospheric is of high importance for materials science, through the discovery of novel materials or previously unknown properties with technological applications, as well as geoscience, through the simulation of the conditions that exist in the Earth's and planetary bodies interiors.

The pressure conditions can be dynamic -through the generation of shock waves-, or static. The simplest definition of pressure is $P = \frac{F}{A}$, where F is the applied normal force, and A is the area, on which the force is applied. According to this relation, there are two ways of reaching very high pressures; either by increasing the applied force, or by decreasing the area, to which the force is applied.

There are many different designs of devices used to apply static pressure on large volume samples. The generation of axial stress with a piston-cylinder design has roots at the end of the 19th century. In 1970, the multi-anvil press has been introduced¹, as a method to apply pressure on more than one axes². These devices are, as expected, large and are designed to maximize the applied force on relatively large samples.

By reducing the size of the sample (from volumes of cm³ into μm³), the same amount of pressure can be generated with devices that can fit into one's hand. Since its inception in 1959³, the diamond anvil cell has been popularized⁴, being the only apparatus that can achieve static pressure as high as 1 TPa⁵, simulating the conditions of the Earth's core and larger

planetary bodies.

3.1.1 Diamond Anvil Cells

The diamond anvil cell applies pressure to sample by compressing it between the flattened culets of two opposed diamond anvils. The culet diameter can vary from 1 millimeter to a few tens of micrometers. A smaller culet diameter allows higher achievable pressures, but also confines the size of the sample that can be placed between the anvils. The anvils are placed on seats that transport the load from the external metallic cell onto the anvils. The maximum achievable pressure is limited to the mechanical strength of the anvils and the seats, therefore, the use of anvils made of diamond and seats made of ultra-hard materials such as tungsten carbide (WC) (Figure 3.1-1) increases the maximum achievable pressure.

Directly compressing the diamonds against each other can cause several problems, such as their fracture and the escape of the compressed material due to axial stress. For this reason, a metallic gasket with a circular hole is placed between them that also helps confine the sample within a cylindrical pressure chamber (Figure 3.1-2). The most commonly used gasket material is rhenium, due to its sufficiently high hardness and low brittleness.

The transparency of diamonds in a wide range of radiation (including the optical spectrum) allows the sample to be observed and probed using different types of radiation. In measurements where the rotation of the sample is necessary, such as single-crystal X-ray diffraction, the Boehler-Almax⁶ diamond anvil and seat design has been developed as an alternative to the brilliant-cut diamonds, that increases the opening angle of the DAC.

In the present thesis, BX90-type⁷ DACs were used, a DAC design developed at BGI at Bayreuth, equipped with brilliant-cut, modified brilliant-cut, or Boehler-Almax diamonds. For some experiments conducted at the ESRF, LeToullec-type⁸ membrane DACs were used instead.

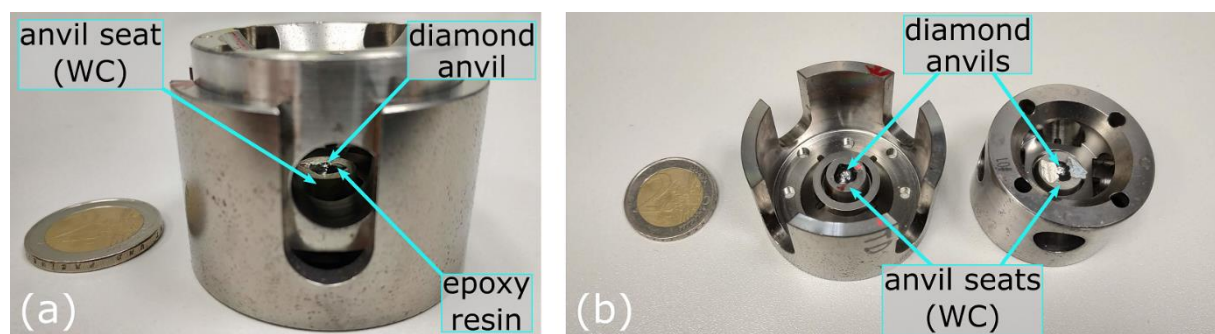


Figure 3.1-1. Photos of a closed (a) and open (b) BX-90 type diamond anvil cell.

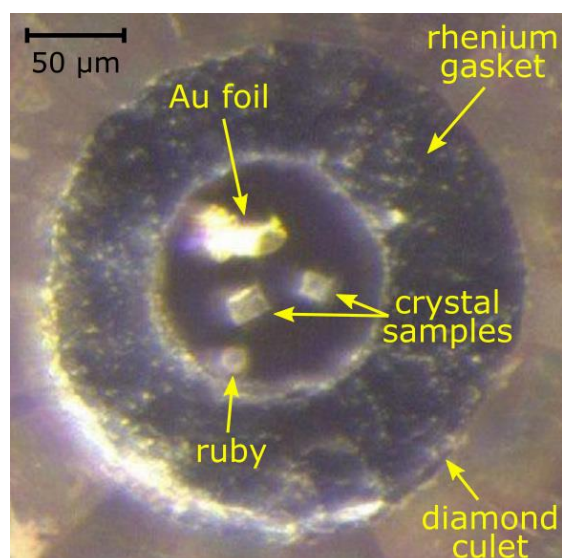


Figure 3.1-2. A photograph of the pressure chamber taken under an optical microscope through the diamond anvil (top view). The culet size of the diamond pair is 250 μm . Ruby and Au foil are used as internal pressure standards.

3.1.2 Pressure transmitting media

The sample is almost never placed directly between the two diamond anvils. In the contrary, inside the pressure chamber it is surrounded by a material acting as a pressure transmitting medium from the anvils to the sample. Without a pressure medium, the uniaxial compression of the two opposing diamond anvils would cause uniaxial stress on the sample and lead to high shear strains. This is usually not wanted in most scientific cases. The material surrounding the sample helps to make the stress isotropic (hydrostatic), which can be achieved when the pressure medium is gas or liquid, but above a certain pressure any material will solidify and be subject to anisotropic stresses. Nonetheless, quasi-hydrostatic conditions can be achieved even at high pressures, when inert gases are loaded into the pressure chamber. Such choice of pressure medium provides also a chemically inert environment for the sample.

Apart from inert gases, solid materials, e.g. NaCl, KCl and MgO, are used as pressure media inside the DAC pressure chamber, surrounding the sample forming a “sandwich”-like assembly. Such materials are usually chosen for their transparency and relatively low thermal conductivity, properties that are important in the case of laser heating in the DAC (see Section 3.2).

The pressure media that were used in the experimental studies of the present thesis were gaseous neon and argon, as well as solid potassium chloride. In the case of neon and argon, the pressure media were loaded in the respective DACs using the gas-loading system developed and installed at BGI⁹. Using this method, the DAC is placed inside a pressure vessel and the gas of choice is pumped and pressurized surrounding the DAC. The DAC is externally closed using a piston and secured at place with screws. Lastly, the gas is released, and the DAC retrieved, with the pressure medium confined inside the pressure chamber.

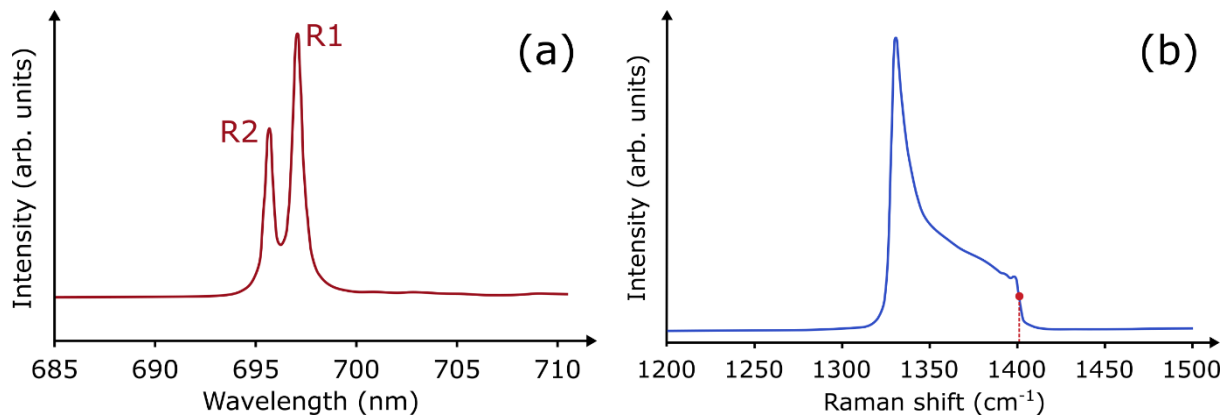


Figure 3.1-3

Figure 3.1-4. Indicators of pressure inside the diamond anvil cell; (a) Ruby fluorescence spectral peaks R1 and R2. The position of peak R1 is used as a pressure gauge; (b) Raman shift spectrum of a diamond anvil under stress. The high-wavenumber edge position (red circle) is used as a pressure gauge.

3.1.3 Pressure determination

DAC experiments rely on the accurate *in situ* determination of pressure inside the pressure chamber. Different methods are used, usually relying on calibrants with a known response to pressure or a known equation of state. In the studies presented here, three different methods were used, each depending on the accuracy required or the ease of access.

The most common method is the pressure dependence of the ruby (Cr-doped Al_2O_3) fluorescence^{10,11}. Typically, a micrometer-sized ruby sphere is placed inside the pressure chamber and its fluorescence induced by laser light is observed. The wavelength λ of the R_1 spectral peak is directly connected to pressure using the equation:

$$P(\text{GPa}) = \frac{A}{B} \left[\left(\frac{\lambda}{\lambda_0} \right)^B - 1 \right],$$

where A and B are constants that depend on the calibration^{10,11}, and λ_0 is the wavelength of the peak at ambient pressure conditions (Figure 3.1-4 (a)). This method of pressure determination is accurate and wide-spread due to the ease of use, but the ruby fluorescence is weaker and not easily measured at pressures above a megabar. At such high pressures, the danger for the ruby to be directly squeezed between the diamond anvil increases and in such a case, the non-hydrostatic pressure applied on the ruby affects the fluorescence signal and thus, the accuracy of the measurements. Moreover, the addition of a ruby inside the pressure chamber complicates the chemical conditions at the sample environment and this is usually not wanted in chemically sensitive experiments, especially when high temperatures are involved. For this reason, the ruby fluorescence method had only limited use in the experiments of the present work.

As an alternative to ruby, the diamond anvil itself can be used for pressure determination. In this case, the pressure-dependent frequency of the first-order Raman mode of the diamond

is calibrated and the signal is collected from the center of the culet. Since the stress within the diamond anvil follows a steep gradient from ambient pressure at the table of the diamond to the maximum pressure at the culet, the whole Raman band is usually collected in this way, due to the imperfect spatial focus of the laser used to induce the Raman scattering (Figure 3.1-4 (b)). The high-wavenumber edge corresponds to the part of the diamond with the highest stress, i.e. the culet face, and the wavenumber value can be correlated to the pressure in the sample chamber¹². This method is preferred for experiments above megabar pressures, or when the application of ruby is not possible or not desirable. The method is, however, sensitive to the focusing of the laser, since the stress gradients can be steep even along the surface of the diamond culet.

The most precise technique for pressure determination is the X-ray diffraction of a material with a well-known equation of state, it requires, however, the availability of a diffractometer. The unit cell parameters can be determined with high precision leading to an accurate calibration. A small amount of a material with well-studied equation of state can be added to the sample chamber to be used as calibrant, usually chosen to be inert and compressible. Alternatively, as in the experiments reported of this study, the pressure medium itself is used as a pressure gauge without the addition of an extra substance. Materials commonly used as pressure media, such as KBr¹³, KCl¹⁴, Ne¹⁵, MgO¹⁶ and NaCl¹⁶, have been extensively studied in a wide pressure range. KCl and Ne are the materials used as pressure gauges in the XRD experiments of this thesis.

3.2 Laser Heating in the Diamond Anvils Cell

One of the advantages of using diamond anvils is their transparency at a broad range of the electromagnetic spectrum that permits the probing and observation of the sample pressurized between them with different types of radiation. This characteristic allows a laser beam of appropriate wavelength to be focused on the sample through the diamond anvils and heat the sample, provided that the laser power is high enough and the material is sufficiently absorbing the laser radiation¹⁷.

The radiation absorption is a function of wavelength and is unique for every material. Due to this, lasers of different wavelength are better suited for heating different types of samples. The most commonly used lasers in modern high-pressure science are emitting either at the near-infrared radiation (NIR) wavelength of 1064 nm, produced by a Nd-doped yttrium aluminum garnet crystal (Nd:YAG), or the infrared radiation (IR) wavelength of 10.6 μm , produced by gaseous CO₂. The former, being close to the visible spectrum, is usually utilized with materials that are visibly non-transparent, e.g. metals, metal alloys and various oxides. The latter is absorbed by more substances, including lighter elements and molecules, such as silicon and water. The easy absorption of the CO₂ laser by many different materials makes it more difficult to handle, reflect and focus by conventional optics. It is therefore utilized mainly in the heating of materials transparent to visible and NIR light, which would not absorb a

shorter wavelength laser beam.

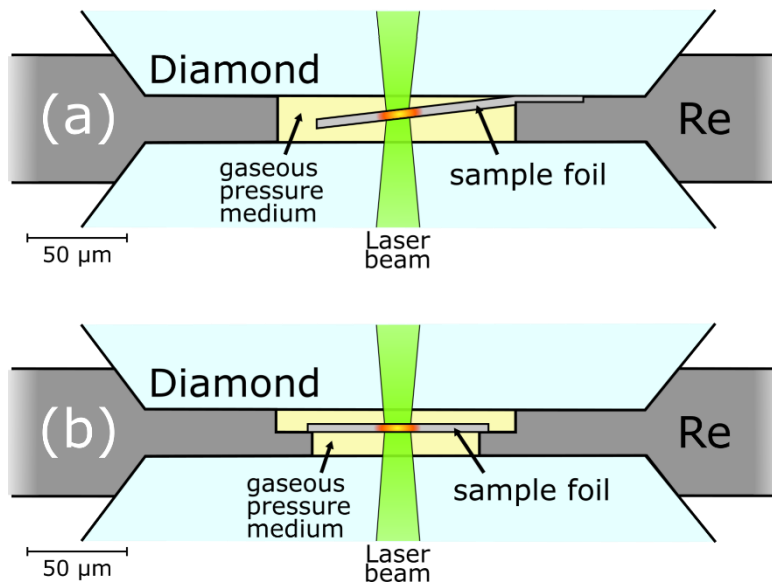


Figure 3.2-1. Typical pressure chamber configurations to insulate the sample in the LHDAC when gaseous pressure medium is used; (a) sample foil compressed between the Re gasket and the diamond anvil and bent into the pressure chamber; (b) sample foil set on a stepped gasket.

Diamond is the hardest material found in nature, but it is also one of the best thermal conductors. One of the biggest challenges of laser heating inside the diamond anvil cell (LHDAC) is to decrease the temperature gradients and stabilize the laser heating of a sample that lies micrometers away from the diamond anvils. Double-sided laser heating is used to reduce the vertical temperature gradient while the lateral gradients are reduced by transforming the common Gaussian-shaped laser beam to a flat-top with the use of specialized optical components called π -shapers¹⁸.

The insulation of the sample from the diamond anvils is another very important aspect and special care is taken during sample loading to isolate the sample from the diamonds, by interposing a thermal insulator. It is common that the pressure medium acts also as thermal insulator. Different pressure chamber assemblages are used, depending on the type of the pressure medium; gaseous or solid. In the case of solid pressure media, the sample is usually placed between two compressed layers of the insulator material, creating a “sandwich” assemblage. Different solutions have been proposed for the case when the pressure medium is gaseous. One common method is to place the sample on a base made of two or three rubies before gas loading, that also act as pressure gauge. However, the placement of several rubies inside the sample chamber is not always acceptable in certain experimental cases. In the present thesis, two different methods of sample assemblages have been used, as seen in Figure 3.2-1. In the first method (Figure 3.2-1 (a)), the sample is compressed between the rhenium gasket and the diamond, and bent in a small angle so that it does not have contact with neither of the diamond anvils allowing for gas pressure medium to feel the intermediate space. In the second method (Figure 3.2-1 (b)), the gasket is firstly carved up to a certain depth creating a cavity of a certain diameter and then a hole with a smaller diameter is drilled,

creating a “table” that the sample can be placed upon. Both techniques ensure that the sample is kept at a distance of a few micrometers from both diamond anvils. When the sample is appropriately insulated and the laser power high enough, temperatures of as high as 5700 K can be achieved at pressures above 350 GPa¹⁹, and even higher at lower pressures.

The most common method of laser heating inside the DAC is by providing a constant laser power to the sample, making an effort to keep the sample temperature spatially and temporally stable. This method is referred to as continuous-wave (CW) heating. In addition to CW, pulsed lasers have been used starting from the first attempts to laser heat samples in a DAC, with the advantage of achieving significantly higher temperatures^{20,21} due to the concentration of the high laser power in a short impulse. The repetitive heating and cooling of the sample makes time an extra variable in addition to pressure and temperature, which is not possible with continuous-wave laser heating.

For the purposes of pulsed laser heating setups, Q-switched or pulsed lasers are used, with pulse duration ranging from a few nanoseconds up to several milliseconds, depending on the experimental conditions. At such timescales, the sample can still be considered under thermal equilibrium, provided that appropriate time-resolved measurements follow the laser excitation. This is the main method of pulse heating under static pressure in in-house and synchrotron facilities. With the advance of high-pressure science at X-ray free-electron lasers (XFELs), the sample is probed at the femtosecond range and thus, ultrafast lasers need to be employed for such pump-probe experiments.

The LHDAC technique is used widely in high-pressure geoscience and material science and has been coupled with various experimental set-ups, such as X-ray diffraction^{22,23}, Nuclear Inelastic Scattering (NIS), the Synchrotron Mössbauer Source^{24,25}, and X-ray Absorption Near Edge Structure spectroscopy (XANES)^{26,27}. The present thesis includes the development of a NIR double-sided pulsed laser heating setup and its applications when coupled with different experimental set-ups at synchrotron facilities.

3.3 Temperature Measurement

All matter with a temperature above absolute zero emits radiation that is called thermal radiation. The intensity and range of energies (i.e. the band of wavelengths) of the emitted radiation is mainly a function of temperature but also partially depends on the type of the material. An ideal physical body that absorbs all the incident radiation falling on it is called a “black body” and it is emitting the maximum amount of thermal radiation at a specific temperature. The thermal radiation at a wavelength λ , emitted by a black body at absolute temperature T and at thermal equilibrium, namely “blackbody radiation” is described by Planck’s law:

$$B(\lambda, T) = \frac{2hc^2}{\lambda^5} \frac{1}{e^{\frac{hc}{\lambda kT}} - 1},$$

where k is the Boltzmann constant, h is the Planck constant, and c is the speed of light in the medium where the radiation is emitted.

In reality, physical bodies emit thermal radiation at a fraction of the idealized blackbody maximum for a given wavelength. Emissivity ε is defined as the ratio of the thermal radiation from a surface to the radiation from an ideal blackbody surface at the same temperature. In practice, the wavelength dependence is considered insignificant and emissivity is defined as a constant number $0 \leq \varepsilon \leq 1$. By definition, a blackbody has $\varepsilon = 1$ and a non-ideal body has $\varepsilon < 1$, also called a “gray body”. The gray body approximation is used in all results of this study.

In high-pressure DAC experiments, the temperature of the heated sample is determined using the spectroradiometry technique. The thermal radiation is focused on a spectrometer and a detector that determines the spectral intensity of incident radiation. The optics and spectrometer are optimized for the visible to near infrared wavelength range (typically at around 600 -900 nm), where the thermal radiation intensity is sufficiently high for the determination of temperatures above 1000 K.

Every optical system has a transfer function that contributes to the signal collected at the detector. In order to separate the optical response, as well as any external “background” radiation, from the thermal radiation of the sample, the system is calibrated before the experiment. This is done using a calibration incandescent lamp that has a known relation between the current provided to the lamp and the temperature developed at the filament (Figure 3.3-1 (a)). The resulting spectrum can be directly compared with the expected “ideal” Planck function for the known temperature of the lamp and by dividing the two, the system response can be determined. During laser heating, the spectrum collected from the heated sample is then corrected from the transfer function of the system and the resulting spectrum is the thermal radiation of the sample. Lastly, the thermal radiation spectrum is compared to the Planck function and a least-square fitting algorithm provides the estimated temperature for the given spectrum (Figure 3.3-1 (b)).

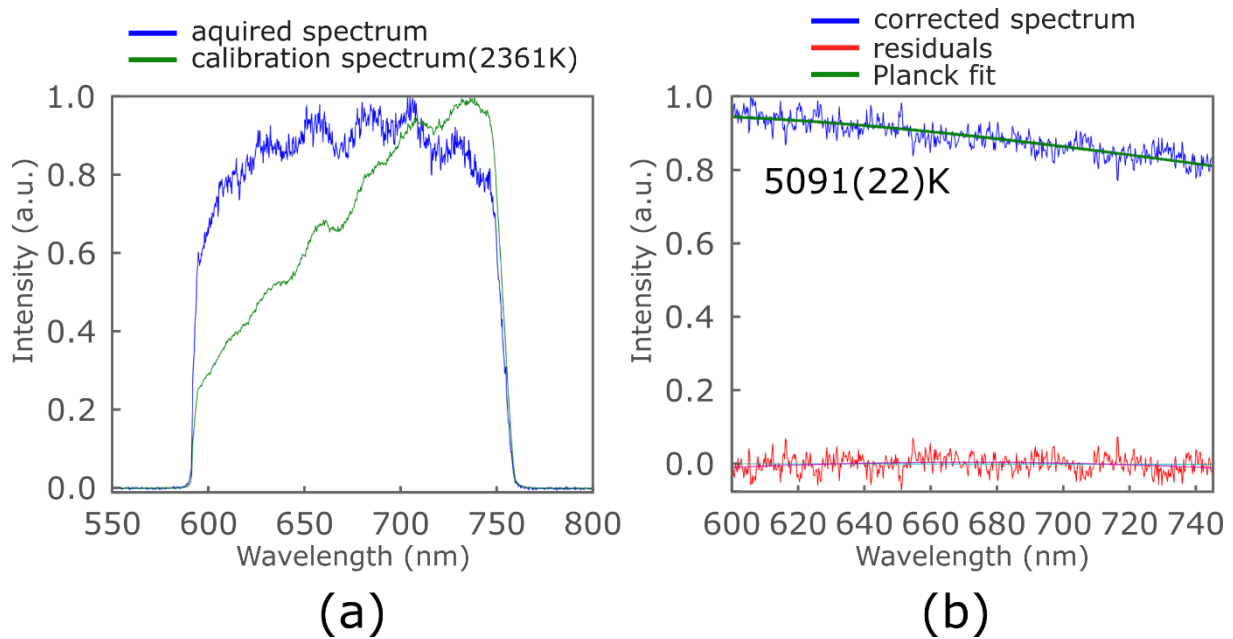


Figure 3.3-1. Examples of thermal radiation spectra collected in the range of 590 – 760 nm. The collected spectrum is compared to the radiation collected from a calibration lamp radiating at a known temperature (a); By removing the optical transfer function of the system, the corrected spectrum can be fitted to the Planck function and estimate the temperature of the radiating sample (b).

3.4 Mössbauer spectroscopy

3.4.1 Basic Principles

Mössbauer spectroscopy is based on the Mössbauer effect, which is the *recoilless* emission and absorption of gamma radiation by nuclei, when bound in a solid. As firstly observed by Rudolf L. Mössbauer in 1958, when nuclei are bound to a crystal structure, they can emit and absorb γ -rays without energy loss due to nuclear recoil. The recoil momentum is instead delivered to the surrounding crystal lattice rather than to the emitting or absorbing nucleus alone, resulting in strong resonance at the same energy level. The energy range of the absorption is, in this case, very narrow and is practically limited only by the natural linewidth of the nuclear transition, a consequence of the uncertainty principle.

The strong resonance observed due to the Mössbauer effect allows to precisely measure very small energy changes in nuclei, atoms, and crystals induced by electrical, magnetic, or gravitational fields. This sensitivity is enough to detect differences in the atomic environment of a crystal lattice through the small changes in the energy levels of the nucleus.

There is a number of elements that have isotopes with appropriate nuclear transition energy and half-life to be used in Mössbauer spectroscopy. Iron is the most commonly studied element and specifically the isotope ^{57}Fe and its nuclear transition at 14.4 keV, due to the importance of iron in technological applications and geological studies.

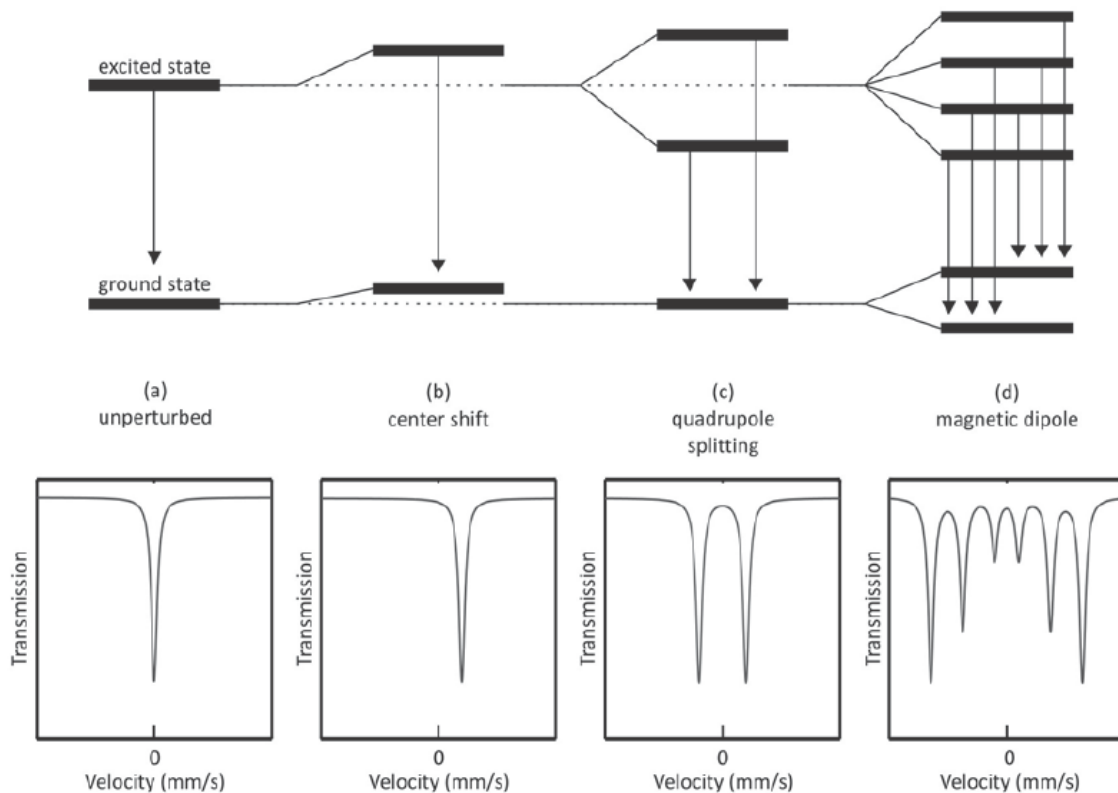


Figure 3.4-1. Nuclear Hyperfine interactions for ^{57}Fe , showing the nuclear energy level diagram for (a) an unperturbed nucleus; (b) a change in center shift; (c) with quadrupole splitting; and (d) with magnetic dipole interaction. Each interaction is accompanied with a resulting Mössbauer spectrum. Modified after ²⁸.

Typically, there are three types of nuclear interactions that are observed: isomeric shift, quadrupole splitting, and hyperfine splitting. The isomer shift describes the relative changes in the resonance energy of a nucleus due to the transition of its s-orbital electrons. A common effect that can alter the isomeric shift of a nucleus is the change of the oxidation state. The quadrupole splitting refers to the splitting of the nucleus spin state into sub-states with slightly different energy levels. It is caused by the asymmetric electronic charge distribution of the atom that creates an electric field gradient surrounding the nucleus. For ^{57}Fe the excited state is split in two sub-states and the ground to excited state transitions create two absorption lines in a Mössbauer spectrum. Hyperfine splitting refers to the splitting of the nucleus spin state into sub-energy levels in the presence of a magnetic field. For ^{57}Fe the excited distinct sub-states are four, leading to totally six possible state transitions and as a result six absorption lines in the Mössbauer spectrum (Figure 3.4-1).

To create a Mössbauer spectrum, the energy levels around the desired resonance energy need to be probed and a nucleus of the same type (i.e. the same isotope) as the absorber, called “source”, needs to be excited at a high-energy state to emit a γ -ray during relaxation. In Mössbauer spectroscopy setups, the source is placed on an oscillating drive, that moves the source towards and away from the absorber. In this way, due to the Doppler effect, the emitted γ -ray energy is modulated to a small range around the initial emitted energy, depending on the velocity of the emitter relatively to the static absorber at the time of the

photon emission. A detector behind the absorber receives the incident photons and when the detection is synchronized with the Mössbauer drive speed, the energy level of each photon can be assigned. This usually requires a modulation of the source in the order of a few millimeters per second and it is common for Mössbauer spectroscopy to represent energy in terms of velocity (mm/s) instead of neV.

3.4.2 Synchrotron Mössbauer Source

Mössbauer spectroscopy at high pressures can benefit from the small focus of the synchrotron radiation beam. The experimental setup developed at the Nuclear Resonance Beamline (ID18) at the ESRF²⁹ allows to perform energy domain Mössbauer spectroscopy on samples inside DACs at high pressures and high temperatures. The technique is known as Synchrotron Mössbauer Source (SMS) and utilizes the ^{57}Fe -enriched iron borate $^{57}\text{FeBO}_3$ crystal³⁰ to achieve neV energy resolution at 14.4 keV. The iron borate crystal has the characteristic of allowing pure nuclear diffraction at specific Bragg reflections where electronic diffraction is instead forbidden³¹. While the hyperfine interactions cause a splitting of the nuclear levels of the crystal, under specific temperature conditions and with the application of a small external magnetic field, a single-line nuclear resonance can be achieved³². When the previous conditions are met, the energy width of the emitted line is close to the natural linewidth of the Mössbauer resonance, thus, allowing Mössbauer spectroscopic studies. In this way, the borate crystal acts as a very fine monochromator of the incident synchrotron radiation. The crystal is then mounted on a drive that provides the velocity oscillations that are necessary for Mössbauer spectroscopy (Figure 3.4-2).

The main advantages of SMS in contrast to a conventional Mössbauer setup are the high radiation intensity and the small focus possibility. The high intensity of the source allows an improved signal-to-noise ratio allowing to collect a spectrum with sufficient statistics usually within 1 hour of measurements (depending on the experiment) while for the same quality of data a conventional radioactive Mössbauer source needs several days. The small beam focus is particularly important for measurements inside the DAC. The typical dimensions of the beam in such experimental setup are in the order of 10-15 μm , which allows Mössbauer spectroscopic studies of a laser-heated sample in the DAC.

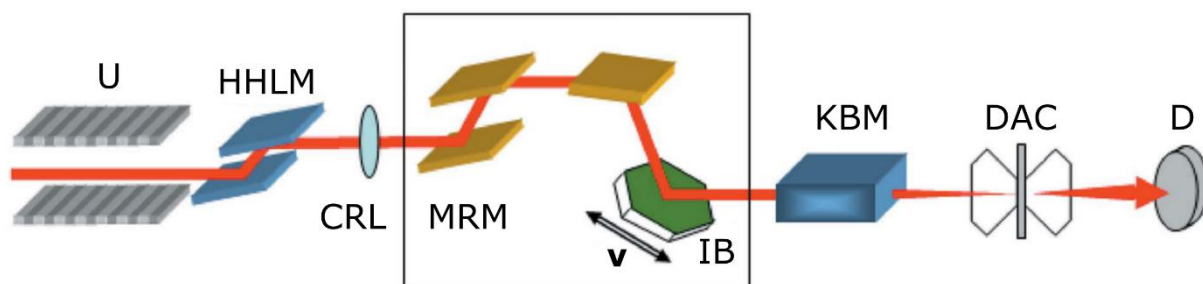


Figure 3.4-2. Optical scheme for a high-pressure experiment with DACs using the Synchrotron Mössbauer Source (SMS) at ID18 of the ESRF. U: undulator; HLM: high-heat-load monochromator; CRL: compound refractive lens; MRM: medium-resolution monochromator; IB: iron borate ($^{57}\text{FeBO}_3$) crystal; KBM: Kirkpatrick-Baez mirrors; DAC: diamond anvil cell; D: avalanche photodiode detector. Modified after ²⁹.

For the purposes of this study, the collected spectra were fitted using a full transmission integral with a normalized Lorentzian-squared source line-shape using the MossA software package³³.

3.4.3 Nuclear Inelastic Scattering

Nuclear inelastic scattering (NIS), in contrast to Mössbauer spectroscopy, focuses on the inelastically scattered phonons after a recoil event instead of the recoil-free resonant γ -ray absorption of the nuclei. When atomic nuclei release or absorb high-energy radiation with recoil and the transferred momentum of the nuclear recoil is high enough to force lattice vibrations, phonons are generated and are inelastically scattered. A phonon is an elementary atom vibration in the crystal lattice at a specific frequency, often considered a quasiparticle.

NIS can only be performed using synchrotron radiation and special instrumentation. Experiments that are part of the present thesis were carried out at the NIS setup of the Nuclear Resonance beamline (ID18) at the ESRF in Grenoble. The initial beam of 6 GeV created in the storage ring is monochromatized in two stages. In the first stage, the bandwidth is reduced to a few eV by a high heat-load monochromator, that is composed of two independent, cryogenically cooled crystals (Si(1 1 1) reflections). In the second stage, the bandwidth is reduced down to the meV regime (a bandwidth of 0.5 to 2 meV) by a high-resolution monochromator^{34,35}, to the desired 14.4 keV energy of the ^{57}Fe transition. As a final step, the beam passes through an ionization chamber where the flux of the incident radiation is monitored before being directed to the sample and exciting the resonant nuclei (Figure 3.4-3). Three avalanche photo diode detectors (APDs) measure the nuclear scattering. Two of them (detectors #1 and #2 in Figure 3.4-3) are located very close to the sample (1-2 mm distance) and count the photons scattered in a large solid angle, while the third (detector #3 in Figure 3.4-3) counts the photons scattered by the nuclei in the forward direction.

The two APD detectors close to the sample measure the inelastic scattering of radiation by the resonant nuclei in a large solid angle. The third detector measures the nuclear forward scattering (NFS), which is a coherent and elastic process. This detector is placed far away from the sample, to avoid contribution from the incoherent scattering.

The incident radiation energy is a function of the angular positions of the crystals in the high-resolution monochromator hence an energy scan can be achieved by rotating them. In this way, the intensity of incoherent (detectors 1# and #2) and coherent (detector #3) scattering can be measured within an energy range of a few hundred meV.

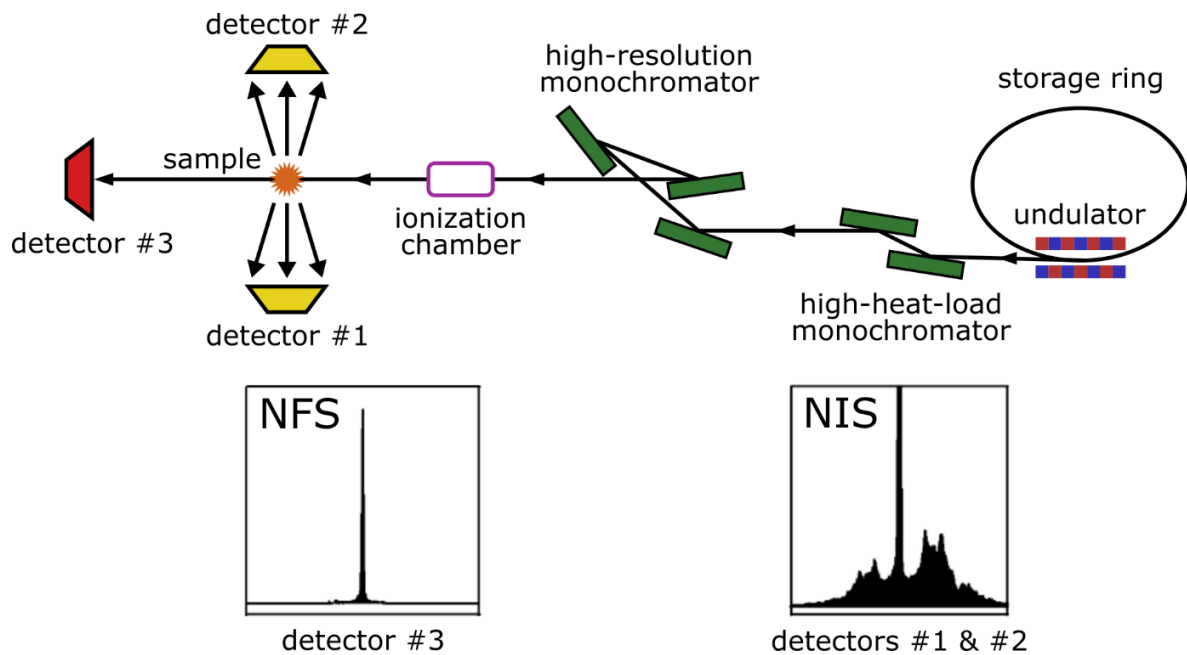


Figure 3.4-3. Experimental setup for measurements of inelastic scattering at the Nuclear Resonance Beamline (ID18) at the ESRF. Three avalanche photo diode detectors (APDs) are placed in different orientations. Detectors #1 and #2 are located close to the sample, measuring the incoherent nuclear inelastic scattering (NIS) at a large angle. Detector #3 measures the coherent nuclear forward scattering (NFS). Modified from ³⁴.

An essential part for the NIS experiments is the synchronization of measurements with the incident synchrotron beam. Therefore, the choice of the storage ring mode is very important. Time-resolved experiments are performed when the storage ring operates in a pulsed mode, such as the 16-bunch or the hybrid mode. In these modes, each pulse has typically a duration of less than 100 ps, with varying delays between the pulses. With the use of fast electronics, only the events after a certain delay from the beam pulse are considered. This is done to avoid the electronic scattering from the sample, a much faster phenomenon than the nuclear resonant scattering. While the beam illuminates the sample, electronic scattering dominates the spectral intensity. It is, therefore, avoided by only counting the delayed events originating from the nuclear scattering.

A NIS spectrum consists of the intense resonant peak at the resonant (E_R) energy, i.e. the energy of the elastic scattering. This energy level is usually set to zero, and all energy levels are expressed relatively to the E_R . On the left ($E < 0$) and right ($E > 0$) side of the elastic peak appear vibrational modes on lower and higher energies, respectively (Figure 3.4-4). The vibrational modes appear symmetrically, but with different intensities. Peaks at higher energies represent phonon creation and peaks of lower energies represent phonon annihilation during the inelastic scattering process. The probability ratio between phonon creation and phonon annihilation for a given energy E , i.e., the symmetry of the spectrum around the elastic line, is a function of temperature^{24,36,37}. At high temperatures the intensity of the two peaks tends to become equal.

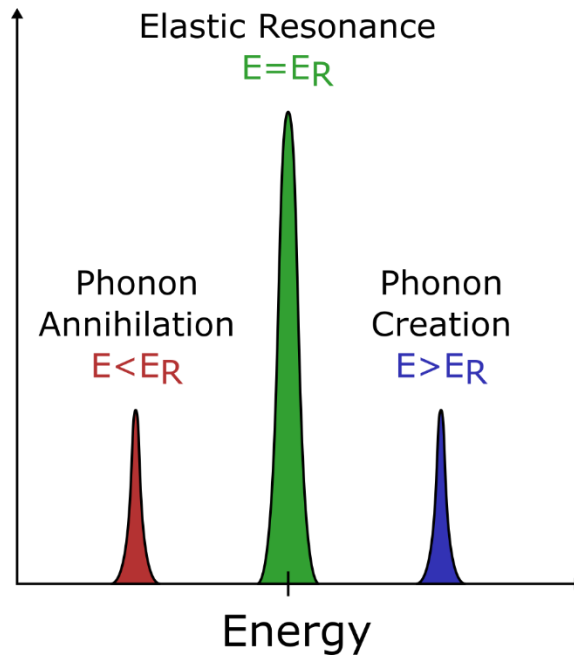


Figure 3.4-4. A NIS spectrum consists of an intense peak at the resonant (E_R) energy, i.e. the energy of the elastic scattering. The left ($E < E_R$) and right ($E > E_R$) sides of the elastic peak appear due to the nuclear inelastic scattering of the incident radiation and correspond to the annihilation $E < E_R$ and creation $E > E_R$ of phonons.

Due to this effect, the ratio of intensities of the two inelastic peaks in either side of the elastic peak can be used for temperature determination. The phonon creation energies $S(E)$ and phonon annihilation energies $S(-E)$ are associated by the Boltzmann factor as follows:

$$S(E) = e^{\beta E} S(-E),$$

where $\beta = 1/(k_B T)$ is the inverse temperature (T), and k_B is the Boltzmann constant.

A NIS spectrum can be used to extract the partial density of states (DOS) of the sample under investigation, and from the DOS function, the sound velocities can be calculated, such as the Debye, primary wave and secondary wave sound velocities.

In the studies presented in this thesis, the NIS method was coupled with pulsed laser heating inside the diamond anvil cell and time-resolved inelastic scattering spectra were collected at high temperatures and pressures.

3.5 X-ray Absorption Spectroscopy

X-ray Absorption Spectroscopy (XAS) is a technique for determining the geometric and electronic structure of matter. It is based on the excitement of the inner-shell electrons of an atom by high-energy photons in the X-ray regime leading to the absorption of the incident photons. Radiation is more likely to be absorbed at frequencies that close to the electron binding energies. The X-ray energy range matches the energy levels of the core electrons of the atoms of most elements whereas lower radiation energies are used to excite electrons of

the outer shells.

The chance of a photon to be absorbed increases rapidly when its energy is just high enough to excite a specific core electron to valence bound states or to emit it, creating a photoelectron. This effect causes an abrupt change in energy spectra at around that energy level, called an absorption edge. This energy level is characteristic for every type of atom and for every electron shell, and the absorption edge gets its name from the shell of the excited core electron. Principal quantum numbers of $n = 1, 2$ and 3 correspond to K-, L- and M-edges, respectively. The present thesis focuses on the K-edge of iron at the energy level of 7112 eV, which corresponds to the excitation of an 1s electron.

At energy levels above the electron binding energy ($E_{binding}$), the high-energy photons are absorbed, and the photoelectrons are ejected having a kinetic energy ($E_{kinetic}$):

$$E_{kinetic} = h\nu - E_{binding},$$

where the $h\nu$ is the energy of the incident photon (h is the Planck's constant and ν the photons frequency). This effect leads to a characteristic change in the absorbance of the atom for the energies below and above the absorption edge.

The study of the spectra around an absorption edge provides information about the atom under investigation and its local environment. A XAS spectrum is usually separated in two main energy ranges (Figure 3.5-1):

- (i) The X-ray absorption near-edge structure (XANES) is the region that includes the rising edge, the energy range immediately before the edge (pre-edge), as well as the region that extends for 50-100 eV after the absorption edge (yellow region in Figure 3.5-1). The characteristics of the absorption at this energy region provide chemical information about the valence and oxidation state of the atom, the coordination environment (e.g., octahedral, tetrahedral coordination) and subtle geometrical distortions of it. The near-edge structure of the spectrum is determined by the multiple scattering of the excited inner-shell photoelectron on several of the atoms neighboring the absorbing atom. The multiple scattering effect is dominant for this energy range due to the low kinetic energy of the emitted photoelectrons.
- (ii) The extended x-ray absorption fine structure (EXAFS) is the region that extends up to 2000 eV from the absorption edge. In the high kinetic energy range of the photoelectron, the scattering cross-section with neighbor atoms is weak and the spectrum region is dominated by the single scattering of the photoelectron on the atoms around the absorbing atom. Due to the wave-like nature of the electron, the electrons backscattering on surrounding atoms interfere with the electrons emitted by the absorbing atom, creating interference patterns in the EXAFS region

of the spectrum (purple region in Figure 3.5-1). With the use of Fourier transformation and model fitting analysis, the radial distribution function (i.e. the variation of electron density around the absorbing atom as a function of distance) can be obtained, providing information about the local interatomic distances around the absorber.

X-ray absorption spectroscopy is a technique that majorly profits from synchrotron radiation facilities that can provide the necessary high intensity and energy tunability for the measurements. The XAS data presented in this thesis were collected at the Energy Dispersive X-ray Absorption Spectroscopy (ED-XAS) beamline at the ESRF (ID24). The experimental setup of ID24 utilizes a bent silicon crystal as polychromator, to focus different beam energies at a different angle on the sample. The collimated pink beam coming from the undulator is previously focused from mirrors at a Kirkpatrick–Baez geometry falling at different angles on the polychromator crystal. An extra vertical focusing mirror downstream of the polychromator is used to refocus the beam on the sample, achieving a focusing size as small as 1 μm at full-width half maximum (FWHM). Behind the sample, that is placed at the focal position of the X-ray beam, a position-sensitive detector collects the incident radiation that was not absorbed at the sample. Using a known sample as calibrant, each position on the detector can be calibrated to a specific energy of the incident X-ray beam, being chromatically dispersed (Figure 3.5-2). This technique allows the collection of a whole X-ray absorption spectrum simultaneously with a single exposure of the detector, usually in the order of a few milliseconds. By bending the polychromator accordingly, the detector can be illuminated by a different energy range, depending on the selected absorption edge of the sample.

The fast spectrum collection and the small focusing size achieved at ID24, allows for detailed X-ray absorption mapping inside the DAC³⁸. The experimental technique is coupled with a laser heating system allowing for XAS on samples at high temperatures and pressures³⁹.

The ED-XAS technique is particularly well-suited for detecting small chemical changes of the sample, due to the chemical element selectivity and the spatial and element high-density sensitivity. Moreover, the short collection time, the small required sample volume and the possibility to measure both crystalline and amorphous samples, make ED-XAS a powerful technique to spatially and temporally track chemical reactions inside the LHDAC, as presented in the experimental results of the present thesis.

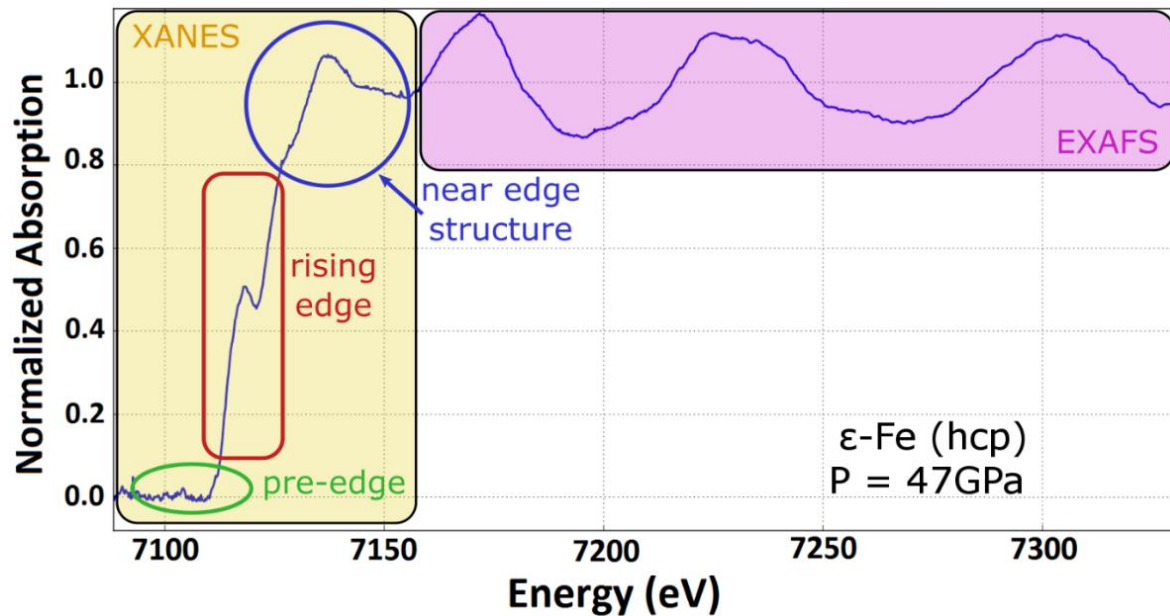


Figure 3.5-1. X-ray absorption spectrum of the K-edge of ϵ -Fe at 47 GPa. The energy regions are separated in two parts: The X-ray Absorption Near-Edge Structure (XANES) region right before and right after the absorption edge (light orange area) and the Extended x-ray Absorption Fine Structure (EXAFS) that is the range well above the absorption edge (purple area).

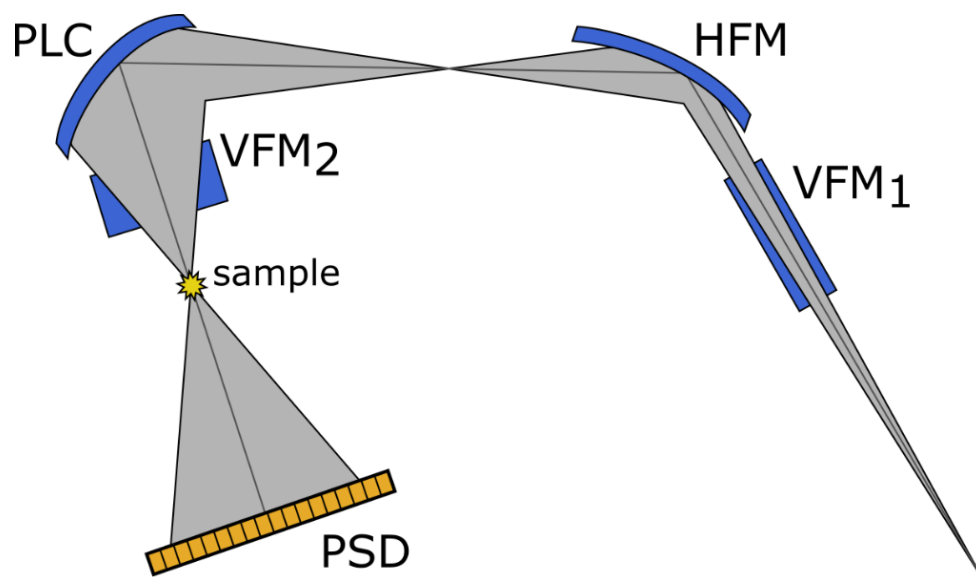


Figure 3.5-2. Experimental setup for Energy Dispersive X-ray Absorption Spectroscopy (ED-XAS) at ID24 at the ESRF. The incident beam is chromatically dispersed using a polychromator crystal (PLC) and the whole range of energies around the selected absorption edge is collected simultaneously from a position-sensitive detector (PSD) in a single exposure. The optical scheme consists of mirrors in a Kirkpatrick–Baez geometry for vertical (VFM_1) and horizontal focusing (HFM). A second vertically focusing mirror (VFM_2) downstream of the polychromator is used to refocus the beam onto the sample. Modified from ³⁸.

3.6 High Pressure SCXRD

X-ray crystallography has extensive use in high-pressure science as the major method to characterize the atomic structure of crystalline solids. It is based on Bragg's law, which is a special case of X-ray diffraction.

X-ray diffraction is the elastic scattering of x-ray photons by the electrons of atoms. X-ray photons have wavelengths in the order of angstroms (0.1 – 100 Å). Such distances are relevant to the interatomic distances in the crystal lattice of a solid, therefore, incident monochromatic x-rays that are in phase can be constructively or destructively interfered when scattered from a periodic crystal lattice. The condition for constructive interference is described by Bragg's law:

$$2d \sin\theta = n\lambda,$$

where d is the spacing between diffracting lattice planes, θ is the angle of the incident X-ray, n is any integer number and λ is the wavelength of the beam (Figure 3.6-1). According to this model, the incoming X-rays are specularly reflected from the atoms. When the scattering atoms are arranged symmetrically in planes with a constant distance d between them, the X-rays scattered from adjacent planes will interfere constructively when the angle θ between the plane and the X-ray results in a difference between the path lengths of the two waves equal to an integer multiple n of the wavelength λ . The total path difference between two waves undergoing interference is given by $2d\sin\theta$.

A crystalline material can be considered an object with a 3-dimensional periodic structure. The periodic positioning of atoms is consisted of a basic unit arrangement of atoms that is repeated in all three dimensions to form the whole body of the crystal. This "building block" is called the unit cell. For the purposes of crystallography, the repetition of atoms is considered infinite in all directions. The relative orientation between the crystal and the incident X-rays defines the way that the X-rays will be scattered. Although the scattered X-rays cancel one another out in most directions through destructive interference, they add constructively in a few specific directions, determined by Bragg's law. As a result, the incident X-rays on the crystal are scattered at different angles from the initial forward direction. When a two-dimensional detector is placed at some distance from the sample, these specific directions appear as spots on the diffraction pattern called reflections (Figure 3.6-2 (b)). The symmetry in the intensity and position of the reflections (also called Bragg peaks) is correlated to the symmetries of the atoms in the crystal lattice and the dimensions of the unit cell. It is possible to retrieve the exact atomic positions in the crystal lattice, when the phase and position of the diffracted photons is known. However, both the creation of a coherent X-ray source as well as the measurement of the phase of the incident photons on a detector is technologically demanding. What is known as the "phase problem" is the biggest hurdle of modern crystallography. Nonetheless, mathematical methods exist that can accurately model the atomic positions and symmetry of a crystal through X-ray diffraction.

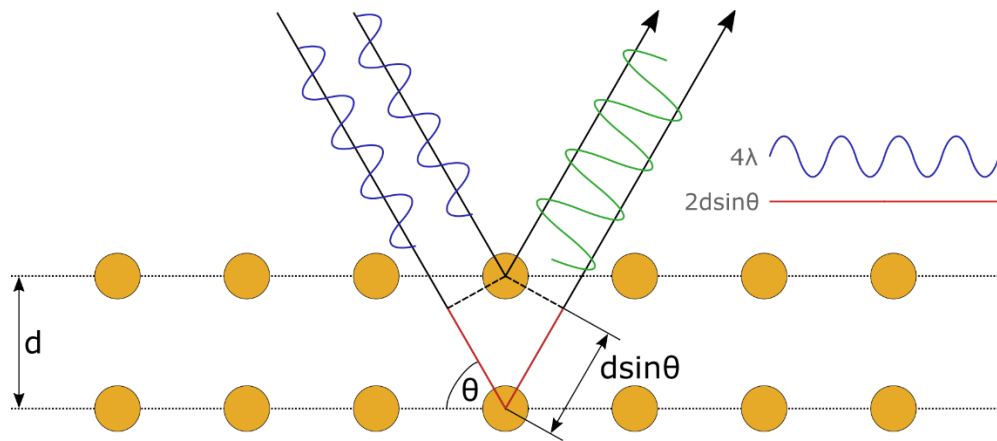


Figure 3.6-1. Bragg diffraction. Two beams with identical wavelength and phase approach a crystalline solid and are scattered off two different atoms within it. The lower beam traverses an extra length of $2d \sin \theta$. Constructive interference (green waveform) occurs when this length is equal to an integer multiple of the wavelength of the radiation.

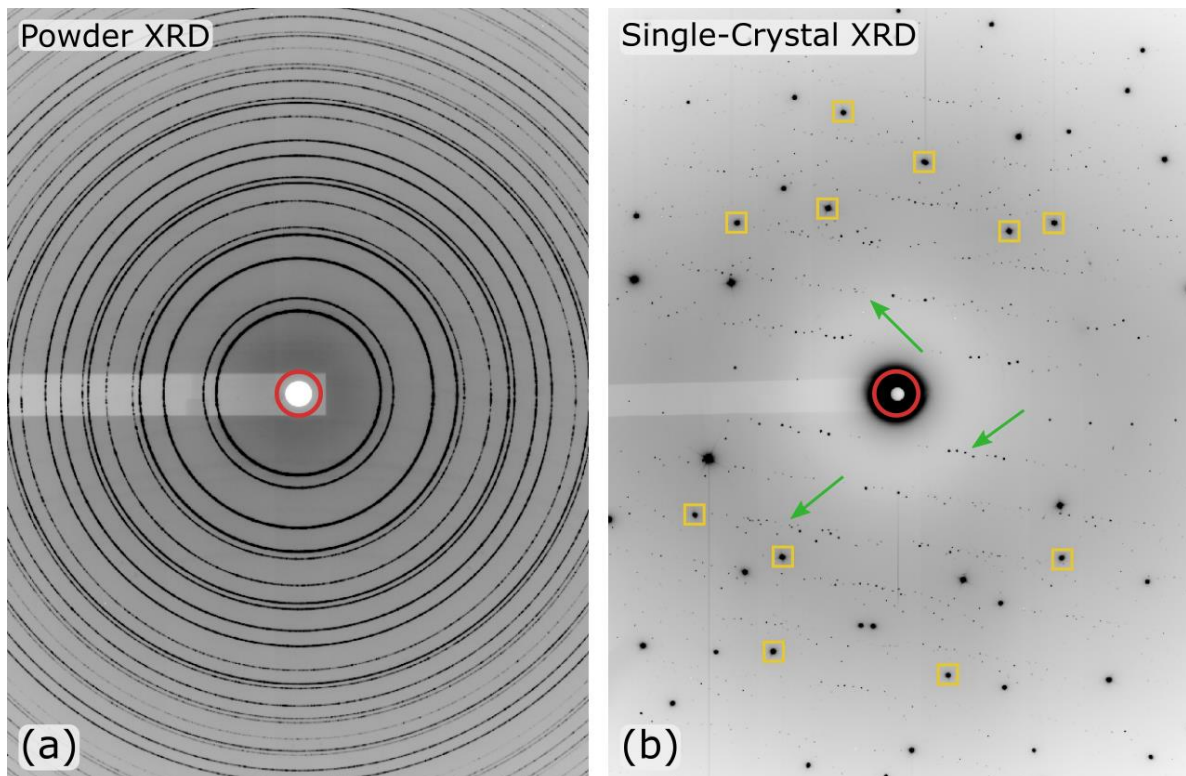


Figure 3.6-2. X-ray diffraction (XRD) patterns produced by a powder (a) and a single crystal sample (b). The red circle marks the positions of the direct beam, where a beamstop is placed to protect the detector from very high radiation. Yellow rectangles show examples of the intense reflections from the diamond anvil. Green arrows point to examples of the reflections from the sample in the DAC, in this case an enstatite crystal.

Not all materials can be easily grown into single crystals of sufficient size and quality for X-ray diffraction experiments. In this case, powder materials can be used instead. When a material is in powder form, it consists of many tiny crystallites, each of them with a random orientation. When a powder material is probed by X-rays, the diffraction pattern does not consist of single reflections, but diffraction rings instead, due to the accumulative contribution of all the randomly oriented crystallites (Figure 3.6-2 (a)).

The information that can be retrieved from a powder sample or a single-crystal sample is different. Powder X-ray diffraction (PXRD) is typically used for phase identification and for determining the unit cell parameters. Due to the lack of information on the intensity of specific Bragg peaks, however, the atomic positions in the crystal lattice cannot be unambiguously determined using PXRD alone. In the contrary, the intensity of the diffraction peaks from single-crystal X-ray diffraction (SCXRD) provides information on the exact content of the unit cell, including the type of atoms, their coordinates in the unit cell, their coordination number, and the interatomic distances.

A big number of reflections needs to be recorded for the determination of the crystal structure during a SCXRD experiment. To do so, the Bragg condition needs to be met various incident angles of the X-rays on the crystal sample. In experiments at ambient conditions, the sample is simply rotated in a series of known angles and the corresponding peaks collected. However, this is not a trivial task in high-pressure experiments where the sample is placed inside the DAC. The device surrounds the sample and, being made from steel and other heavy materials, significantly absorbs the X-rays (Figure 3.6-3). Special care is taken in the design of diamond anvil cells to maximize the opening angle of the seats and diamonds to allow a wider rotation of the cell^{7,40}.

Although X-ray sources are common and many institutions have access to *in-house* diffractometers, x-ray diffraction at synchrotron facilities profits greatly from the high-brilliance and high-energy X-ray beam with small divergence, able to be focused in an area of just a few μm^2 . This is of great importance for the *in situ* X-ray diffraction experiments in the LHDAC, since the small beam size allows to selectively probe only the heated part of the sample, in contrast to the experiments at *in house* facilities.

In most synchrotron experimental setups, the DAC is placed on a motorized goniometer, allowing its rotation (ω angle) around the vertical axis while tracking the angle between the sample and the incident X-ray beam (Figure 3.6-3). An X-ray detector behind the sample collects the diffracted radiation. The distance between the detector and the sample is a trade-off between better resolution at small scattering angles (when detector is further away) and extended field of view for large scattering angles (when the detector is closer to the sample).

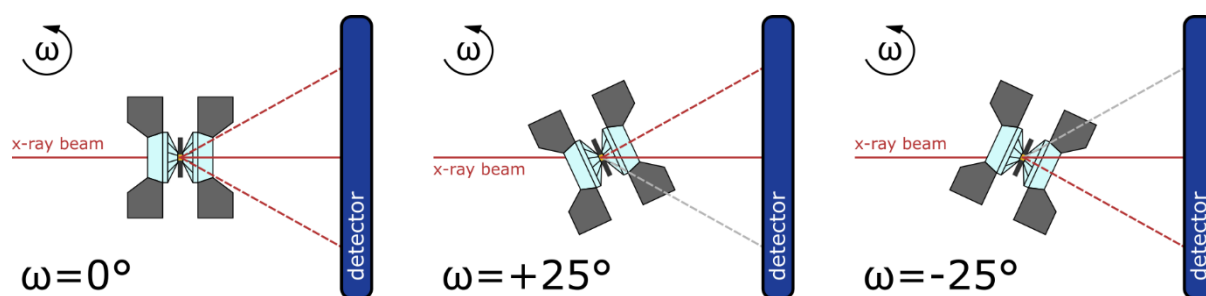


Figure 3.6-3. Schematic of X-ray diffraction experiment in a diamond anvil cell, at three different rotation angles of the diamond anvil cell.

The SCXRD and PXRD experiments of this thesis were performed at X-ray diffraction beamlines dedicated to extreme conditions, namely, ID15b at ESRF (30 keV, $\lambda \approx 0.411 \text{ \AA}$, $\sim 10 \times 10 \mu\text{m}^2$ beam, MAR555 flat-panel detector) and P02.2 at PETRA III (42 keV, $\lambda \approx 0.29 \text{ \AA}$, $\sim 2 \times 2 \mu\text{m}^2$ beam, PerkinElmer XRD 1621 flat-panel detector).

References

1. Kawai, N. & Endo, S. The Generation of Ultrahigh Hydrostatic Pressures by a Split Sphere Apparatus. *Rev. Sci. Instrum.* **41**, 1178–1181 (1970).
2. Liebermann, R. C. Multi-anvil, high pressure apparatus: a half-century of development and progress. *High Press. Res.* **31**, 493–532 (2011).
3. Weir, C. E., Lippincott, E. R., Van Valkenburg, A. & Bunting, E. N. Infrared studies in the 1- to 15-micron region to 30,000 atmospheres. *J. Res. Natl. Bur. Stand. Sect. A Phys. Chem.* **63A**, 55 (1959).
4. Bassett, W. A. Diamond anvil cell, 50th birthday. *High Press. Res.* **29**, 163–186 (2009).
5. Dubrovinskaia, N. *et al.* Terapascal static pressure generation with ultrahigh yield strength nanodiamond. *Sci. Adv.* **2**, e1600341 (2016).
6. Boehler, R. & De Hantsetters, K. New anvil designs in diamond-cells. *High Press. Res.* **24**, 391–396 (2004).
7. Kantor, I. *et al.* BX90: A new diamond anvil cell design for X-ray diffraction and optical measurements. *Rev. Sci. Instrum.* **83**, 125102 (2012).
8. Letoullec, R., Pinceaux, J. P. & Loubeyre, P. The membrane diamond anvil cell: A new device for generating continuous pressure and temperature variations. *High Press. Res.* **1**, 77–90 (1988).
9. Kurnosov, A. *et al.* A novel gas-loading system for mechanically closing of various types of diamond anvil cells. *Rev. Sci. Instrum.* **79**, 045110 (2008).
10. Mao, H. K., Xu, J. & Bell, P. M. Calibration of the ruby pressure gauge to 800 kbar under quasi-hydrostatic conditions. *J. Geophys. Res.* **91**, 4673 (1986).
11. Chijioke, A. D., Nellis, W. J., Soldatov, A. & Silvera, I. F. The ruby pressure standard to 150GPa. *J. Appl. Phys.* **98**, 114905 (2005).
12. Akahama, Y. & Kawamura, H. Pressure calibration of diamond anvil Raman gauge to 310GPa. *J. Appl. Phys.* **100**, 043516 (2006).
13. Dewaele, A. *et al.* High-pressure–high-temperature equation of state of KCl and KBr. *Phys. Rev. B* **85**, 214105 (2012).
14. Tateno, S., Komabayashi, T., Hirose, K., Hirao, N. & Ohishi, Y. Static compression of B2 KCl to 230 GPa and its P-V-T equation of state. *Am. Mineral.* **104**, 718–723 (2019).
15. Dewaele, A., Datchi, F., Loubeyre, P. & Mezouar, M. High pressure–high temperature equations of state of neon and diamond. *Phys. Rev. B* **77**, 094106 (2008).
16. Ye, Y., Shim, S.-H., Prakapenka, V. & Meng, Y. Equation of state of solid Ne intercalibrated with the MgO, Au, Pt, NaCl-B2, and ruby pressure scales up to 130 GPa. *High*

- Press. Res.* **7959**, 1–19 (2018).
17. Bassett, W. A. Diamond Anvil Cells: Laser heating of samples at high pressure: 50 years. (2016). Available at: <https://www.laserfocusworld.com/test-measurement/test-measurement/article/16547047/diamond-anvil-cells-laser-heating-of-samples-at-high-pressure-50-years>. (Accessed: 8th January 2020)
 18. Prakapenka, V. B. *et al.* Advanced flat top laser heating system for high pressure research at GSECARS: application to the melting behavior of germanium. *High Press. Res.* **28**, 225–235 (2008).
 19. Tateno, S., Hirose, K., Ohishi, Y. & Tatsumi, Y. The Structure of Iron in Earth's Inner Core. *Science (80-.)*. **330**, 359–361 (2010).
 20. Bassett, W. A. & Li-Chung Ming. Disproportionation of Fe₂SiO₄ to 2FeO+SiO₂ at pressures up to 250kbar and temperatures up to 3000 °C. *Phys. Earth Planet. Inter.* **6**, 154–160 (1972).
 21. Gold, J. S., Bassett, W. A., Weathers, M. S. & Bird, J. M. Melting of Diamond. *Science (80-.)*. **225**, 921–922 (1984).
 22. Schultz, E. *et al.* Double-sided laser heating system for in situ high pressure–high temperature monochromatic x-ray diffraction at the esrf. *High Press. Res.* **25**, 71–83 (2005).
 23. Meng, Y., Hrubciak, R., Rod, E., Boehler, R. & Shen, G. New developments in laser-heated diamond anvil cell with in situ synchrotron x-ray diffraction at High Pressure Collaborative Access Team. *Rev. Sci. Instrum.* **86**, (2015).
 24. Lin, J. F. *et al.* Absolute temperature measurement in a laser-heated diamond anvil cell. *Geophys. Res. Lett.* **31**, 3–6 (2004).
 25. Kuppenko, I. *et al.* Portable double-sided laser-heating system for Mössbauer spectroscopy and X-ray diffraction experiments at synchrotron facilities with diamond anvil cells. *Rev. Sci. Instrum.* **83**, 124501 (2012).
 26. Aquilanti, G. *et al.* Development of micro-XANES mapping in the diamond anvil cell. *J. Synchrotron Radiat.* **16**, 376–379 (2009).
 27. Marini, C., Kantor, I., Mathon, O. & Pascarelli, S. On-line laser heating setup for ED-XAS at ID24: Preliminary optical design and test results. *High Press. Res.* **33**, 108–113 (2013).
 28. McCammon, C. A. Insights into Phase Transformations from Mossbauer Spectroscopy. *Rev. Mineral. Geochemistry* **39**, 241–264 (2000).
 29. Potapkin, V. *et al.* The ⁵⁷Fe Synchrotron Mössbauer Source at the ESRF. *J. Synchrotron Radiat.* **19**, 559–569 (2012).
 30. Kotrbová, M. *et al.* Growth and perfection of flux grown FeBO₃ and ⁵⁷FeBO₃ crystals. *J. Cryst. Growth* **71**, 607–614 (1985).

31. Smirnov, G. V., Sklyarevskii, V. V., Voskanyan, R. A. & Artem'ev, A. N. Nuclear Diffraction of Resonant Radiation by an Antiferromagnetic Crystal. *JETP Lett.* **9**, 70–73 (1969).
32. Smirnov, G. V., van Bürck, U., Chumakov, A. I., Baron, A. Q. R. & Ruffer, R. Synchrotron Mössbauer source. *Phys. Rev. B* **55**, 5811–5815 (1997).
33. Prescher, C., McCammon, C. & Dubrovinsky, L. MossA : a program for analyzing energy-domain Mössbauer spectra from conventional and synchrotron sources. *J. Appl. Crystallogr.* **45**, 329–331 (2012).
34. Ruffer, R. & Chumakov, A. I. Nuclear inelastic scattering. *Hyperfine Interact.* **128**, 255–272 (2000).
35. Toellner, T. S. Monochromatization of synchrotron radiation for nuclear resonant scattering experiments. *Hyperfine Interact.* **125**, 3–28 (2000).
36. Kuppenko, I. *et al.* Time differentiated nuclear resonance spectroscopy coupled with pulsed laser heating in diamond anvil cells. *Rev. Sci. Instrum.* **86**, 114501 (2015).
37. Chumakov, A. & Ruffer, R. Nuclear inelastic scattering. *Hyperfine Interact.* **113**, 59–79 (1998).
38. Pascarelli, S., Mathon, O., Muñoz, M., Mairs, T. & Susini, J. Energy-dispersive absorption spectroscopy for hard-X-ray micro-XAS applications. *J. Synchrotron Radiat.* **13**, 351–358 (2006).
39. Kantor, I., Marini, C., Mathon, O. & Pascarelli, S. A laser heating facility for energy-dispersive X-ray absorption spectroscopy. *Rev. Sci. Instrum.* **89**, 013111 (2018).
40. Boehler, R. New diamond cell for single-crystal x-ray diffraction. *Rev. Sci. Instrum.* **77**, 115103 (2006).

Chapter 4

Thesis Synopsis

4.1 Summary of research studies

The present cumulative thesis aimed to investigate the capabilities of the experimental technique of pulsed laser heating in the diamond anvil cell (DAC), an important technique for time-resolved studies in high-pressure geosciences and material science. Three laser heating systems have been developed to be coupled with different experimental techniques, in the Bayerisches Geoinstitut (Bayreuth) and the synchrotron facilities of the ESRF (Grenoble) and PETRA III (Hamburg). Experiments conducted using the developed laser heating setups aimed to study the effects of pulsed laser heating on commonly researched scientific cases such as the heating (and melting) of iron and the stability of ferropericlase at high pressures. The results of the present thesis provide a new insight of the capabilities of pulsed laser heating and its effects on the chemistry of pulsed heated samples.

This part is a short overview to the results presented in Chapter 5 that have been published, submitted or are prepared for submission to peer-reviewed journals. Section 5.1 describes the design and development of a portable double-sided pulsed laser heating system that is used for time- and space- resolved studies and can be coupled with experimental setups at a synchrotron, such as synchrotron Mössbauer spectroscopy (SMS) and nuclear inelastic scattering (NIS) at the ESRF. Section 5.2 describes a study on the comparative effects of pulsed and continuous-wave laser heating on the reaction of carbon from the diamond anvils with an iron sample during laser heating in a diamond anvil cell. Section 5.3 describes a study on the effects of pulsed laser heating in the stability of iron-rich ferropericlase ($\text{Fe}_{0.25}\text{Mg}_{0.75}\text{O}$) at high pressures and temperatures. Section 5.4 describes the development of a diffractometer coupled with a double-sided laser heating system used for *in situ* high-pressure high-temperature single-crystal diffraction studies at PETRA III. Lastly, Section 5.5 describes the development of a system for fully time-resolved synchrotron Mössbauer source experiments at high-pressure high-temperature, coupled with a double-sided pulsed laser heating system at the ESRF.

The former three manuscripts were written by me as first author, while the later two as second author. I have actively participated in the system development, conduction and preparation of experiments, and data analysis of all studies presented in this thesis.

4.1.1 Portable double-sided pulsed laser heating system for time- resolved geoscience and materials science applications

In this work, a double-sided pulsed laser heating system was developed, designed to be easily movable between home institutions and synchrotrons, or between different beam-lines, where the need for portability of laser heating systems has already been recognized¹⁻⁴. Its application is demonstrated through a series of experiments conducted at the Nuclear Resonance beamline (ID 18) of the European Synchrotron Radiation Facility (ESRF).

As part of its portability design, the laser system employs a group of optical fibers probe the laser heated area at different spots. The use of optical fibers allows to physically separate the detector (and spectrometer) from the focusing optics and to avoid introducing additional optical components between them. These provide faster alignment and portability of the system that is especially important for synchrotron facilities, where the lack of space makes a free-space optical path solution unfeasible^{5,6}. Moreover, this solution provides a two-dimensional surface temperature map. To our knowledge, there was so far no direct two-dimensional temperature mapping technique before this work, apart from computational estimations such as peak scaling⁷ or multispectral imaging radiometry approaches, in contrast to spectroradiometry⁸.

The system is depicted as a general schematic in Figure 4.1-1 and is shown in Figure 4.1-2. The system consists of the following main components:

- Two lasers that independently heat a sample in the DAC from two sides.
- Two Unihead modules (by Precitec GmbH) with optical components to shape and focus each laser beam.
- Laser modulation and synchronization units, including photo-detectors, custom electronics and an oscilloscope for control and visualization of the pulse shapes.
- Two VIS/NIR fiber bundles for collecting thermal radiation which are optically aligned on the sample.
- High-precision spectrometer coupled with a fast, intensified CCD detector used for time-resolved spectroradiometry measurements from both sides.

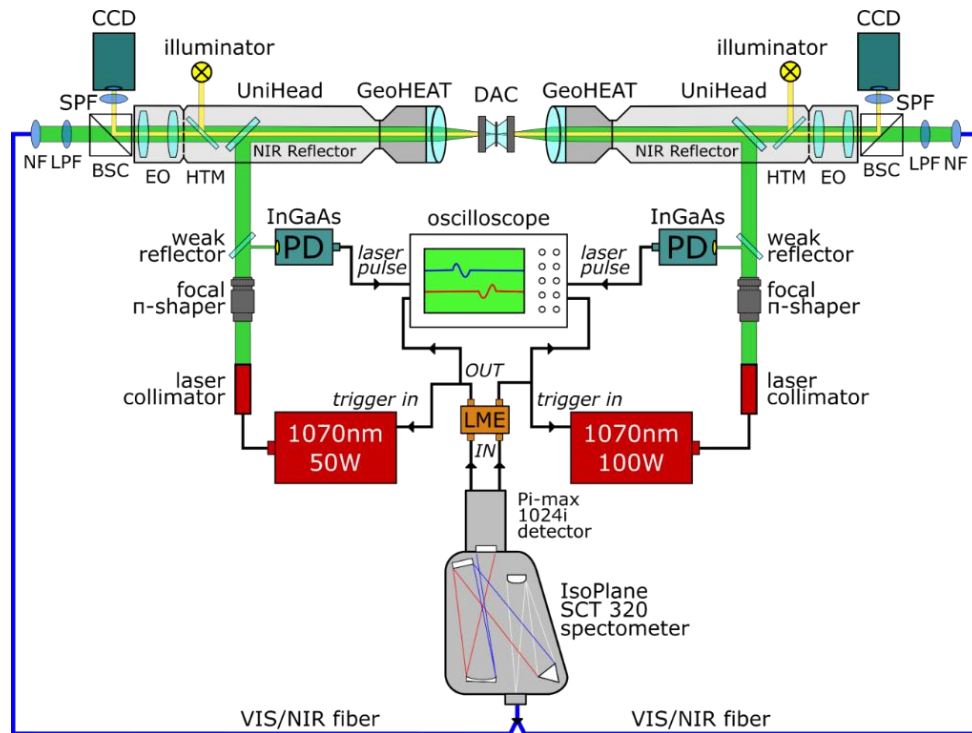


Figure 4.1-1. Double-sided pulsed laser heating system for diamond anvil cells. SPFs are short-pass filters with a cut-off at 850 nm; CCDs are the cameras for sample visual observation; NFs are notch filters at 1064 nm used to isolate the laser beam from the detector; LPFs are longpass filters with cut-on wavelength of 550 nm in order to avoid contamination from the second order diffraction of the grating; BSCs are the beam-splitter cubes; EOs are the “eyepiece” optics of the UniHead modules that focus the image on the viewing cameras and optical fibers; HTMs are half-transparent mirrors that reflect illumination light; GeoHEATs are achromatic lenses for laser focusing and collection of thermal radiation; PDs are the fast InGaAs photo-detectors used to capture laser pulses; and LMEs are the laser modulation electronics (The figure is not drawn to scale)

The lasers produce a collimated output beam that is very wide for the intended applications; therefore, it needs to be shaped and focused accordingly. Each laser beam is collected by a Focal- π Shaper (Focal- π Shaper_9_1064 by AdlOptica GmbH), which is designed to shape a TEM_{00} beam into a flat-top when combined with focusing optics^{9,10}. The resulting beam spot can have a radius as small as 20 μm , when a flat-top beam is used at the focusing distance.

The optical transparency of the diamond anvils allows the collection of the emitted radiation of the heated sample and the estimation of its temperature using the gray body approximation of Planck's law¹¹. The thermal radiation is collected from both sides through the same optical path that is used to focus the laser (Figure 4.1-2 (b)). This is done with a set of two UniHead modules, in order to maintain the portability of the system.

The accurate, *in situ* determination of the temperature of the laser-heated sample inside the DAC is crucial. For this reason, special care is taken for the laser beam shaping and improvement of the focusing optics to minimize the temperature estimation error caused by chromatic aberrations^{12,13}. Specifically, two sets of GeoHEAT 40_NIR lenses are used (Figure 4.1-2 (a)). GeoHEATs are achromatic objectives made to minimize chromatic aberration and are specially designed for laser heating applications with DACs.

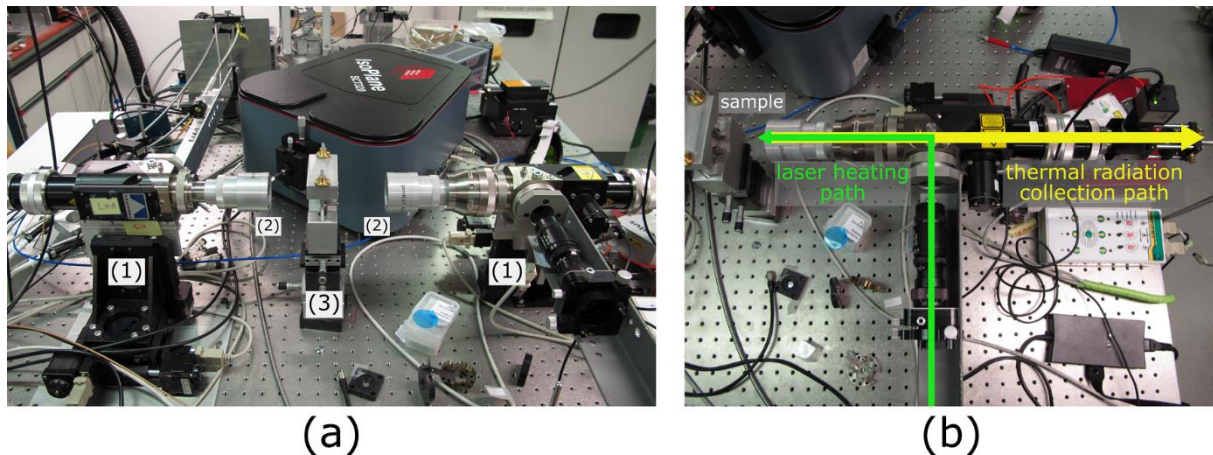


Figure 4.1-2. (a) Overview of the double-sided pulsed laser heating system developed at Bayerisches Geoinstitut: the UniHead modules (1) are equipped with GeoHEAT 40_NIR achromatic objectives (2) and are located on both sides of the sample holder (3). The spectrometer (IsoPlane SCT 320) is visible behind the optics and sample holder setup; (b) Overview of the optical paths (laser and thermal radiation, respectively) inside a UniHead module.

The image of the sample inside the DAC is magnified by the UniHead optics, working as a microscope, and projected through a beam-splitter into both the cameras that are used for optical observation and the collecting optical fibers. The light from the fibers is guided into an IsoPlane SCT 320 spectrometer (Princeton Instruments) and the resulting spectrum is collected by a PI-MAX 4 with a 1024×256 ICCD detector. The Intensified CCD camera with enhanced Quantum Efficiency gives the possibility of very fast collection. It can work on gated mode, which allows time-resolved collection of the emitted thermal radiation.

The gated detector exposure allows to create a time series of temperatures along the duration of the laser pulse (Figure 4.1-3). To do so, it is crucial to correlate the laser pulse period with the gated exposure windows of the camera. A common modulation trigger is used for the lasers and the spectrometer camera signifying the beginning of each pulse period, created internally by the pulse generator of the PI-MAX detector.

The time-resolved temperature measurement technique, when combined with multiple temperature acquisitions from a multi-core fiber bundle, results in a two-dimensional map of surface temperatures that resolve the sample thermal response both spatially and temporally. In the present setup, a set of 30 fiber cores is used, divided into two groups of 15 fibers each, in fiber bundles that are aligned optically to the center of the laser heating area from both sides of the DAC. This method can potentially reveal much information regarding the thermal dynamics of the sample and accurately determine the temperature of the sample within the heated spot.

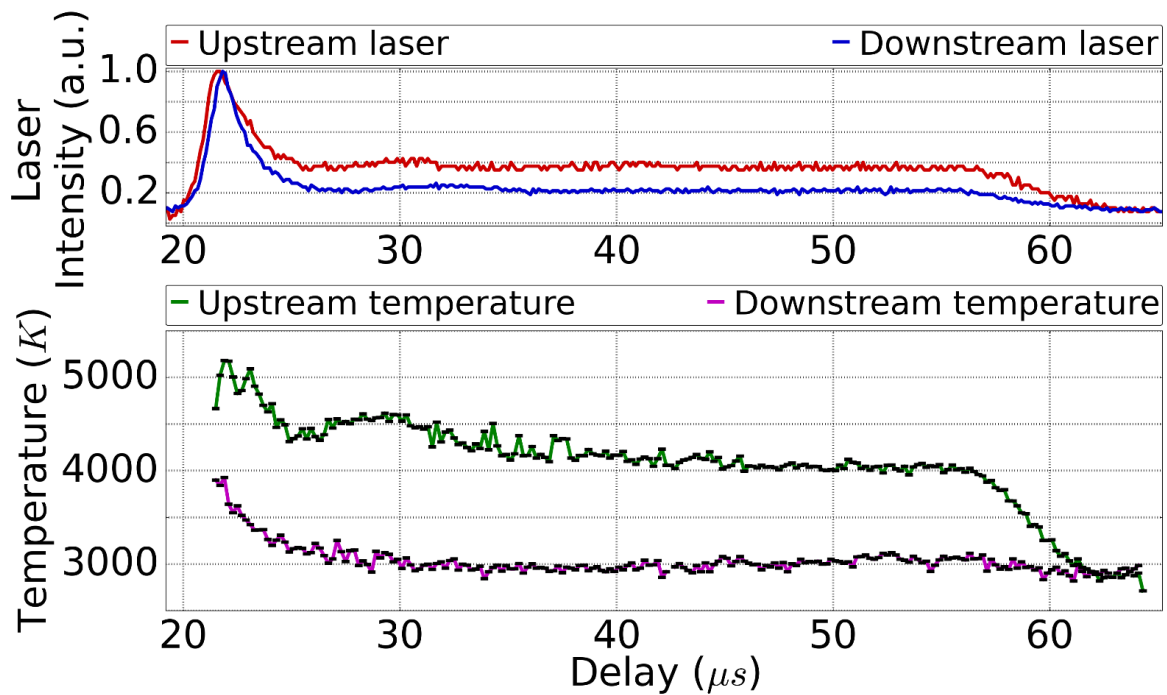


Figure 4.1-3. Temperature measured during double-sided pulsed laser heating of solid ϵ - O_2 inside a DAC at 46 GPa with 10 kHz repetition rate. For the purpose of this experiment, the laser pulse width was set to approximately 40% duty cycle, i.e., a duration of 40 μs . The 100 μs pulse period is divided into windows of 200 ns each. The figure includes the part of the period when the heat radiation was sufficiently high to be detected. The collection windows are denoted by black horizontal lines and the solid colored lines are guides for the eye.

An example of the two-dimensional temperature mapping is shown for an experiment on pulsed laser heating of an Fe_2O_3 crystal at high pressure. Furthermore, the stability and portability of the system are demonstrated in a series of experiments using Synchrotron Mössbauer Source spectroscopy¹⁴ and Nuclear Inelastic Scattering (NIS) spectroscopy coupled with pulsed LHDAC at the Nuclear Resonance (ID18) beamline^{15,16} of the European Synchrotron Radiation Facility (ESRF).

For the experimental purposes, the system was transported to ESRF and mounted in the experimental hutch of the Nuclear Resonance beamline (Figure 4.1-4). The entire procedure of connecting and aligning usually requires only 4 to 6 hours at the beginning of an experiment. It may be easily performed during a shut down or maintenance day, so that precious experimental time lost to preparation is kept to a minimum. The laser heating system was successfully used for up to 24 hours of stable heating of an ^{57}Fe -enriched iron foil in time-resolved NIS experiments, as well as for laser heating an iron hydride (FeH_x) sample while collecting time-resolved SMS spectra, using the system presented in Section 5.5.

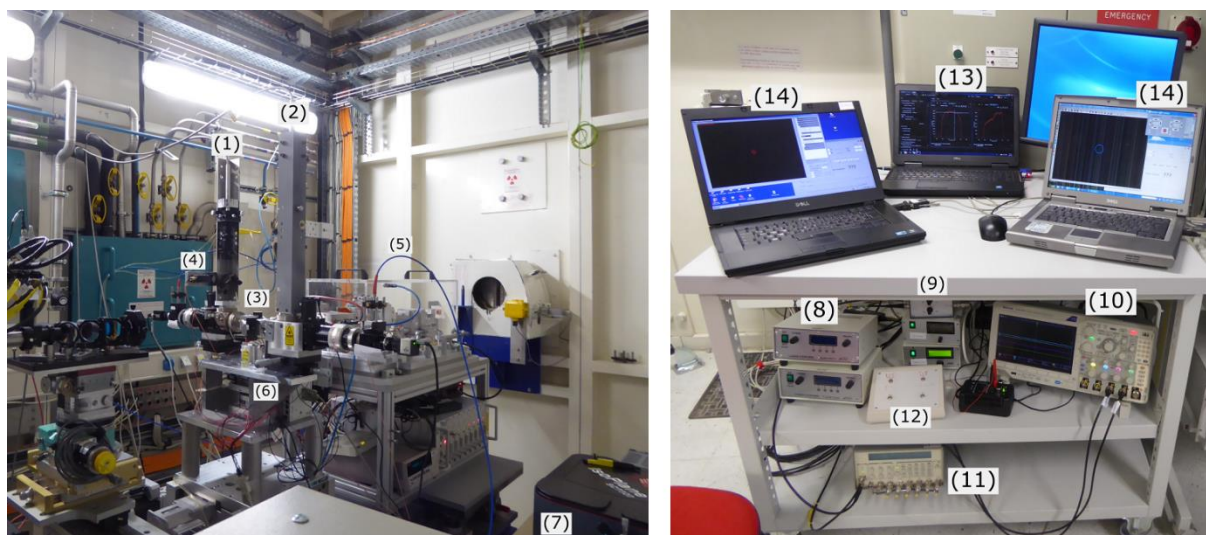


Figure 4.1-4. The double-sided pulsed laser heating system coupled with the experimental setup of the Nuclear Resonance beamline (ID18) at the ESRF. Overview of the experimental hutch (left) and the control room (right); upstream (1) and downstream (2) UniHead modules; (3) DAC holder, on top of a XYZ-motor stage; (4) photodiode for laser pulse observation; (5) optical fiber bundle for the collection of thermal radiation from the heated sample; (6) XYZ-motor stage for the alignment of the whole optical setup to the X-ray beam; (7) IsoPlane SC 320 spectrometer for temperature determination; Electronics for laser intensity (8) and duration (9) regulation; (10) oscilloscope for the observation and synchronization of the laser pulses; (11) multi-channel delay generator for time-resolved Mössbauer spectroscopy; (12) motor control for laser positioning; (13) computer for spectroradiometry; (14) computers for upstream and downstream *in situ* sample observation.

In conclusion, the developed double-sided pulsed laser heating system is able to acquire time-resolved and space-resolved surface temperature information of samples under high pressure inside a diamond anvil cell, with temporal and spatial resolution of a few nanoseconds and micrometers, respectively. The portability and stability of the system were demonstrated, as well as the possibility to couple it with different spectroscopic techniques at a synchrotron light source facility, allowing the *in situ* investigation of transitional phenomena. Possible applications include the determination of thermal conductivity, melting curve and rheological properties of materials of geological and materials science significance at conditions of the Earth's interior. Heating with pulses can potentially provide solutions for the study of materials in cases that were difficult with continuous heating.

4.1.2 Comparative study of the influence of pulsed and continuous wave laser heating on the mobilization of carbon and its chemical reaction with iron in a diamond anvil cell

The high-pressure melting curve of iron is of a particular interest for geosciences, as it provides crucial constraints for modelling thermal conditions in the Earth's core and at the core-mantle boundary. Despite extensive research, it still remains uncertain and available data are contradictory^{17–20}. Among the major experimental obstacles are undesirable chemical reactions. It is well known that laser heating of iron in a DAC may lead to formation of iron carbides or a solution of carbon in iron^{21–24} as a result of a chemical reaction between the sample and carbon diffusing from a diamond anvil into the sample chamber. This is highly

unwanted in melting experiments, since the presence of carbides or Fe-C solid solutions can significantly affect the melting temperature²⁵⁻²⁷. The carbon contamination problem is not limited to iron²⁸ but due to the important geological implications of its melting curve, iron is a highly investigated material.

As the pulsed laser (PL) heating minimizes the heating duration in individual pulses down to microseconds or even shorter, it is considered to be a technique that suppresses diffusion and, consequently, improves the chemical stability of the system under investigation. However, there have not been studies so far, which could allow a direct comparison of the effects of pulsed laser (PL) and continuous wave (CW) laser heating on the mobilization of carbon in a DAC and its chemical reaction with the sample.

In this project, the chemical interaction between iron and carbon of the diamond anvils during continuous wave and pulsed laser heating was examined. Iron samples were loaded into DACs along with different materials, Ne, Ar, and KCl, which served as pressure media and provided different chemical environments. The chosen pressure media are often used in laser-heated diamond anvil cell (LHDAC) experiments, as they are chemically inert, serve as good thermal insulators, and have been suggested as good choices for diminishing the diffusion of carbon from the diamond anvils²⁸. In course of a series of experiments, in which different spots of iron samples were heated by either a PL or a CW laser and by varying the duration of heating, we kept track of the iron-carbon interaction using Energy Dispersive X-ray Absorption spectroscopy, as implemented at the ID24 beamline at the European Synchrotron Radiation Facility (ESRF)²⁹. The compositions of the heated samples were examined afterwards using Mössbauer spectroscopy at the Synchrotron Mössbauer Source (SMS) at the ID18 beamline at the ESRF³⁰, and X-ray diffraction (XRD) at High-Pressure Diffraction Beamline ID15B at the ESRF³⁰ and the P02.2 beamline at PETRA III, DESY³¹.

The DACs of all experiments were compressed in the pressure range of 41 - 53 GPa, where iron is in the form of ϵ -Fe. The iron samples were PL or CW laser heated at temperatures ranging from 1600 K to 3450 K, i.e. both below and above the melting point of iron for the selected pressure range. Each laser heating sequence was realized through a number of cycles characterized by the number of pulses of a certain duration (in μ s) for PL or by duration (in seconds) for CW laser heating, so that sample was heated progressively longer, while keeping track of the total heating time. X-ray Absorption Spectroscopy (XAS) spectra at the Fe K-edge energy ($E_o = 7112$ eV) were collected from the quenched sample spot during the time between two heating cycles. At the end of each heating sequence a full mapping of the sample was made in a grid with a step size of $2 \times 2 \mu\text{m}^2$. An X-ray absorption spectrum was collected at each position³² in the grid to detect all possible chemical changes in the sample (Figure 4.1-5).

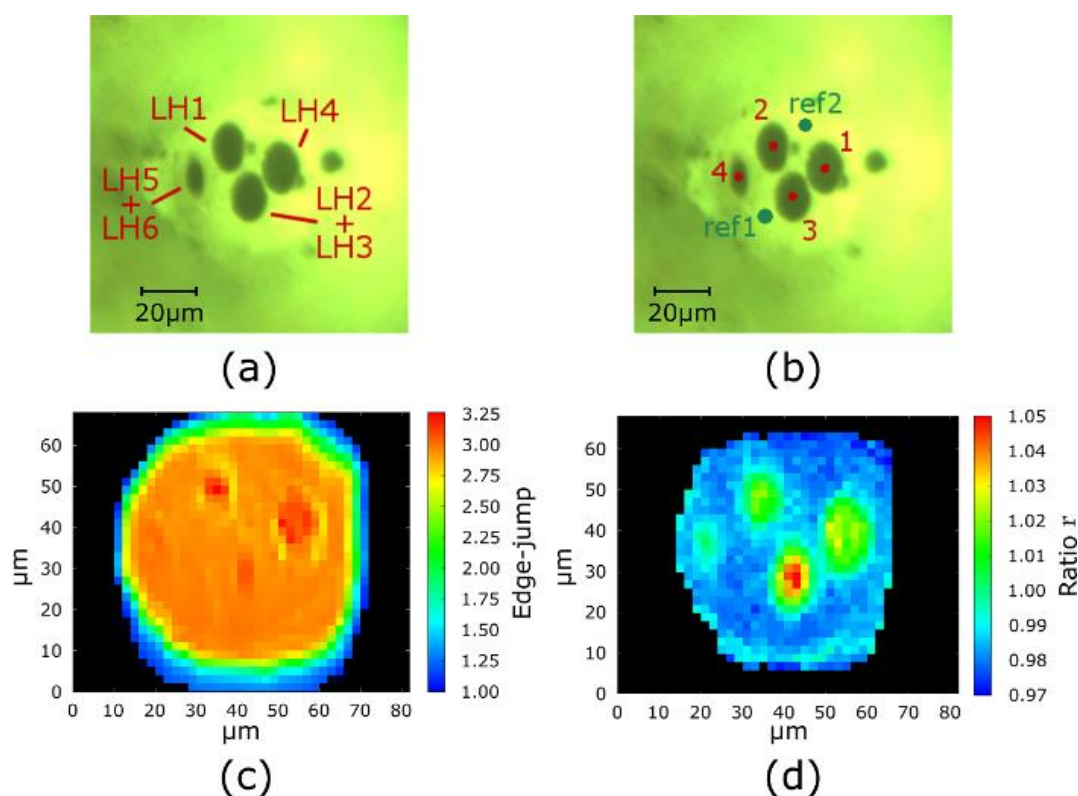


Figure 4.1-5. Upper panel - Microscope image of Fe in Ne quenched at 41 GPa: (a) positions of the laser heated spots on the sample; (b) positions of the spots for the X-ray diffraction data collection - dots 1 through 4 mark heated spots and the dots labeled “ref1” and “ref2” mark the positions on unheated reference points. Lower panel - A XAS map of Fe in Ne color-coded for: (c) the edge jump and (d) the ratio r of the XANES spectra. Each black pixel marks a position without iron or relates to an unusable spectrum.

Changes in the X-ray Absorption Near Edge Structure (XANES) region of XAS spectra give evidence of changes in the iron chemical environment. Figure 4.1-6 shows, as an example, the X-ray absorption spectra of Fe in Ne taken from a sample quenched at 41 GPa (the XANES region outlined by the dashed rectangle is enlarged in the inset). The shoulder of the rising K-edge in the XAS spectra at approximately 7119 eV (pointed out by the blue arrow in Figure 4.1-6) is a characteristic feature of ϵ -Fe^{33,34}. It was recently recognized that vanishing of this shoulder after heating indicates a chemical reaction between iron and carbon, which comes from the diamond anvils, that results in the synthesis of iron carbide Fe₃C²⁷.

To quantify the difference in the spectra, we introduced the value r , which is the ratio of the normalized absorption within the two energy regions ROI 1 and ROI 2 (Regions of Interest 1 and 2), which represent the peak and the valley of the shoulder. The regions are chosen to be equally wide, with a range of 1 eV (highlighted by different colors in Figure 4.1-6). For ϵ -Fe iron at room temperature before heating, r is equal to about 0.97. The ratio increases up to 1.06 for the points close to the centers of the heated spots. Thus, the transition from $r < 1$ to $r > 1$ indicates a significant change in the rising edge of the spectrum and marks the disappearance of the local maximum in the shoulder. Using the XAS mapping of the sample and the value of the ratio r , it is possible to detect local chemical changes in the sample and correlate them with the laser-heated areas (Figure 4.1-5 (a) and (d)).

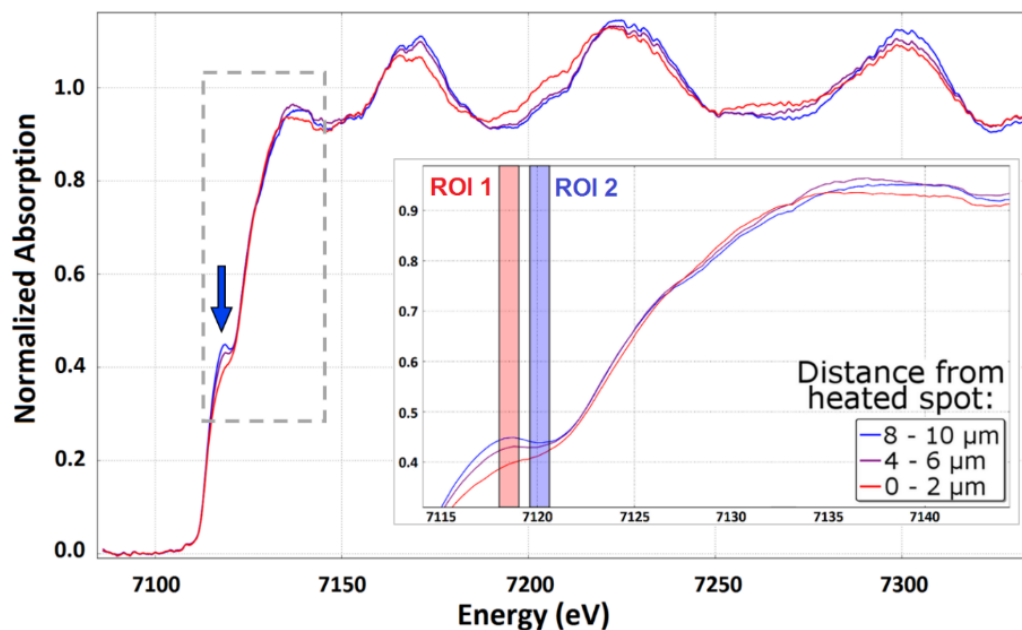


Figure 4.1-6. X-ray absorption spectra of Fe in Ne taken from a sample quenched at 41 GPa after heating at a maximum temperature of 2500 K. The inset shows the enlarged XANES region of the spectra (dashed grey rectangle). The spectra were collected at room temperature from three locations at different distances (0-2, 4-6, and 8 μm) from the center of the heated spot (red, magenta, and blue curves, respectively). The rising edge feature is pointed out by the blue arrow. The blue spectrum resembles those taken from non-heated areas of the sample and is characterised by the most pronounced shoulder, which is specific for ϵ -Fe. ROI 1 and ROI 2 designate the two energy regions (Regions of Interest 1 and 2, highlighted in pink and blue colors), which were used to define the ratio r .

4.1.2.1 Fe in Ne at 41 GPa

In most of the cases, the change in the shoulder of the rising edge in the XANES spectra was observed immediately after the first heating cycle, i.e. after a few seconds of total heating time. This was the case for both CW and PL heating with relatively long pulses. It is important to note that even in the case of heating at peak temperatures of approximately 1600 K, i.e. well below the melting point of iron and below the ϵ -to- γ -Fe transition, the alteration was almost immediate, happening after a few seconds (

Table 4.1-I).

Diffraction patterns collected from the heated areas revealed reflections which do not belong to ϵ -Fe³⁵, Re³⁶, or Ne³⁷. Particularly, at least three peaks with the d-spacings 1.665(1), 1.715(1), and 1.754(1) Å were observed in all heated spots. Although these data are insufficient to determine the phase unambiguously, all these peaks may be assigned to iron carbide(s) (Fe₃C²⁶ or Fe₇C₃³⁸).

4.1.2.2 Fe in Ar at 42 GPa

The only observed change was the transition from ϵ -Fe to γ -Fe, which is in agreement with the spectral changes observed by Aquilanti et al.¹⁹, although in this case, the spectra are from the quenched sample at room temperature and not at high temperatures. It is known from the Fe-C diagram at ambient conditions that even a small amount of carbon can stabilize γ -Fe at lower temperatures³⁹. It was shown by Narygina et al.⁴⁰ that quenching of γ -Fe at room temperature may be the result of stabilization of this iron phase by a small amount of carbon, which prevents its transformation to ϵ -Fe upon temperature decrease. Thus, it is still possible that in this experiment carbon might have been mobilized, but there is only indirect evidence of this. The calculation of the ratio r that tracks changes in the Fe rising edge shoulder did not reveal any differences between the non-heated and heated areas of the sample after all heating sequences.

Similarly, no contamination was observed by Mössbauer spectroscopy, since all probed areas of the sample revealed only the presence of elemental Fe, which was also confirmed by XAS. However, since γ -Fe was observed in the quenched sample, the possibility of carbon diffusion in iron cannot be ruled out.

4.1.2.3 Fe in KCl

Two samples of ⁵⁷Fe-enriched iron in DACs with KCl as a pressure transmitting medium were investigated, pressurized to 41 and 47 GPa, respectively. For the sample at 41 GPa, continuous heating at temperatures up to 3000 K resulted in a significant deformation of the surface of the sample. It was found that the quality of the XANES spectra was insufficient to conclude whether chemical changes took place, due to the sample deformation.

SMS spectroscopy revealed changes in the quenched sample, both in the heated areas and around them. In all SMS spectra, the singlet, characteristic for metallic iron at this pressure⁴¹, featured a shoulder, which suggested the appearance of an additional chemical component in the sample after heating, that could be fitted with a doublet with hyperfine parameters that are in close agreement with the hyperfine parameters of Fe₃C at similar pressure⁴².

The second ⁵⁷Fe-enriched iron sample was pulse-heated for several minutes in total, at temperatures up to 3800 K (peak temperature of the pulse), using the double-sided pulsed laser heating system of ID18 at the ESRF⁴³. Apart from the pure Fe singlet of the non-heated

sample a second absorption component appeared (similarly to the previous case) after less than a minute of alignment heating. Alignment heating was done at low laser power (sample temperature was < 1500 K) to align and synchronize the lasers for the pulsed operation. X-ray diffraction patterns collected at ID15 beamline of ESRF revealed both ϵ -Fe and γ -Fe in the sample at room temperature, but iron carbide could not be detected.

Table 4.1-I. Characteristics of all heating cycles for Fe in KCl at 42 GPa.

Sample	Pressure Medium	Pressure (GPa)		Analysis	Evidence of reaction
		before heating	after heating		
Fe	Ne	41	41	XANES	Yes
				XRD	Yes
Fe	Ar	42	49	XANES	Uncertain
				SMS	No
⁵⁷ Fe enriched	KCl	41	42	XANES	Uncertain
				SMS	Yes
⁵⁷ Fe enriched	KCl	47	53	SMS	Yes
				XRD	No

Iron carbide formation was detected in most experiments, by either XRD, XANES, or SMS, regardless of the laser heating method (

Table 4.1-I). While pulsed laser heating is generally considered advantageous in preventing the mobilization of carbon from the diamond anvils and its chemical interaction with the sample, this is refuted by our results. To the contrary, laser heating by any means can lead to chemical reactions, and this effect must be considered, particularly, for interpretation of experiments on melting of iron and other metals.

Our observations suggest that in cases when a chemical reaction with carbon occurs, it happens almost immediately, after only a very few seconds of heating at moderate temperatures (independently of heating method, CW or pulsed). It means that chemical contamination by carbon may be an important factor even if efforts are applied to minimize the heating time, because, as a rule, tens of seconds are usually necessary to characterize the temperature and the state of the hot sample.

In all experiments, formation of γ -Fe was observed at sufficiently high temperatures, and this phase was quenchable. Preservation of γ -Fe at ambient temperature in both the multi-anvil apparatus and laser heated DAC experiments^{44,45} has been previously reported as an effect of slow transformation kinetics to ϵ -Fe, or due to the high cooling rate. However, Narygina et al.⁴⁰ demonstrated that γ -Fe can be also stabilized by a small amount of carbon that hinders martensitic transformation during quenching. Thus, in experiments, in which carbides are not detected (e.g. the experiments with Ar pressure medium), but γ -Fe is quenched at ambient temperature, carbon contamination cannot be ruled out.

Generally, one experimental technique was not enough to fully characterize the chemistry of the sample, and a cross-validation of techniques was necessary. For this reason, extra precautions should be taken in experiments with iron in a laser-heated diamond anvil cell and the application of more than one analytical technique is strongly suggested, as well as *ex situ* analysis of the recovered sample if possible.

4.1.3 The effect of pulsed laser heating on the stability of ferropericlase at high pressures

Currently, it is widely accepted that the lower mantle consists of mainly three major minerals - ferropericlase, bridgmanite and calcium silicate perovskite⁴⁶⁻⁴⁸. Ferropericlase is believed to be the second most abundant of the three, comprising approximately 16-20 wt% of the lower mantle⁴⁹⁻⁵¹. The expected percentage of iron (expressed as Fe/(Mg+Fe)) in (Fe,Mg)O in the lower mantle is 10-25%^{52,53}. Ferropericlase with such composition is so far considered to be stable in a NaCl-type (B1) structure ($Fm\bar{3}m$) throughout the lower mantle⁵⁴ and above ~50 GPa iron in ferropericlase undergoes a spin crossover from high-spin to low-spin⁵⁵.

There are, however, reports that (Mg,Fe)O with relatively large amount of Fe may decompose at pressure-temperature conditions of the lowermost mantle into an Fe-richer and a Mg-richer phases^{56,57}. In contrast to the earlier reports on decomposition, subsequent studies in laser-heated diamond anvil cells (LHDACs) did not observe any segregation between iron and

magnesium^{54,58-60}. Ferropericlyase inclusions in super-deep diamonds show very large variations of Mg/Fe ratio⁶¹ suggesting that there are natural processes which lead to compositional differentiation in the formation of (Mg,Fe)O. The behavior of ferropericlyase as well as partitioning of iron between co-existing in lower mantle minerals play a crucial role in understanding the dynamics, geophysics, and geochemistry of the Earth^{55,62}.

In experiments with DACs, pulsed laser (PL) heating was considered as an option to prevent or minimize (in comparison with continuous wave, CW) reactions between diamond anvils (carbon) and heated matter^{63,64}. However, the results of a study that is part of this thesis (presented in Section 5.2) show no obvious advantage due to heating in pulse mode.

This study investigated the effect of pulsed laser heating on the stability of ferropericlyase with a geochemically relevant composition of (Fe_{0.25}Mg_{0.75})O (Fp25) at pressure conditions corresponding to the upper part of the lower mantle^{65,66} and over a wide temperature range. The decomposition of Fp25 with formation of a high-pressure (Mg,Fe)₃O₄ phase with CaTi₂O₄-type structure was reported, as well as the dissociation of Fp25 into an Fe-rich and a Mg-rich phases induced by PL heating.

The single-crystal samples were synthesized at Bayerisches Geoinstitut (BGI) from (Fe_{0.25}Mg_{0.75})O powder. Electronic microprobe analysis indicated a ferric iron component of 11(4) wt%, which was also confirmed by Synchrotron Mössbauer spectra collected from the crystals at 30 GPa. In total five crystals were selected and loaded in two DACs that were loaded with neon as pressure-transmitting medium.

For the first experiment, three (Fe_{0.25}Mg_{0.75})O crystals were placed inside the sample chamber and pressurized to 26(1) GPa. After laser heating the pressure increased to 30.0(5) GPa. The samples were heated to temperatures ranging from 1550 K to 2300 K at ID18 of the ESRF using the portable laser-heating system¹. Each crystal was heated using a different heating method - continuous wave (CW), pulsed at 25 kHz repetition rate with pulses of 3 μs, and pulsed at 1 kHz with pulses of 500 μs. *In situ* high-pressure single-crystal diffraction experiments (SCXRD) were performed at ID15b at the ESRF and Synchrotron Mössbauer Source (SMS) experiments at ID18¹⁴ at the ESRF.

For the second experiment, two (Fe_{0.25}Mg_{0.75})O crystals were placed inside the sample chamber of a DAC and then pressurized to 48(1) GPa (increased to 53.5(5) GPa after heating). Both crystals were laser heated for approximately 30 seconds from both sides using the double-sided pulsed laser heating system of BGI that was developed as part of this thesis. One crystal (C01) was heated with laser pulses of 250 μs duration at 2 kHz frequency, reaching temperatures of 2800 K and 3100 K respectively on each side, at the peak of the pulses. The second crystal (C02) was heated with laser pulses of 11 μs duration at a frequency of 25 kHz. The temperatures achieved at the peak of the pulses on each heating side was in this case 3100 K and 3400 K respectively. The quenched materials were investigated at the Extreme Conditions Beamline (ECB) P02.2 of PETRA III³¹. A grid with 1 μm step in both vertical and

horizontal directions of wide scans was collected from each crystal, covering the whole crystal surface.

X-ray diffraction experiments on the DAC heated at 30 GPa have revealed a different response of each $(\text{Fe}_{0.25}\text{Mg}_{0.75})\text{O}$ crystal to the high-temperature treatment. While the CW-heated crystal has persisted, diffraction patterns of the PL-heated crystals featured appearance of new Bragg peaks, coexisting with peaks of starting material. Based on single-crystal diffraction data peaks belonging to the new phase were indexed in the orthorhombic unit cell with $a = 2.7419(1) \text{ \AA}$, $b = 9.170(4) \text{ \AA}$, $c = 9.313(3) \text{ \AA}$, $V = 234.2(2) \text{ \AA}^3$. The crystal structure was solved in the space group $Cmcm$ (N.63) and was found to be of CaTi_2O_4 -type, isostructural to the high-pressure form of Fe_3O_4 ⁶⁷. The unit cell volume of the observed phase is smaller than that reported for pure hp- Fe_3O_4 at 41 GPa (238.68 \AA^3) and calculated from published EOS (Ref.⁶⁷, 242.4 \AA^3 at 30 GPa) (Figure 4.1-7). Refinement of the two cation sites occupancies yielded $\text{Fe}_{0.46(7)}\text{Mg}_{0.54(7)}$ (site *FeMg1*) and $\text{Fe}_{0.68(7)}\text{Mg}_{0.32(7)}$ (site *FeMg2*), resulting in the formula $(\text{Fe}_{1.82(21)}, \text{Mg}_{1.18(21)})\text{O}_4$, or $(\text{Fe}_{0.61(7)}, \text{Mg}_{0.39(7)})_3\text{O}_4$ (Figure 4.1-7).

The same hp- $(\text{Fe}, \text{Mg})_3\text{O}_4$ phase was also observed at 53.5 GPa alongside ferropericlase on both crystals that were PL heated. The detailed X-ray diffraction mapping revealed the formation of hp- $(\text{Fe}, \text{Mg})_3\text{O}_4$ in small amounts at the heated area of both, confirming the decomposition of ferropericlase at both pressure points.

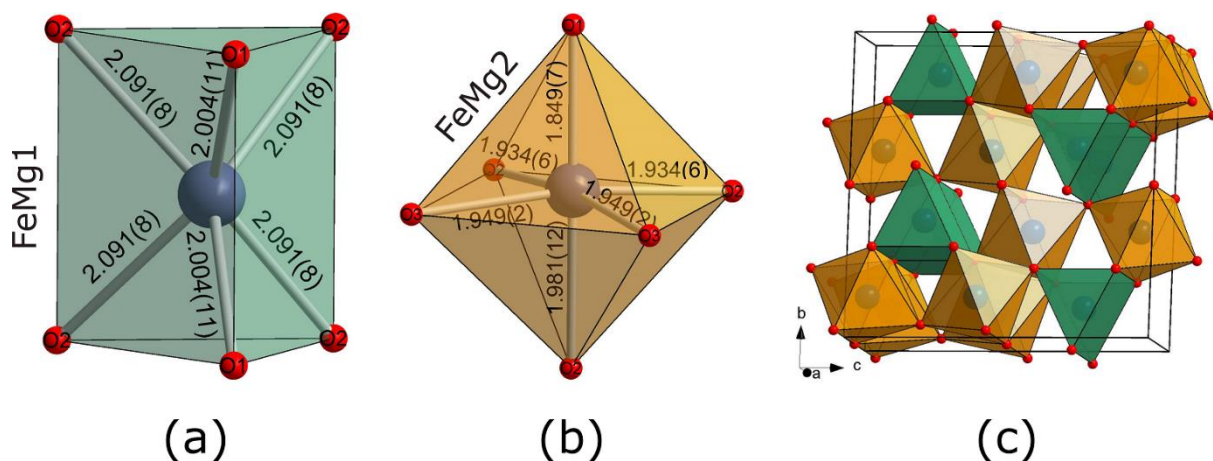


Figure 4.1-7. Coordination polyhedra of FeMg1 (a) and FeMg2 (b) crystallographic sites in the crystal structure of $(\text{Fe}_{1.82}, \text{Mg}_{1.18})\text{O}_4$. The bond distances are given in angstroms. The crystal structure of $(\text{Fe}_{1.82}, \text{Mg}_{1.18})\text{O}_4$ (c) is built of trigonal prisms and octahedra $(\text{FeMg})\text{O}_6$. Trigonal prisms share trigonal faces while the octahedra connect through common edges. Oxygen atoms are shown as red spheres.

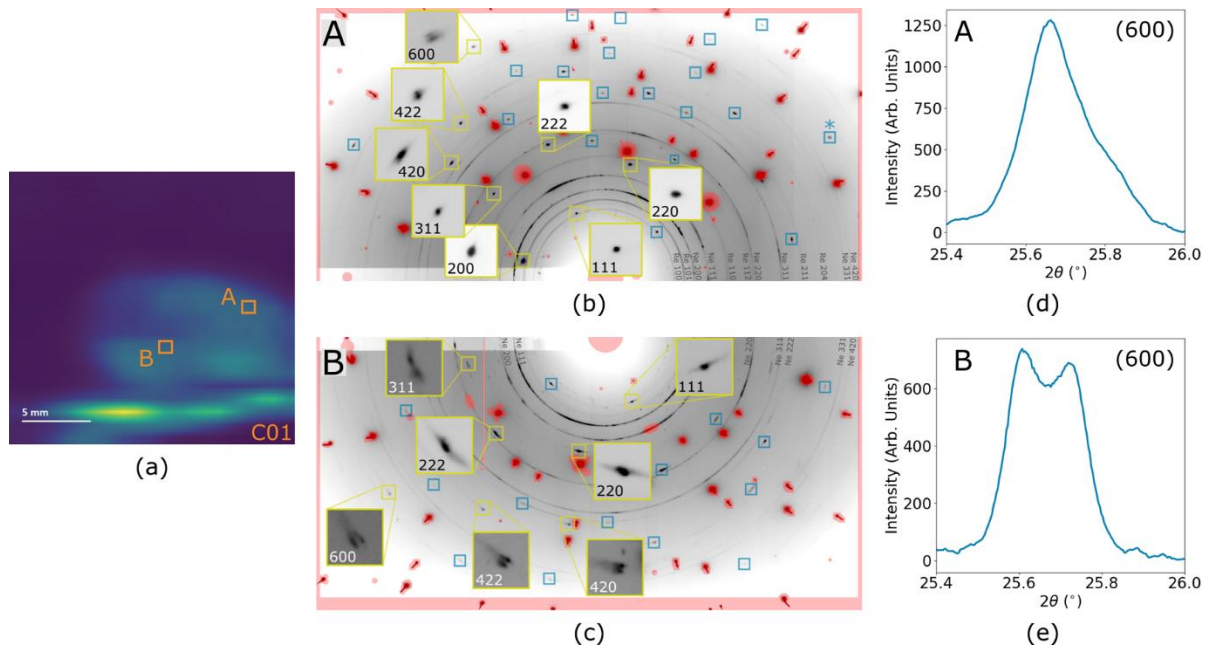


Figure 4.1-8. Splitting of Bragg reflections of ferropericlase after pulse laser heating of C01 crystal at 53.5 GPa. (a) X-ray diffraction map of the crystal showing the relative intensity of the (220) reflection of ferropericlase at the selected positions at the edge (“A”) and close to the center (“B”) of the heated area; (b) and (c) show 2D diffraction patterns for positions A and B respectively with selected reflections magnified (yellow rectangles). Diamond reflections and inactive areas of the detector (including edges) are masked (red areas). The rest are ferropericlase peaks marked by blue rectangles. Continuous diffraction rings are due to Ne. (d) and (e) Integrated diffraction profiles of Bragg (600) reflection (marked by blue asterisk on (b)) of ferropericlase at positions A and B of the crystal respectively.

After laser heating, the broadening (at low 2θ angles) and splitting (at high 2θ) of Bragg peaks of ferropericlase was observed on quenched samples. The diffraction domains of ferropericlase have the same orientations but are characterized by slightly different d-spacings of the corresponding reflections, suggesting the existence of two coherently grown phases with different lattice parameters. In the case of the experiment at 30 GPa, the effect was mainly observed on the crystal heated with short pulses of 3 μs . The separation of diffraction peaks was less prominent on the crystal that was heated with long pulses of 500 μs duration and even less on the crystal heated with CW laser. The splitting of ferropericlase diffraction peaks was similarly detected on both pulse laser heated ferropericlase crystals of the experiment at 53.5 GPa. Furthermore, analysis of the diffraction patterns using X-ray diffraction mapping revealed that the separation into two phases was more intense at the center and less pronounced at the edges of the heated area where the heating temperatures were lower (Figure 4.1-8).

Upon laser heating at pressures of about 30 GPa and 50 GPa, ferropericlase ($\text{Mg}_{0.75}\text{Fe}_{0.25}\text{O}$) underwent chemical reaction resulting in the formation of a CaTi_2O_4 -type structured post-spinel oxide ($\text{Fe}_{0.61}, \text{Mg}_{0.39}$) $_3\text{O}_4$. The formation of the hp- $(\text{Mg},\text{Fe})_3\text{O}_4$ phase can be possibly the result of the decomposition of the solid solution of MgO-FeO with a partial release of the ferric component that was present (~11 wt%) in the starting material.

The structure of high-pressure magnesioferrite solid solution was unambiguously determined to be of the CaTi_2O_4 -type using single-crystal X-ray diffraction, revealing a structure with composition $(\text{Fe}_{0.73}, \text{Mg}_{0.27})(\text{Fe}_{0.64}, \text{Mg}_{0.36})_2\text{O}_4$ and Fe occupying both crystallographic positions.⁶⁸ The high-pressure polymorph is reportedly stable at pressures above 27 GPa and was synthesized by compression at room temperature, supporting that the pressure conditions of this study lie within the stability field of the high-pressure polymorph of the oxide.

Magnesioferrite-magnetite solid solutions with iron-rich compositions ($\text{Mg}_{0.5}\text{Fe}_{2.5}\text{O}_4$ ⁶⁹ and non-stoichiometric $\text{Mg}_{1.30}\text{Fe}_{1.80}\text{O}_4$ ⁷⁰) were found in magnesiowüstite inclusions of natural diamonds, formed around crystal defects of $(\text{Fe},\text{Mg})\text{O}$. The hypothesis that the magnesioferrite-magnetite solid solution is directly exsolved from $(\text{Fe},\text{Mg})\text{O}$ is further supported by our results, thus, reinforcing the interpretation of a deep, lower mantle origin of the diamond inclusions^{69,71}.

Considering that Fe^{3+} -bearing ferropericlase can form at upper and lower mantle conditions⁷², the decomposition of Fe^{3+} -bearing ferropericlase into a high-iron composition post-spinel hp- $(\text{Fe},\text{Mg})_3\text{O}_4$ phase and the ability of complex oxides such as Fe_4O_5 and Fe_7O_9 to form solid solutions with their Mg-end-members⁷³⁻⁷⁵ have implications for the possible existence of complex Mg-Fe oxides in oxidized slabs and/or mantle and, thus, indicate that the phase composition of the lower mantle may not be limited to only the three major minerals of ferropericlase, bridgmanite and CaSi-perovskite.

The heating of ferropericlase single crystals at both pressure points induced broadening or splitting of the diffraction peaks due to the decomposition of Fp25 into two different phases with the same NaCl-type structure and two different compositions, an Fe-rich and an Mg-rich, respectively, providing strong evidence that there is a range of temperatures above 1800 K where the miscibility gap of $(\text{Fe}_{0.25}, \text{Mg}_{0.75})\text{O}$ exists, as it has also been suggested for higher pressures⁷⁶. For the sample heated at 53.5 GPa close to solidus temperatures it is hard to draw an unambiguous conclusion if melting was responsible or not for the decomposition.

Lately, the model of a homogeneous lower mantle with pyrolytic composition has been under discussion^{70,77}. The results of this study provide further arguments that the chemical composition of the lower mantle is more complex than initially thought and that the compositional inhomogeneity is not only a characteristic of the lowermost part but includes depths as shallow as below the transition zone.

Lastly, the results indicate that the type of laser heating may also affect the results. For similar temperature ranges and heating duration applied to the crystals at the same pressure, the crystals that were pulsed (and especially the one heated with short laser pulses) had a significantly higher amount of hp- $(\text{Mg}, \text{Fe})_3\text{O}_4$, and demonstrated much clearer signs of dissociation of Fp25 to iron- and magnesium-rich phases. The results of this study qualitatively agree with the study presented in Subsection 4.1.2, suggesting that pulsed laser-heating not only does not prevent chemical reactions, but probably accelerates them.

4.1.4 Single-crystal diffractometer coupled with double-sided laser heating system at the Extreme Conditions Beamline P02.2 at PETRAIII

Single-crystal X-ray diffraction (SCXRD) in DACs is a strong tool to determine not only the crystal structure of a material, but also to refine its chemical composition for even very complex multi-phase and/or multigrain samples. Heating is an important parameter for high-pressure experiments, especially for studies dedicated to modelling of processes in deep Earth's interior. Double-sided laser-heating (dsLH) systems are widely used at synchrotron facilities^{2,10,78,79}. However, until recently, all of them were stationary and did not allow DAC rotation during simultaneous heating, making *in situ* high-pressure high-temperature SCXRD impossible.

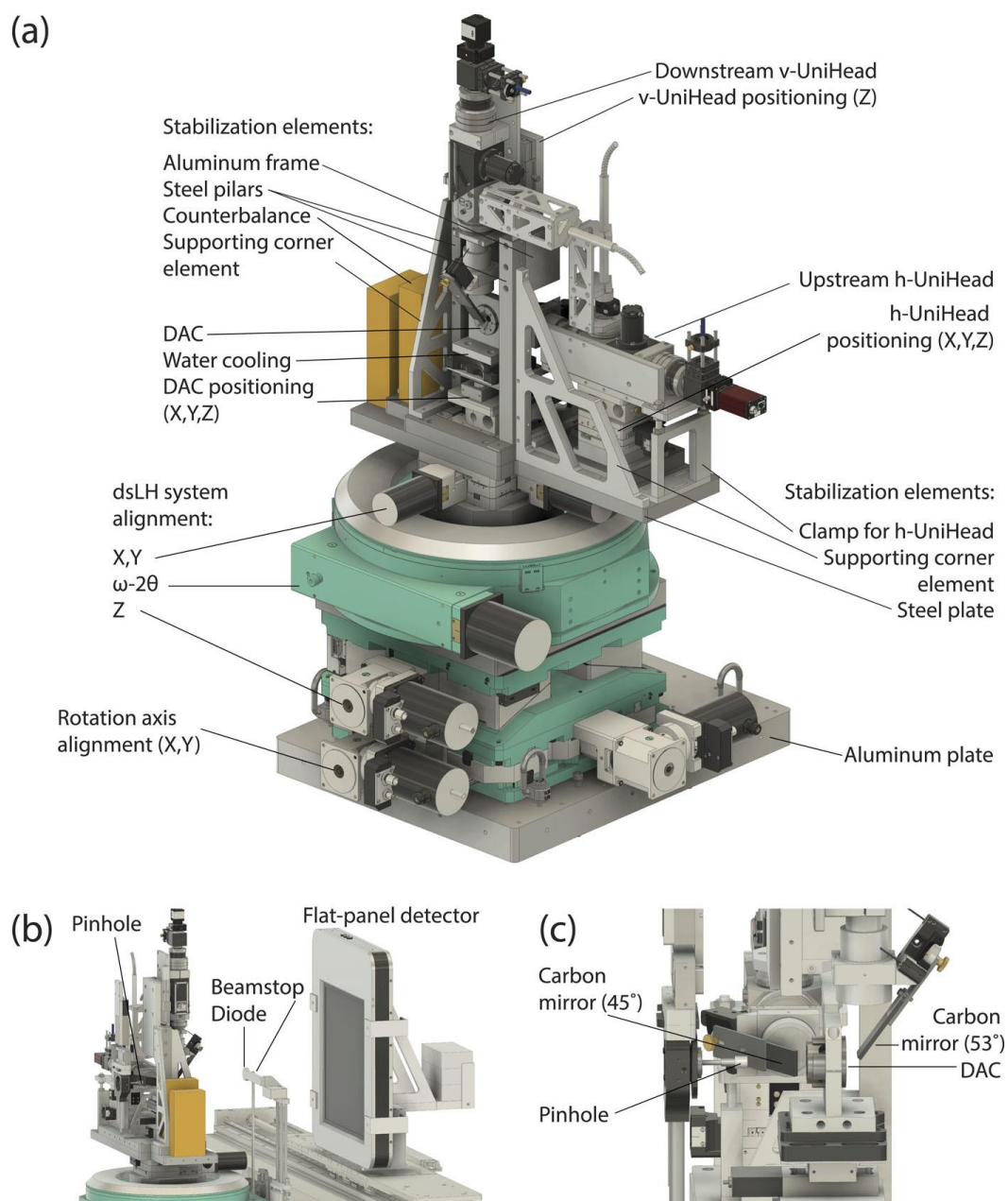


Figure 4.1-9. ScXRD/dsLH setup: view from the downstream side (a); from the upstream side (b) and perpendicular to the X-ray beam (c).

In this work, the first dedicated SCXRD/dsLH setup consisting of a single-crystal X-ray diffractometer coupled with double-sided laser heating system was developed. The setup was developed for beamline P02.2 the Extreme Conditions Beamline (ECB) at PETRA III³¹ and became available for the general users in 2017. The major components of the setup (from the top to the bottom) are listed below and shown in Figure 4.1-9:

- *Sample holder* equipped with water cooling;
- *Two portable universal laser heating heads* (UniHeads, PrecitecTM) equipped with 4 mm-thick glassy carbon mirrors; one UniHead is mounted horizontally (the upstream h-UniHead), the other one vertically (the downstream v-UniHead);
- *Multi-axis positioning systems* realized through the combination of translation positioning stages:
 - motorized X-, Y- and Z-stages for DAC alignment;
 - motorized X-, Y- and Z-stages for upstream h-UniHead;
 - manual Z-stage for downstream v-UniHead;
- *Stabilization elements* (aluminum frame with steel pillars and supporting corner elements, clamp for h-Unihead, counterbalance for the dsLH system, etc.) to decrease vibrations and improve the stability of heating during rotation;
- *4-axis positioning system* for alignment of dsLH system composed of following translation stages:
 - Huber motorized XY-stage;
 - Rotational positioning device, 2-circle (ω - 2θ) Huber goniometer;
 - Heavy-load Huber motorized Z-stage;
- *Heavy-load Huber motorized XY-stages* for the alignment of the ω rotation axis to the focus of the X-ray beam;
- *Aluminum base plate* (50 mm thick) integrating the entire setup, including an X-ray diode, and a beamstop;
- *Additional components of the setup*, which are not shown in Figure 4.1-9:
 - *Two SPI RedPower R4 fiber lasers* (50 W, excitation wavelength of 1070 nm);
 - *Two Ocean Optics QE65000 spectrometers* for collection of the thermal radiation

Two UniHeads¹ are used to focus the laser beams on the sample from the both sides (Figure 4.1-9). Each of them includes a compact set of optical components. The 90° arrangement of

the two UniHeads serves to minimize shadows cast on the detector by various components of the system, to reduce possible vibrations of the optical components, and to achieve the largest possible ω rotation range. The glassy carbon mirrors are mounted at an angle to the axes of the UniHeads (Figure 4.1-9 (c)) and serve as a reflector of the laser light in order to direct it to the sample. The upstream mirror is mounted precisely at 45° , which aligns the laser beam parallel (coaxial) to the X-rays that penetrate the mirror. The downstream mirror is placed at a larger angle, between 50 and 55° , to avoid primary X-ray beam interaction and prevent strong unwanted diffuse scattering.

Thermal radiation from both sides of the sample is collected using two optical fibers with core diameter of $400\ \mu\text{m}$, which are connected to the spectrometers. Each optical fiber is aligned to the heating spot and focused on the image plane. In this way, due to the $20\times$ magnification of the system, the sample temperature is probed from an area of $20\ \mu\text{m}$ diameter, centered at the heated spot. The thermal radiation spectra are analyzed using spectroradiometry³ and fitted using the gray body approximation of Planck's law in the wavelength range of $650\text{--}800\ \text{nm}$ with software developed for this purpose. The spectra are collected every second with exposure time of a few hundred of milliseconds. The stage rotation and the temperature data collection of the detector are synchronized manually. The setup allows maintaining the laser heated sample under stable temperature during the entire data collection with a temporal variation that is well below the typical temperature measurement uncertainty of $\pm 100\ \text{K}$.

The SCXRD data collection is realized in an *oscillation (= narrow slicing) mode*, i.e. when the diffraction is recorded while rotating the sample about a single ω -axis in small steps of $0.5\text{--}1^\circ$. During the data collection combined with the laser heating it is possible to collect the frames in ranges of ω from -38 to $+25^\circ$. Data collection time lasts approximately one or two minutes for the entire ω rotation range.

Two experiments are presented, that demonstrate the capabilities of the SCXRD/dsLH setup for *in situ* studies of materials, during which high pressures and high temperatures are applied simultaneously.

In the first experiment, a piece of Cr was loaded into a DAC and was gas-loaded with N_2 as pressure-transmitting medium and reaction agent. Laser-heating of Cr in nitrogen to $1300\ \text{K}$ at $47\ \text{GPa}$ resulted in the formation of CrN^{80} . The CrN crystal showed thermal expansion upon laser heating (the unit cell volumes $V = 63.135(14)$ and $62.10(15)\ \text{\AA}^3$ were obtained during and after laser heating, respectively). The thermal parameters acquired during laser heating were larger than those at ambient temperature (Figure 4.1-10).

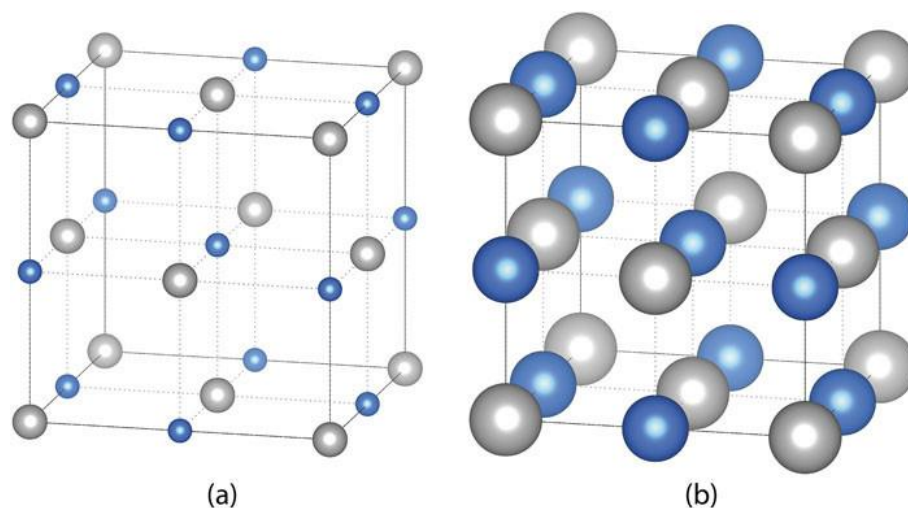


Figure 4.1-10. The crystal structure of CrN at 293 K (a) and 1300 K (b). Blue and grey balls show the positions of Cr and N atoms, respectively. Thermal ellipsoids are shown at the 90% probability level.

In the second experiment, NiAs-type FeN^{81,82} was synthesized and its crystal structure was characterized at high-pressure and high-temperature conditions using the SCXRD/dsLH setup. The cell was pressurized to about 50 GPa and laser heated at 1900(200) K, provoking a chemical reaction between iron and nitrogen resulting in the synthesis of iron nitride FeN as single crystals. As expected, the unit cell parameters obtained during and after laser heating ($V = 29.853(7)$ and $28.86(4) \text{ \AA}^3$, respectively) differ due to the thermal expansion of the crystal. The thermal parameters acquired during laser heating are about twice as large as those at room temperature. The difference in the quality of the structural refinements for the room- ($R_1=0.0594 / wR_2= 0.0692$) and high-temperature data ($R_1 = 0.0772/wR_2 =0.0793$) is insignificant, proving the technical feasibility of SCXRD for *in-situ* studies of materials at high pressures and simultaneous high temperatures in laser-heated DACs.

The SCXRD/dsLH setup encompasses all the components required for SCXRD data collection and simultaneous double-sided laser heating in a single module, which can be mounted/unmounted on the General-Purpose experiment of beamline P02.2 (ECB) at PETRA III within a few hours. The alignment of the optical components and preparation of the beamline takes approximately one working day. The setup has been tested in high-pressure high-temperature experiments aimed at studying chemical reactions between nitrogen and two metals, iron and chromium. It enabled to obtain reliable results in the structure solution and refinement of iron and chromium nitrides.

4.1.5 Fully time-resolved synchrotron Mössbauer spectroscopy for pulsed laser heating experiments in diamond anvil cell

Synchrotron Mössbauer Source is a powerful tool for experiments in laser heated diamond anvil cells^{1,14}, taking advantage of the high spectral flux of third generation synchrotron sources. The combination of Mössbauer spectroscopy with pulsed laser irradiation for samples at ambient pressure has already been demonstrated along with the possible applications of the method⁸³. It was immediately clear that it is necessary to have time-

resolved information of the Mössbauer absorption in order to take full advantage of the dynamic nature of pulsed laser heating in the DAC.

In this work, a detection scheme to perform fully time-resolved SMS at high pressures, in combination with pulsed laser heating in DACs was developed. The Mössbauer absorption of the sample can be fully tracked along the duration of the laser pulse, and its temperature can be estimated on both heated surfaces using spectroradiometry as well as in bulk from the central shift (CS) of the Mössbauer spectra. The method was demonstrated by heating iron in KCl at 32 GPa, iron in argon at 36 GPa, and $\text{Fe}_{25}\text{O}_{32}$ in Ne at 77 GPa.

The experiments were carried out using the synchrotron Mössbauer source¹⁴ at the nuclear resonance beamline ID18⁸⁴ at the ESRF, that employs the pure nuclear reflection from an iron borate ($^{57}\text{FeBO}_3$) crystal to reduce the broadband spectrum of the undulator source to a bandwidth of the order of few times the natural linewidth of the 14.413 keV Mössbauer transition of ^{57}Fe . For the heating of the sample, the portable double-sided pulsed laser heating setup was used, that was developed as part of this thesis.

Apart from the temperature determination on both surfaces of the heated sample provided by spectroradiometry, Mössbauer spectroscopy also provides a measure of temperature: the relative energy resolution of $\sim 10^{-13}$ for ^{57}Fe allows the observation of the second order Doppler shift^{85,86}. The temperature determination through the second order Doppler shift ideally complements spectroradiometry: it is bulk sensitive, it does not require calibration in order to account for the emissivity and optical transfer function, and it is applicable for temperatures below 1000 K, where the peak of the black-body radiation spectrum is shifted to the infrared, and the intensity in the bandwidth of typical spectrometer setups is low.

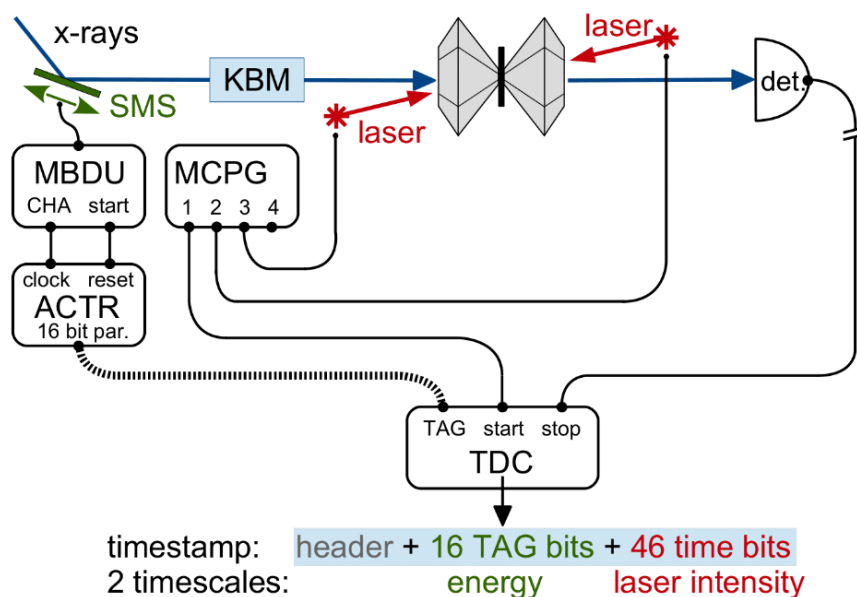


Figure 4.1-11. Experimental setup. KBM: focusing mirrors in Kirkpatrick Baez configuration. MBDU: Mössbauer drive unit. ACTR: auxiliary counter, MCPG: multi-channel pulse and delay generator, TDC: time to digital converter. Each laser trigger starts a TDC sweep. The phase of the transducer is encoded in a 16 bit tag which is inserted into the timestamp for each stop event from the detector.

The experimental setup employs fast electronics for the detection of photons and their energy level. The photons transmitted through the sample are detected with a scintillation detector. The detector signal is discriminated into fast NIM pulses and these events (that correspond to detected photons) are then recorded by a Fast Comtech 7889 multi-stop time to digital converter (TDC) with respect to the periodic laser trigger, serving as start signal. This TDC generates a timestamp for each event. In addition, a parallel 16-bit TTL tag input is evaluated for each stop event and included in the timestamp. This tag input is used to encode the phase and, thus, the velocity of the transducer as a binary number. The number corresponds to the channel index of the multi-channel analyzer often used in conventional Mössbauer spectroscopy. As a result, each timestamp contains information on both, the excitation energy, and the time within the laser period of every detected photon. Figure 4.1-11 shows the schematic of the setup. Figure 4.1-12 shows an example of a two-dimensional histogram of the data constructed from the transducer and laser timescales.

The timestamps of every detection from the TDC are written to a continuous list-file which can not only be explored in the two dimensions of transducer velocity and laser intensity, but additionally in the order of acquisition, i.e. representing different generations of the histogram during data collection. The temporal resolution of the present detection scheme is only limited by the nuclear lifetime (~ 98 ns for the transition of ^{57}Fe at 14.4 keV).

In the first experiment, the experimental setup was tested on an Fe sample in KCl at 32 GPa and the stability of heating was verified.

In the second experiment, a sample of Fe was gas-loaded in argon and compressed to 36 GPa in a DAC and heated from both sides with a laser repetition rate of 50 kHz. It was observed that although at the beginning of the laser pulse and heating of the sample, the center of absorption first moves towards negative velocities, as expected, when the laser intensity reaches its maximum the resonant absorption is lost. Following that, the absorption is recovered with a huge positive shift, that cannot be explained by the temperature increase.

The experiment was repeated with different relative laser timing revealing that the response of the center shift strongly depends on the side from which the sample is heated. This suggests that the large velocities are the results of actual displacements of the sample, as previously reported⁸³. From the data it can be concluded that the sample is directed away from the respective laser for increasing and towards the laser for decreasing temperatures.

In an experiment with $\text{Fe}_{0.94}\text{O}$ loaded in Ne and compressed to 77 GPa, the material quickly reacted *in situ* to $\text{Fe}_{25}\text{O}_{32}$ upon heating as evidenced by x-ray diffraction performed after completion of the experiment. In order to observe the magnetic transition, the sample was heated from both sides with a repetition rate of 20 kHz. The collapse of the magnetic hyperfine splitting upon heating is clearly observed (Figure 4.1-12). However, pinpointing the magnetic transition temperatures during the heating and cooling cycle requires precise control of the laser pulse shape in order to obtain ramp-profiles in the resulting sample temperatures.

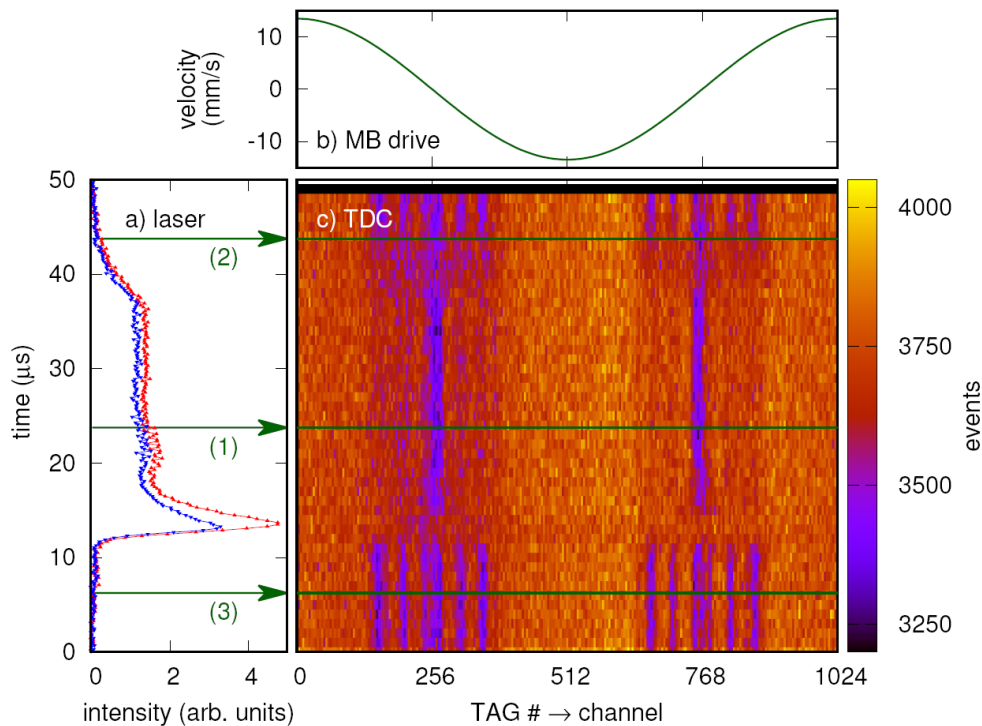


Figure 4.1-12. SMS in $\text{Fe}_{25}\text{O}_{32}$ at 77 GPa. 2D histogram of the raw data, as a function of the transducer phase (tag) and laser time, with the corresponding laser pulse shapes (a) from both heating sides and Mössbauer drive velocity (b).

The detection scheme developed in this work is capable of fully time resolved Synchrotron Mössbauer spectroscopy for experiments with pulsed laser heating in diamond anvil cells. The determination of melting, of structural, and of magnetic phase transitions directly benefits from the dynamics of pulsed laser heating in combination with the flexible binning scheme, as the transition lines are crossed twice, first in rising and then in falling temperatures, and with a well-defined velocity. In addition, the whole temperature time-series can be acquired simultaneously. Results provide the first evidence for the observation of thermal dilatation effects inside the sample chamber of the laser heated DAC that is to be investigated and discussed in further studies.

4.2 Outlook and perspectives

The main goal of this thesis was to investigate the capabilities of the experimental technique of pulsed laser heating inside the diamond anvil cell, that, despite its use from the first years of laser-heated diamond anvil cell experiments, has started only recently to be employed by the high-pressure science community as a method for time-resolved studies of materials.

So far, whenever the pulsed laser heating technique was presented, it was followed by a series of arguments that constitute pulsed heating an improvement of the continuous-wave heating method. These included the long-term heating stability, the higher achievable heating temperatures and the prevention of chemical interactions through the minimization of heating time during measurements. However, due to the lack of extensive methodological studies, the arguments were mainly based on experience.

In the course of this thesis, a pulsed laser heating system was developed and was employed in studies with different spectroscopic techniques in various synchrotron beamlines, validating the long-term heating stability at high temperatures of pulsed heating. The results of the following study on the reaction of carbon from the diamond anvils with iron led to the reconsideration of the effects of pulsed heating on the chemical stability inside the DAC, indicating that there might not be an obvious advantage in comparison to continuous wave heating. Following these observations, the effects of pulsed laser heating on the stability of ferropericlase were studied. The experimental results further supported the fact that pulsed laser heating might actually accelerate chemical processes inside the DAC. The study produced results that are important for geochemistry, signifying the utility of pulsed laser heating for such studies. The thesis includes the development of two more experimental systems that further demonstrate the capabilities of laser heating studies and the possibility to be coupled with different experimental techniques, yielding important conclusions for high-pressure science.

The results of this thesis demonstrate the importance of pulsed laser heating in geoscience and material science. Through its course, the view on the effects of pulsed laser heating has been revised, with indications that pulsed laser heating causes the acceleration of chemical processes. However, our results suggest that even though this is not desired for some types of experiments, pulsed laser heating is indeed a method that can help to investigate chemical processes that were previously not easily observable with different heating methods.

4.3 List of manuscripts and statement of authors' contribution

[1] G. Aprilis (GA), C. Strohm (CS), I. Kuppenko (IK), S. Linhardt (SL), A. Laskin (AL), D.M. Vasiukov (DMV), V. Cerantola (VC), E.G. Koemets (EGK), C. McCammon (CM), A. Kurnosov (AK), A.I. Chumakov (AIC), R. Rüffer (RR), N. Dubrovinskaia (ND), and L. Dubrovinsky (LD). Portable double-sided pulsed laser heating system for time-resolved geoscience and materials science applications. *Review of Scientific Instruments*, **88**(8), 084501 (2017).

The laser system described in the paper was developed by GA with the technical support of SL, LD and ND. The laser focusing optics were designed and provided by AL. The synchrotron Mössbauer and nuclear inelastic scattering data were collected and analyzed by GA, CS, IK, DMV, VC, CM, AK, AIC, RR, ND and LD, employing the time-resolved Mössbauer collection scheme developed by CS. The laser heating was conducted by GA with the help of IK and the temperature data were collected and analyzed by GA with the help of EGK and IK. GA did a final assessment of the results and wrote the manuscript with contributions from all co-authors.

[2] G. Aprilis (GA), I. Kantor (IKa), I. Kuppenko (IKu), V. Cerantola (VC), A. Pakhomova (AP), I.E. Collings (IEC), R. Torchio (RT), T. Fedotenko (TF), S. Chariton (SC), M. Bykov (MB), E. Bykova (EB), E. Koemets (EK), D.M. Vasiukov (DMV), C. McCammon (CM), L. Dubrovinsky (LD),

and N. Dubrovinskaia (ND). Comparative study of the influence of pulsed and continuous wave laser heating on the mobilization of carbon and its chemical reaction with iron in a diamond anvil cell, *Journal of Applied Physics*, **125**(9), 095901 (2019).

The experiment at ID24 of the ESRF was proposed by IKu, LD and ND. The X-ray absorption spectroscopy data were collected and analyzed by IKa, GA, RT and LD, employing the laser heating system of ID24 developed by IKa and modified by IKa and GA. The X-ray diffraction data were collected and analyzed by GA, AP, IEC, SC, MB, EB and EK. The synchrotron Mössbauer data were collected and analyzed by GA, VC, DMV, TF, EK, CM and LD. The laser heating was conducted by GA with the help of IK and TF and the temperature data were collected and analyzed by GA. GA did a final assessment of the results and wrote the manuscript with contributions from all co-authors.

[3] G. Aprilis (GA), A. Pakhomova (AP), S. Chariton (SC), S. Khandarkhaeva (SK), C. Melai (CM), E. Bykova (EB), M. Bykov (MB), T. Fedotenko (TF), E. Koemets (EK), C. McCammon (CMcC), L. Dubrovinsky (LD), and N. Dubrovinskaia (ND). The effect of pulsed laser heating on the stability of ferropicriase at high pressures. *Prepared for submission to Journal of Solid State Chemistry*.

The samples were synthesized by CM and characterized by CM, CMcC and LD. The X-ray diffraction data were collected and analyzed by SC, SK, EB, MB, EK, GA, LD and ND. The synchrotron Mössbauer data were collected and analyzed by GA, TF, EK and CMcC. The laser heatings were conducted by GA and TF with the help of EK and the temperature data were collected and analyzed by GA. The single-crystal diffraction data were analyzed and refined by EB, LD and AP. GA did a final assessment of the results and wrote the manuscript with the help of AP and with contributions from all co-authors.

[4] E. Bykova (EB), G. Aprilis (GA), M. Bykov (MB), K. Glazyrin (KG), M. Wendt (MW), S. Wenz (SW), H.-P. Liermann (HPL), J.T. Roeh (JTR), A. Ehnes (AE), N. Dubrovinskaia (ND), and L. Dubrovinsky (LD). Single-crystal diffractometer coupled with double-sided laser heating system at the Extreme Conditions Beamline P02.2 at PETRAIII. *Review of Scientific Instruments*, **90**(7), 073907 (2019).

The single-crystal diffractometer described in the paper was designed and developed by EB and MB with the technical support of KG, MW, SW, HPL, JTR and AE. The laser heating system was developed by GA, EB and MB and the whole experimental setup was tested and finalized by EB, GA and MB. The experiments were conducted by EB, GA, MB, LD and ND with the support of KG. The laser heatings were conducted by GA with the help of EB and MB and the temperature data were collected and analyzed by GA. The *in situ* single-crystal data were analyzed and refined by MB with the help of EB. EB did a final assessment of the results and wrote the manuscript with contributions from all co-authors.

[5] C. Strohm (CS), G. Aprilis (GA), I. Kuppenko (IK), D.M. Vasiukov (DMV), V. Cerantola (VC), A.I. Chumakov (AIC), R. Ruffer (RR), C. McCammon (CM), and L. Dubrovinsky (LD). Fully time-resolved synchrotron Mössbauer spectroscopy for pulsed laser heating experiments in diamond anvil cell. *Prepared for submission to Journal of Synchrotron Radiation*.

The system described in the paper was developed by CS with the technical support of IK, AIC and RR. The laser heating system used in the presented experiments was developed by IK and GA. The laser heatings were conducted by GA and IK and the temperature data were collected and analyzed by GA. The synchrotron Mössbauer data were collected and analyzed by CS, GA, IK, DMV, VC, CM and LD. CS did a final assessment of the results and wrote the manuscript with contributions from all co-authors.

References

1. Kuppenko, I. *et al.* Portable double-sided laser-heating system for Mössbauer spectroscopy and X-ray diffraction experiments at synchrotron facilities with diamond anvil cells. *Rev. Sci. Instrum.* **83**, 124501 (2012).
2. Boehler, R., Musshoff, H. G., Ditz, R., Aquilanti, G. & Trapananti, A. Portable laser-heating stand for synchrotron applications. *Rev. Sci. Instrum.* **80**, 045103 (2009).
3. Shen, G., Wang, L., Ferry, R., Mao, H. & Hemley, R. J. A portable laser heating microscope for high pressure research. *J. Phys. Conf. Ser.* **215**, 012191 (2010).
4. Dubrovinsky, L. *et al.* Portable laser-heating system for diamond anvil cells. *J. Synchrotron Radiat.* **16**, 737–741 (2009).
5. Sinmyo, R. & Hirose, K. The Soret diffusion in laser-heated diamond-anvil cell. *Phys. Earth Planet. Inter.* **180**, 172–178 (2010).
6. Watanuki, T., Shimomura, O., Yagi, T., Kondo, T. & Isshiki, M. Construction of laser-heated diamond anvil cell system for in situ x-ray diffraction study at SPring-8. *Rev. Sci. Instrum.* **72**, 1289 (2001).
7. Rainey, E. S. G. & Kavner, A. Peak scaling method to measure temperatures in the laser-heated diamond anvil cell and application to the thermal conductivity of MgO. *J. Geophys. Res. Solid Earth* **119**, 8154–8170 (2014).
8. Campbell, A. J. Measurement of temperature distributions across laser heated samples by multispectral imaging radiometry. *Rev. Sci. Instrum.* **79**, 015108 (2008).
9. Laskin, A. & Laskin, V. π Shaper – Refractive Beam Shaping Optics for Advanced Laser Technologies. *J. Phys. Conf. Ser.* **276**, 012171 (2011).
10. Prakapenka, V. B. *et al.* Advanced flat top laser heating system for high pressure research at GSECARS: application to the melting behavior of germanium. *High Press. Res.* **28**, 225–235 (2008).
11. Heinz, D. L. & Jeanloz, R. Temperature measurements in the laser-heated diamond cell. in *High pressure research in mineral physics: A Volume in Honor of Syun-iti Akimoto* (eds. Manghnani, M. H. & Syono, Y.) 113–127 (American Geophysical Union, 1987).
12. Walter, M. J. & Koga, K. T. The effects of chromatic dispersion on temperature measurement in the laser-heated diamond anvil cell. *Phys. Earth Planet. Inter.* **143–144**, 541–558 (2004).
13. Benedetti, L. R. & Loubeyre, P. Temperature gradients, wavelength-dependent emissivity, and accuracy of high and very-high temperatures measured in the laser-heated diamond cell. *High Press. Res.* **24**, 423–445 (2004).
14. Potapkin, V. *et al.* The ^{57}Fe Synchrotron Mössbauer Source at the ESRF. *J. Synchrotron*

- Radiat.* **19**, 559–569 (2012).
15. Chumakov, A. & Rüffer, R. Nuclear inelastic scattering. *Hyperfine Interact.* **113**, 59–79 (1998).
 16. Rüffer, R. & Chumakov, A. I. Nuclear inelastic scattering. *Hyperfine Interact.* **128**, 255–272 (2000).
 17. Boehler, R. Temperatures in the Earth’s core from melting-point measurements of iron at high static pressures. *Nature* **363**, 534–536 (1993).
 18. Anzellini, S., Dewaele, A., Mezouar, M., Loubeyre, P. & Morard, G. Melting of Iron at Earth’s Inner Core Boundary Based on Fast X-ray Diffraction. *Science (80-.)*. **340**, 464–466 (2013).
 19. Aquilanti, G. *et al.* Melting of iron determined by X-ray absorption spectroscopy to 100 GPa. *Proc. Natl. Acad. Sci.* **112**, 12042–12045 (2015).
 20. Sinmyo, R., Hirose, K. & Ohishi, Y. Melting curve of iron to 290 GPa determined in a resistance-heated diamond-anvil cell. *Earth Planet. Sci. Lett.* **510**, 45–52 (2019).
 21. Prakapenka, V. B., Shen, G. & Dubrovinsky, L. S. Carbon transport in diamond anvil cells. *High Temp. - High Press.* **35–36**, 237–249 (2003).
 22. Rouquette, J. *et al.* Iron-carbon interactions at high temperatures and pressures. *Appl. Phys. Lett.* **92**, 121912 (2008).
 23. Frost, D. J. *et al.* Partitioning of oxygen between the Earth’s mantle and core. *J. Geophys. Res.* **115**, B02202 (2010).
 24. Tateno, S., Hirose, K., Ohishi, Y. & Tatsumi, Y. The Structure of Iron in Earth’s Inner Core. *Science (80-.)*. **330**, 359–361 (2010).
 25. Lord, O. T., Walter, M. J., Dasgupta, R., Walker, D. & Clark, S. M. Melting in the Fe–C system to 70 GPa. *Earth Planet. Sci. Lett.* **284**, 157–167 (2009).
 26. Morard, G. *et al.* Fe–FeO and Fe–Fe 3 C melting relations at Earth’s core–mantle boundary conditions: Implications for a volatile-rich or oxygen-rich core. *Earth Planet. Sci. Lett.* **473**, 94–103 (2017).
 27. Morard, G. *et al.* Solving Controversies on the Iron Phase Diagram Under High Pressure. *Geophys. Res. Lett.* **45**, 11074–11082 (2018).
 28. Dewaele, A., Mezouar, M., Guignot, N. & Loubeyre, P. High Melting Points of Tantalum in a Laser-Heated Diamond Anvil Cell. *Phys. Rev. Lett.* **104**, 255701 (2010).
 29. Pascarelli, S. *et al.* The Time-resolved and Extreme-conditions XAS (TEXAS) facility at the European Synchrotron Radiation Facility: the energy-dispersive X-ray absorption spectroscopy beamline ID24. *J. Synchrotron Radiat.* **23**, 353–368 (2016).

30. Merlini, M. & Hanfland, M. Single-crystal diffraction at megabar conditions by synchrotron radiation. *High Press. Res.* **33**, 511–522 (2013).
31. Liermann, H. P. *et al.* The Extreme Conditions Beamline P02.2 and the Extreme Conditions Science Infrastructure at PETRA III. *J. Synchrotron Radiat.* **22**, 908–924 (2015).
32. Aquilanti, G. *et al.* Development of micro-XANES mapping in the diamond anvil cell. *J. Synchrotron Radiat.* **16**, 376–379 (2009).
33. Torchio, R. *et al.* Probing local and electronic structure in Warm Dense Matter: single pulse synchrotron x-ray absorption spectroscopy on shocked Fe. *Sci. Rep.* **6**, 26402 (2016).
34. Mazevet, S. *et al.* Ab initio calculation of x-ray absorption of iron up to 3 Mbar and 8000 K. *Phys. Rev. B* **89**, 100103 (2014).
35. Dewaele, A. *et al.* Quasihydrostatic equation of state of Iron above 2 Mbar. *Phys. Rev. Lett.* **97**, 29–32 (2006).
36. Zha, C.-S., Bassett, W. A. & Shim, S.-H. Rhenium, an in situ pressure calibrant for internally heated diamond anvil cells. *Rev. Sci. Instrum.* **75**, 2409–2418 (2004).
37. Fei, Y. *et al.* Toward an internally consistent pressure scale. *Proc. Natl. Acad. Sci.* **104**, 9182–9186 (2007).
38. Nakajima, Y. *et al.* Thermoelastic property and high-pressure stability of Fe₇C₃: Implication for iron-carbide in the Earth's core. *Am. Mineral.* **96**, 1158–1165 (2011).
39. Okamoto, H. The C-Fe (carbon-iron) system. *J. Phase Equilibria* **13**, 543–565 (1992).
40. Narygina, O. *et al.* Phase relations in Fe–Ni–C system at high pressures and temperatures. *Phys. Chem. Miner.* **38**, 203–214 (2011).
41. Glazyrin, K. *et al.* Importance of Correlation Effects in hcp Iron Revealed by a Pressure-Induced Electronic Topological Transition. *Phys. Rev. Lett.* **110**, 117206 (2013).
42. Prescher, C. *et al.* Structurally hidden magnetic transitions in Fe₃C at high pressures. *Phys. Rev. B* **85**, 140402 (2012).
43. Kuppenko, I. *et al.* Time differentiated nuclear resonance spectroscopy coupled with pulsed laser heating in diamond anvil cells. *Rev. Sci. Instrum.* **86**, 114501 (2015).
44. Komabayashi, T., Fei, Y., Meng, Y. & Prakapenka, V. In-situ X-ray diffraction measurements of the γ - ϵ transition boundary of iron in an internally-heated diamond anvil cell. *Earth Planet. Sci. Lett.* **282**, 252–257 (2009).
45. Kubo, A. *et al.* In situ X-ray observation of iron using Kawai-type apparatus equipped with sintered diamond: Absence of β phase up to 44 GPa and 2100 K. *Geophys. Res. Lett.* **30**, 1126 (2003).

46. Lee, K. K. M. *et al.* Equations of state of the high-pressure phases of a natural peridotite and implications for the Earth's lower mantle. *Earth Planet. Sci. Lett.* **223**, 381–393 (2004).
47. Tschauner, O. *et al.* Discovery of bridgmanite, the most abundant mineral in Earth, in a shocked meteorite. *Science (80-.)*. **346**, 1100–1102 (2014).
48. Xu, W., Lithgow-Bertelloni, C., Stixrude, L. & Ritsema, J. The effect of bulk composition and temperature on mantle seismic structure. *Earth Planet. Sci. Lett.* **275**, 70–79 (2008).
49. Irifune, T. Absence of an aluminous phase in the upper part of the Earth's lower mantle. *Nature* **370**, 131–133 (1994).
50. Wood, B. J. Phase transformations and partitioning relations in peridotite under lower mantle conditions. *Earth Planet. Sci. Lett.* **174**, 341–354 (2000).
51. Kaminsky, F. V. *The Earth's Lower Mantle*. (Springer International Publishing, 2017). doi:10.1007/978-3-319-55684-0
52. Mao, H., Guoyin, S. & Hemley, R. J. Multivariable Dependence of Fe-Mg Partitioning in the Lower Mantle. *Science (80-.)*. **278**, 2098–2100 (1997).
53. Katsura, T. & Ito, E. Determination of Fe-Mg partitioning between perovskite and magnesiowüstite. *Geophys. Res. Lett.* **23**, 2005–2008 (1996).
54. Lin, J.-F. *et al.* Stability of magnesiowüstite in Earth's lower mantle. *Proc. Natl. Acad. Sci.* **100**, 4405–4408 (2003).
55. Badro, J. *et al.* Iron Partitioning in Earth's Mantle: Toward a Deep Lower Mantle Discontinuity. *Science (80-.)*. **300**, 789–791 (2003).
56. Dubrovinsky, L. S. Stability of Ferropericlase in the Lower Mantle. *Science (80-.)*. **289**, 430–432 (2000).
57. Dubrovinsky, L., Dubrovinskaia, N., Annersten, H., Hålenius, E. & Harryson, H. Stability of (Mg_{0.5}Fe_{0.5})O and (Mg_{0.8}Fe_{0.2})O magnesiowüstites in the lower mantle. *Eur. J. Mineral.* **13**, 857–861 (2001).
58. Kondo, T., Ohtani, E., Hirao, N., Yagi, T. & Kikegawa, T. Phase transitions of (Mg,Fe)O at megabar pressures. *Phys. Earth Planet. Inter.* **143–144**, 201–213 (2004).
59. Lin, J.-F. *et al.* Electrical conductivity of the lower-mantle ferropericlase across the electronic spin transition. *Geophys. Res. Lett.* **34**, 2–5 (2007).
60. Fei, Y. *et al.* Spin transition and equations of state of (Mg, Fe)O solid solutions. *Geophys. Res. Lett.* **34**, L17307 (2007).
61. Kaminsky, F. Mineralogy of the lower mantle: A review of 'super-deep' mineral inclusions in diamond. *Earth-Science Rev.* **110**, 127–147 (2012).

62. Deng, J. & Lee, K. K. M. Viscosity jump in the lower mantle inferred from melting curves of ferropericlase. *Nat. Commun.* **8**, 1997 (2017).
63. Goncharov, A. F. *et al.* Laser heating in diamond anvil cells: developments in pulsed and continuous techniques. *J. Synchrotron Radiat.* **16**, 769–772 (2009).
64. Goncharov, A. F. *et al.* X-ray diffraction in the pulsed laser heated diamond anvil cell. *Rev. Sci. Instrum.* **81**, 113902 (2010).
65. Katsura, T., Yoneda, A., Yamazaki, D., Yoshino, T. & Ito, E. Adiabatic temperature profile in the mantle. *Phys. Earth Planet. Inter.* **183**, 212–218 (2010).
66. Trubitsyn, V. P. & Trubitsyna, A. P. Effects of compressibility in the mantle convection Equations. *Izv. Phys. Solid Earth* **51**, 801–813 (2015).
67. Dubrovinsky, L. S. *et al.* The structure of the metallic high-pressure Fe₃O₄ polymorph: experimental and theoretical study. *J. Phys. Condens. Matter* **15**, 7697–7706 (2003).
68. Greenberg, E. *et al.* High-pressure magnetic, electronic, and structural properties of MFe₂O₄ (M = Mg,Zn,Fe) ferric spinels. *Phys. Rev. B* **95**, 195150 (2017).
69. Wirth, R., Dobrzhinetskaya, L., Harte, B., Schreiber, A. & Green, H. W. High-Fe (Mg, Fe)O inclusion in diamond apparently from the lowermost mantle. *Earth Planet. Sci. Lett.* **404**, 365–375 (2014).
70. Kaminsky, F. V. & Lin, J.-F. Iron partitioning in natural lower-mantle minerals: Toward a chemically heterogeneous lower mantle. *Am. Mineral.* **102**, 824–832 (2017).
71. Anzolini, C. *et al.* Depth of diamond formation obtained from single periclase inclusions. *Geology* **47**, 219–222 (2019).
72. Bataleva, Palyanov, Borzdov & Bayukov. Processes and Conditions of the Origin for Fe³⁺-Bearing Magnesiowüstite under Lithospheric Mantle Pressures and Temperatures. *Minerals* **9**, 474 (2019).
73. Boffa Ballaran, T., Uenver-Thiele, L. & Woodland, A. B. Complete substitution of Fe²⁺ by Mg in Fe₄O₅: The crystal structure of the Mg₂Fe₂O₅ end-member. *Am. Mineral.* **100**, 628–632 (2015).
74. Uenver-Thiele, L., Woodland, A. B., Ballaran, T. B., Miyajima, N. & Frost, D. J. Phase relations of Fe-Mg spinels including new high-pressure post-spinel phases and implications for natural samples. *Am. Mineral.* **102**, 2054–2064 (2017).
75. Ishii, T., Uenver-Thiele, L., Woodland, A. B., Alig, E. & Ballaran, T. B. Synthesis and crystal structure of Mg-bearing Fe₉O₁₁: New insight in the complexity of Fe-Mg oxides at conditions of the deep upper mantle. *Am. Mineral.* **103**, 1873–1876 (2018).
76. Martirosyan, N. S. *et al.* The Mg-carbonate–Fe interaction: Implication for the fate of subducted carbonates and formation of diamond in the lower mantle. *Geosci. Front.* **10**, 1449–1458 (2019).

77. Kaminsky, F. V., Wirth, R. & Schreiber, A. A microinclusion of lower-mantle rock and other minerals and nitrogen lower-mantle inclusions in a diamond. *Can. Mineral.* **53**, 83–104 (2015).
78. Shen, G., Rivers, M. L., Wang, Y. & Sutton, S. R. Laser heated diamond cell system at the advanced photon source for in situ x-ray measurements at high pressure and temperature. *Rev. Sci. Instrum.* **72**, 1273–1282 (2001).
79. Schultz, E. *et al.* Double-sided laser heating system for in situ high pressure–high temperature monochromatic x-ray diffraction at the esrf. *High Press. Res.* **25**, 71–83 (2005).
80. Hasegawa, M. & Yagi, T. Systematic study of formation and crystal structure of 3d-transition metal nitrides synthesized in a supercritical nitrogen fluid under 10 GPa and 1800 K using diamond anvil cell and YAG laser heating. *J. Alloys Compd.* **403**, 131–142 (2005).
81. Bykov, M. *et al.* Fe-N system at high pressure reveals a compound featuring polymeric nitrogen chains. *Nat. Commun.* **9**, (2018).
82. Clark, W. P. *et al.* High-Pressure NiAs-Type Modification of FeN. *Angew. Chemie Int. Ed.* **56**, 7302–7306 (2017).
83. Vagizov, F., Kolesov, R., Olariu, S., Rostovtsev, Y. & Kocharovskaya, O. Experimental observation of vibrations produced by pulsed laser beam in MgO:57Fe. *Hyperfine Interact.* **167**, 917–921 (2006).
84. Ruffer, R. & Chumakov, A. I. Nuclear Resonance Beamline at ESRF. *Hyperfine Interact.* **97–98**, 589–604 (1996).
85. Pound, R. V. & Rebka, G. A. Variation with Temperature of the Energy of Recoil-Free Gamma Rays from Solids. *Phys. Rev. Lett.* **4**, 274–275 (1960).
86. Josephson, B. D. Temperature-Dependent Shift of γ -Rays Emitted by a Solid. *Phys. Rev. Lett.* **4**, 341–342 (1960).

Chapter 5

Results

5.1 Portable double-sided pulsed laser heating system for time- resolved geoscience and materials science applications

G. Aprilis^{1,2,*}, C. Strohm³, I. Kuppenko^{4,5}, S. Linhardt¹, A. Laskin⁶, D. Vasiukov^{1,2}, V. Cerantola^{1,5}, E. G. Koemets¹, C. McCammon¹, A. Kurnosov¹, A. I. Chumakov⁵, R. Ruffer⁵, N. Dubrovinskaia², L. Dubrovinsky¹

¹ Bayerisches Geoinstitut, Universität Bayreuth, D-95440 Bayreuth, Germany

² Materials Physics and Technology at Extreme Conditions, Laboratory of Crystallography, Universität Bayreuth, D-95440 Bayreuth, Germany

³ Photon Science, DESY, D-22607 Hamburg, Germany

⁴ Institut für Mineralogie, University of Münster, D-48149 Münster, Germany

⁵ ESRF – The European Synchrotron, CS 40220, 38043 Grenoble Cedex 9, France

⁶ AdlOptica Optical Systems GmbH, D-12489 Berlin, Germany

* Correspondent author (e-mail: georgios.aprilis@uni-bayreuth.de)

Review of Scientific Instruments, **88**(8), 084501 (2017)

5.1.1 Abstract

A portable double-sided pulsed laser heating system for diamond anvil cells has been developed that is able to stably produce laser pulses as short as a few microseconds with repetition frequencies up to 100 kHz. *In situ* temperature determination is possible by collecting and fitting the thermal radiation spectrum for a specific wavelength range (particularly, between 650 nm and 850 nm) to the Planck radiation function. Surface temperature information can also be time-resolved by using a gated detector that is synchronized with the laser pulse modulation, and space-resolved with the implementation

of a multi-point thermal radiation collection technique. The system can be easily coupled with equipment at synchrotron facilities, particularly for nuclear resonance spectroscopy experiments. Examples of applications include investigations of high-pressure high-temperature behavior of iron oxides, both in house and at the European Synchrotron Radiation Facility (ESRF) using the Synchrotron Mössbauer Source (SMS) and Nuclear Inelastic Scattering (NIS).

5.1.2 Introduction

Modern high-pressure research demands that properties of materials be studied *in situ*, for example inside diamond anvil cells (DAC), ideally simultaneously at high temperature and high pressure. Among the two major methods of heating in DACs, namely laser and resistive heating^{1,2}, laser heating has been already used for more than five decades^{3,4} and has numerous applications in mineral physics and high pressure chemistry, physics, Earth and material sciences. The laser heated diamond anvil cell (LHDAC) technique is used, for example, for simulating conditions similar to those in the deep Earth and planetary interiors, or for investigating chemical processes and physical phenomena at extreme conditions. At synchrotron light source facilities the LHDAC technique has been coupled with various experimental set-ups, such as X-ray diffraction^{5,6}, Nuclear Inelastic Scattering (NIS), the Synchrotron Mössbauer Source^{7,8}, and X-ray Absorption Near Edge Structure spectroscopy (XANES)^{9,10}.

In addition to continuous-wave (CW) heating, pulsed lasers have been used starting from the first attempts to laser heat samples in a DAC, with the advantage of achieving significantly higher temperatures^{11,12} due to the concentration of the high laser power in a short impulse. Since the beginning of the 2000s, pulsed heating has been coupled with time-resolved measurements^{13,14}. The repetitive heating and cooling of the sample makes time an extra variable in addition to pressure and temperature, which is not possible with continuous-wave laser heating. An entirely new field of research has been introduced, allowing determination of important material properties such as thermal conductivity and diffusivity, and melting temperatures^{15–18}.

The spatial distribution of temperatures at and around the heated spot is of great importance in a LHDAC experiment. The significance of a surface temperature map has been noted in many studies^{19–24}. Such a map is relevant especially to high-pressure melting experiments^{21–24}, but not exclusively^{19,20}. The methods used so far to determine the surface temperature distribution estimate the temperature profile along one line on the sample by leading the thermal emission into a spectrometer through a slit^{21–23}.

In this work we present a laser heating system in which a group of optical fibers probe the laser heated area at different spots. This solution provides a two-dimensional surface temperature map. To the authors' knowledge, there is so far no direct two-dimensional temperature mapping technique, apart from computational estimations such as peak scaling²⁰

or multispectral imaging radiometry approaches, in contrast to spectroradiometry²⁵. Use of optical fibers also allows us to physically separate the detector (and spectrometer) from the focusing optics and to avoid introducing additional optical components between them. These provide faster alignment and portability of the system that is especially important for synchrotron facilities, where the lack of space makes a free-space optical path solution unfeasible^{19,26}. Special care is taken for the laser beam shaping and improvement of the focusing optics in order to minimize the temperature estimation error caused by chromatic aberrations^{27,28}.

Thus, our portable pulsed laser heating system provides a solution for both temporally and spatially resolved temperature measurements in a double-sided LHDAC. It is designed to be easily movable between home institutions and synchrotrons, or between different beamlines, where the need for portability of laser heating systems has already been recognized^{8,29–31}. We demonstrate its application through a series of experiments conducted at the Nuclear Resonance beamline (ID 18) of the European Synchrotron Radiation Facility (ESRF).

5.1.3 System overview

The system is shown as a general schematic in Figure 5.1-1. The system consists of the following main components (described in more detail in the following sections):

- Two lasers that independently heat a sample in the DAC from two sides.
- Two Unihead modules (by Precitec GmbH) with optical components to shape and focus each laser beam.
- Laser modulation and synchronization units, including photo-detectors, custom electronics and an oscilloscope for control and visualization of the pulse shapes.
- Two VIS/NIR fiber bundles for collecting thermal radiation which are optically aligned on the sample.
- High-precision spectrometer coupled with a fast, intensified CCD detector used for time-resolved spectroradiometry measurements from both sides.

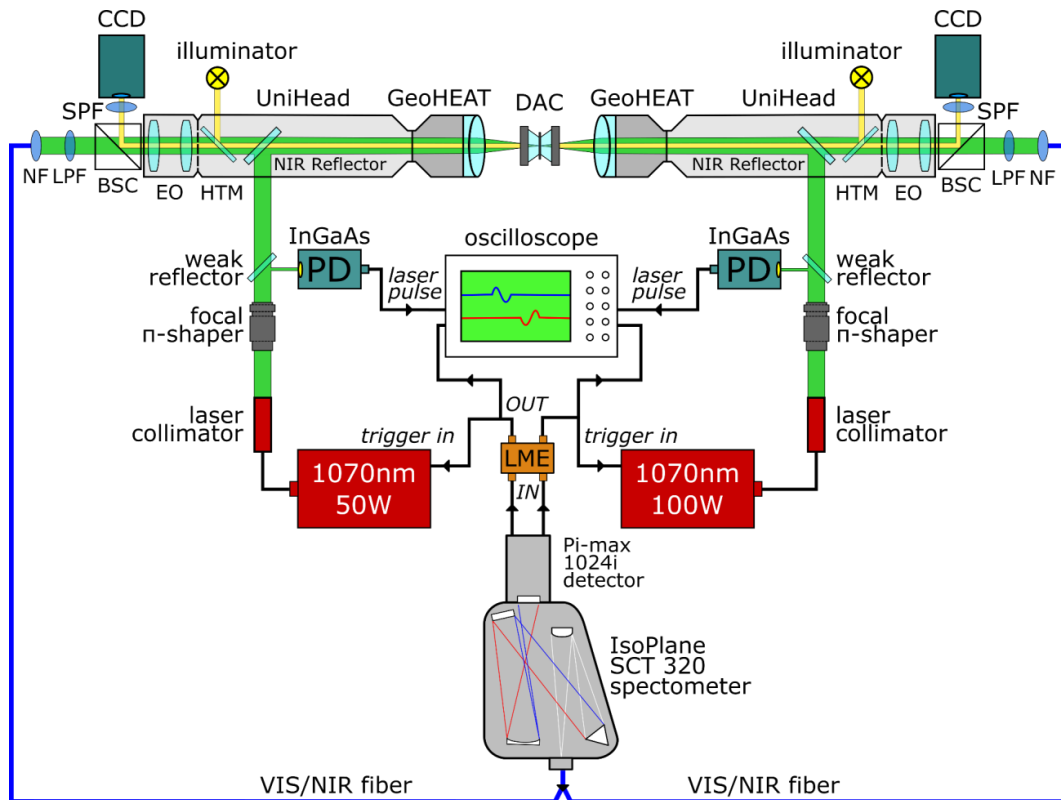


Figure 5.1-1. Double-sided pulsed laser heating system for diamond anvil cells. SPDs are short-pass filters with a cut-off at 850 nm; CCDs are the cameras for sample visual observation; NFs are notch filters at 1064 nm used to isolate the laser beam from the detector; LPFs are longpass filters with cut-on wavelength of 550 nm in order to avoid contamination from the second order diffraction of the grating; BSCs are the beam-splitter cubes; EOs are the “eyepiece” optics of the UniHead modules that focus the image on the viewing cameras and optical fibers; HTMs are half-transparent mirrors that reflect illumination light; GeoHEATs are achromatic lenses for laser focusing and collection of thermal radiation; PDs are the fast InGaAs photo-detectors used to capture laser pulses; and LMEs are the laser modulation electronics (The figure is not drawn to scale)

5.1.3.1 Lasers

We use two SPI RedPower R4 Fiber lasers emitting at the near-infrared (NIR) central wavelength of $1070 \pm 10 \text{ nm}$ — one with maximal power of 100 W and the other with 50 W. The lasers produce a randomly polarized Gaussian beam (TEM_{00}) with a full width at $1/e^2$ of $5 \pm 0.5 \text{ mm}$. The lasers can be operated in both continuous-wave mode as well as modulated with maximum frequency up to 100 kHz. The minimum possible laser pulse width is on the order of a few microseconds, but a very short pulse increases the power control error of the feedback loop of the laser; therefore a hard limit of $5 \mu\text{s}$ is set by the system's modulation electronics to avoid power instabilities. Laser heating experiments can last up to many hours, and the data quality relies greatly on the laser power stability. In the system described here the laser manufacturer provides a power deviation of $< 1.0\%$ over 8 hours for continuous-wave emission.

5.1.3.2 Beam shaping and focusing

The collimated output beam of the laser is very wide for the intended applications; therefore it needs to be shaped and focused accordingly. Each laser beam is collected by a Focal- π Shaper

(Focal- π Shaper_9_1064 by AdlOptica GmbH), which is designed to shape a TEM_{00} beam into a flat-top when combined with focusing optics^{32,33}.

The output beams of the Focal- π Shapers from both sides are focused using two sets of GeoHEAT 40_NIR lenses (Figure 5.1-2 (a)). GeoHEAT lenses are specially designed for laser heating applications with DACs. The required portability of the system prohibits the redundancy of optical paths; therefore, the optical elements for collection of thermal radiation are common with the ones used for laser heating. This setup demands focusing optics that can reliably operate in both spectral bands. GeoHEATs are achromatic objectives made to minimize chromatic aberration at the optimum spectral ranges of 600 nm – 900 nm and 1020 nm – 1100 nm. The nominal chromatic focal shift for GeoHEAT 40_NIR can be seen in Figure 5.1-3.

Samples under high pressure inside a DAC can have dimensions on the order of a few tens of micrometers; hence in order to be able to create a distinct temperature spatial map, a physical resolution of 2.5 μm is set as a specification. According to the Rayleigh criterion³⁴ to provide a 2.5 μm physical resolution, the diameter d_p of the central spot of an Airy distribution in the focal plane of the lens has to be about 5 μm . The f-number (or diaphragm number) of the lens $f/\#$ is calculated using the formula³⁴:

$$f/\# = d_p/(2.44\lambda).$$

For $\lambda = 750 \text{ nm}$, the center of spectral band for measurements, the f-number results in $f/\# = 2.7$. The GeoHEAT 40_NIR is designed with $f/\# = 2.6$ and the focal distance $f' = 40.8 \text{ mm}$ (at 1064 nm); thus, it meets the requirements. This combination provides a large enough field of view for optical sample alignment, as well as a narrow depth of field that is necessary for precision in temperature measurements. The new optical setup is an improvement over previous designs^{8,31} by increasing the numerical aperture and magnification of the system, and thus the resolution.

For simple objectives the working distance is equal to the focal distance, but in the case of a portable system used for synchrotron applications, 40.8 mm is not enough. The space around a DAC should be larger and sufficient for inserting additional optical or X-ray optical elements, for example carbon mirrors for synchrotron single-crystal X-ray diffraction studies in laser-heated DACs⁸. The optical design of the GeoHEAT 40_NIR is implemented as a retrofocus (reverse telephoto) lens, as shown in Figure 5.1-2 (b). It is composed from two optical components (i.e., groups of lenses); the first one has a negative optical power, while the second one has a positive power³⁵. By choosing optical powers of the components as well as an air-gap between them, it is possible to fulfil the conditions of the required focal length and working distance.

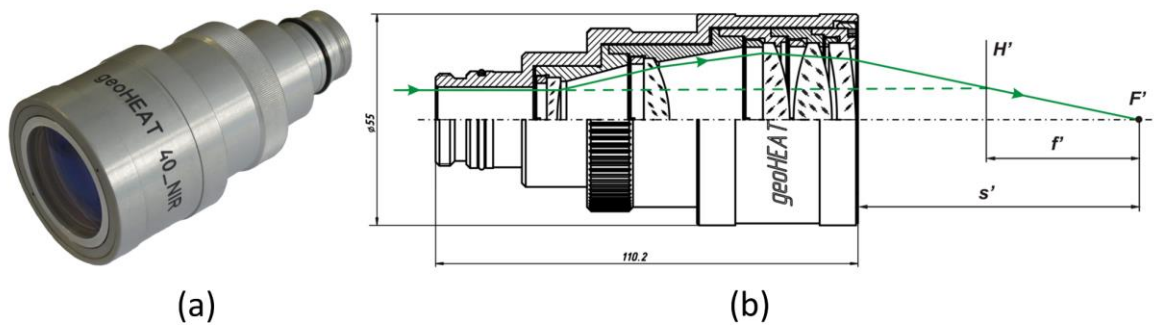


Figure 5.1-2. Photo (a) and optical layout (b) of a geoHEAT 40_NIR built as a reverse telephoto lens. H' is the principle plane and F' the focal spot that define the focal distance f' , which is shorter than s' , the working distance.

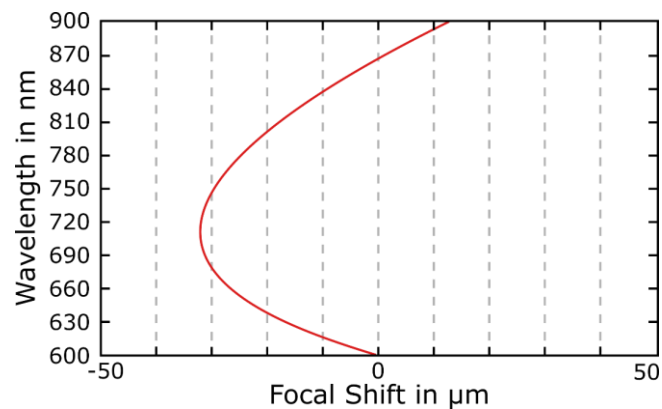


Figure 5.1-3. Diagram of Chromatic Shift for geoHEAT 40_NIR

The beam spot can have a radius as small as $20\ \mu\text{m}$, when a flat-top is used at the focusing distance. An even smaller size can be achieved by adjusting the Focal- π Shaper, but with a Gaussian distribution. With a smooth transmission curve of 96% over the entire spectral range used for temperature determination, the geoHEAT 40_NIR optics facilitate both spectroradiometry and laser heating of the sample, improving significantly the experimental conditions of LHDAC.

5.1.3.3 Laser modulation and synchronization

Synchronization of the lasers is crucial. In order to heat a sample as homogeneously as possible, the peak and duration of the laser pulses should match from both sides. Observation of the laser pulse is done by reflecting a small portion of the laser beam into a photodiode and then recording the response on the oscilloscope (Figure 5.1-1). Two fast InGaAs detectors (DET08CL model from Thorlabs, Inc.) are used in this case, with rise and fall response times of less than a nanosecond. This allows an accurate capturing of the shape of short pulses lasting only a few microseconds.

The main trigger of the system comes directly from the internal trigger generator of the PI-MAX detector. The detector's generator provides a set of two triggers (named SyncMaster1

and SyncMaster2) with a common frequency and a relative delay with respect to each other that can be set by software. These two outputs are led to a custom electronics module that converts the fixed-width triggers into modulation pulses with adjustable width that control the laser behavior.

The modulation electronics are depicted in Figure 5.1-4. The two inputs have a fixed width of 500 ns. Two timer circuit modules connected as monostable multivibrators can shape the incoming triggers into square modulation pulses. The width of the output pulses can be manually set with the help of an oscilloscope and two variable resistors.

In this way, it is possible to easily control the common modulation frequency of the lasers, the duty cycle of their emission independently from each other, and their relative delay. The latter is important, since the response time of the laser depends strongly on the working conditions, such as the duty cycle and the emitting power; thus, it is likely that the two lasers will not respond in exactly the same way, even if they receive their trigger at the same time.

An example of an oscilloscope screen is shown in Figure 5.1-5. A relative delay between two laser triggers and modulation pulse width can be easily adjusted using the screen as a reference, in order to match the laser peak position and pulse width. Their synchronization can be finely tuned with a precision on the order of a few nanoseconds, and it is possible to investigate the thermal response of the sample, especially in the area around the laser peaks. This usually appears at the beginning of the pulse, when even a very small delay between the laser impulses can strongly affect the sample's thermal response between the two heated sides³⁶.

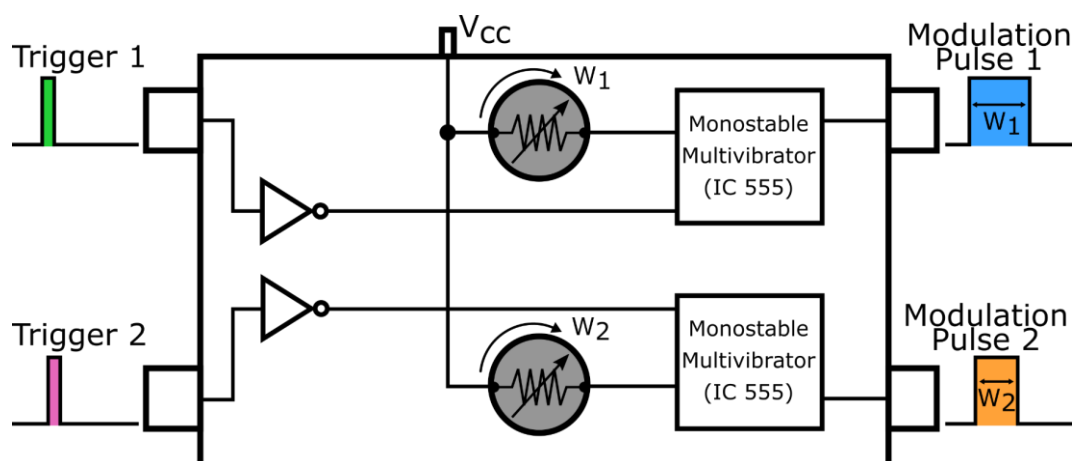


Figure 5.1-4. Schematic of the electronics module that controls the laser modulation. The two input triggers are generated by the PI-MAX detector with fixed width and have adjustable relative delay. Two square pulse outputs independently modulate the two lasers in the pulsed mode.

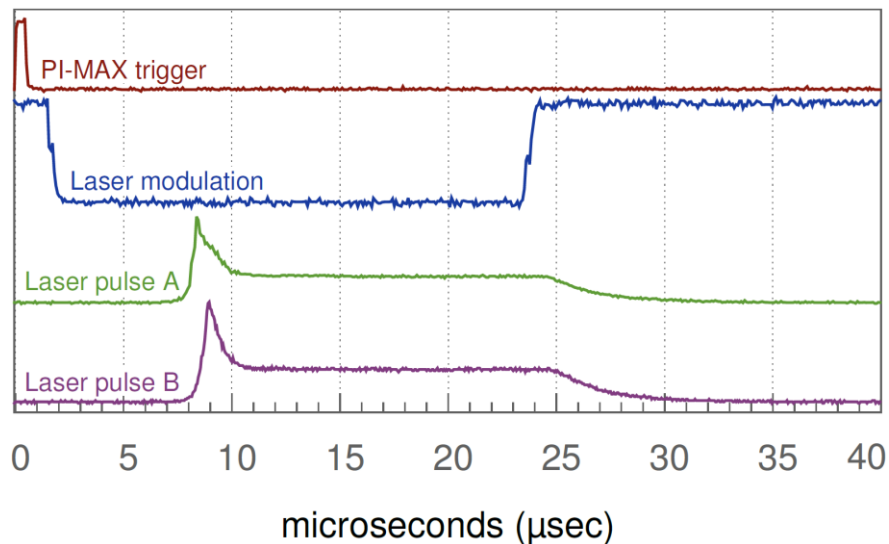


Figure 5.1-5. Example of an oscilloscope screen. PI-MAX sets the frequency by generating short triggers. The lasers are modulated with negative logic, i.e., laser is ON when voltage is LOW. This figure demonstrates the signals needed to create Laser Pulse A. A similar set of PI-MAX trigger and modulation signals are also sent to the second laser, creating the Laser Pulse B. (Colors online)

5.1.3.4 Collection of thermal radiation and temperature determination

The accurate, *in situ* determination of the temperature of the laser-heated sample inside the DAC is crucial. The optical transparency of the diamond anvils allows the collection of the emitted radiation of the heated sample and the estimation of its temperature using the gray body approximation of Planck's law³⁷ (Figure 5.1-6). The thermal radiation is collected from both sides through the same optical path that is used to focus the laser. This is done with a set of two UniHead modules, in order to maintain the portability of the system.

The image of the sample inside the DAC is magnified by the UniHead optics, working as a microscope, and projected into the cameras that are used for optical observation. A proportion of this light is collected by a pair of fiber bundles using a pair of 50–50 beam-splitter cubes (Figure 5.1-1). The core size and the number of fibers of the bundle can vary according to the experimental needs in order to change the spatial alignment relative to the heated sample and the amount of collected heat radiation. The eyepiece optics are a combination of lenses, designed and installed by Precitec GmbH⁸, which allow a working distance of 150 mm from the last lens surface to the fiber, providing a total of 20x magnification to the system, when used in combination with the geoHEAT 40_NIR focusing lenses.

A notch filter with center wavelength of 1064 nm is placed right in front of the fiber bundles on each collection side to isolate them from any reflected laser radiation (Figure 5.1-1). Similarly, long-pass filters with cut-on wavelengths of 550 nm are used to avoid contamination from the second order diffraction of the grating, especially during the measurement of very high temperatures (above 4000 K) when the intensity of radiation with wavelengths shorter than 500 nm is significant³⁸.

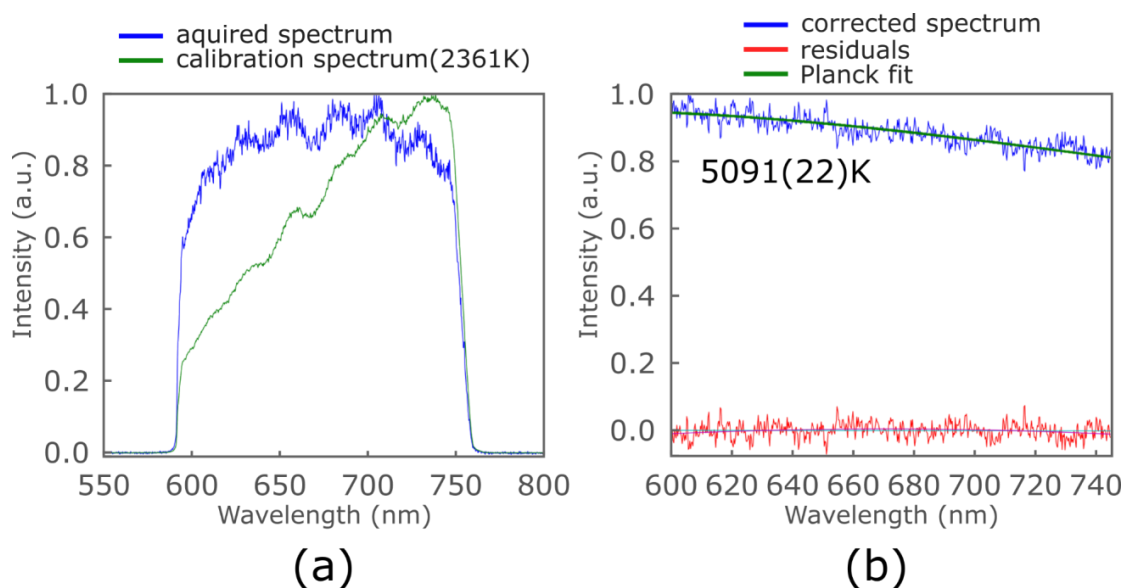


Figure 5.1-6. Example of a successful temperature determination of heated ϵ -O₂ at 46 GPa inside a DAC using the gray body approximation of Planck's law: (a) calibration and acquired spectra; (b) fitting using gray body approximation. (Colors online)

The light is guided into an IsoPlane SCT 320 spectrometer (Princeton Instruments) and the resulting spectrum is collected by a PI-MAX 4 with a 1024×256 ICCD detector. The Intensified CCD camera with enhanced Quantum Efficiency gives the possibility of very fast collection. It can work on gated mode, which allows time-resolved collection of the emitted thermal radiation.

The exposure window during which a thermal radiation spectrum is collected in the current set-up can be as short as ≈ 4 nanoseconds. Moreover, delay increments down to 0.1 nanosecond can be selected, with the possibility to create a time-resolved temperature series with overlapping exposure windows. For a given spectrum, a minimum amount of counts is necessary in order to overcome the background noise and successfully determine the temperature. Therefore, whereas optical spectra may in principle be collected from every individual laser pulse, usually each gated window of the detector is collected over many repetitions, some hundreds or thousands of pulses accumulating during the total exposure time. For this reason, it is crucial that the laser heating is sufficiently stable; i.e., that all pulses have identical shape and cause the same effect on the sample.

In order to create a time series of temperatures along the duration of the laser pulse (Figure 5.1-7), it is crucial to correlate the laser pulse period with the gated exposure windows of the camera. A common modulation trigger is used for the lasers and the spectrometer camera signifying the beginning of each pulse period, created internally by the pulse generator of the PI-MAX detector. The laser response and trigger signal are observed using an oscilloscope as described in Subsection 5.1.3.3. Using the trigger signal as a time reference point, the arrival of the laser pulse relative to the trigger can be correlated with the relative delay of each gated exposure window of the camera, making it possible to determine the time-resolved temperature response of the sample to laser heating.

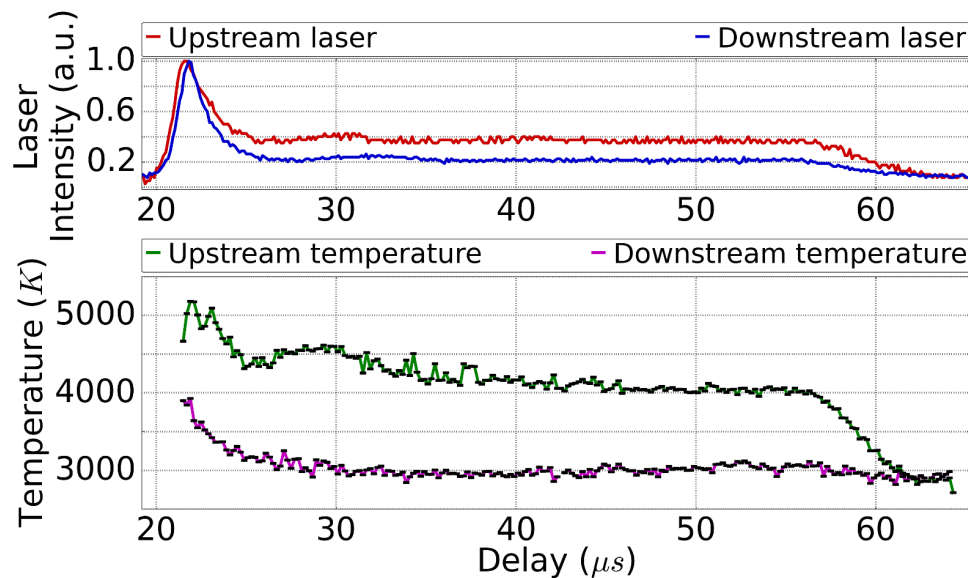


Figure 5.1-7 . Temperature measured during double-sided pulsed laser heating of solid ϵ - O_2 inside a DAC at 46 GPa with 10 kHz repetition rate. For the purpose of this experiment, the laser pulse width was set to approximately 40% duty cycle, i.e., a duration of 40 μs . The 100 μs pulse period is divided into windows of 200 ns each. The figure includes the part of the period when the heat radiation was sufficiently high to be detected. The collection windows are denoted by black horizontal lines and the solid colored lines are guides for the eye. (Colors online)

When working in the nanosecond timing range, cable and equipment delays become significant. Hence, special care is taken to correct the temperature – laser synchronization by taking into account the response delays of cables and electronics. Using the internal trigger T_0 of the PI-MAX detector as a time reference point, all cable and equipment delays are recorded on the oscilloscope and subtracted to give an absolute timestamp to every event. The delay of the photodiodes and their cables is calculated using the spectrometer to capture the real laser pulse (attenuated significantly). A time-resolved collection gives the absolute laser pulse delay which is then compared with the delay of the laser pulse recorded using the oscilloscope and appropriately corrected.

5.1.3.5 Temperature distribution in the heated spot

The time-resolved temperature measurement technique, when combined with multiple temperature acquisitions from a multi-core fiber bundle, results in a two-dimensional map of surface temperatures that resolve the sample thermal response both spatially and temporally. This method can potentially reveal much information regarding the thermal dynamics of the sample and accurately determine the temperature of the sample within the heated spot.

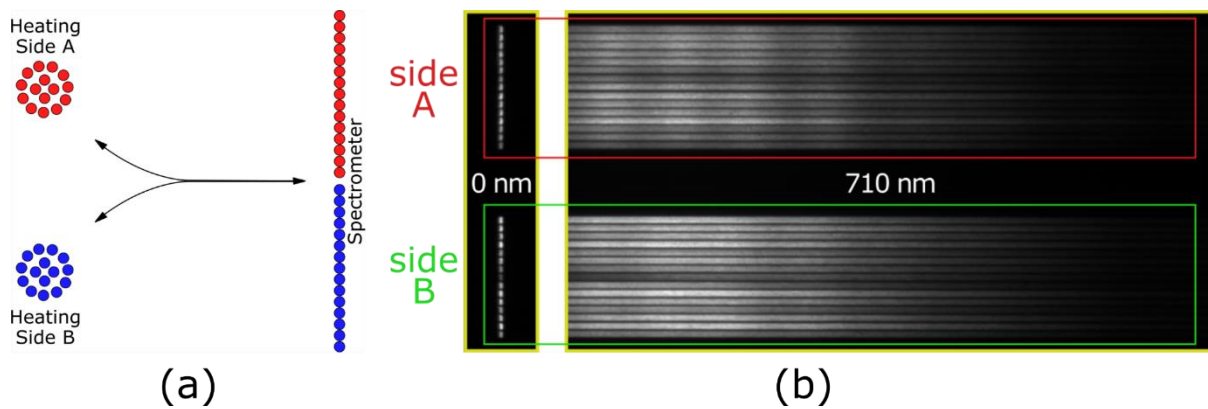


Figure 5.1-8. (a) The bifurcated fiber optic bundle used for spectroradiometry measurements consists of two bundles with 15 fiber cores of 100 μm each, aligned in a 'bunch' formation at the collection side. At the spectrometer side, the alignment is linear, with both legs joined at the same ferrule. (b) Portions of the detector images showing the signal from all fibers when both sides are focused on an illuminated platinum foil, at two grating positions. Left: grating is at 'zero position', i.e., the detector is aligned with its zero-order diffraction. Right: the center position of the grating is at 710 nm, showing the dispersion of the illumination light.

In our system, a set of 30 fiber cores is used, divided into two groups of 15 fibers each, in fiber bundles that are aligned optically to the center of the laser heating area from both sides of the DAC. The fibers have a diameter of 100 μm and are grouped in two circular clusters (Figure 5.1-8 (a)), one from each side, but there is flexibility to switch between different fiber sets, depending on the desired application. The actual temperature probing diameter of each fiber depends on the fiber core size as well as on the optical focus and magnification. This can be easily determined during the alignment process by shining light into the fibers as well as on a reflective surface that is placed at the DAC position looking at the actual lit area. Typical values for a 400 μm core fiber patch cable are approximately 20 – 25 μm .

At the spectrometer side, both fiber bundles are aligned linearly, one on top of the other, so that each thermal radiation spectrum lies on a different area of the detector. In the case of I-MAX 4 1024 \times 256, the pixel size is 26 μm \times 26 μm , which defines the limits of fiber core size and inter-fiber spacing. Each region of interest of the detector can be correlated with a spot on the heated sample that has a specific diameter and position, and it is possible to create a two dimensional surface temperature map for each side of the sample (Figure 5.1-8 (b)). Examples of applications are presented in Subsection 5.1.4.

The fast alignment process allows the use of different temperature collection set-ups by simply exchanging and adjusting the fibers without requiring a realignment of the entire optical path. This feature is a useful capability of the system, especially when used during a synchrotron experiment where time is usually limited and therefore precious.

5.1.4 Examples of application

Some examples of successful application of the developed system are presented in the next sections and demonstrate the capabilities of the system. Two-dimensional temperature mapping is shown for an *in house* experiment on pulsed laser heating of an Fe_2O_3 crystal at

high pressure. The stability and portability of the system is demonstrated in a series of experiments using Synchrotron Mössbauer Source spectroscopy³⁹ and Nuclear Inelastic Scattering (NIS) spectroscopy coupled with pulsed LHDAC at the Nuclear Resonance (ID18) beamline^{40,41} of the European Synchrotron Radiation Facility (ESRF).

For the experiment, the system was transported to ESRF and mounted in the experimental hutch of the Nuclear Resonance beamline. The entire procedure of connecting and aligning usually requires only 4 to 6 hours at the beginning of an experiment. It may be easily performed during a shut down or maintenance day, so that precious experimental time lost to preparation is kept to a minimum.

In order to allow the X-ray beam to probe the sample along the compression axis of the DAC, it is necessary to partially modify the geometry of the system. In the case of NIS experiments, the laser heads are placed in the same co-axial orientation and perpendicular to the X-ray beam, while the DAC compression axis coincides with the direction of the beam. The sample is heated from both sides, “on-axis” with the X-rays, using two carbon mirrors positioned at $\approx 45^\circ$ angles in front of the geoHEAT 40_NIR focusing optics, similar to the set-up in³⁶. While X-ray absorption of the carbon mirrors is low, it is a crucial consideration for SMS experiments when the beam intensity is weak. The carbon mirrors are therefore replaced by a pair of D-shaped, silver-coated glass mirrors at $\approx 42^\circ$ angles from the focusing optics. In this way, the incident X-ray beam is allowed to pass without going through the mirrors and the heating laser beam is as close to the DAC compression axis as possible.

5.1.4.1 Time – space resolved measurements

In a series of *in house* experiments, we acquired both time- and space-resolved surface temperature data for an Fe_2O_3 crystal inside a DAC. The sample was loaded in the pressure chamber (Re gasket indented to 27 μm with a 100 μm diameter hole mounted in a DAC with diamond anvils of 150 μm culet size) with Ne as both a pressure transmitting medium and thermal insulator. The pressure chamber was compressed to 106 GPa and heated from one side (hereafter ‘Side B’) with laser pulses of 31.5 W power using a defocused beam. The pulse duration was 14 μs with a frequency of 25 kHz, resulting in a 40% duty cycle. The heating spot was aligned to be roughly at the center of the observation area of the fiber cluster. As seen in Figure 5.1-9, it was possible to detect the propagation of heat and measure temperature at one side of the sample during pulsed heating on the opposite side. The temperature initially increases at the heated side during the first moments of laser heating at time point ‘A’, and right after the peak of the pulse at time point ‘B’, detectable temperature appears also at the center of the non-heated side, being some hundreds of degrees lower. At time point ‘C’ a few microseconds after the pulse peak, the non-heated side cools down to undetectable temperatures when the temperature on the heated side is not high enough.

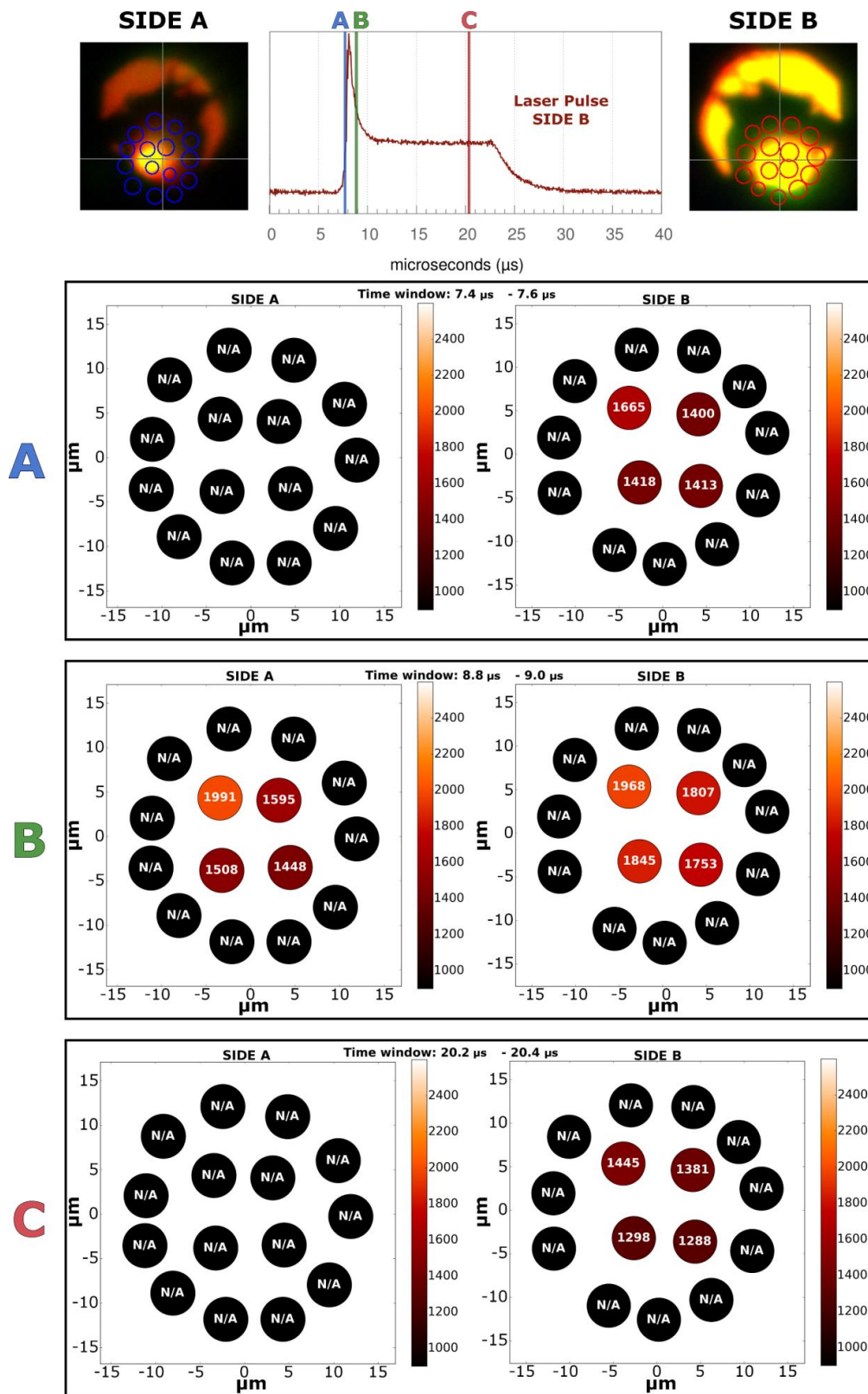


Figure 5.1-9. Time dependence of the laser pulse (red). Vertical green, blue and red bars indicate 200 μs time windows starting respectively at 7.4, 8.8 and 20.2 μs after the spectrometer trigger. Left and right insets show an image of two heating sides. Parts A) B) and C) show time-resolved temperature maps of Fe_2O_3 obtained at 106 GPa using one-sided pulsed heating of 31.5 W pulse power and frequency of $f = 25 \text{ kHz}$. The temperature induced at the back (non-heated side) of the sample can be seen close to the peak of the pulse at time window 'B'. Temperatures noted as 'N/A' denote temperature values that are too low to be estimated using spectroradiometry, usually below 1100 K.

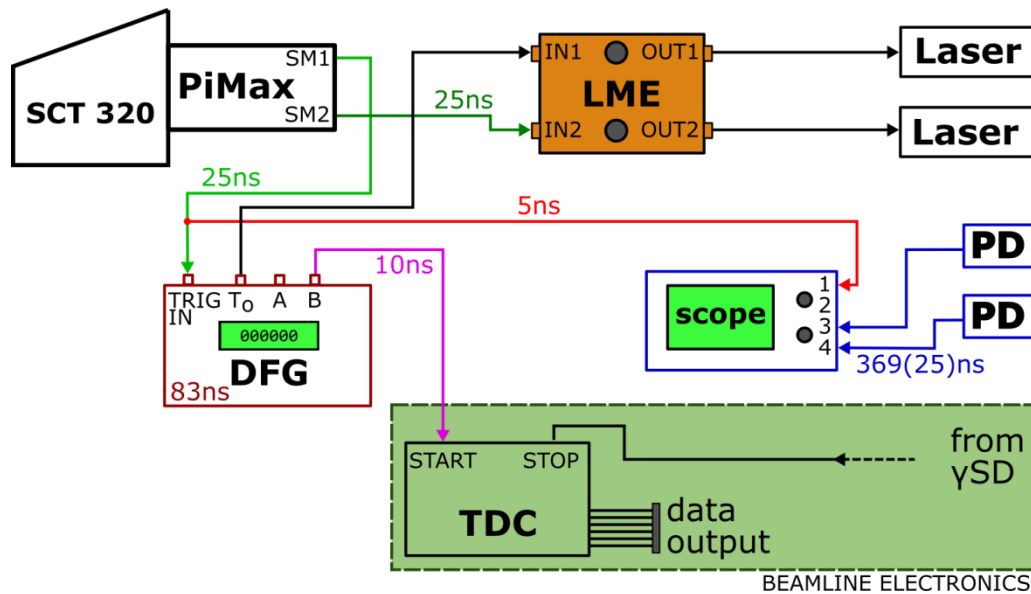


Figure 5.1-10. System layout and signal paths for time-resolved SMS experiments with pulsed laser heating. SCT 320 and PiMax are the spectrometer and detector, respectively, the latter producing two triggering pulses for the lasers; LME are the laser modulation electronics; DFG is a digital function generator used to signal the beamline electronics at the beginning of each pulse period; scope is the oscilloscope for observing the laser pulses; PD are the InGaAs photodiodes; TDC is a time-to-digital converter that collects and treats the time-resolved SMS data; and γ SD is the gamma scintillation detector used in the SMS set-up

Within the heated spot, which in this case is only the central part of the probing area, it is possible to detect a temperature gradient of more than 200 K over a distance of 15 – 20 μm . This demonstrates the importance of having a flat laser beam to avoid steep temperature gradients, especially when temperature is determined by probing a relatively large area.

It is worth mentioning that temperatures at the non-heated side sometimes appear to be slightly higher than on the heated side, as in the example of Figure 5.1-9 at time point 'B'. Such an observation can be due to individual fibers not being exactly aligned on the same spot on each side of the sample, where there can be a distance of a few micrometers between the observation spots, each having a slightly different temperature. Moreover, temperature differences of a few tens of degrees Kelvin are within the detection uncertainty, which is generally accepted to be on the order of one hundred degrees for laser heating experiments.

Time-resolved SMS absorption spectra can be collected during pulsed heating of the sample by combining the pulsed laser heating system with newly developed beamline electronics. In this way, the pulsed heating period can be 'sliced' into time windows of specified width and the Mössbauer absorption of the sample as well as its surface temperature corresponding to each time window can be calculated accordingly. The system cabling and assembly is shown in Figure 5.1-10 as well as the delay for each signal path, which is necessary for the correct synchronization of the data. The photodiode signal timing was measured by directly capturing the laser pulse using the spectrometer and comparing it with the photodiode response. All other delays were measured using a direct comparison of the signals on the oscilloscope. The time-resolved SMS set-up including synchrotron electronics and data treatment is beyond the

scope of this publication and will be described in detail elsewhere as a separate system.

An iron foil enriched in ^{57}Fe was placed into a DAC using paraffin as a pressure transmitting medium and pressurized to 64 GPa, with the goal to form iron hydride FeH_x upon heating. First, the sample was heated continuously for several minutes at a maximum temperature of 1500 K from both sides. Then, it was double-sided pulse heated at 20 kHz frequency. The two laser pulses were synchronized, and both had lengths of approximately 20 μm , i.e., around 50% duty cycle, and both were at a power of $P \approx 10\text{ W}$ at the pulse plateau. Temperature was estimated with spectroradiometry using two single-core fiber patch cables with cores of 400 μm diameter, collecting light from an area of approximately 20 μm in diameter that was centered at the heating spot. The laser pulses, as well as the sample temperature response with 1 μs temporal resolution, are presented in Figure 5.1-11 (c). The mean value of a series of data collections is shown, along with one standard deviation (STD) margins. The heating run lasted around 30 minutes with temperature collection approximately every 5 minutes.

The center shift (CS) of a Mössbauer absorption line is linearly dependent on temperature⁴², so the temperature of the entire probed volume of the sample can be estimated from the difference of the CS of the component(s) relative to the CS of the same component(s) at a known temperature. The sample is coldest during the heating cycle at the moment right before the peak of the pulse. The actual temperature during cooling depends on the sample conditions, as well as on heating properties such as duty cycle, power and frequency. It is expected to be close to room temperature compared to the temperatures developed during heating. In this way, Mössbauer spectroscopy provides an estimation of the variation in sample temperature at different moments of heating.

The SMS absorption spectrum corresponding to 6.5 – 8.5 μs delay from the beginning of the pulse period, right before the laser pulse, is shown in Figure 5.1-11 (a). The center shift is 0.42(3) mm/s based on a fit using MossA software⁴³. Figure 5.1-11 (b) shows the SMS absorption spectrum collected at a time window of 23 – 25 μs that has a CS of $-0.39(6)\text{ mm/s}$. Using the relation described in Ref. ⁴², the sample in this time interval is 1115(89) K hotter than right before the arrival of the laser pulse. Considering that the surface temperature during the hot period is estimated to be approximately 1700 K on both sides of the sample, cooling to around 600K takes place right before the next pulse arrives.

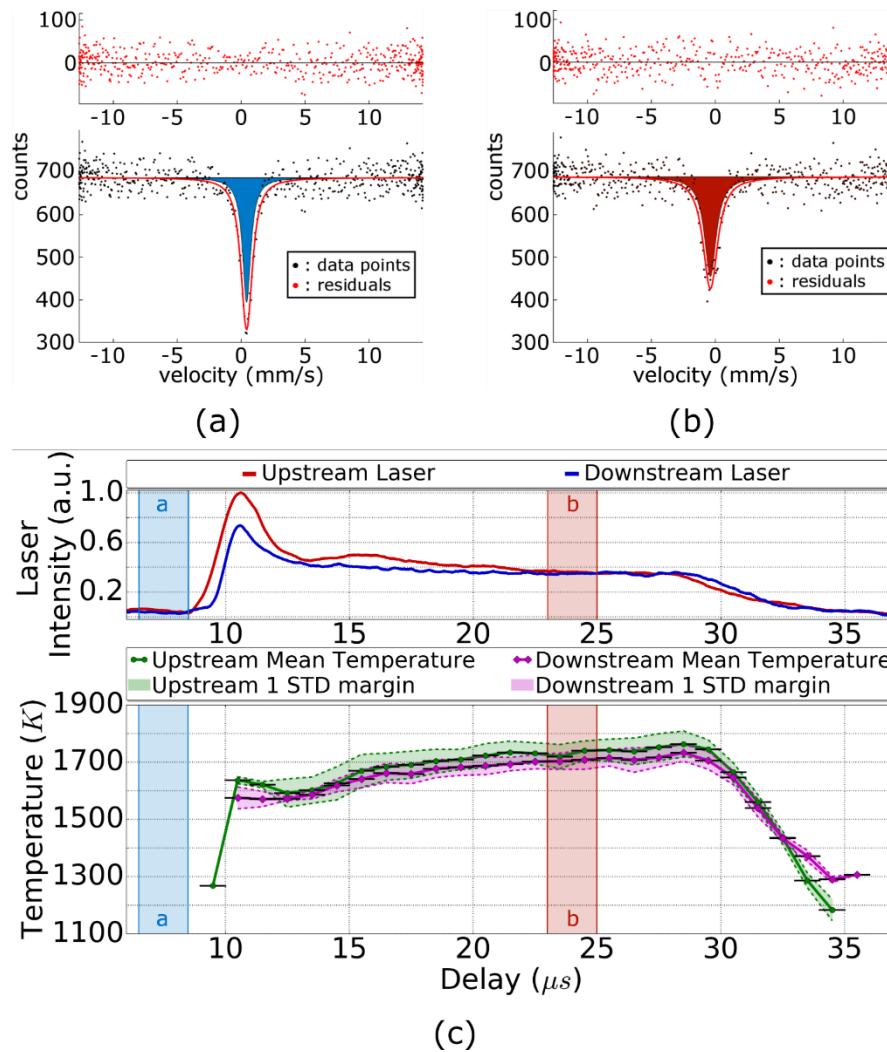


Figure 5.1-11. Mössbauer absorption spectra corresponding to cooled (a, right before pulse, 6.5 – 8.5 μs delay from the beginning of the pulse period) and heated sample (b, collected at the time window 23 – 25 μs) (c) Mean temperatures along the pulse as determined from spectroradiometric measurements (with one standard deviation margins) compared to the laser pulse profiles for upstream and downstream. The shaded time windows correspond to the cold and hot spectra from (a) and (b).

5.1.4.2 Nuclear inelastic scattering at ESRF

Nuclear Inelastic Scattering requires very long data acquisition time in order to obtain sufficient statistics for meaningful results. A single energy scan can last from half an hour to one hour, and many repetitions are necessary to improve statistics, resulting in a collection time of many hours. In the case of NIS inside a pulsed laser heated DAC, the main challenge is to maintain the stability of heating over time. Every pulse should produce the same temperature response on the sample, or at least the difference over time should be traceable to any possible correlations with experimental conditions (e.g., chemical reaction of the sample).

An iron foil enriched with ^{57}Fe was loaded into a DAC of 250 μm culet size, with Al_2O_3 as a pressure transmitting medium as well as thermal insulator. The sample was pressurized to 30 GPa, taking extra care to insulate the sample from the diamond anvils that act as good thermal

conductors. The sample was laser heated from both sides using pulses of $\approx 20 \mu\text{s}$ duration, a frequency of 16 kHz (i.e., 32% duty cycle) and pulse powers at the pulse plateau of $P_{up} = 14.6W$ and $P_{down} = 15.1W$ for upstream and downstream heating sides, respectively. The surface temperature of the heated sample was estimated with spectroradiometry, using two fiber patch cables with 400 μm core diameter that were focused on an area of approximately 20 μm around the center of the laser heated spot. The run duration of the temperatures presented here lasted ≈ 12 hours while maintaining a stable laser heating setup. In total, 54 temperature time-series were collected with ≈ 15 -minute intervals between them. Each window of the time-series is 500 ns long and was collected from a repetition of a few tens of thousands of pulses, as described in Section 5.1.3.4. This resulted in ≈ 3 minutes of total acquisition time for each dataset. The pulse shapes and power of the two lasers were manually adjusted to be synchronized and result in a similar surface temperature on both sides of the Fe sample.

The mean temperature for each time window is depicted in Figure 5.1-12 (a) and (b) for upstream and downstream sides, respectively, including the areas of ± 1 standard deviation (STD) over a total of 54 collections. The standard deviation was around 100 K at the flat part (plateau) of the pulse and 300 K at the peak position, close to the uncertainty level of spectroradiometry measurements.

The heated sample was probed with an X-ray beam size of 12 $\mu\text{m} \times 7 \mu\text{m}$ and the energy dependence of NIS for Fe was collected. Details of the time-resolved technique for NIS measurements will be published elsewhere. Time windows can be selected along the period of the pulse and the corresponding scattering spectra can be calculated, tracking the behavior of the sample during each heating cycle. For demonstration purposes three time-windows were selected: before the pulse, after the peak, and after the drop of the pulse, as shown in Figure 5.1-12. NIS can be used to determine the mean temperature of the sample volume that is probed by the X-ray beam, along with the surface temperature provided by spectroradiometry. The probability ratio between phonon creation and phonon annihilation for a given energy E , i.e., the symmetry of the spectrum around the elastic line, is a function of temperature^{7,36,40}. In Figure 5.1-12 (c) the estimated temperatures for each time window can be seen, where the phonon creation/annihilation ratio is calculated using the energy range of 10 – 20 meV (shaded areas). Before and after the laser pulse, the temperatures are low, hence not detectable using spectroradiometry at the visible light wavelength range. Nevertheless, the sample is still approximately 300 – 400 degrees above room temperature even when the laser is not emitting. During the pulse, the mean temperature in the heated spot appears to be around 2320 K, which is 200 – 400 degrees lower than the surface temperatures on both sides of the sample. This is good agreement if we consider the expected temperature gradients between the surface and the center of the sample.

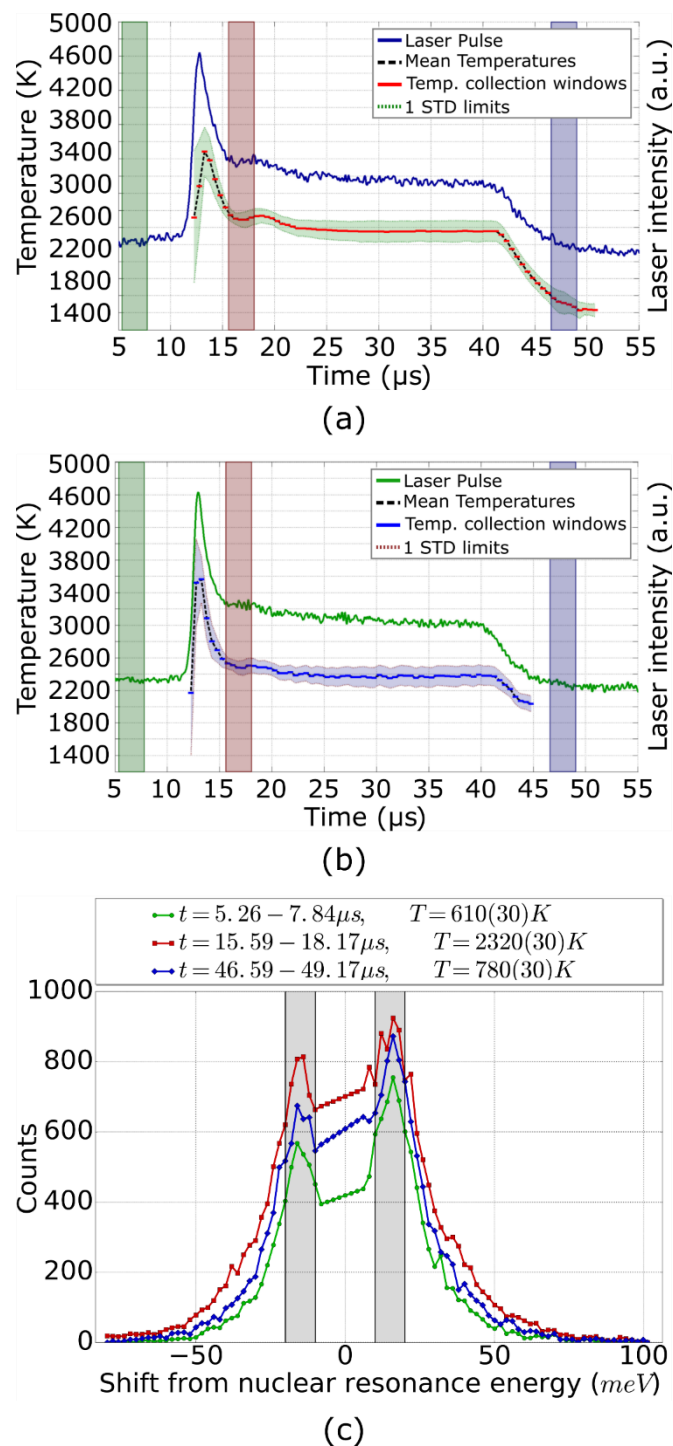


Figure 5.1-12. (a) Upstream and (b) Downstream side mean surface temperatures and their standard deviations for the entire duration of data collection. Three different time windows are highlighted that correspond to the NIS spectra. (c) Energy dependence of nuclear inelastic scattering (elastic component removed) of ^{57}Fe for three different temporal positions along the pulse period. Temperatures are determined using the detailed balance law.

5.1.5 Conclusions

A double-sided pulsed laser heating system was developed that is able to acquire time-resolved and space-resolved surface temperature information of samples under high pressure inside a diamond anvil cell, with temporal and spatial resolution of a few nanoseconds and

micrometers, respectively. The portability and stability of the system were demonstrated, as well as the possibility to couple it with various techniques such as nuclear inelastic scattering at a synchrotron light source facility.

Special care was taken to minimize the chromatic aberration of the system, which is a known problem in laser heating set-ups with spectroradiometry temperature determination, and to keep the two laser pulses independent with respect to the power, delay and duration, in order to maximize experimental flexibility.

The pulsed laser heating system can be successfully used for time-resolved studies and coupled with different spectroscopic techniques. This allows the *in situ* investigation of transitional phenomena, including the determination of thermal conductivity, melting curve and rheological properties of materials of geological and materials science significance at conditions of the Earth's interior. Heating with pulses can potentially provide solutions for the study of materials in cases that were difficult with continuous heating. Materials such as hydrogen and hydrides have a high risk of destroying diamond anvils, and other materials can react with them during persistent heating, forming carbides. In many of these cases, pulsed laser heating can minimize the heating time during measurements and prevent chemical interactions. The portable laser heating system can be a versatile tool, employed in a wide range of different applications.

5.1.6 Acknowledgements

We acknowledge the European Synchrotron Radiation Facility (ESRF) for provision of beam time at ID18. N.D. thanks the German Research Foundation [Deutsche Forschungsgemeinschaft (DFG)] for financial support through the DFG Heisenberg Programme and projects DU 954-8/1 and DU 954-11/1, and the Federal Ministry of Education and Research [BMBF; Germany] for BMBF grants 5K13WC3 (Verbundprojekt O5K2013, Teilprojekt 2, PT-DESY) and 5K16WC1. L.D. thanks the DFG and the BMBF (Germany) for grants DU 393/10-1 and DU 393/10-1. The project was also supported by funds from the DFG through the CarboPaT Research Unit FOR2125 (Mc 3/20, Du 393/9).

5.1.7 References

1. Eremets, M. I. *High pressure experimental methods*. (Oxford University Press, 1996).
2. Dubrovinskaia, N. & Dubrovinsky, L. *Advances in High-Pressure Technology for Geophysical Applications*. (Elsevier, 2005).
3. Bassett, W. A. The birth and development of laser heating in diamond anvil cells. *Rev. Sci. Instrum.* **72**, 1270 (2001).
4. Bassett, W. A. Diamond Anvil Cells: Laser heating of samples at high pressure: 50 years. (2016). Available at: <https://www.laserfocusworld.com/test-measurement/test-measurement/article/16547047/diamond-anvil-cells-laser-heating-of-samples-at->

- high-pressure-50-years. (Accessed: 8th January 2020)
5. Schultz, E. *et al.* Double-sided laser heating system for in situ high pressure–high temperature monochromatic x-ray diffraction at the esrf. *High Press. Res.* **25**, 71–83 (2005).
 6. Meng, Y., Hrubciak, R., Rod, E., Boehler, R. & Shen, G. New developments in laser-heated diamond anvil cell with in situ synchrotron x-ray diffraction at High Pressure Collaborative Access Team. *Rev. Sci. Instrum.* **86**, (2015).
 7. Lin, J. F. *et al.* Absolute temperature measurement in a laser-heated diamond anvil cell. *Geophys. Res. Lett.* **31**, 3–6 (2004).
 8. Kuppenko, I. *et al.* Portable double-sided laser-heating system for Mössbauer spectroscopy and X-ray diffraction experiments at synchrotron facilities with diamond anvil cells. *Rev. Sci. Instrum.* **83**, 124501 (2012).
 9. Aquilanti, G. *et al.* Development of micro-XANES mapping in the diamond anvil cell. *J. Synchrotron Radiat.* **16**, 376–379 (2009).
 10. Marini, C., Kantor, I., Mathon, O. & Pascarelli, S. On-line laser heating setup for ED-XAS at ID24: Preliminary optical design and test results. *High Press. Res.* **33**, 108–113 (2013).
 11. Bassett, W. A. & Li-Chung Ming. Disproportionation of Fe₂SiO₄ to 2FeO+SiO₂ at pressures up to 250kbar and temperatures up to 3000 °C. *Phys. Earth Planet. Inter.* **6**, 154–160 (1972).
 12. Gold, J. S., Bassett, W. A., Weathers, M. S. & Bird, J. M. Melting of Diamond. *Science (80-)*. **225**, 921–922 (1984).
 13. Funamori, N. & Sato, T. Heating in a diamond-anvil cell using relaxation oscillations of a Q- switched Nd:YAG laser. *Rev. Sci. Instrum.* **77**, 77–80 (2006).
 14. Goncharov, A. F. & Crowhurst, J. C. Pulsed laser Raman spectroscopy in the laser-heated diamond anvil cell. *Rev. Sci. Instrum.* **76**, 063905 (2005).
 15. McWilliams, R. S., Dalton, D. A., Konôpková, Z., Mahmood, M. F. & Goncharov, A. F. Opacity and conductivity measurements in noble gases at conditions of planetary and stellar interiors. *Proc. Natl. Acad. Sci.* **112**, 7925–7930 (2015).
 16. Yang, L., Karandikar, A. & Boehler, R. Flash heating in the diamond cell: Melting curve of rhenium. *Rev. Sci. Instrum.* **83**, 1–6 (2012).
 17. Goncharov, A. F. *et al.* Thermal conductivity of argon at high pressures and high temperatures. *J. Appl. Phys.* **111**, 112609 (2012).
 18. Beck, P. *et al.* Measurement of thermal diffusivity at high pressure using a transient heating technique. *Appl. Phys. Lett.* **91**, 10–13 (2007).
 19. Sinmyo, R. & Hirose, K. The Soret diffusion in laser-heated diamond-anvil cell. *Phys.*

- Earth Planet. Inter.* **180**, 172–178 (2010).
20. Rainey, E. S. G. & Kavner, A. Peak scaling method to measure temperatures in the laser-heated diamond anvil cell and application to the thermal conductivity of MgO. *J. Geophys. Res. Solid Earth* **119**, 8154–8170 (2014).
 21. Thomson, A. R., Walter, M. J., Lord, O. T. & Kohn, S. C. Chemistry and mineralogy of earth's mantle. Experimental determination of melting in the systems enstatite-magnesite and magnesite-calcite from 15 to 80 GPa. *Am. Mineral.* **99**, 1544–1554 (2014).
 22. Lord, O. T. *et al.* The NiSi melting curve to 70GPa. *Phys. Earth Planet. Inter.* **233**, 13–23 (2014).
 23. Lord, O. T., Walter, M. J., Dasgupta, R., Walker, D. & Clark, S. M. Melting in the Fe–C system to 70 GPa. *Earth Planet. Sci. Lett.* **284**, 157–167 (2009).
 24. Lord, O. T. *et al.* The melting curve of Ni to 1 Mbar. *Earth Planet. Sci. Lett.* **408**, 226–236 (2014).
 25. Campbell, A. J. Measurement of temperature distributions across laser heated samples by multispectral imaging radiometry. *Rev. Sci. Instrum.* **79**, 015108 (2008).
 26. Watanuki, T., Shimomura, O., Yagi, T., Kondo, T. & Isshiki, M. Construction of laser-heated diamond anvil cell system for in situ x-ray diffraction study at SPring-8. *Rev. Sci. Instrum.* **72**, 1289 (2001).
 27. Walter, M. J. & Koga, K. T. The effects of chromatic dispersion on temperature measurement in the laser-heated diamond anvil cell. *Phys. Earth Planet. Inter.* **143–144**, 541–558 (2004).
 28. Benedetti, L. R. & Loubeyre, P. Temperature gradients, wavelength-dependent emissivity, and accuracy of high and very-high temperatures measured in the laser-heated diamond cell. *High Press. Res.* **24**, 423–445 (2004).
 29. Boehler, R., Musshoff, H. G., Ditz, R., Aquilanti, G. & Trapananti, A. Portable laser-heating stand for synchrotron applications. *Rev. Sci. Instrum.* **80**, 045103 (2009).
 30. Shen, G., Wang, L., Ferry, R., Mao, H. & Hemley, R. J. A portable laser heating microscope for high pressure research. *J. Phys. Conf. Ser.* **215**, 012191 (2010).
 31. Dubrovinsky, L. *et al.* Portable laser-heating system for diamond anvil cells. *J. Synchrotron Radiat.* **16**, 737–741 (2009).
 32. Laskin, A. & Laskin, V. π Shaper – Refractive Beam Shaping Optics for Advanced Laser Technologies. *J. Phys. Conf. Ser.* **276**, 012171 (2011).
 33. Prakapenka, V. B. *et al.* Advanced flat top laser heating system for high pressure research at GSECARS: application to the melting behavior of germanium. *High Press. Res.* **28**, 225–235 (2008).

34. Smith, W. J. *Modern optical engineering*. (Tata McGraw-Hill Education, 2007).
35. Greivenkamp, J. E. *Field Guide to Geometrical Optics, Vol. 1*. (SPIE, 2004). doi:10.1117/3.547461
36. Kuppenko, I. *et al.* Time differentiated nuclear resonance spectroscopy coupled with pulsed laser heating in diamond anvil cells. *Rev. Sci. Instrum.* **86**, 114501 (2015).
37. Heinz, D. L. & Jeanloz, R. Temperature measurements in the laser-heated diamond cell. in *High pressure research in mineral physics: A Volume in Honor of Syun-iti Akimoto* (eds. Manghnani, M. H. & Syono, Y.) 113–127 (American Geophysical Union, 1987).
38. Petitgirard, S., Salamat, A., Beck, P., Weck, G. & Bouvier, P. Strategies for in situ laser heating in the diamond anvil cell at an X-ray diffraction beamline. *J. Synchrotron Radiat.* **21**, 89–96 (2014).
39. Potapkin, V. *et al.* The ⁵⁷Fe Synchrotron Mössbauer Source at the ESRF. *J. Synchrotron Radiat.* **19**, 559–569 (2012).
40. Chumakov, A. & Rüffer, R. Nuclear inelastic scattering. *Hyperfine Interact.* **113**, 59–79 (1998).
41. Rüffer, R. & Chumakov, A. I. Nuclear inelastic scattering. *Hyperfine Interact.* **128**, 255–272 (2000).
42. Maradudin, A. A., Flinn, P. A. & Ruby, S. Velocity Shift of the Mössbauer Resonance. *Phys. Rev.* **126**, 9–23 (1962).
43. Prescher, C., McCammon, C. & Dubrovinsky, L. MossA : a program for analyzing energy-domain Mössbauer spectra from conventional and synchrotron sources. *J. Appl. Crystallogr.* **45**, 329–331 (2012).

5.2 Comparative study of the influence of pulsed and continuous wave laser heating on the mobilization of carbon and its chemical reaction with iron in a diamond anvil cell

G. Aprilis^{1,2,*}, I. Kantor³, I. Kuppenko⁴, V. Cerantola⁵, A. Pakhomova⁶, I. Collings⁵, R. Torchio⁵, T. Fedotenko¹, S. Chariton², M. Bykov², E. Bykova^{2,6}, E. Koemets², D. M. Vasiukov^{1,2}, C. McCammon², L. Dubrovinsky² and N. Dubrovinskaia¹

¹ Materials Physics and Technology at Extreme Conditions, Laboratory of Crystallography, Universität Bayreuth, D-95440 Bayreuth, Germany

² Bayerisches Geoinstitut, Universität Bayreuth, D-95440 Bayreuth, Germany

³ Department of Physics, Technical University of Denmark, 2800 Lyngby, Denmark

⁴ Institut für Mineralogie, University of Münster, D-48149 Münster, Germany

⁵ ESRF – The European Synchrotron, CS 40220, 38043 Grenoble Cedex 9, France

⁶ Deutsches Elektronen-Synchrotron (DESY), D-22607 Hamburg, Germany

* Correspondent author (e-mail: georgios.aprilis@uni-bayreuth.de)

Journal of Applied Physics, **125**(9), 095901 (2019)

5.2.1 Abstract

Laser heating in a diamond anvil cell (DAC) is a common method for studying material behavior at high-pressure and high-temperature conditions. It has been previously proven that during continuous wave laser heating of a sample, carbon of the diamond anvils is mobilized and its diffusion into the sample can lead to undesirable chemical reactions, which, if not detected, may cause misinterpretations of the results of the experiment. Minimizing the heating time with the use of a pulsed laser (PL) is thought to reduce the risk of possible carbon contamination of the sample, however, this has not been proven experimentally. Here we report the results of our comparative study of the effect of pulsed and continuous wave (CW) laser heating on the mobilization of carbon and its chemical interaction with iron in a diamond anvil cell. Using X-ray Absorption Near Edge Structure (XANES) spectroscopy, Synchrotron Mössbauer Source (SMS) spectroscopy, and Synchrotron X-ray diffraction (XRD) we examined iron samples that were laser heated in DACs in various pressure transmitting media (neon, argon, and potassium chloride). According to our results, use of the PL heating does not prevent the sample from carbon contamination. A reaction between carbon and iron happens within a few seconds even at moderate temperatures. We found that one analytical technique was generally insufficient to fully characterize the phase composition of the laser-heated samples.

5.2.2 Introduction

Laser heating of materials inside a diamond anvil cell allows one to study various chemical and physical phenomena which happen at non-ambient conditions. Knowledge of melting of metals is of a fundamental importance, but the high-pressure melting curve of iron is of a particular interest for geosciences, as it provides crucial constrains for modelling thermal conditions in the Earth's core and at the core-mantle boundary. Despite extensive research, it still remains uncertain and available data are contradictory¹⁻⁴

The results of studies of melting depend on many factors including the heating method, melting criterion, and the temperature measurement technique. Undesirable chemical reactions are among the major experimental obstacles. It is well known that laser heating of iron in a DAC may lead to formation of iron carbides or a solution of carbon in iron⁵⁻⁸ as a result of a chemical reaction between the sample and carbon diffusing from a diamond anvil into the sample chamber. This is highly unwanted in melting experiments, since the presence of carbides or Fe-C solid solutions can significantly affect the melting temperature⁹⁻¹¹. The carbon contamination problem is not limited to iron¹² but due to the important geological implications of its melting curve, iron is a highly investigated material.

Detection of products of undesirable chemical reactions often presents a separate complex task. Indeed, laser heating affects the surface of the sample and the volume of the laser-heated material may be very small. Thus, the amount of products of undesirable chemical reactions can appear to be below the detection limit of the applied analytical methods. The question of whether a chemical reaction indeed took place becomes crucial for establishing correct melting curves of metals (or, more generally, for any experiments in laser-heated DACs).

Solid state chemical reactions are driven by mutual diffusion of the components, which is promoted by high temperature and prolonged heating. As the pulsed laser (PL) heating minimizes the heating duration in individual pulses down to microseconds or even shorter, it is considered to be a technique that suppresses diffusion and thus improves the chemical stability of the system under investigation. However, there have not been studies so far, which could allow a direct comparison of the effects of pulsed laser (PL) and continuous wave (CW) laser heating on the mobilization of carbon in a DAC and its chemical reaction with the sample. Such experiments require a sample in a particular chemical environment to be heated using both a PL and a CW laser.

In this study, we examine the chemical interaction between iron and carbon of the diamond anvils during continuous wave and pulsed laser heating. Iron samples were loaded into DACs along with different materials, Ne, Ar, and KCl, which served as pressure media and provided different chemical environments. The chosen pressure media are often used in laser-heated diamond anvil cell (LHDAC) experiments, as they are chemically inert, serve as good thermal insulators, and have been suggested as good choices for diminishing the diffusion of carbon

from the diamond anvils¹². In course of a series of experiments, in which different spots of iron samples were heated by either a PL or a CW laser and by varying the duration of heating, we kept track of the iron-carbon interaction using Energy Dispersive X-ray Absorption spectroscopy, as implemented at the ID24 beamline at the European Synchrotron Radiation Facility (ESRF). The compositions of the heated samples were examined afterwards using Mössbauer spectroscopy at the Synchrotron Mössbauer Source (SMS) at the ID18 beamline at the ESRF, and X-ray diffraction (XRD) at the P02.2 beamline at PETRA III, DESY. Our results suggest that upon laser heating Fe and carbon chemically react independently of the heating mode applied (CW or PL). Products of the Fe-C chemical reaction could be detected if appropriate, sufficiently sensitive analytical technique is applied.

We report our experimental results in detail in the following three sections. Section 5.2.3 (*Experimental methods*) provides information about the sample preparation and DAC design (subsection 5.2.3.1), the laser heating procedure and the methodology of the data collection (subsection 5.2.3.2). The XANES data analysis is described in subsection 5.2.3.3, which aims at explaining our approach to the X-ray absorption data processing that allows quantifying the changes in the chemical composition of the samples. subsection 5.2.3.4 presents the Mössbauer spectroscopy and X-ray diffraction methods used for sample characterization. Section 5.2.4 (*Results and Analysis*) includes a detailed description of our results and their analysis in the context of previous observations. It is divided into three subsections dedicated to examining different iron samples in Ne (subsection 5.2.4.1), in Ar (subsection 5.2.4.2) and in KCl (subsection 5.2.4.3) pressure media. Section 5.2.5 (*Discussion*) briefly summarizes the results and provides their discussion in respect of the available literature. In Section 5.2.6 (*Conclusions*) we give some suggestions regarding future experiments.

5.2.3 Experimental Methods

5.2.3.1 Sample Preparation

BX90-type¹³ and membrane-type¹⁴ DACs equipped with Boehler-Almax anvils¹⁵ (culet size 250 μm) were prepared. Rhenium gaskets were pre-indented from an initial thickness of 200 μm down to 25 – 35 μm and laser-drilled to create circular pressure chambers of 100 – 120 μm in diameter. A strip of an iron foil (Goodfellow Inc. 99.99%) with the thickness of 5 – 10 μm was used as a sample. To improve the SMS data quality, a ⁵⁷Fe-enriched iron foil (thickness of 5 μm or thinner) was used. Ar, Ne, and KCl were used as pressure media.

Prior to loading into a DAC, a powder of KCl was dried in an oven at 250°C for at least 48 hours. The iron foil was placed between two KCl disks to assure a distance of at least a couple of micrometers between the sample and the diamond anvils. In the case of Ne and Ar, the cells were gas loaded using the gas loading system in Bayerisches Geoinstitut¹⁶ at 140(5) MPa. A small portion of the iron foil strip was clamped between the rhenium gasket and the diamond anvil to secure its position during gas loading (Figure 5.2-1). The rest of the iron strip was slightly folded inside the pressure chamber to suspend it in the pressure medium so that

neither of the sides of the foil would be lying on diamond anvils (Figure 5.2-1). The spots for heating were chosen to be relatively in the middle of the strip, avoiding the ends, where the sample is closer to the diamond anvils. In different experiments the DACs were compressed to 41 - 53 GPa.

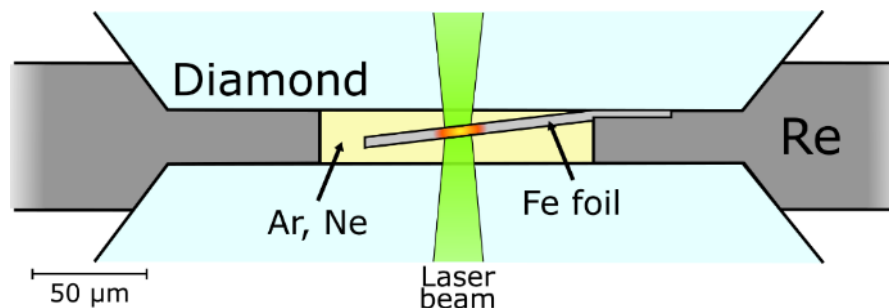


Figure 5.2-1. Configuration of the pressure chamber in experiments with gaseous pressure media (argon or neon). The schematic is drawn to scale.

5.2.3.2 Laser heating procedure and X-ray Absorption Spectroscopy

Laser heating experiments were conducted at the ESRF in Grenoble with the Energy Dispersive X-ray Absorption setup of ID24¹⁷. The X-ray beam was focused horizontally using a curved polychromator Si 111 crystal in Bragg geometry and vertically with a bent Si mirror. The obtained focus at the sample position was approximately 3 μm (horizontal) x 4 μm (vertical) full width at half maximum (FWHM). The second-order polynomial for the pixel to energy conversion parameters was calibrated using a reference α-Fe foil spectrum.

The iron samples were PL or CW laser heated at temperatures ranging from 1600 K to 3450 K, i.e. both below and above the melting point of iron for the selected pressure range. Two IR ytterbium-doped fiber lasers (YLR-100-AC of IPG Photonics) operating at 1070 nm with a maximum power of 100 W were used each time to heat the sample from both sides with a focal spot of approximately 10 – 15 μm in diameter, which is larger than the X-ray beam size^{18,19}.

Each laser heating (LH) sequence, numbered LH1 – LH6, was realized through a number of cycles characterized by the number of pulses of a certain duration (in μs) for PL or by duration (in seconds) for CW laser heating. In the case of pulsed heating, the pulse duration ranged between 2 and 12 μs at 25 kHz laser frequency, except of one case, when pulses of 100 μs at 10 kHz were used. The number of cycles (repetitions) varied from 1 to 15 with the total heating time in the range of 2 seconds to 3 minutes. X-ray Absorption Spectroscopy (XAS) spectra at the Fe K-edge ($E_o = 7112 \text{ eV}$) with energy resolution of approximately 0.24 eV were collected from the quenched sample spot during the time between two heating cycles.

The temperatures were measured during heating from both sides of the sample using spectroradiometry¹⁹, and an effort was made to keep the temperature similar on both sides of the sample and the same for each heating cycle during one LH sequence. In PL heating temperatures were tracked along the pulse duration using time-resolved spectroradiometry,

as described in ²⁰, with a PI-MAX 4 detector. Reported temperature values refer to the highest temperature achieved with the uncertainty of ± 150 K arising from possible temperature gradients, heating instability, and inaccuracy of the gray body approximation. At the end of each heating sequence a full mapping of the sample was made in a grid with a step size of $2 \times 2 \mu\text{m}^2$. An X-ray absorption spectrum was collected at each position²¹ in the grid to detect all possible chemical changes in the sample, even if the heated area slightly moved from the focus of the X-ray beam upon heating.

The data maps were treated using the ROI Imaging Tool of the PyMCA software²², which allowed the batch normalization of the XAS spectra for consistency within every mapping and the visualization of maps with a pixel representing each spectrum. Before or after normalization, using appropriate color-coding, the value of every pixel could be chosen to represent the edge-jump on Fe (i.e. the difference in X-ray absorption between energies below and above the K-edge), or a feature in a specific energy range on the XAS spectrum.

5.2.3.3 XANES data analysis

Changes in the X-ray Absorption Near Edge Structure (XANES) region of XAS spectra give evidence of changes in the iron chemical environment. Figure 5.2-2 shows, as an example, the X-ray absorption spectra of Fe in Ne taken from a sample quenched at 41 GPa after the heating sequence LH3 (the XANES region outlined by the dashed rectangle is enlarged in the inset). The shoulder of the rising K-edge in the XAS spectra at approximately 7119 eV (pointed out by the blue arrow in Figure 5.2-2) is a characteristic feature of ϵ -Fe^{23,24}. It was recently recognized that vanishing of this shoulder after heating indicates a chemical reaction between iron and carbon, which comes from the diamond anvils, that results in the synthesis of iron carbide Fe_3C ¹¹.

As seen in Figure 5.2-2, vanishing of the shoulder directly correlates with the distance from the center of the heated spot. The closer to the center of the heated spot, the less pronounced is the shoulder. This was interpreted as change in the chemistry of the sample, as it will be shown below. The further from the center of the heated spot, the more pronounced is the shoulder, indicating the absence of a chemical reaction. To quantify the difference in the spectra, we introduced the value r , which is the ratio of the normalized absorption within the two energy regions ROI 1 and ROI 2 (Regions of Interest 1 and 2), which represent the peak and the valley of the shoulder. The regions are chosen to be equally wide, with a range of 1 eV (highlighted by different colors in Figure 5.2-2). The energy range of 7118.3 – 7119.3 eV (pink in the inset in Figure 5.2-2) corresponds to ROI 1, and the range of 7119.6 – 7120.6 eV (light blue the inset in Figure 5.2-2) corresponds to ROI 2. Then r is defined as follows:

$$r = \frac{\int_{ROI2} \mu(E)}{\int_{ROI1} \mu(E)}$$

where $\int_{ROI2} \mu(E)$ and $\int_{ROI1} \mu(E)$ are the integrals of the normalized X-ray absorption μ , over the respective energy ranges.

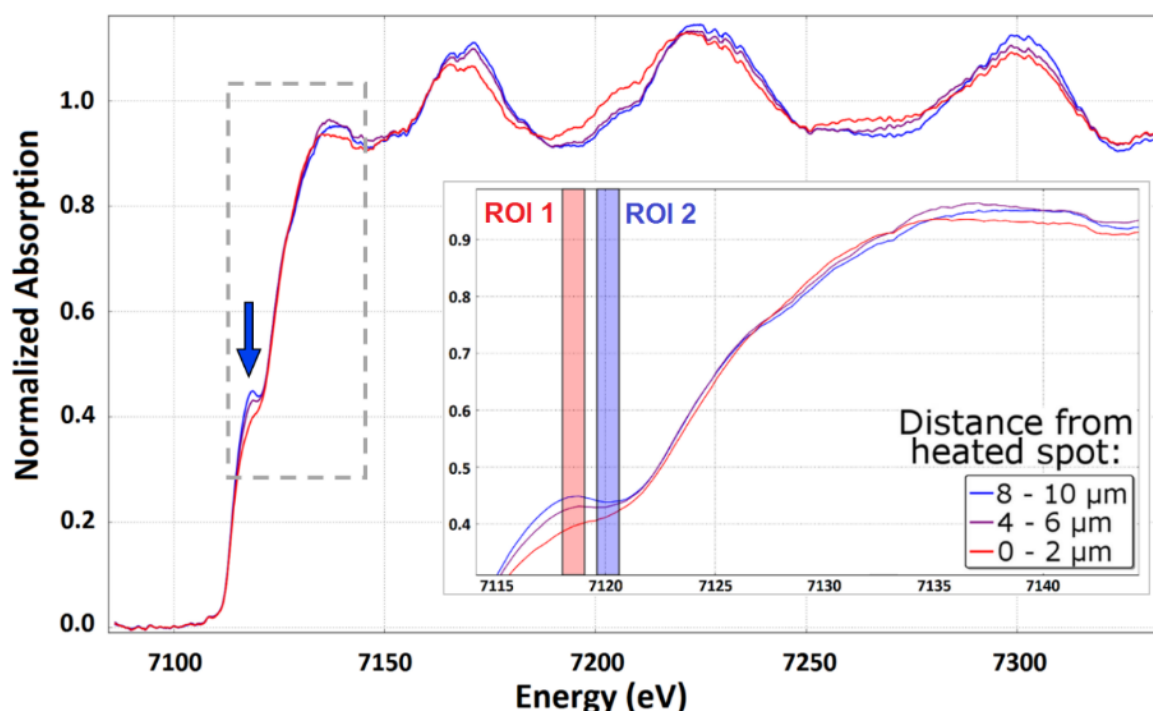


Figure 5.2-2. X-ray absorption spectra of Fe in Ne taken from a sample quenched at 41 GPa after heating at a maximum temperature of 2500 K (heating sequence LH3). The inset shows the enlarged XANES region of the spectra (dashed grey rectangle). The spectra were collected at room temperature from three locations at different distances (0-2, 4-6, and 8 μm) from the center of the heated spot (red, magenta, and blue curves, respectively). The rising edge feature is pointed out by the blue arrow. The blue spectrum resembles those taken from non-heated areas of the sample and is characterised by the most pronounced shoulder, which is specific for ϵ -Fe. ROI 1 and ROI 2 designate the two energy regions (Regions of Interest 1 and 2, highlighted in pink and blue colors), which were used to define the ratio r (see text)

For ϵ -Fe iron at room temperature before heating, r is equal to about 0.97. The ratio increases up to 1.06 for the points close to the centers of the heated spots. Thus, the transition from $r < 1$ to $r > 1$ indicates a significant change in the rising edge of the spectrum and marks the disappearance of the local maximum in the shoulder. Such change is observed in the absorption spectra of both ϵ -Fe and γ -Fe under high temperatures^{3,24,25}, but a value of $r > 1$ at room temperature is a sign of iron contamination¹¹.

5.2.3.4 Sample Characterization: Synchrotron SMS and XRD

The phase composition of the samples was investigated using different experimental techniques. Mössbauer spectra were collected using the **Synchrotron Mössbauer Source (SMS)** of ID18²⁶ at the ESRF, where a $^{57}\text{FeBO}_3$ single-crystal monochromator was used to obtain pure nuclear reflection (approximately 6 neV FWHM) at the Mössbauer energy of 14.4 keV from a wide spectrum of synchrotron radiation. Kirkpatrick-Baez mirrors were used to focus the beam to a cross-section size of 14×13 [horizontal \times vertical] μm^2 . The velocity scales of all Mössbauer spectra were calibrated relative to a 25 μm thick α -Fe foil. Each SMS spectrum took approximately 30 min to collect, and all spectra were fit using the MossA software package²⁷.

X-ray diffraction experiments were conducted at the High-Pressure Diffraction Beamline ID15B (ESRF, Grenoble) ²⁸ and Extreme Conditions Beamline (ECB) P02.2 of PETRA III (DESY, Hamburg) ²⁹. At the ECB, data were collected with a Perkin Elmer XRD1621 flat panel detector using X-rays with a wavelength of 0.29 Å and a size of 2.5 × 2.5 μm² at the focal position. At ID15B, a large area MAR555 flat panel detector was used and X-rays (λ = 0.41 Å) were focused at approximately 10 × 10 μm². At each position of interest, 90- or 180-second wide-scans of continuous exposure were collected during ω rotations of ±15° of the DAC (it took 3 or 6 seconds per degree of rotation, respectively). The resulting diffraction images from both experiments were analyzed using Dioptas software ³⁰.

5.2.4 Results and Analysis

Iron samples in Ne and Ar pressure media were pressurized to 41 and 42 GPa, respectively. Two samples of iron investigated in KCl pressure medium were made of ⁵⁷Fe-enriched iron to improve the SMS data quality. They were pressurized to 41 and at 47 GPa, respectively. In this section we present the results of our experiments in detail.

5.2.4.1 Fe in Ne pressure medium

A strip of an Fe foil was loaded into a DAC in a Ne pressure transmitting medium and pressurized to 41(1) GPa. The pressure was determined from the change in the position of the high-frequency edge of the diamond Raman line in Raman spectra taken from the culet of one of the diamond anvils ³¹. The sample was heated at different points and XAS spectra were collected as described in *Experimental Methods*. After heating, X-ray diffraction patterns were collected from the quenched sample *in situ* in the DAC. The patterns were taken from the center of each heated spot and from two different non-heated spots as references. The pressure after heating was 41(1) GPa, as determined from the X-ray diffraction of iron using the equation of state of ε-Fe ³².

Figure 5.2-3 (a) shows a microscope image of the quenched iron sample after heating. The sample was heated six times (heating sequences), to which the numbers from LH1 through LH6 were assigned (Table 5.2-I), at 4 different locations. After LH2, and after the mapping of the area, the alignment of the lasers was realized prior to pulsed heating at the same location as LH2 and was named LH3. Heating sequences LH5 and LH6 had similar laser pulse settings for different laser powers. After increasing the laser power (LH6), the sample was heated at the same position to track the progress of the changes. The locations of all LH spots are marked in Figure 5.2-3 (a).

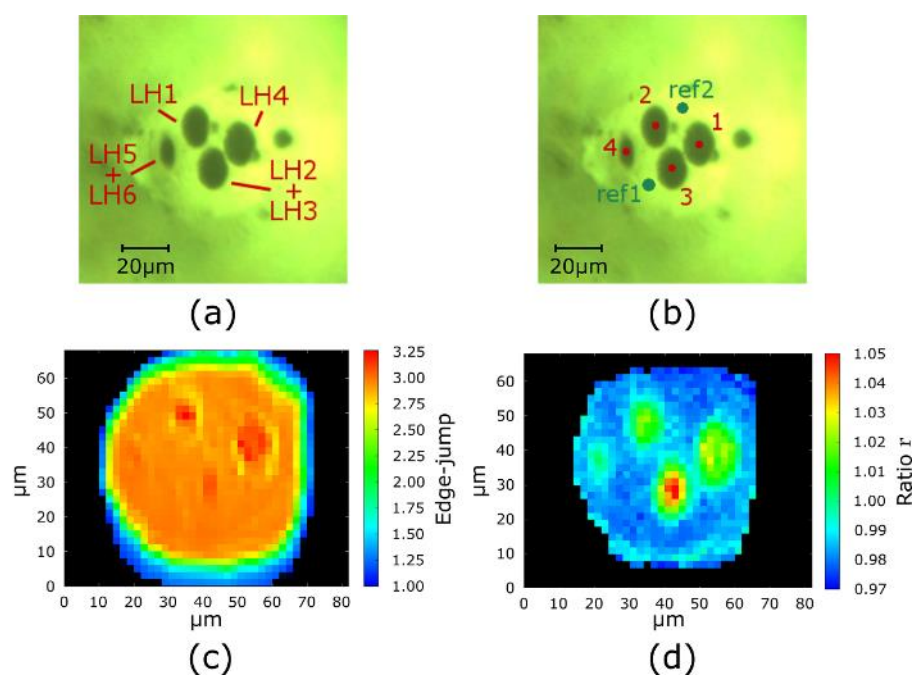


Figure 5.2-3. Upper panel - Microscope image of Fe in Ne quenched at 41 GPa: (a) positions of the laser heated spots on the sample; (b) positions of the spots for the X-ray diffraction data collection - dots 1 through 4 mark heated spots and the dots labeled “ref1” and “ref2” mark the positions on unheated reference points. Lower panel - A XAS map of Fe in Ne color-coded for: (c) the edge jump and (d) the ratio r of the XANES spectra (for details see subsections 5.2.3.2 and 5.2.3.3). Each black pixel marks a position without iron or relates to an unusable spectrum.

The mapping of the whole sample after each heating revealed a difference in the edge jump (i.e. the difference in X-ray absorption between energies below and above the K-edge) around each LH area (Figure 5.2-3 (c)), which is directly correlated with the amount of Fe at that location. However, the analysis of the edge jump variation is insufficient to judge whether it is due to a change in the thickness of the iron foil or because of a change in the sample composition. To resolve the question, a detailed analysis of jump normalized XAS spectra was performed, as described in subsection 5.2.3.2. The map of the sample with the calculated r value at each sample position is presented in Figure 5.2-3 (d).

Table 5.2-I summarizes experimental details for all heating cycles in the experiment with Fe in Ne pressure medium at 41 GPa. In most of the cases, the change in the shoulder of the rising edge was observed immediately after the first heating cycle, i.e. after a few seconds of total heating time. This was the case for both CW and PL heating with relatively long pulses. It is important to note that even in the case of heating at peak temperatures of approximately 1600 K, i.e. well below the melting point of iron and below the ϵ -to- γ -Fe transition, the alteration was almost immediate, happening after a few seconds. In three different heating attempts (LH4, LH5 and LH6) with very short pulses of approximately 2 μ s, there was no visible change in any of the spectra taken from the center of the heating spot between the heating cycles. However, mapping of the whole sample area at the end of the heating cycles revealed sample positions, at which the rising edge shoulder in the spectrum was visibly reduced. One possible explanation is that the short-pulse heating produces high temperatures in smaller

sample areas³³, which are difficult to focus on. The mapping of the quenched sample after LH5 is shown as an example in Figure 5.2-4.

Table 5.2-I. Characteristics of all heating cycles for Fe in Ne at 41 GPa.

Heating sequence	Heating cycle	Repetitions (cycles)	Total heating time	Max. T (K)	Remarks*
LH1	50000 x 100 μ s (PL)	4	20 s	1600	$r > 1$ after two heating cycles (no spectra collected at first cycle)
LH2	10 s (CW)	6	60 s	2500	$r > 1$ after one heating cycle
LH3	alignment heating	-	-	-	same spot position as LH2 (after mapping)
LH4	100000 x 2 μ s (PL)	10	20 s	2800	no changes ($r < 1$) in single collections between 10 cycles, but mapping** reveals $r > 1$ on heated area
LH5	100000 x 2 μ s (PL)	2	4 s	1700	no changes ($r < 1$) in single XAS collections between 2 cycles, but mapping** reveals $r > 1$ on heated area.
LH6	100000 x 2 μ s (PL)	1	2 s	2700	no changes ($r < 1$) in the single collection after 1 cycle, but mapping** reveals $r > 1$ on heated area

* The ratio r of the normalized absorption values for two energy regions in the X-ray absorption spectra of Fe (Figure 5.2-2) was introduced to quantify the difference in the spectra collected at different points within and around a heated spot (see subsection 5.2.3.2 and Figure 5.2-2). $r > 1$ indicates that chemical reaction(s) occurred.

** Upon heating, the heated spot can slightly shift because of thermal expansion and optical effects in the laser optics, and the mapping on quenched samples reveals chemical reaction(s), which could not be detected in situ.

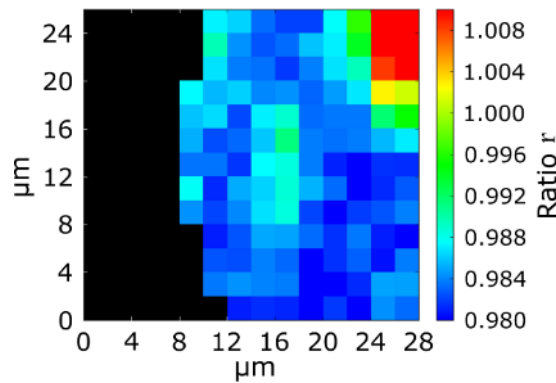


Figure 5.2-4. A XAS map of Fe in Ne color-coded for the ratio r of the XANES spectra (for details see sections II.B and II.C) around the quenched spot after LH5 (2 μ s pulses), visible at approximately the center of the image. Each black pixel marks a position without iron or relates to an unusable spectrum. The heated area after LH1 (100 μ s pulses) is visible in the upper right corner.

In order to address the question of the phase composition of the sample in laser-heated spots, *in situ* X-ray diffraction was performed at the Extreme Conditions Beamline (P02.2) at PETRA III. The positions of the X-ray beam on the sample are designated in Figure 5.2-3 (b). Diffraction patterns collected from the heated areas revealed reflections which do not belong to ϵ -Fe³², Re³⁴, or Ne³⁵, that was not the case for the reference unheated points. Particularly, at least three peaks with the d-spacings 1.665(1), 1.715(1), and 1.754(1) \AA were observed in all heated spots (Figure 5.2-5). Although these data are insufficient to determine the phase unambiguously, all these peaks may be assigned to iron carbide(s) (Fe_3C ¹⁰ or Fe_7C_3 ³⁶).

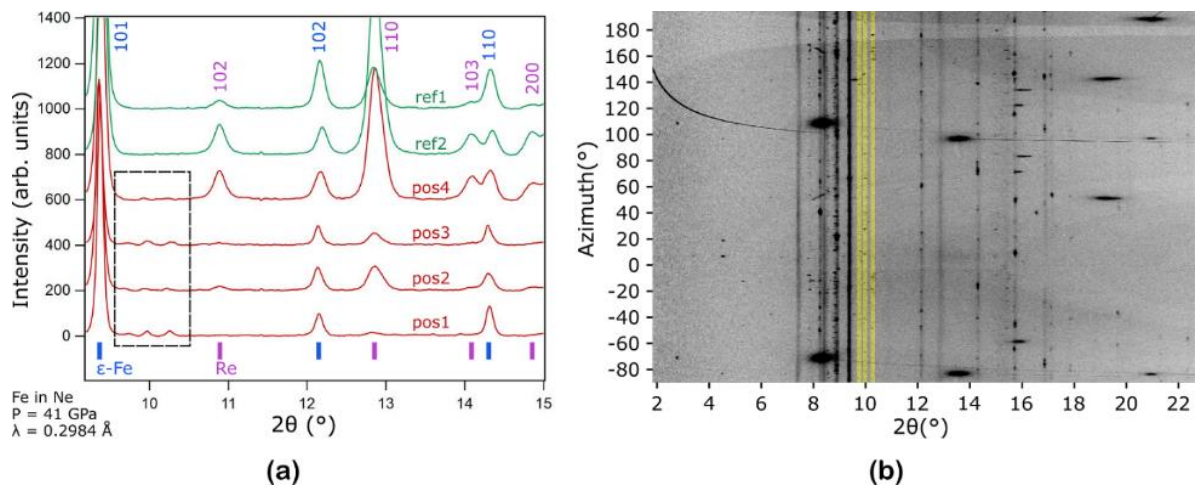


Figure 5.2-5. (a) Diffraction patterns collected from the sample of iron in Ne at 41 GPa at positions 1 through 4 (red curves, heated spots) and reference positions ref1 and ref2 (green curves, non-heated areas) (see Figure 5.2-3 (b)); reflections from diamond anvils are masked. The dashed rectangle highlights the region with three new peaks. (b) The same three peaks highlighted in the image of the integrated pattern collected at position 3 (see Figure 5.2-3 (b)).

5.2.4.2 Fe in Ar pressure medium

An iron foil (thickness 10 μm) along with a ruby sphere was pressurized to 42(1) GPa in an Ar pressure transmitting medium (see Figure 5.2-1 for experimental design). The sample was heated at different spots with a CW laser (LH1 and LH2) and a PL (LH3). XAS spectra were collected as described in Section 5.2.3 (*Experimental Methods*).

The pressure increased to 49(1) GPa after heating, as determined using the ruby pressure scale³⁷. SMS spectra were collected from heated spots of the quenched sample and from two unheated (reference) locations.

Table 5.2-II. Characteristics of all heating cycles for Fe in Ar at 49 GPa.

Heating sequence	Heating cycle	Repetitions (cycles)	Total heating time	Max. T (K)	Remarks
LH1	5 s (CW)	15	75 s	2600	Transition hcp \rightarrow fcc between 1900 K and 2050 K
LH2	5 s (CW)	6	30 s	2700	Flashes during heating (\gg 2700 K), no qualitative changes, distortion of absorption spectra due to inhomogeneous sample surface.
LH3	1000000 x (5.5 – 12) μs (PL)	7	39 – 84 s	3450	Strong distortion of absorption spectra, no evident qualitative changes.

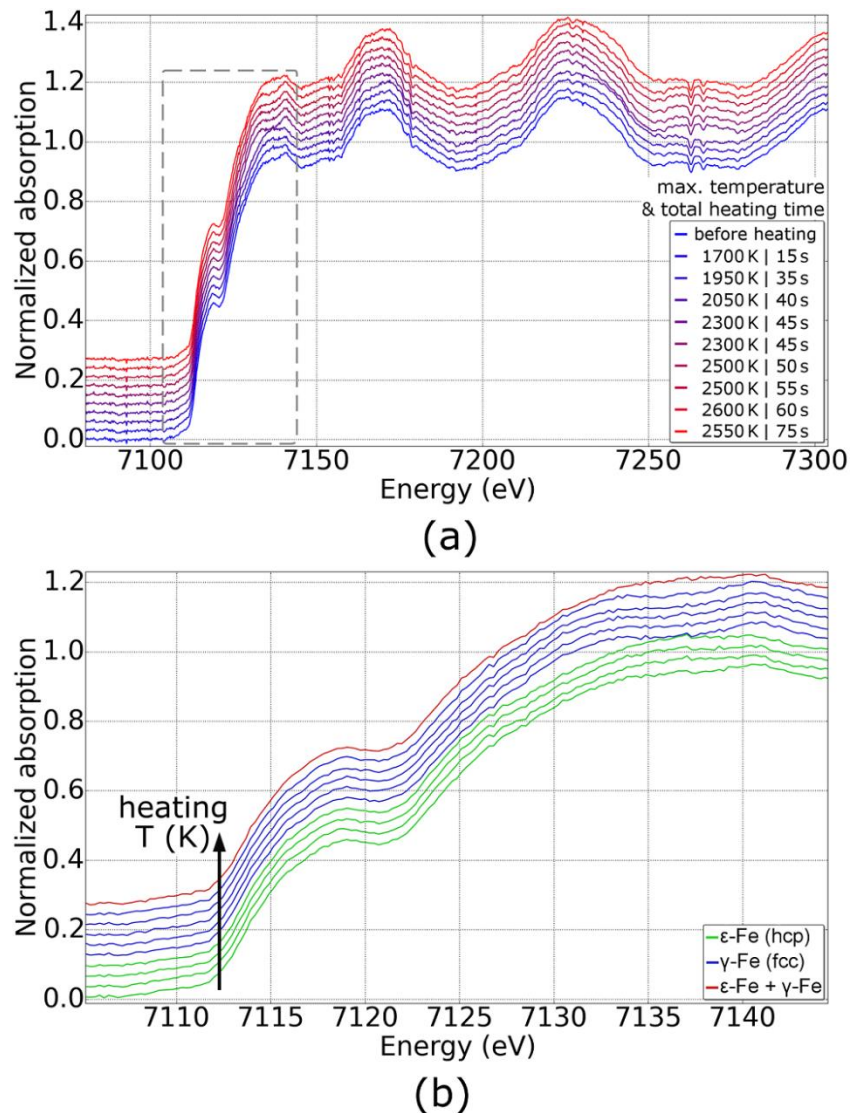


Figure 5.2-6. (a) Normalized X-ray absorption spectra of quenched Fe in Ar taken from the center of the heated area in the course of LH1 (15 exposures of CW heating for 5 seconds each). The legend in the inset shows the maximum temperature recorded during each step of heating and the total heating duration before the spectrum was collected. (b) enlarged region of the same spectra (outlined by dashed grey rectangle in figure a); first only ϵ -Fe is observed (green curves), the appearance of γ -Fe is indicated in spectra shown in blue. The red spectrum evidences the coexistence of both phases. (Successive spectra are vertically shifted for clarity. Increase in temperature during heating follows the positive direction)

Table 5.2-II presents details for all heating cycles. Heating sequences LH1 and LH2 consisted of CW heating cycles with single exposures for 5 seconds on the same sample spot. The temperature was gradually increased after every heating cycle starting from 1700 K (the first temperature recorded) and achieved 2700 K in LH2. Figure 5.2-6 shows the XANES spectra collected on the quenched sample between the heating cycles of LH1. The only observed change is the transition from ϵ -Fe to γ -Fe, which is in agreement with the spectral changes observed in ³, although in the present study spectra are from the quenched sample at room temperature and not at high temperatures. The transition only occurred when the temperature reached 2050 K, which is in general agreement with the study of Anzellini et al.² It is known from the Fe-C diagram at ambient conditions that even a small amount of carbon

can stabilize γ -Fe at lower temperatures³⁸. It was shown by Narygina et al.³⁹ that quenching of γ -Fe at room temperature may be the result of stabilization of this iron phase by a small amount of carbon, which prevents its transformation to ϵ -Fe upon temperature decrease. Thus, it is still possible that in this experiment carbon might have been mobilized, but we have only indirect evidence of this.

Heating sequence LH2 also consisted of CW heating cycles. After a few cycles, due to the surface deformation of the iron foil, the absorption spectra were strongly affected, i.e. the relevant intensity of the absorption oscillations was modified, making the background level indistinguishable. This effect is known for inhomogeneous samples or samples with an irregular surface and is normally observed at the edges of the sample, making the spectra unusable. No other qualitative change was observed. The edge jump maps (Figure 5.2-7 (a) and (b)) directly reflect variations in the sample thickness and show locations of cavities produced on the sample by laser heating at high temperatures. There is no surface deformation after LH1, but two cavities appear after LH2 and LH3.

Pulsed heating (LH3) consisted of relatively short pulses of 5.5 to 12 microseconds (Table 5.2-II). The duration of the pulses varied due to minor adjustments of the laser power after every heating cycle. The sample was heated initially at 3050 K (pulse peak temperature) and its deformation was immediate. The next cycles resulted in increasing peak temperatures up to 3450 K. As in LH2, no other qualitative changes were observed.

The calculation of the ratio r that tracks changes in the Fe rising edge shoulder did not reveal any differences between the non-heated and heated areas of the sample (Figure 5.2-7 (c)) after all three heating sequences.

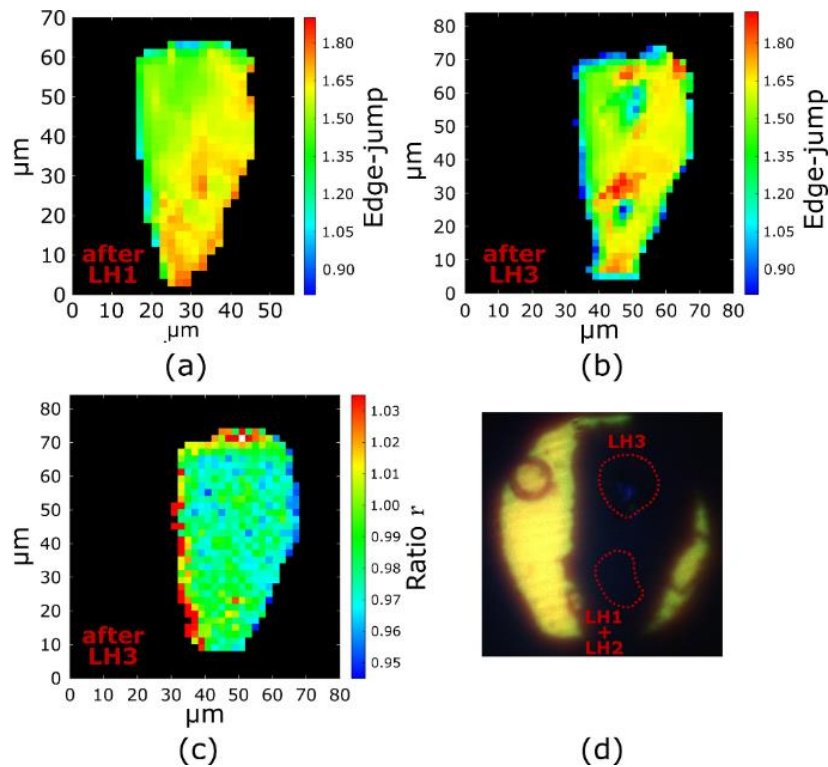


Figure 5.2-7. A XAS map of quenched Fe in Ar representing (a) the edge jump after LH1, (b) the edge jump after LH3 and (c) the ratio r (after LH3) of the XANES spectra (see text). Each black pixel marks a position without iron or unusable spectrum. (d) Annotated microscope image showing the heated areas.

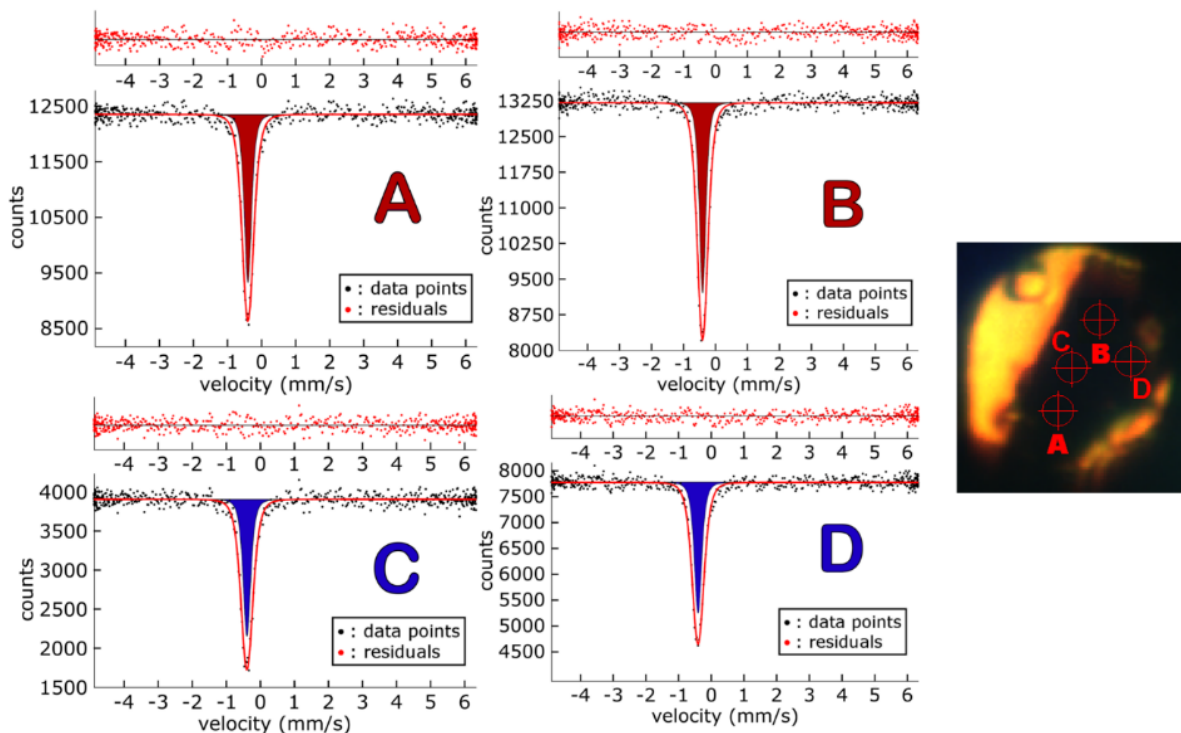


Figure 5.2-8. SMS spectra of Fe pressurized in Ar at 49 GPa (black dots). The spectra were collected at different locations (A, B, C, and D) designated in the microscope image on the right. Positions A and B correspond to laser heated areas; the sample was not directly heated at the spots C and D. The red solid lines show the theoretical fit and the residuals are indicated above the spectra (red dots). Singlets marked blue correspond to unheated Fe; singlets marked red - to heated Fe. The size of the crosshair in the microscope image matches approximately the size of the focused X-ray beam on the sample.

Mössbauer absorption spectra were collected at room temperature on four different locations on the sample (Figure 5.2-8). Position A corresponds to the area of LH1 and LH2 and position B is in the area of LH3. The spectra could be fit using a singlet with a center shift of $-0.399(5)$ mm/s and $-0.403(3)$ mm/s for positions A and B, respectively, using the full transmission integral with a normalized Lorentzian-squared source line. The spectra for the reference positions C and D (not heated) could be similarly fit with center shifts $-0.399(6)$ mm/s for C and $-0.405(5)$ mm/s for D, which are expected values for pure iron at this pressure⁴⁰. Before fitting, a correction was applied by subtracting a known small contribution due to iron impurities in the Be refractive lenses used to decrease the divergence of the beam incident to the SMS.

No contamination is observed by Mössbauer spectroscopy, since all probed areas of the sample reveal only the presence of elemental Fe, which is also confirmed by XAS. However, since γ -Fe was observed in the quenched sample, the possibility of carbon diffusion in iron cannot be ruled out.

5.2.4.3 Fe in KCl pressure medium

Two samples of ^{57}Fe -enriched iron in DACs with KCl as a pressure transmitting medium were investigated. They were pressurized to 41(1) GPa (increased to 42(1) GPa after heating) and 47(1) GPa (increased to 53(1) GPa after heating), as determined using Raman spectra of diamond taken from the culets of the anvils³¹.

Table 5.2-III. Characteristics of all heating cycles for Fe in KCl at 42 GPa.

Heating sequence	Heating cycle	Repetitions (cycles)	Total heating time	Max. T (K)	Remarks
LH1	15 s (CW)	7	105 s	2300	No evident qualitative changes apart from sample deformation at the heated area.
LH2	15 s (CW)	4	60 s	3000	
LH3	long (CW)	1	3 mins	2700	Flashes during heating ($\gg 2700$ K). Evidence of hcp \rightarrow fcc transition after heating at 2500 K
LH4a	500000 x 2 μ s (PL)	1	1 s	3400	Significant deformation of the sample, hole formation, no evident qualitative changes in the spectra from the heated areas. Each burst of pulses on different sample position (LH4a and LH4b)
LH4b	500000 x 2 μ s (PL)	1	1 s	3300	

The first sample was heated at different positions during four heating cycles (Table 5.2-III). XAS spectra were collected as described in *Experimental Methods*.

Continuous heating at temperatures up to 3000 K (LH1 and LH2) resulted in a significant deformation of the surface of the sample. Figure 5.2-9 shows the maps of the ratio r for the first sample before heating (a) and after LH3 (b) and LH4 (c). All spectra with $r > 1$ were checked individually. It was found that the quality of these spectra was insufficient to conclude whether chemical changes took place, as $r > 1$ could be attributed to the effect of heavily deformed sample surface and/or to the increased noise in the collected data. A transition from ϵ -Fe to γ -Fe was observed in the course of LH3.

Pulsed heating (LH4a, LH4b) deformed the sample even more than CW heating LH1 and LH2, that along with the sample thinning caused reduction of the area from which valid absorption spectra could be collected (Figure 5.2-9 (c)).

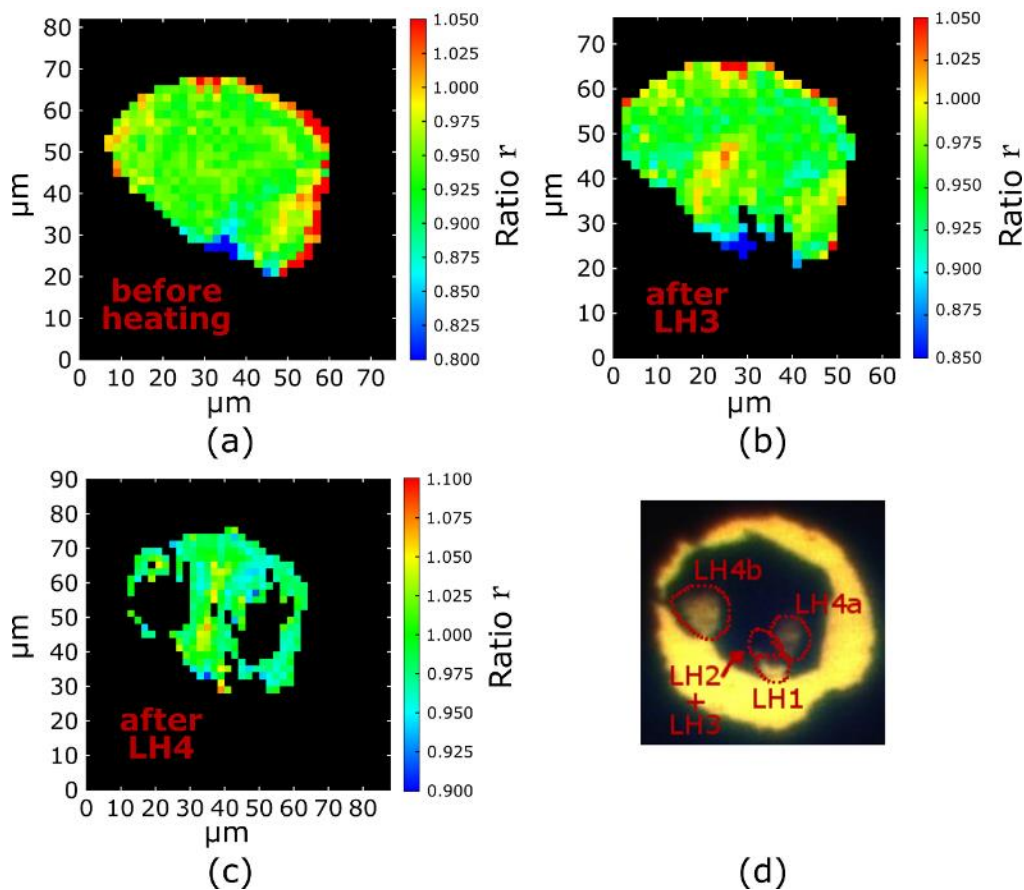


Figure 5.2-9. XAS map of quenched Fe in KCl based on the ratio r of the XANES spectra (a) before heating (b) after heating cycle LH3 and (c) after heating cycle LH4. Each black pixel marks a position without iron or unusable spectrum. (d) Annotated microscope image showing the positions of the heated spots.

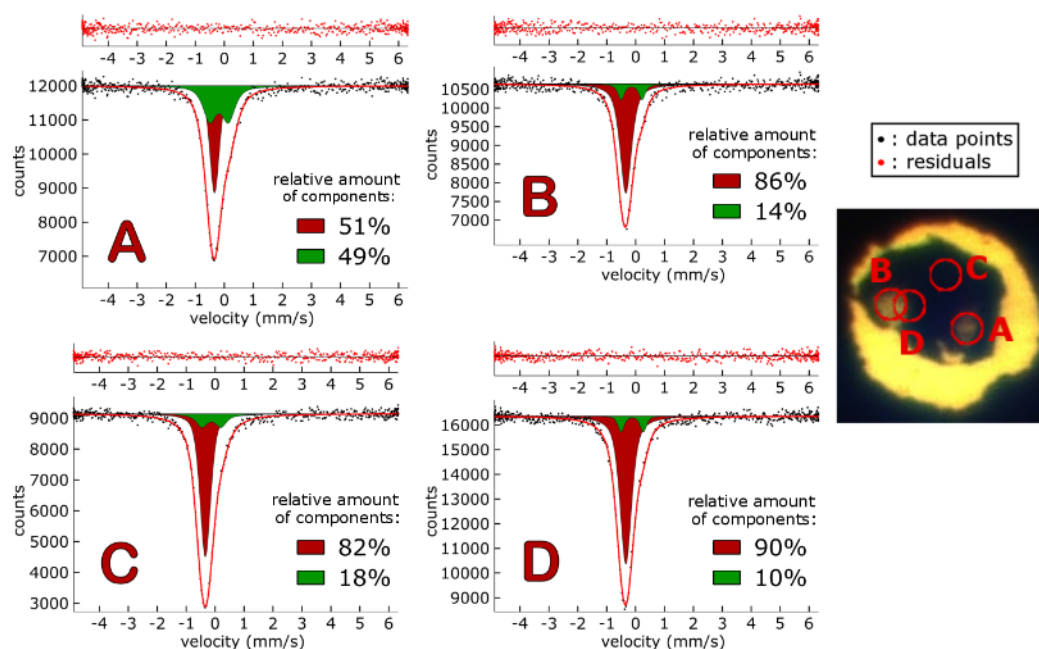


Figure 5.2-10. SMS spectra at different areas of the ^{57}Fe -enriched iron sample pressurized in KCl at 42 GPa (microscope photo on the right). Positions A, B and D correspond to laser heated areas of the sample, while C was not directly heated. The red solid line shows the theoretical fit and the residuals are indicated above the spectrum (red dots). Singlets marked red correspond to iron and doublets marked green to the new compound that appeared after heating (see text for details). The crosshair size marked on the photograph matches approximately the size of the focused X-ray beam on the sample.

After heating, SMS spectra were collected from the quenched sample at the heated spots and at one other unheated position (Figure 5.2-10). Position A corresponds to the area of heating sequences LH2, LH3 and LH4a and positions B and D are in the area of LH4b. Position C was selected to be as far as possible from the heated spots. The SMS spectra were fit using the full transmission integral with a normalized Lorentzian-squared source line after having corrected the contribution from iron impurities in Be lenses.

SMS spectroscopy revealed changes in the quenched sample, both in the heated areas and around them. In all spectra, the singlet, characteristic for metallic iron at this pressure ⁴⁰, featured a shoulder, which suggested the appearance of an additional chemical component in the sample after heating. The singlet had center shift (CS) of approximately $-0.34(4)$ mm/s in all spectra, as expected. To take into account the additional component, a paramagnetic doublet was added to achieve the best fit of the experimental data. The CS of the doublet ranges from $-0.18(11)$ mm/s to $-0.12(44)$ mm/s and quadrupole splitting (QS) from $0.64(4)$ mm/s to $0.77(6)$ mm/s. The hyperfine parameters of the doublet are in close agreement with the hyperfine parameters of Fe_3C at similar pressure ⁴¹. It should be noted that the observed new component cannot be interpreted as $\gamma\text{-Fe}$, since such a component is not observed in the SMS spectra of Fe with Ar, while the presence of $\gamma\text{-iron}$ is identified in both cases by XANES.

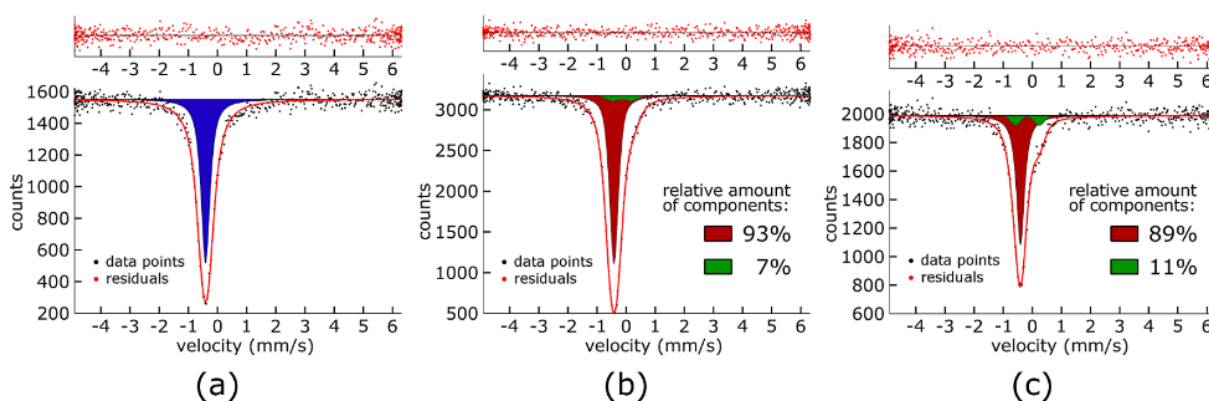


Figure 5.2-11. SMS spectra at different positions of the ^{57}Fe -enriched iron sample pressurized in KCl at 53 GPa. The red solid line shows the theoretical fit and the residuals are indicated above the spectrum: (a) before heating (singlet marked by blue surface corresponds to unheated iron), (b) after less than one minute of low-power pulsed heating for laser alignment (singlet marked by red surface corresponds to heated iron; doublet marked by green surface - to the new compound that appeared after heating and was interpreted as iron carbide - see text), (c) after several minutes of pulsed heating ($f = 1$ kHz, pulse duration $700 \mu\text{s}$) at temperatures up to 3800 K (red singlet - heated iron; green doublet - the new compound).

The second ^{57}Fe -enriched iron sample was heated for several minutes in total, at temperatures up to 3800 K (peak temperature of the pulse), using the double-sided pulsed laser heating system of the Nuclear Resonance beamline at the ESRF⁴², with laser modulation frequency at 1 kHz and pulses of $700 \mu\text{s}$ duration. Apart from the pure iron singlet of the non-heated sample (Figure 5.2-11 (a), blue singlet indicates non-heated iron), the second absorption component appeared after less than a minute of alignment heating (Figure 5.2-11 (b), green doublet; red singlet indicates heated iron). Alignment heating was done at low laser power (sample temperature was less than 1500 K) to align and synchronize the lasers for the pulsed operation. After heating, the second component became more prominent, as seen in Figure 5.2-11 (c). The spectra were fit using the full transmission integral with a normalized Lorentzian-squared source line. The single line has a central shift (CS) of $-0.410(6)$ mm/s. The best fit was obtained with the addition of a paramagnetic doublet with CS of $-0.15(22)$ mm/s and quadrupole splitting (QS) of $0.65(32)$ mm/s after alignment, and CS $-0.17(12)$ mm/s and QS $0.81(19)$ at the end of the heating experiment. The uncertainties are large but expected, considering the small contribution of the new component and the high degree of overlap. Nevertheless, the Fe_3C interpretation is plausible and in close agreement with the literature⁴¹.

X-ray diffraction at ID15 beamline of ESRF revealed both ϵ -Fe and γ -Fe in the sample at room temperature, but iron carbide could not be detected. The sample was mapped at several locations covering the whole heated area. The pressure of $53.0(5)$ GPa was determined using the KCl equation of state⁴³.

5.2.5 Discussion

In most of the cases examined here, laser heating of iron resulted in formation of iron carbides, which were detected by either XRD, XANES, or SMS in agreement with the literature. Each time, two different techniques were used to investigate the heated samples in order to

cross-validate the results, which are summarized in Table 5.2-IV. Mössbauer spectroscopy was very sensitive for detection of carbides in two experiments with ^{57}Fe -enriched iron in KCl as a pressure medium, whereas XANES gave an uncertain result and XRD appeared to be insufficiently sensitive as the amount of the carbide was negligibly small in comparison with the amount of Fe and KCl, which dominated the XRD pattern.

Table 5.2-IV. Summarized results.

Sample	Pressure Medium	Pressure (GPa)		Analysis	Evidence of reaction
		before heating	after heating		
Fe	Ne	41	41	XANES	Yes
				XRD	Yes
Fe	Ar	42	49	XANES	Uncertain
				SMS	No
^{57}Fe enriched	KCl	41	42	XANES	Uncertain
				SMS	Yes
^{57}Fe enriched	KCl	47	53	SMS	Yes
				XRD	No

In all experiments reported here, no significant difference was observed in the effect of CW and PL heating on iron-carbon reactivity. Thus, we could conclude that pulsed laser heating (microseconds pulses duration, up to 100 kHz repetition rate) does not provide an obvious advantage in the prevention of chemical reactions between the heated iron sample and carbon from the diamond anvils. There are examples when more reacted material was observed in the CW laser heated areas (Figure 5.2-3 (d), Figure 5.2-10). However, no definitive conclusions can be drawn regarding advantages of PL for minimizing reactions, because other factors, such as heating temperature, sample thickness, heating duration, etc. could not be quantified in our experiments. Thus, the only solid conclusion is that laser heating in DACs can lead to chemical reactions, and this effect must be taken into account, particularly, for interpretation of experiments on melting of iron and other metals.

Our observations suggest that in cases when a chemical reaction with carbon occurs, it happens almost immediately, after only a very few seconds of heating at moderate temperatures (independently of heating method, CW or pulsed). It means that chemical contamination by carbon may be an important factor even if efforts are applied to minimize the heating time, because, as a rule, tens of seconds are usually necessary to characterize the temperature and the state of the hot sample.

In all experiments in this study, at sufficiently high temperatures we observed formation of γ -Fe, and this phase was quenchable. Preservation of γ -Fe at ambient temperature in both the

multi-anvil apparatus and laser heated DAC experiments^{44,45} has been previously reported as an effect of slow transformation kinetics to ϵ -Fe, or due to the high cooling rate. However, *Narygina et al.*³⁹ demonstrated that γ -Fe can be also stabilized by a small amount of carbon that hinders martensitic transformation during quenching. Thus, in experiments, in which carbides are not detected (like in our experiments with Ar pressure medium), but γ -Fe is quenched at ambient temperature, carbon contamination cannot be ruled out.

5.2.6 Conclusions

For the purposes of this study, a series of DACs were heated using continuous wave (CW) and pulsed laser (PL) heating and the quenched samples were analyzed *in situ* using energy dispersive X-ray absorption spectroscopy, X-ray diffraction, and synchrotron Mössbauer source spectroscopy. Iron carbide formation was detected in most experiments regardless of the laser heating method. While pulsed laser heating is generally considered advantageous in preventing the mobilization of carbon from the diamond anvils and its chemical interaction with the sample, this is refuted by our results. Generally, one experimental technique was not enough to fully characterize the chemistry of the sample, and a cross-validation of techniques was necessary. For this reason, extra precautions should be taken in experiments with iron in a laser-heated diamond anvil cell and the application of more than one analytical technique is strongly suggested, as well as *ex situ* analysis of the recovered sample if possible.

5.2.7 Acknowledgements

N.D. and L.D. thank the Deutsche Forschungsgemeinschaft (DFG projects DU 954-11/1 and DU 393-10/1) and the Federal Ministry of Education and Research, Germany (BMBF, grant no. 5K16WC1) for financial support. Parts of this research were carried out at the light source PETRA III at DESY, a member of the Helmholtz Association (HGF), and at the European Synchrotron Radiation Facility (ESRF).

5.2.8 References

1. Boehler, R. Temperatures in the Earth's core from melting-point measurements of iron at high static pressures. *Nature* **363**, 534–536 (1993).
2. Anzellini, S., Dewaele, A., Mezouar, M., Loubeyre, P. & Morard, G. Melting of Iron at Earth's Inner Core Boundary Based on Fast X-ray Diffraction. *Science (80-.)*. **340**, 464–466 (2013).
3. Aquilanti, G. *et al.* Melting of iron determined by X-ray absorption spectroscopy to 100 GPa. *Proc. Natl. Acad. Sci.* **112**, 12042–12045 (2015).
4. Sinmyo, R., Hirose, K. & Ohishi, Y. Melting curve of iron to 290 GPa determined in a resistance-heated diamond-anvil cell. *Earth Planet. Sci. Lett.* **510**, 45–52 (2019).
5. Prakapenka, V. B., Shen, G. & Dubrovinsky, L. S. Carbon transport in diamond anvil cells. *High Temp. - High Press.* **35–36**, 237–249 (2003).

6. Rouquette, J. *et al.* Iron-carbon interactions at high temperatures and pressures. *Appl. Phys. Lett.* **92**, 121912 (2008).
7. Frost, D. J. *et al.* Partitioning of oxygen between the Earth's mantle and core. *J. Geophys. Res.* **115**, B02202 (2010).
8. Tateno, S., Hirose, K., Ohishi, Y. & Tatsumi, Y. The Structure of Iron in Earth's Inner Core. *Science (80-.)*. **330**, 359–361 (2010).
9. Lord, O. T., Walter, M. J., Dasgupta, R., Walker, D. & Clark, S. M. Melting in the Fe–C system to 70 GPa. *Earth Planet. Sci. Lett.* **284**, 157–167 (2009).
10. Morard, G. *et al.* Fe–FeO and Fe–Fe₃C melting relations at Earth's core–mantle boundary conditions: Implications for a volatile-rich or oxygen-rich core. *Earth Planet. Sci. Lett.* **473**, 94–103 (2017).
11. Morard, G. *et al.* Solving Controversies on the Iron Phase Diagram Under High Pressure. *Geophys. Res. Lett.* **45**, 11074–11082 (2018).
12. Dewaele, A., Mezouar, M., Guignot, N. & Loubeyre, P. High Melting Points of Tantalum in a Laser-Heated Diamond Anvil Cell. *Phys. Rev. Lett.* **104**, 255701 (2010).
13. Kantor, I. *et al.* BX90: A new diamond anvil cell design for X-ray diffraction and optical measurements. *Rev. Sci. Instrum.* **83**, 125102 (2012).
14. Letoullec, R., Pinceaux, J. P. & Loubeyre, P. The membrane diamond anvil cell: A new device for generating continuous pressure and temperature variations. *High Press. Res.* **1**, 77–90 (1988).
15. Boehler, R. & De Hantsetters, K. New anvil designs in diamond-cells. *High Press. Res.* **24**, 391–396 (2004).
16. Kurnosov, A. *et al.* A novel gas-loading system for mechanically closing of various types of diamond anvil cells. *Rev. Sci. Instrum.* **79**, 045110 (2008).
17. Pascarelli, S. *et al.* The Time-resolved and Extreme-conditions XAS (TEXAS) facility at the European Synchrotron Radiation Facility: the energy-dispersive X-ray absorption spectroscopy beamline ID24. *J. Synchrotron Radiat.* **23**, 353–368 (2016).
18. Torchio, R. *et al.* Probing the local, electronic and magnetic structure of matter under extreme conditions of temperature and pressure. *High Press. Res.* **36**, 293–302 (2016).
19. Kantor, I., Marini, C., Mathon, O. & Pascarelli, S. A laser heating facility for energy-dispersive X-ray absorption spectroscopy. *Rev. Sci. Instrum.* **89**, 013111 (2018).
20. Aprilis, G. *et al.* Portable double-sided pulsed laser heating system for time-resolved geoscience and materials science applications. *Rev. Sci. Instrum.* **88**, 084501 (2017).
21. Aquilanti, G. *et al.* Development of micro-XANES mapping in the diamond anvil cell. *J. Synchrotron Radiat.* **16**, 376–379 (2009).

22. Solé, V. A., Papillon, E., Cotte, M., Walter, P. & Susini, J. A multiplatform code for the analysis of energy-dispersive X-ray fluorescence spectra. *Spectrochim. Acta Part B At. Spectrosc.* **62**, 63–68 (2007).
23. Torchio, R. *et al.* Probing local and electronic structure in Warm Dense Matter: single pulse synchrotron x-ray absorption spectroscopy on shocked Fe. *Sci. Rep.* **6**, 26402 (2016).
24. Mazevet, S. *et al.* Ab initio calculation of x-ray absorption of iron up to 3 Mbar and 8000 K. *Phys. Rev. B* **89**, 100103 (2014).
25. Raji, A. T., Scandolo, S., Härting, M. & Britton, D. T. Probing the structure of iron at extreme conditions by X-ray absorption near-edge structure calculations. *High Press. Res.* **33**, 119–123 (2013).
26. Potapkin, V. *et al.* The ⁵⁷Fe Synchrotron Mössbauer Source at the ESRF. *J. Synchrotron Radiat.* **19**, 559–569 (2012).
27. Prescher, C., McCammon, C. & Dubrovinsky, L. MossA : a program for analyzing energy-domain Mössbauer spectra from conventional and synchrotron sources. *J. Appl. Crystallogr.* **45**, 329–331 (2012).
28. Merlini, M. & Hanfland, M. Single-crystal diffraction at megabar conditions by synchrotron radiation. *High Press. Res.* **33**, 511–522 (2013).
29. Liermann, H. P. *et al.* The Extreme Conditions Beamline P02.2 and the Extreme Conditions Science Infrastructure at PETRA III. *J. Synchrotron Radiat.* **22**, 908–924 (2015).
30. Prescher, C. & Prakapenka, V. B. DIOPTAS: A program for reduction of two-dimensional X-ray diffraction data and data exploration. *High Press. Res.* **35**, 223–230 (2015).
31. Akahama, Y. & Kawamura, H. Pressure calibration of diamond anvil Raman gauge to 310GPa. *J. Appl. Phys.* **100**, 043516 (2006).
32. Dewaele, A. *et al.* Quasihydrostatic equation of state of Iron above 2 Mbar. *Phys. Rev. Lett.* **97**, 29–32 (2006).
33. Goncharov, A. F. *et al.* Laser heating in diamond anvil cells: developments in pulsed and continuous techniques. *J. Synchrotron Radiat.* **16**, 769–772 (2009).
34. Zha, C.-S., Bassett, W. A. & Shim, S.-H. Rhenium, an in situ pressure calibrant for internally heated diamond anvil cells. *Rev. Sci. Instrum.* **75**, 2409–2418 (2004).
35. Fei, Y. *et al.* Toward an internally consistent pressure scale. *Proc. Natl. Acad. Sci.* **104**, 9182–9186 (2007).
36. Nakajima, Y. *et al.* Thermoelastic property and high-pressure stability of Fe₇C₃: Implication for iron-carbide in the Earth's core. *Am. Mineral.* **96**, 1158–1165 (2011).

37. Dewaele, A., Torrent, M., Loubeyre, P. & Mezouar, M. Compression curves of transition metals in the Mbar range: Experiments and projector augmented-wave calculations. *Phys. Rev. B* **78**, 104102 (2008).
38. Okamoto, H. The C-Fe (carbon-iron) system. *J. Phase Equilibria* **13**, 543–565 (1992).
39. Narygina, O. *et al.* Phase relations in Fe–Ni–C system at high pressures and temperatures. *Phys. Chem. Miner.* **38**, 203–214 (2011).
40. Glazyrin, K. *et al.* Importance of Correlation Effects in hcp Iron Revealed by a Pressure-Induced Electronic Topological Transition. *Phys. Rev. Lett.* **110**, 117206 (2013).
41. Prescher, C. *et al.* Structurally hidden magnetic transitions in Fe₃C at high pressures. *Phys. Rev. B* **85**, 140402 (2012).
42. Kuppenko, I. *et al.* Time differentiated nuclear resonance spectroscopy coupled with pulsed laser heating in diamond anvil cells. *Rev. Sci. Instrum.* **86**, 114501 (2015).
43. Dewaele, A. *et al.* High-pressure–high-temperature equation of state of KCl and KBr. *Phys. Rev. B* **85**, 214105 (2012).
44. Komabayashi, T., Fei, Y., Meng, Y. & Prakapenka, V. In-situ X-ray diffraction measurements of the γ - ϵ transition boundary of iron in an internally-heated diamond anvil cell. *Earth Planet. Sci. Lett.* **282**, 252–257 (2009).
45. Kubo, A. *et al.* In situ X-ray observation of iron using Kawai-type apparatus equipped with sintered diamond: Absence of β phase up to 44 GPa and 2100 K. *Geophys. Res. Lett.* **30**, 1126 (2003).

5.3 The effect of pulsed laser heating on the stability of ferropericlase at high pressures

Georgios Aprilis^{1,*}, Anna Pakhomova², Stella Chariton³, Saiana Khandarkhaeva³, Caterina Melai³, Elena Bykova², Maxim Bykov³, Timofei Fedotenko¹, Egor Koemets³, Catherine McCammon³, Leonid Dubrovinsky³, Natalia Dubrovinskaia¹

¹ Materials Physics and Technology at Extreme Conditions, Laboratory of Crystallography, Universität Bayreuth, D-95440 Bayreuth, Germany

² Deutsches Elektronen-Synchrotron (DESY), D-22607 Hamburg, Germany

³ Bayerisches Geoinstitut, Universität Bayreuth, D-95440 Bayreuth, Germany

* Correspondent author (e-mail: georgios.aprilis@uni-bayreuth.de)

Minerals, **10**(6), 542 (2020)

5.3.1 Abstract

It is widely accepted that the lower mantle consists of mainly three major minerals – ferropericlase, bridgmanite and calcium silicate perovskite. Ferropericlase ((Fe,Mg)O) is believed to be the second most abundant of the three, comprising approximately 16-20 wt% of the lower mantle. The stability of ferropericlase at conditions of the lowermost mantle has been highly investigated with controversial results. Amongst other reasons, the experimental conditions during laser heating (such as duration and achieved temperature) have been suggested as a possible explanation for the discrepancy. In this study, we investigate the effect of pulsed laser heating on the stability of ferropericlase with a geochemically relevant composition of (Fe_{0.25}Mg_{0.75})O (Fp25) at pressure conditions corresponding to the upper part of the lower mantle and at a wide temperature range. We report on the decomposition of Fp25 with formation of a high-pressure (Mg,Fe)₃O₄ phase with CaTi₂O₄-type structure as well as the dissociation of Fp25 into an Fe-rich and a Mg-rich phases induced by pulsed laser heating. Our results provide further arguments that the chemical composition of the lower mantle is more complex than initially thought and that the compositional inhomogeneity is not only a characteristic of the lowermost part but includes depths as shallow as below the transition zone.

5.3.2 Introduction

The Earth's lower mantle constitutes more than half of the volume of the planet, from the transition zone at the depth of 660 km to the core-mantle boundary (CMB) at 2900 km¹. Currently, it is widely accepted that the lower mantle consists of mainly three major minerals - ferropericlase, bridgmanite and calcium silicate perovskite²⁻⁴. Ferropericlase is believed to be the second most abundant of the three, comprising approximately 16-20 wt% of the lower mantle^{4,5,6}.

The expected percentage of iron (expressed as $\text{Fe}/(\text{Mg}+\text{Fe})$) in $(\text{Fe},\text{Mg})\text{O}$ in the lower mantle is 10-25%, as follows, particularly, from studies of Mg-Fe partitioning between bridgmanite and ferropericlase^{7,8}. Ferropericlase with such composition is so far considered to be stable in a NaCl-type (B1) structure ($Fm\bar{3}m$) throughout the lower mantle⁹ (in contrast to bridgmanite that is replaced by post-perovskite near the CMB¹⁰); above ~ 50 GPa iron in ferropericlase undergoes a spin crossover from high-spin to low-spin¹¹.

There are, however, reports that $(\text{Mg},\text{Fe})\text{O}$ with relatively large amount of Fe may decompose at pressure-temperature conditions of the lowermost mantle into an Fe-richer and a Mg-richer phases^{12,13}. In contrast to the earlier reports on decomposition, subsequent studies in laser-heated diamond anvil cells (LHDACs) did not observe any segregation between iron and magnesium^{9,14-16} (although extra diffraction lines were observed, see Ref. 9, for example). Ferropericlase inclusions in super-deep diamonds show very large variations of Mg/Fe ratio¹⁷ suggesting that there are natural processes which lead to compositional differentiation in the formation of $(\text{Mg},\text{Fe})\text{O}$. The behavior of ferropericlase as well as partitioning of iron between co-existing in lower mantle minerals play a crucial role in understanding the dynamics, geophysics, and geochemistry of the Earth^{11,18}.

Pulsed laser heating has been used for the initiation and study of chemical reactions in different systems at ambient pressure over decades¹⁹. In experiments with DACs, pulsed laser heating (PLH) was considered as an option to prevent or minimize (in comparison with continuous wave, CW) reactions between diamond anvils (carbon) and heated matter^{20,21}. However, a recent study on the reactivity of iron with the diamond anvils inside a DAC shows no obvious advantage due to heating in pulse mode²². Still, PLH in DACs is more stable (spatially and in term of overall duration) and often easier controllable in comparison with CW.

In this study, we investigate the effect of pulsed laser heating on the stability of ferropericlase with a geochemically relevant composition of $(\text{Fe}_{0.25}\text{Mg}_{0.75})\text{O}$ (Fp25) at pressure conditions corresponding to the upper part of the lower mantle^{23,24} and at wide temperature range. We report on the decomposition of Fp25 with formation of a high-pressure $(\text{Mg},\text{Fe})_3\text{O}_4$ phase with CaTi_2O_4 -type structure as well as the dissociation of Fp25 into an Fe-rich and a Mg-rich phases induced by pulsed laser heating.

5.3.3 Experimental

5.3.3.1 Sample Preparation

Ferropericlase starting material was synthesized by *Longo et al.*²⁵ Magnesium and iron metal were mixed in stoichiometric proportions to obtain crystalline powder of $(\text{Mg},\text{Fe})\text{O}$. Metals were dissolved in HNO_3 and NH_3 has been added in order to obtain oxide precipitate. The excess water (10ml), HNO_3 and NO_3 were removed by drying the gel in a Pt crucible at 1200-1500°C on a Bunsen and then in the furnace at 800°C. The powders were finally equilibrated in the gas-mixing furnace under different CO/CO_2 ratios well mixed at 1300°C in order to

guarantee a wide range of $\text{Fe}^{3+}/\Sigma\text{Fe}$. $\log f_{\text{O}_2}$ has been estimated on activity-composition relation and oxygen activity at 1300°C: it has been varied between $\log(-7)$ and $\log(-11)$ on the Fe-FeO buffer. The mixtures were enriched in ^{57}Fe of approximately 10% of the total Fe to facilitate Mossbauer spectroscopy measurements.

The powder ferropericlasite with composition $(\text{Fe}_{0.25}\text{Mg}_{0.75})\text{O}$ was filled into Re-foil capsules for single crystal growth. 10wt% ReO_2 powder was added as redox sensor. The starting material was pressurized to 15 GPa and heated to 1800°C for a maximum heating time of 1 hour, using a Sumitomo press, one of the 6-8 Kawai-types of presses at Bayerisches Geoinstitut (BGI) and a LaCrO_3 heater. The elevated temperature was monitored by a $\text{W}_{97\%}\text{Re}_{3\%}$ - $\text{W}_{75\%}\text{Re}_{25\%}$ thermocouple directly in contact with the Re capsule. The experimental run followed the standard procedure of cold pressurizing with subsequent heating to target temperature with a 100 °C/min rate. Isobaric quenching of the experiments was achieved by turning off the power to the furnace, after which the sample was slowly decompressed. The cooling rate was approximately 200 – 250 °C/s. The homogeneity of the recovered sample was checked using scanning electron microscopy (SEM, EDX) and electron microprobe analysis (EMPA). No variations in chemical composition within the accuracy of the method (about 1 at%) were detected by EDX. EMPA measurements were performed at several different locations on the recovered sample reporting an average chemical composition of Mg: 70(5) wt%, Fe^{2+} : 19(3) wt% and Fe^{3+} : 11(4) wt%. Single crystal X-ray diffraction was performed on several particles with linear dimensions of 15 to 25 μm that were selected from the recovered sample. The lattice parameter of the material was found to be 4.218(1) Å with refined chemical composition $(\text{Fe}_{0.24(2)}\text{Mg}_{0.76(2)})\text{O}$.

For the high-pressure experiments in total five crystals of ferropericlasite were loaded in two BX90-type²⁶ diamond anvil cells (DACs) with Boehler-Almax²⁷ diamonds. Three crystals were placed in a DAC with anvil culets of 350 μm in diameter and two crystals in a DAC with anvil culets of 250 μm in diameter and were pressurized as described in the following sections. Rhenium gaskets were pre-indented from an initial thickness of 200 μm down to 25 – 35 μm and laser-drilled to create circular pressure chambers of 100 – 120 μm in diameter. Both DACs were loaded with neon as pressure-transmitting medium using the in-house gas loading system at Bayerisches Geoinstitut (BGI)²⁸.

5.3.3.2 Experiment 1

For the first experiment, three $(\text{Fe}_{0.25}\text{Mg}_{0.75})\text{O}$ crystals with dimensions of approximately 20x20x7 μm^3 were placed inside the sample chamber of a diamond anvil cell (DAC), and pressurized to 26(1) GPa (as determined from Raman shift of diamond anvil²⁹). After laser heating (see Table 5.3-I) the pressure increased to 30.0(5) GPa (determined using X-ray diffraction data and the equation of state of Ne³⁰). The samples were heated at ID18 of the ESRF using the portable laser-heating system³¹. Each crystal was heated using a different heating method - continuous wave (CW), pulsed at 25 kHz repetition rate with pulses of 3 μs , and pulsed at 1 kHz with pulses of 500 μs .

Table 5.3-I presents the details of each heating sequence. All crystals were heated using one-sided heating (upstream side) but the temperature was recorded from both observation sides. The thermal gradient was usually 100 – 200 K between the heated and the non-heated side, thus providing a constraint for the heating temperature of the whole volume of the crystal. Temperatures were measured using spectroradiometry and, particularly for the pulsed laser heating, the temperature reported is the one being the highest at the peak of the pulse, collected as described by Aprilis et al.³²

Mössbauer spectra were collected using the Synchrotron Mössbauer Source (SMS) of ID18³³ at the ESRF, where a $^{57}\text{FeBO}_3$ single-crystal monochromator was used to obtain pure nuclear reflection (approximately 6 neV FWHM) at the Mössbauer energy of 14.4 keV from a wide spectrum of synchrotron radiation. Kirkpatrick-Baez mirrors were used to focus the beam to a cross-section size of 14×18 [horizontal \times vertical] μm^2 . The velocity scales of all Mössbauer spectra were calibrated relative to a 25 μm thick α -Fe foil. Each SMS spectrum took approximately 30 min to collect and single line spectra were collected before and after each ferropentacis spectrum to monitor source linewidth. All spectra were fit using the MossA software package³⁴, using the full transmission integral with a normalized Lorentzian-squared source line-shape.

In situ high-pressure single-crystal diffraction experiments (SCXRD) were performed at ID15b at the ESRF. Monochromatic X-ray diffraction experiments were performed using X-rays with wavelength of 0.41107 Å. The X-ray beam was focused to approximately $10 \times 10 \mu\text{m}^2$ full-width at half maximum (FWHM) by a spherical mirror and a bent Si(111) Laue monochromator³⁵. Diffraction patterns were collected using a large area MAR555 flat panel detector. Before the experiment the detector-sample distance was calibrated with a Si standard using the procedure implemented in the program Dioptas³⁶.

Both a wide-scan and a stepped ω -scan were collected for each quenched crystal at 30 GPa. Wide-scans consisted of 40 s exposures during rotations of $\pm 20^\circ$ of the DAC. Stepped scans consisted of individual exposures of 1 s taken over 0.5° intervals in the range of $\pm 35^\circ$ rotation to constrain the ω angle of maximum intensity of each peak. Collected diffraction images were analyzed using the program CrysAlis PRO³⁷. A single crystal of an orthoenstatite ($\text{Mg}_{1.93}\text{Fe}_{0.06}$)($\text{Si}_{1.93}\text{Al}_{0.06}$) O_6 (*Pbca*, $a=8.8117(2)$, $b=5.18320(10)$, $c=18.2391(3)$ Å) was used to calibrate the instrument model of CrysAlis PRO³⁷ (sample-to-detector distance, the detector's origin, offsets of the goniometer angles, and rotation of the x-ray beam and the detector around the instrument axis). All structure solutions and refinements were performed with the JANA2006 crystallographic computing system³⁸.

5.3.3.3 Experiment 2

For the second experiment, two ($\text{Fe}_{0.25}\text{Mg}_{0.75}$)O crystals with dimensions of approximately $20 \times 20 \times 7 \mu\text{m}^3$ were placed inside the sample chamber of a DAC and then pressurized to 48(1) GPa (as determined from Raman shift of diamond anvil²⁹). Both crystals were laser heated from

both sides using the double-sided pulsed laser heating system of BGI³². One crystal (C04) was heated with laser pulses of 250 μs duration at 2 kHz frequency, reaching temperatures of 2800 K and 3100 K respectively on each side, at the peak of the pulses. The second crystal (C05) was heated with laser pulses of 11 μs duration at a frequency of 25kHz. The temperatures achieved at the peak of the pulses on each heating side was in this case 3100 K and 3400 K respectively. The heating run for both crystals lasted approximately 30 seconds.

The quenched materials were investigated at the Extreme Conditions Beamline (ECB) P02.2 of PETRA III (DESY, Hamburg)³⁹. Data were collected with a Perkin Elmer XRD1621 flat panel detector using X-rays with a wavelength of 0.2907 \AA and a size of $2.5 \times 2.5 \mu\text{m}^2$ (FWHM) at the focal position. After heating, the pressure increased to 53.5(5) GPa, as determined from X-ray diffraction data and the equation of state of Ne³⁰. A grid with 1 μm step in both vertical and horizontal directions of wide scans of 20 s exposure during ω rotation of $\pm 20^\circ$ was collected from each crystal. Each grid covered a total area of $23 \times 23 \mu\text{m}^2$, i.e. the whole crystal surface. The X-ray diffraction maps of the crystals were analyzed using the XDI software⁴⁰.

5.3.4 Results

Pulsed laser heating induced different chemical changes to the crystals observed at both 30 and 53.5 GPa: the decomposition of Fp25 with formation of a new phase or/and dissociation of Fe-rich and Mg-rich ferropericlase. Evidence for two scenarios for both experiments are described below separately in the following sections.

5.3.4.1 Formation of CaTi_2O_4 -structured hp-(Fe,Mg)₃O₄ phase

The performed X-ray diffraction experiments on the DAC heated at 30 GPa (Experiment 1) have revealed a different response of $(\text{Fe}_{0.25}\text{Mg}_{0.75})\text{O}$ crystals #1-3 to the high-temperature treatment. While crystal C03 have persisted upon CW laser heating experiment, diffraction patterns of crystals C01 and C02 featured appearance of new Bragg peaks, coexisting with peaks of starting material (Figure 5.3-1). The quality of the diffraction data collected on crystal C02 is better than on the crystal C01 therefore these data are used for further discussion. Based on single-crystal diffraction data, peaks belonging to the new phase were indexed in the orthorhombic unit cell with $a = 2.7419(1) \text{\AA}$, $b = 9.170(4) \text{\AA}$, $c = 9.313(3) \text{\AA}$, $V = 234.2(2) \text{\AA}^3$. The crystal structure was solved in the space group $Cmcm$ (N.63) and was found to be of CaTi_2O_4 - type (Table 5.3-III), isostructural to the high-pressure form of Fe_3O_4 ⁴¹. The unit cell volume of the observed phase is smaller than that reported for pure hp- Fe_3O_4 at 41 GPa (238.68\AA^3) and calculated from published EOS (Ref.⁴¹, 242.4\AA^3 at 30 GPa). This may indicate that Fe^{2+} was substituted by Mg^{2+} . According to the results of single-crystal diffraction data analysis, the structure of the phase possesses two crystallographically independent sites occupied by Fe and Mg (FeMg1 and FeMg2 with Wyckoff positions 4c and 8f, respectively) and three oxygen sites. The FeMg1 and FeMg2 sites are coordinated by six oxygen atoms with a formation of trigonal prisms and octahedra, respectively (Figure 5.3-2 (a) and (b)). Trigonal prisms share common triangular faces along the a axis while the octahedra share common

edges (Figure 5.3-2 (c)). The average *FeMg*-O bond distances are 2.06(1) and 1.932(6) Å for *FeMg1* and *FeMg2*, respectively (Table 5.3-IV). Refinement of the cation sites occupancies yielded $\text{Fe}_{0.46(7)}\text{Mg}_{0.54(7)}$ for *FeMg1* and $\text{Fe}_{0.68(7)}\text{Mg}_{0.32(7)}$ for *FeMg2*, resulting in the formula $(\text{Fe}_{1.82(21)}, \text{Mg}_{1.18(21)})\text{O}_4$, or $(\text{Fe}_{0.61(7)}, \text{Mg}_{0.39(7)})_3\text{O}_4$.

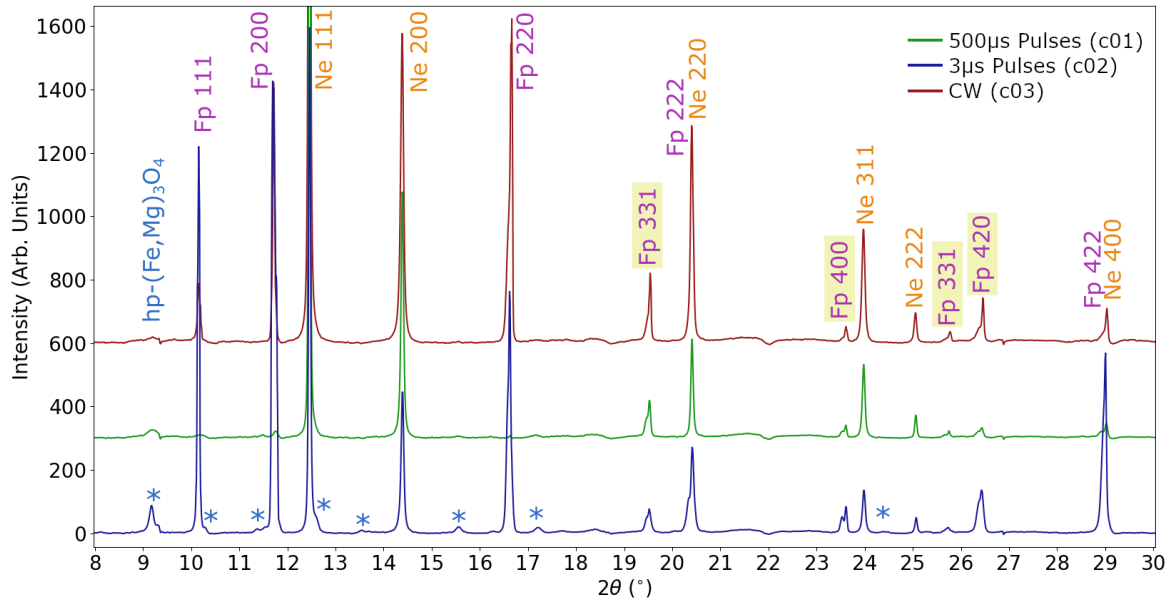


Figure 5.3-1. Representative powder diffraction patterns of crystals C01, C02 and C03 of Experiment 1 at 30 GPa after being laser-heated correspondingly by CW, short (3 μs), and long (500 μs) pulses. Diamond reflections have been masked. Reflections (331), (400), (331) and (420) of ferropericlasite (highlighted) are visibly broadened or split; asterisks mark the most prominent reflections of $\text{hp}-(\text{Fe},\text{Mg})_3\text{O}_4$ phase formed after laser heating.

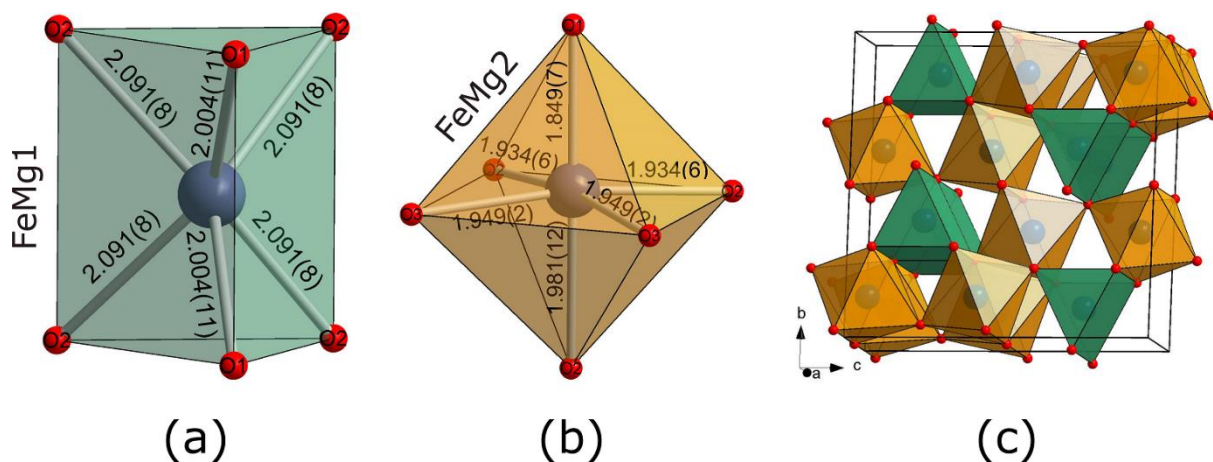


Figure 5.3-2. Coordination polyhedra of *FeMg1* (a) and *FeMg2* (b) crystallographic sites in the crystal structure of $(\text{Fe}_{1.82}, \text{Mg}_{1.18})\text{O}_4$. The bond distances are given in angstroms. The crystal structure of $(\text{Fe}_{1.82}, \text{Mg}_{1.18})\text{O}_4$ (c) is built of trigonal prisms and octahedra $(\text{FeMg})\text{O}_6$. Trigonal prisms share trigonal faces while the octahedra connect through common edges. Oxygen atoms are shown as red spheres.

Synchrotron Mössbauer spectra collected from each crystal at 30 GPa (Experiment 1) show minor changes before and after heating (Figure 5.3-3). Fitting of the spectra confirms the existence of an Fe^{3+} component (example of crystal C03 is shown in Figure 5.3-4), in agreement with the electron microprobe analysis, although the high overlap between the paramagnetic doublets increases the uncertainty of the fit. The Mössbauer absorption of all crystals can be

explained solely by the components of pure ferropericlase. More specifically, the spectra could be fit using two doublets with center shifts (CS) that correspond to iron Fe^{2+} and a doublet that with CS that corresponds to Fe^{3+} . This may be due to the small amount of the hp- $(\text{Fe,Mg})_3\text{O}_4$ phase and/or the too small domains distributed in the ferropericlase matrix. However, there seems to be a visible reduction in the Fe^{3+} component after heating, being more pronounced in crystals C01 and C03, that were laser heated using 500 μs pulses and CW operation, respectively (Figure 5.3-3, Figure 5.3-4).

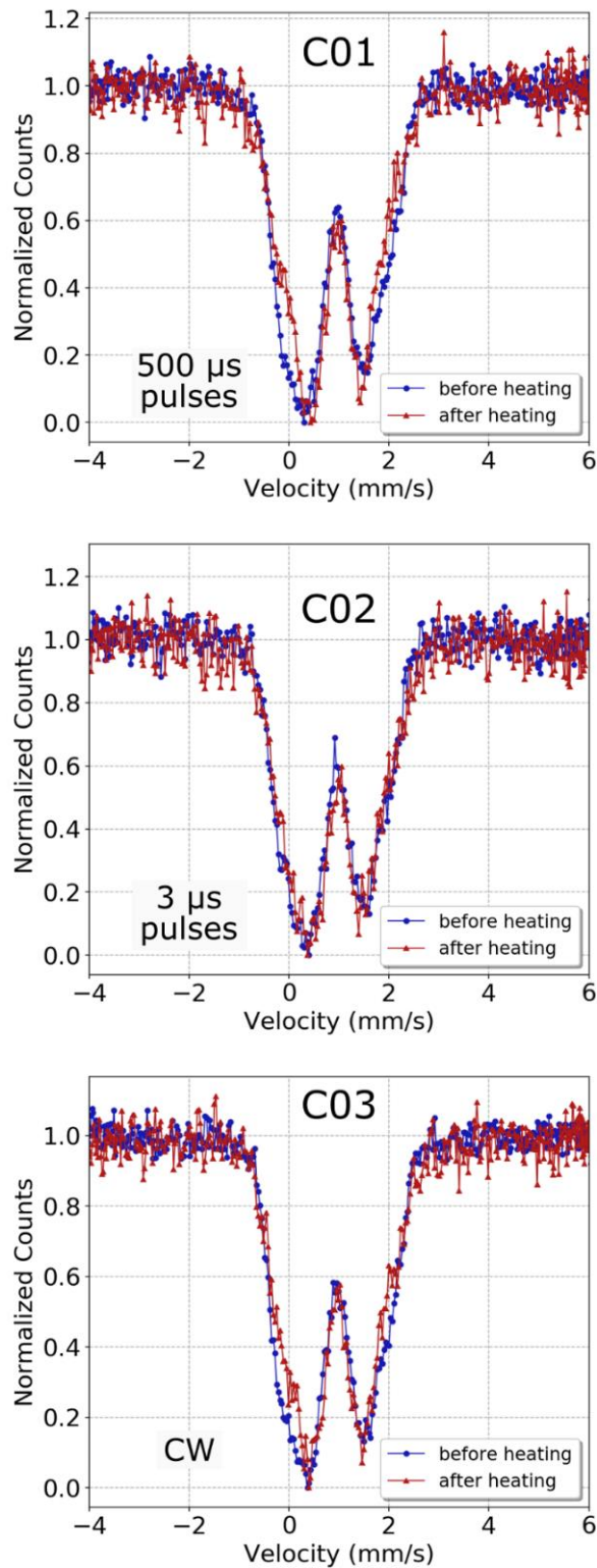


Figure 5.3-3. Normalized SMS spectra collected from each ferropericlasite crystal before and after heating at 30 GPa (Experiment 1). Blue circles correspond to absorption spectra collected before heating and red triangles correspond to absorption spectra collected from the quenched samples. Solid lines are guides for the eye. The spectra are normalized from 0 to 1 that correspond to the lowest count point (i.e. maximum absorption) and the average of the baseline, respectively.

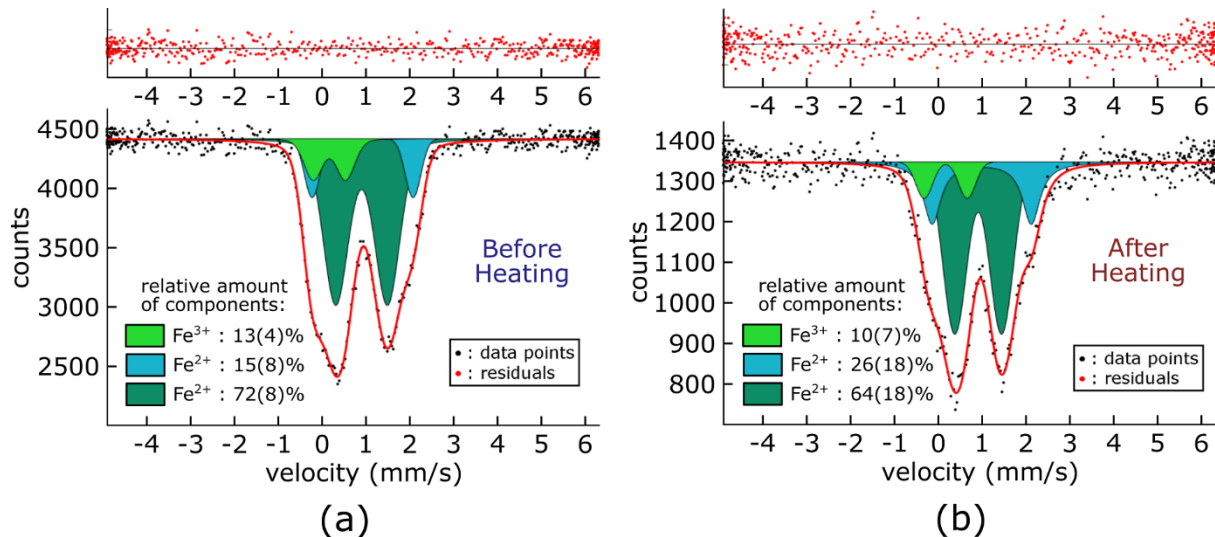


Figure 5.3-4. Fitted SMS spectra of ferropericlase crystal (C03 of Experiment 1) before heating (a) and after being heated continuously at 30 GPa (b). The red solid lines show the theoretical fit of the data points (black dots) and the residuals are indicated above the spectra (red dots). Dark green and cyan doublets correspond to Fe²⁺ components and light green doublet corresponds to the Fe³⁺ component. The fitting parameters are presented in detail in Table 5.3-II.

The same hp-(Fe,Mg)₃O₄ phase was also observed at 53.5 GPa alongside ferropericlase on both crystals that were pulsed laser heated. While the diffraction data quality was not sufficient for structural refinement, the lattice parameters of hp-(Fe,Mg)₃O₄ were unambiguously determined from powder Le Bail refinement with orthorhombic unit cell: $a = 2.660(2) \text{ \AA}$, $b = 8.892(4) \text{ \AA}$, $c = 9.094(3) \text{ \AA}$, $V = 215.14(16) \text{ \AA}^3$. The unit cell volume is smaller than that of pure hp-Fe₃O₄ at the same pressure⁴¹, as expected for a material that contains both iron and magnesium. The detailed X-ray diffraction mapping revealed the formation of hp-(Fe,Mg)₃O₄ in small amounts at the heated area of both crystals (Figure 5.3-5), confirming the decomposition of ferropericlase at both pressure points.

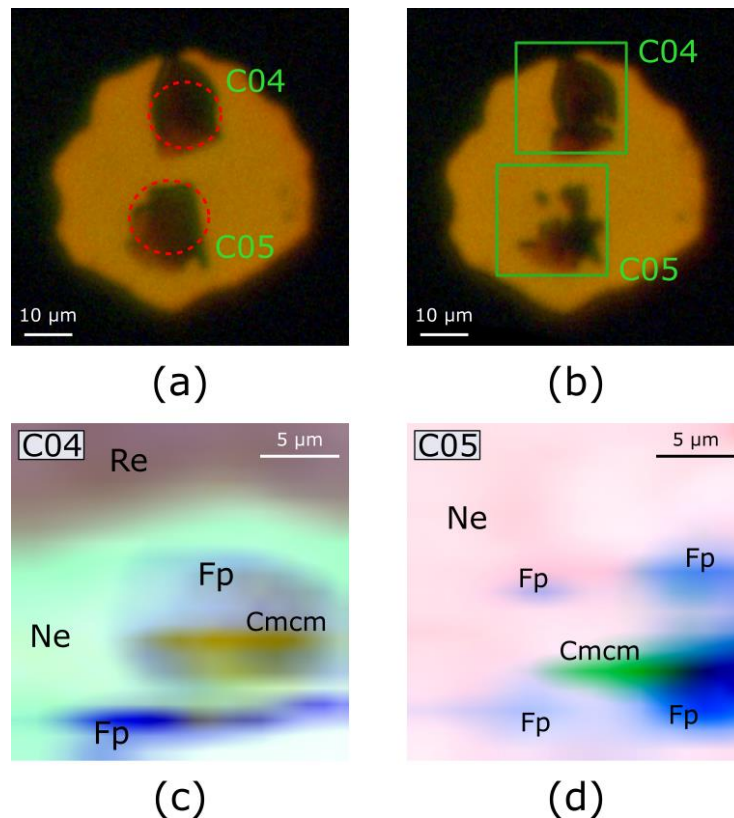


Figure 5.3-5. Optical microscope images of two crystals of (Fe,Mg)O (named C04, C05) at 53.5(5) GPa before (a) and after (b) pulsed laser heating and X-ray diffraction maps of the quenched products at the locations of C04 (c) and C05 (d) crystals. The approximate heated areas are depicted as red dashed circles in (a). The areas of diffraction mapping are shown as green rectangles in (b), for crystals C04 and C05 respectively. The color intensity is proportional to the intensity of the corresponding reflections used for mapping. Diffraction lines and color coding are as follows: for crystal C04 (c) - the (211) reflection of Re for the gray region, the (111) reflection of Ne for the light green region, the (220) reflection of ferropericlase (Fp) for the blue region, the sum of (006) and (023) reflections of the hp-(Fe,Mg)₃O₄ (Cmcm) for the orange region; for crystal C05 (d) - the sum of the (111) and (200) reflections of Ne for the pink region, the sum of (200) and (220) reflections of ferropericlase (Fp) for the blue region, the (023) reflection of the hp-(Fe,Mg)₃O₄ (Cmcm) for the dark green region.

5.3.4.2 Dissociation of (Fe,Mg)O

After laser heating, the broadening (at low 2θ angles) and splitting (at high 2θ) of Bragg peaks of ferropericlase was observed on quenched samples. The diffraction domains of ferropericlase have the same orientations but are characterized by slightly different d -spacings of the corresponding reflections, thus, suggesting the existence of two coherently grown phases with different lattice parameters.

In the case of Experiment 1 at 30 GPa, the effect was mainly observed on the crystal heated with short pulses of 3 μ s (C02) where the splitting of ferropericlase Bragg peaks is also clearly visible at the diffraction profile pattern (Figure 5.3-1). The separation of diffraction peaks was less prominent on the crystal that was heated with long pulses of 500 μ s duration (C01) and even less on the crystal heated with CW laser. In the latter case, the peaks were only broadened and there was no distinct splitting even for the high 2θ angles.

The splitting of ferropericlyase diffraction peaks is similarly detected on both pulse laser heated ferropericlyase crystals of Experiment 2 (at 53.5 GPa). Furthermore, analysis of the diffraction patterns using X-ray diffraction mapping revealed that the separation into two phases was more intense at the center and less pronounced at the edges of the heated area where the heating temperatures were lower (Figure 5.3-6).

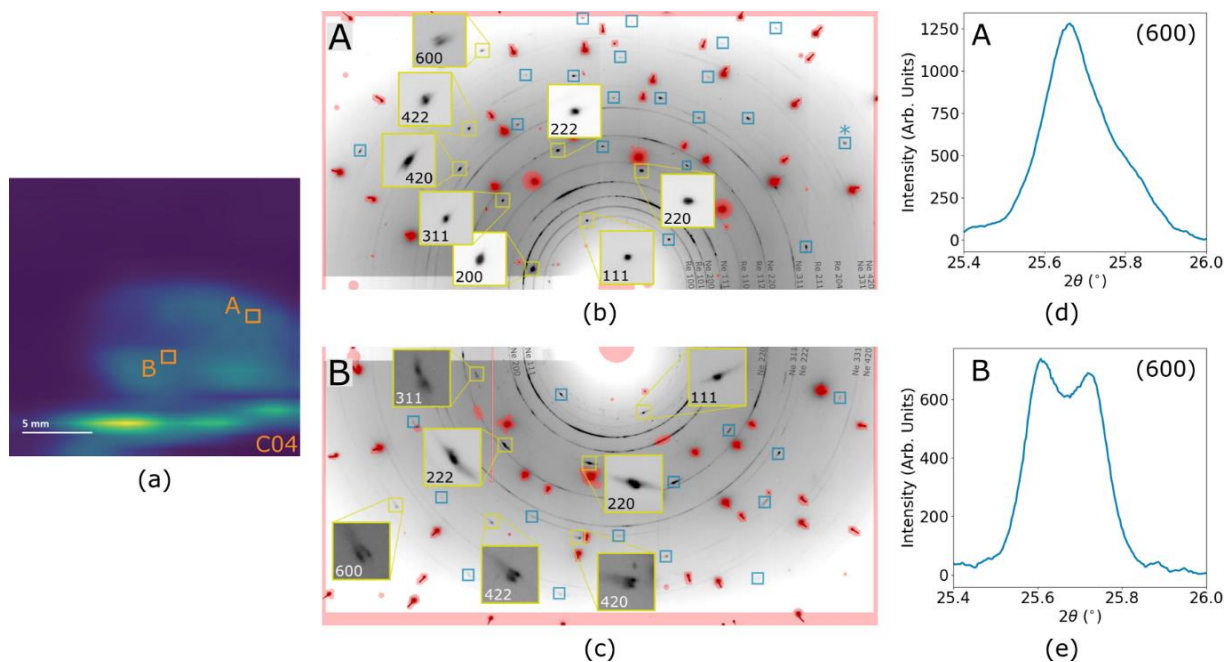


Figure 5.3-6. Splitting of Bragg reflections of ferropericlyase after pulse laser heating of C04 crystal in Experiment 2 (53.5 GPa). (a) X-ray diffraction map of the crystal showing the relative intensity of the (220) reflection of ferropericlyase at the selected positions at the edge (“A”) and close to the center (“B”) of the heated area; (b) and (c) show 2D diffraction patterns for positions A and B respectively with selected reflections magnified (yellow rectangles). Diamond reflections and inactive areas of the detector (including edges) are masked (red areas). The rest are ferropericlyase peaks marked by blue rectangles. Continuous diffraction rings are due to Ne. (d) and (e) Integrated diffraction profiles of Bragg (600) reflection (marked by blue asterisk on (b)) of ferropericlyase at positions A and B of the crystal respectively.

5.3.5 Discussion

5.3.5.1 Formation of hp-(Fe,Mg)₃O₄ by laser heating of ferropericlase.

Upon laser heating at pressures of about 30 GPa and 50 GPa, ferropericlase (Mg_{0.75}Fe_{0.25})O underwent chemical reaction resulting in the formation of a CaTi₂O₄-type structured post-spinel oxide (Fe_{0.61}, Mg_{0.39})₃O₄. The formation of the hp-(Mg,Fe)₃O₄ phase can be possibly the result of the decomposition of the solid solution of MgO-FeO with a partial release of the ferric component that was present (~11 wt%) in the starting material.

The iron end-member of Fe₃O₄ is known to transform into the same CaTi₂O₄-type of structure (hp-Fe₃O₄) upon compression and, reportedly, the formation of hp-Fe₃O₄ is facilitated by heating^{41,42}. Recent studies based on quenched samples produced in multi-anvil presses reported that the magnesium end-member MgFe₂O₄ (magnesioferrite) decomposes into MgFe₂O₅ and hematite upon compression without transforming into a high-pressure phase⁴³, but the solid solution with (Mg_{0.5},Fe_{0.5})Fe₂O₄ composition quenched from pressures of about 20 GPa and high temperatures transforms into an orthorhombic post-spinel phase with yet unknown structure⁴⁴.

The structure of high-pressure magnesioferrite solid solution was unambiguously determined to be of the CaTi₂O₄-type using single-crystal X-ray diffraction, revealing a structure with composition (Fe_{0.73},Mg_{0.27})(Fe_{0.64},Mg_{0.36})₂O₄ and Fe occupying both crystallographic positions.⁴⁵ The high-pressure polymorph is reportedly stable at pressures above 27 GPa and was synthesized by compression at room temperature, supporting that the pressure conditions of this study lie within the stability field of the high-pressure polymorph of the oxide.

Magnesioferrite-magnetite solid solutions with iron-rich compositions (Mg_{0.5}Fe_{2.5}O₄⁴⁶ and non-stoichiometric Mg_{1.30}Fe_{1.80}O₄⁴⁷) were found in magnesiowüstite inclusions of natural diamonds, formed around crystal defects of (Fe,Mg)O. The hypothesis that the magnesioferrite-magnetite solid solution is directly exsolved from (Fe,Mg)O is further supported by our results, thus, reinforcing the allegations of a deep, lower mantle origin of the diamond inclusions^{46,48}.

Considering that Fe³⁺-bearing ferropericlase can form in upper and lower mantle conditions⁴⁹, the decomposition of Fe³⁺-bearing ferropericlase into a high-iron composition post-spinel hp-(Fe,Mg)₃O₄ phase and the ability of complex oxides such as Fe₄O₅ and Fe₇O₉ to form solid solutions with their Mg-end-members^{44,50,51} have implications for the possible existence of complex Mg-Fe oxides in oxidized slabs and/or mantle and, thus, indicate that the phase composition of the lower mantle may not be limited to only the three major minerals of ferropericlase, bridgmanite and CaSi-perovskite.

5.3.5.2 Dissociation of (Fe,Mg)O into Fe-rich and Fe-poor components

The heating of ferropericlase single crystals at both pressure points presented in this study induce the broadening or splitting of the diffraction peaks due to the decomposition of Fp25 into two different phases with the same NaCl-type structure and two different compositions, an Fe-rich and an Mg-rich, respectively. The difference in the compositions results in slightly different lattice parameters and, thus, the separation of the diffraction peaks, the effect being more obvious at higher diffraction angles.

The splitting of the Bragg reflections in ferropericlase has been attributed to the rhombohedral distortion of the cubic lattice under non-hydrostatic conditions⁵². However, this cause is excluded since the transition to the rhombohedral $R\bar{3}m$ phase does not affect the (200) and (400) reflections of the cubic $Fm\bar{3}m$ phase. In the results presented here, both reflections appear either broadened or split (Figure 5.3-1).

The iron partitioning in ferropericlase upon heating has been experimentally reported at pressure conditions of the lowermost mantle¹². All the studies have been so far on powder samples and the results have been attributed to the effect of the Fe^{2+} spin transition⁵³, the Soret effect⁵⁴ or the non-ideal melting of the FeO-MgO system^{18,55}. Some studies support the stability of different ferropericlase compositions upon heating and no inhomogeneity is reported for hot or quenched samples^{9,16,56}. The lack of inhomogeneity after heating has been attributed to short heating duration¹⁴, suggesting the influence of chemical kinetics as a possible reason for the discrepancy. Another LHDAC study on (Fe,Mg)O resulted in a homogeneous quenched sample after 60 minutes of heating but at a range of temperatures of 1600 – 1800 K, relatively lower than the other studies in comparison.⁵⁴ Another reason for this discrepancy could be the overlap of the diffraction peaks of the B2 phase of NaCl used as pressure medium with the strong peaks of ferropericlase that could cover a possible change in the latter, the lack of resolution of the diffraction patterns in the small diffraction angles that were taken into consideration, or, in some cases, the low heating temperature of the annealing process.

None of the causes proposed for powder data can be applied here since the formation of two phases on a single crystal sample takes place even at a pressure well below the spin crossover in Fe¹⁶, and after heating at temperatures below melting (for the samples heated at 30 GPa)^{18,55}. The two different phases of ferropericlase have a small difference in the lattice parameters but the same orientation, as seen in the diffraction images of the quenched samples (an example presented in Figure 5.3-6). The coherent intergrowth of phases with different composition is commonly observed in minerals forming lamellae due to exsolution⁵⁷ and is known to be induced by heating in single crystal studies⁵⁸. The results of this study at 30 GPa (Experiment 1) provide strong evidence that there is a range of temperatures above 1800 K where the miscibility gap of $(Fe_{0.25},Mg_{0.75})O$ exists, as it has been also suggested for higher pressures⁵⁹. For the samples heated at 53.5 GPa (Experiment 2) close to solidus temperatures it is hard to draw an unambiguous conclusion if melting was responsible or not

for the decomposition.

Lately, the model of a homogeneous lower mantle with pyrolytic composition has been under discussion^{47,60}. Our results provide further arguments that the chemical composition of the lower mantle is more complex than initially thought and that the compositional inhomogeneity is not only a characteristic of the lowermost part but includes depths as shallow as below the transition zone.

5.3.5.3 Effect of pulsed laser heating

Ferropericlase is a majorly investigated oxide due to its importance in the Earth interior mineralogy. However, its decomposition into a high-pressure magnesioferrite solid solution has not been reported so far, and the decomposition into of Fe- and Mg-rich components has also been disputed.

The formation of hp-(Mg,Fe)₃O₄ is obviously limited in amount in comparison to the bulk of (Mg,Fe)O, and for the samples laser heated at 53.5 GPa (Experiment 2), detection of the new phase was possible by very detailed high-intensity X-ray beam mapping of the entire sample. Therefore, regular analysis of only powder X-ray diffraction data might not be enough for identification of the phase.

Our observations indicate that the type of laser heating may also affect the results. As seen in Figure 5.3-1 and Table 5.3-I, for similar temperature ranges and heating duration applied to the crystals at the same pressure, the crystals that were pulsed (and especially the one heated with short laser pulses) had a significantly higher amount of hp-(Mg,Fe)₃O₄, and demonstrated much clearer signs of dissociation of Fp25 on iron- and magnesium-rich phases. Thus, our current results qualitatively agree with previous report²² suggesting that pulsed laser-heating not only does not prevent chemical reactions, but probably accelerates them.

5.3.6 Tables

Table 5.3-I. Details of laser heating on three different (Fe_{0.25}Mg_{0.75})O crystals at 30.0(5) GPa.

Crystal	Heating method	Heating time	Temperature (Upstream)	Temperature (Downstream)
C01	Pulsed, 1 kHz / 500 μ s	25 min	1800 – 2100 K	1550 – 1650 K
C02	Pulsed, 25 kHz / 3 μ s	12 min	1800 - 2100 K	1650 – 1950 K
C03	Continuous wave	11 min	1900 – 2300 K	1700 – 1800 K

Table 5.3-II. Fitted parameters of center shift (CS) and quadrupole splitting (QS) of ferropericlase crystal C03 of Experiment 1 at 30 GPa before heating and after being heated continuously.

	Fe²⁺ doublet <i>(dark green in Figure 5.3-4)</i>		Fe²⁺ doublet <i>(cyan in Figure 5.3-4)</i>		Fe³⁺ doublet <i>(light green in Figure 5.3-4)</i>	
	CS (mm/s)	QS (mm/s)	CS (mm/s)	QS (mm/s)	CS (mm/s)	QS (mm/s)
Before heating	0.91(1)	1.18(5)	0.93(11)	2.30(22)	0.17(20)	0.73(29)
After CW heating	0.92(2)	1.06(9)	1.00(6)	2.26(14)	0.17(15)	0.98(18)

Table 5.3-III. Crystallographic data and refinement parameters for crystal C02 at 30.0(5) GPa.

Crystal Data	
Composition	Mg _{4.71} Fe _{7.29} O ₁₆
Space group	<i>Cmcm</i>
<i>a</i> , Å	2.742(1)
<i>b</i> , Å	9.170(4)
<i>c</i> , Å	9.313(3)
Volume, Å ³	234.2(2)
<i>Z</i>	1
Data Collection	
Wavelength, Å	0.41107
Max. θ°	20.68
Index ranges	-3 ≤ <i>h</i> ≤ 3 -12 ≤ <i>k</i> ≤ 9 -12 ≤ <i>l</i> ≤ 12
No. Meas. Refl.	247
No. Unique Refl.	135
No. Obs. Refl. (<i>I</i> > 3σ(<i>I</i>))	107
Refinement	
No. of variables	14
<i>R</i> _{int}	0.0575
<i>R</i> _σ	0.0709
<i>R</i> ₁ , <i>I</i> > 3σ(<i>I</i>)	0.0766
<i>R</i> ₁ , all data	0.0915
w <i>R</i> ₂ , <i>I</i> > 3σ(<i>I</i>)	0.2018
w <i>R</i> ₂ , all data	0.2279
Goof	1.134

Table 5.3-IV. Bond distances and polyhedral parameters for hp-(Fe,Mg)₃O₄ at 30.0(5) GPa.

FeMg1O₆ trigonal prism		FeMg2O₆ octahedra			
<i>FeMg1-O1</i>	2.004(11) Å x2	<i>FeMg2-O1</i>	1.849(7) Å	<i>FeMg1- FeMg1</i>	2.7419(10) Å
<i>FeMg1-O2</i>	2.091(9) Å x4	<i>FeMg2-O2</i>	1.933(7) Å x2	<i>FeMg1- FeMg2</i>	2.822(5) Å
		<i>FeMg2-O3</i>	1.9496(17) Å x2	<i>FeMg2- FeMg2</i>	2.7419(10) Å
		<i>FeMg2-O2</i>	1.981(12) Å	<i>FeMg2- FeMg2</i>	2.772(5) Å
				<i>FeMg2- FeMg2</i>	2.901(4) Å
< <i>FeMg1-O</i> >	2.06(1) Å	< <i>FeMg2-O</i> >	1.932(6) Å		
<i>Volume</i>	8.2718 Å ³	<i>Volume</i>	9.5666 Å ³		

5.3.7 Refereces

1. Kaminsky, F. V. *The Earth's Lower Mantle*. (Springer International Publishing, 2017). doi:10.1007/978-3-319-55684-0
2. Lee, K. K. M. *et al.* Equations of state of the high-pressure phases of a natural peridotite and implications for the Earth's lower mantle. *Earth Planet. Sci. Lett.* **223**, 381–393 (2004).
3. Tschauner, O. *et al.* Discovery of bridgmanite, the most abundant mineral in Earth, in a shocked meteorite. *Science (80-.)*. **346**, 1100–1102 (2014).
4. Xu, W., Lithgow-Bertelloni, C., Stixrude, L. & Ritsema, J. The effect of bulk composition and temperature on mantle seismic structure. *Earth Planet. Sci. Lett.* **275**, 70–79 (2008).
5. Irifune, T. Absence of an aluminous phase in the upper part of the Earth's lower mantle. *Nature* **370**, 131–133 (1994).
6. Wood, B. J. Phase transformations and partitioning relations in peridotite under lower mantle conditions. *Earth Planet. Sci. Lett.* **174**, 341–354 (2000).
7. Mao, H., Guoyin, S. & Hemley, R. J. Multivariable Dependence of Fe-Mg Partitioning in the Lower Mantle. *Science (80-.)*. **278**, 2098–2100 (1997).
8. Katsura, T. & Ito, E. Determination of Fe-Mg partitioning between perovskite and magnesiowüstite. *Geophys. Res. Lett.* **23**, 2005–2008 (1996).
9. Lin, J.-F. *et al.* Stability of magnesiowüstite in Earth's lower mantle. *Proc. Natl. Acad. Sci.* **100**, 4405–4408 (2003).
10. Murakami, M., Hirose, K., Kawamura, K., Sata, N. & Ohishi, Y. Post-Perovskite Phase Transition in MgSiO₃. *Science (80-.)*. **304**, 855–858 (2004).
11. Badro, J. *et al.* Iron Partitioning in Earth's Mantle: Toward a Deep Lower Mantle Discontinuity. *Science (80-.)*. **300**, 789–791 (2003).
12. Dubrovinsky, L. S. Stability of Ferropericlase in the Lower Mantle. *Science (80-.)*. **289**, 430–432 (2000).
13. Dubrovinsky, L., Dubrovinskaia, N., Annersten, H., Hålenius, E. & Harryson, H. Stability of (Mg_{0.5}Fe_{0.5})O and (Mg_{0.8}Fe_{0.2})O magnesiowüstites in the lower mantle. *Eur. J. Mineral.* **13**, 857–861 (2001).
14. Kondo, T., Ohtani, E., Hirao, N., Yagi, T. & Kikegawa, T. Phase transitions of (Mg,Fe)O at megabar pressures. *Phys. Earth Planet. Inter.* **143–144**, 201–213 (2004).
15. Lin, J.-F. *et al.* Electrical conductivity of the lower-mantle ferropericlase across the electronic spin transition. *Geophys. Res. Lett.* **34**, 2–5 (2007).
16. Fei, Y. *et al.* Spin transition and equations of state of (Mg, Fe)O solid solutions. *Geophys.*

- Res. Lett.* **34**, L17307 (2007).
17. Kaminsky, F. Mineralogy of the lower mantle: A review of ‘super-deep’ mineral inclusions in diamond. *Earth-Science Rev.* **110**, 127–147 (2012).
 18. Deng, J. & Lee, K. K. M. Viscosity jump in the lower mantle inferred from melting curves of ferropericlase. *Nat. Commun.* **8**, 1997 (2017).
 19. Karlov, N. V, Kirichenko, N. A. & Luk’yanchuk, B. S. *Laser Thermochemistry: Fundamentals and Applications*. (Cambridge International Science Pub., 2000).
 20. Goncharov, A. F. *et al.* Laser heating in diamond anvil cells: developments in pulsed and continuous techniques. *J. Synchrotron Radiat.* **16**, 769–772 (2009).
 21. Goncharov, A. F. *et al.* X-ray diffraction in the pulsed laser heated diamond anvil cell. *Rev. Sci. Instrum.* **81**, 113902 (2010).
 22. Aprilis, G. *et al.* Comparative study of the influence of pulsed and continuous wave laser heating on the mobilization of carbon and its chemical reaction with iron in a diamond anvil cell. *J. Appl. Phys.* **125**, 095901 (2019).
 23. Katsura, T., Yoneda, A., Yamazaki, D., Yoshino, T. & Ito, E. Adiabatic temperature profile in the mantle. *Phys. Earth Planet. Inter.* **183**, 212–218 (2010).
 24. Trubitsyn, V. P. & Trubitsyna, A. P. Effects of compressibility in the mantle convection Equations. *Izv. Phys. Solid Earth* **51**, 801–813 (2015).
 25. Longo, M., McCammon, C. A. & Jacobsen, S. D. Microanalysis of the iron oxidation state in (Mg,Fe)O and application to the study of microscale processes. *Contrib. to Mineral. Petrol.* **162**, 1249–1257 (2011).
 26. Kantor, I. *et al.* BX90: A new diamond anvil cell design for X-ray diffraction and optical measurements. *Rev. Sci. Instrum.* **83**, 125102 (2012).
 27. Boehler, R. & De Hantsetters, K. New anvil designs in diamond-cells. *High Press. Res.* **24**, 391–396 (2004).
 28. Kurnosov, A. *et al.* A novel gas-loading system for mechanically closing of various types of diamond anvil cells. *Rev. Sci. Instrum.* **79**, 045110 (2008).
 29. Akahama, Y. & Kawamura, H. Pressure calibration of diamond anvil Raman gauge to 310GPa. *J. Appl. Phys.* **100**, 043516 (2006).
 30. Dewaele, A., Datchi, F., Loubeyre, P. & Mezouar, M. High pressure–high temperature equations of state of neon and diamond. *Phys. Rev. B* **77**, 094106 (2008).
 31. Kuppenko, I. *et al.* Portable double-sided laser-heating system for Mössbauer spectroscopy and X-ray diffraction experiments at synchrotron facilities with diamond anvil cells. *Rev. Sci. Instrum.* **83**, 124501 (2012).

32. Aprilis, G. *et al.* Portable double-sided pulsed laser heating system for time-resolved geoscience and materials science applications. *Rev. Sci. Instrum.* **88**, 084501 (2017).
33. Potapkin, V. *et al.* The ^{57}Fe Synchrotron Mössbauer Source at the ESRF. *J. Synchrotron Radiat.* **19**, 559–569 (2012).
34. Prescher, C., McCammon, C. & Dubrovinsky, L. MossA : a program for analyzing energy-domain Mössbauer spectra from conventional and synchrotron sources. *J. Appl. Crystallogr.* **45**, 329–331 (2012).
35. Merlini, M. & Hanfland, M. Single-crystal diffraction at megabar conditions by synchrotron radiation. *High Press. Res.* **33**, 511–522 (2013).
36. Prescher, C. & Prakapenka, V. B. DIOPTAS: A program for reduction of two-dimensional X-ray diffraction data and data exploration. *High Press. Res.* **35**, 223–230 (2015).
37. Agilent. CrysAlis PRO. (2014).
38. Petříček, V., Dušek, M. & Palatinus, L. Crystallographic Computing System JANA2006: General features. *Zeitschrift für Krist. - Cryst. Mater.* **229**, (2014).
39. Liermann, H. P. *et al.* The Extreme Conditions Beamline P02.2 and the Extreme Conditions Science Infrastructure at PETRA III. *J. Synchrotron Radiat.* **22**, 908–924 (2015).
40. Hrubciak, R., Smith, J. S. & Shen, G. Multimode scanning X-ray diffraction microscopy for diamond anvil cell experiments. *Rev. Sci. Instrum.* **90**, 025109 (2019).
41. Dubrovinsky, L. S. *et al.* The structure of the metallic high-pressure Fe_3O_4 polymorph: experimental and theoretical study. *J. Phys. Condens. Matter* **15**, 7697–7706 (2003).
42. Haavik, C., Stølen, S., Fjellvåg, H., Hanfland, M. & Häusermann, D. Equation of state of magnetite and its high-pressure modification: Thermodynamics of the Fe-O system at high pressure. *Am. Mineral.* **85**, 514–523 (2000).
43. Uenver-Thiele, L., Woodland, A. B., Ballaran, T. B., Miyajima, N. & Frost, D. J. Phase relations of MgFe_2O_4 at conditions of the deep upper mantle and transition zone. *Am. Mineral.* **102**, 632–642 (2017).
44. Uenver-Thiele, L., Woodland, A. B., Ballaran, T. B., Miyajima, N. & Frost, D. J. Phase relations of Fe-Mg spinels including new high-pressure post-spinel phases and implications for natural samples. *Am. Mineral.* **102**, 2054–2064 (2017).
45. Greenberg, E. *et al.* High-pressure magnetic, electronic, and structural properties of MFe_2O_4 (M = Mg,Zn,Fe) ferric spinels. *Phys. Rev. B* **95**, 195150 (2017).
46. Wirth, R., Dobrzhinetskaya, L., Harte, B., Schreiber, A. & Green, H. W. High-Fe (Mg, Fe)O inclusion in diamond apparently from the lowermost mantle. *Earth Planet. Sci. Lett.* **404**, 365–375 (2014).

47. Kaminsky, F. V. & Lin, J.-F. Iron partitioning in natural lower-mantle minerals: Toward a chemically heterogeneous lower mantle. *Am. Mineral.* **102**, 824–832 (2017).
48. Anzolini, C. *et al.* Depth of diamond formation obtained from single periclase inclusions. *Geology* **47**, 219–222 (2019).
49. Bataleva, Palyanov, Borzdov & Bayukov. Processes and Conditions of the Origin for Fe³⁺-Bearing Magnesiowüstite under Lithospheric Mantle Pressures and Temperatures. *Minerals* **9**, 474 (2019).
50. Boffa Ballaran, T., Uenver-Thiele, L. & Woodland, A. B. Complete substitution of Fe²⁺ by Mg in Fe₄O₅: The crystal structure of the Mg₂Fe₂O₅ end-member. *Am. Mineral.* **100**, 628–632 (2015).
51. Ishii, T., Uenver-Thiele, L., Woodland, A. B., Alig, E. & Ballaran, T. B. Synthesis and crystal structure of Mg-bearing Fe₉O₁₁: New insight in the complexity of Fe-Mg oxides at conditions of the deep upper mantle. *Am. Mineral.* **103**, 1873–1876 (2018).
52. Kantor, I. *et al.* Pressure-induced phase transition in Mg_{0.8}Fe_{0.2}O ferropericlase. *Phys. Chem. Miner.* **33**, 35–44 (2006).
53. Dubrovinsky, L. *et al.* Decomposition of ferropericlase (Mg_{0.80}Fe_{0.20})O at high pressures and temperatures. *J. Alloys Compd.* **390**, 41–45 (2005).
54. Sinmyo, R. & Hirose, K. The Soret diffusion in laser-heated diamond-anvil cell. *Phys. Earth Planet. Inter.* **180**, 172–178 (2010).
55. Fu, S. *et al.* Melting behavior of the lower-mantle ferropericlase across the spin crossover: Implication for the ultra-low velocity zones at the lowermost mantle. *Earth Planet. Sci. Lett.* **503**, 1–9 (2018).
56. Lin, J.-F. *et al.* Spin Transition Zone in Earth's Lower Mantle. *Science (80-.)*. **317**, 1740–1743 (2007).
57. Zhang, R. Y. & Liou, J. G. Exsolution Lamellae in Minerals from Ultrahigh-Pressure Rocks. *Int. Geol. Rev.* **41**, 981–993 (1999).
58. Pakhomova, A. S. *et al.* High-temperature induced dehydration, phase transition and exsolution in amicitite: A single-crystal X-ray study. *Microporous Mesoporous Mater.* **182**, 207–219 (2013).
59. Martirosyan, N. S. *et al.* The Mg-carbonate–Fe interaction: Implication for the fate of subducted carbonates and formation of diamond in the lower mantle. *Geosci. Front.* **10**, 1449–1458 (2019).
60. Kaminsky, F. V., Wirth, R. & Schreiber, A. A microinclusion of lower-mantle rock and other minerals and nitrogen lower-mantle inclusions in a diamond. *Can. Mineral.* **53**, 83–104 (2015).

5.4 Single-crystal diffractometer coupled with double-sided laser heating system at the Extreme Conditions Beamline P02.2 at PETRAIII

Elena Bykova^{1,*}, [Georgios Aprilis](#)², Maxim Bykov³, Konstantin Glazyrin¹, Mario Wendt¹, Sergej Wenz¹, Hanns-Peter Liermann¹, Jan Torben Roeh⁴, Anita Ehnes⁴, Natalia Dubrovinskaia² and Leonid Dubrovinsky³

¹ Photon Science, Deutsches Elektronen-Synchrotron (DESY), Notkestrasse 85, Hamburg, 22607, Germany

² Material Physics and Technology at Extreme Conditions, Laboratory of Crystallography, University of Bayreuth, Universitaetsstrasse 30, Bayreuth, 95440, Germany

³ Bavarian Research Institute of Experimental Geochemistry and Geophysics, Universität Bayreuth, Universitaetsstrasse 30, Bayreuth, 95440, Germany

⁴ Sample Environment and Extreme Conditions Science Infrastructure (ECSI), Deutsches Elektronen-Synchrotron (DESY), Notkestrasse 85, Hamburg, 22607, Germany

* Correspondent author (e-mail: elena.bykova@desy.de)

Review of Scientific Instruments, **90**(7), 073907 (2019)

5.4.1 Abstract

Combination of *in situ* laser heating with single-crystal X-ray diffraction (SCXRD) in diamond anvil cells (DACs) provides a tool to study crystal structures and/or chemistry of materials at simultaneous high pressures and high temperatures. Here we describe the first dedicated single-crystal X-ray diffractometer coupled with double-sided laser heating (dsLH) system. The SCXRD/ dsLH setup was developed for the P02.2 Extreme Conditions Beamline (ECB) at PETRA III and became available for general users in 2017. It enables the collection of reliable SCXRD data at simultaneous high pressure and high temperature. We demonstrate the performance of the setup on example of studies of iron and chromium nitrides.

5.4.2 Introduction

Diamond anvil cell (DAC) technique provides a tool to generate pressures, which can exceed those in the center of the Earth (360 GPa), and to collect *in situ* spectroscopy (Raman, Mössbauer, X-ray absorption, etc.) and/or X-ray diffraction data. However, the analysis and interpretation of the data obtained at multimegabar pressures is extremely difficult, especially due to multiple phase transitions and/or chemical reactions, formation of unusual crystal structures and/or chemical compounds unknown at ambient conditions.

Single-crystal X-ray diffraction in DACs opens a way to determine not only the crystal structure of a material, but also to refine its chemical composition for even very complex multi-phase and/or multigrain samples. Due to significant progress in the field of high-pressure technology,

since a decade SCXRD became available at pressures above ~ 15 GPa. Novel gas-loading systems¹⁻⁶ allow one to use soft pressure transmitting media (helium or neon) in DACs, thus preserving single crystals to megabar pressures. New types of diamond anvils and DACs with wide X-ray opening up to 90 degrees⁷ enlarge the coverage of the reciprocal space and thus improve the data redundancy which leads to the higher quality of the final structural models.

Heating is an important parameter for high-pressure experiments, especially for studies dedicated to modelling of processes in deep Earth's interior. Double-sided laser-heating (dsLH) systems are widely used at synchrotron facilities⁸⁻¹¹. However, until recently, all of them were stationary and did not allow DAC rotation during simultaneous heating, thus making *in situ* high-pressure high-temperature SCXRD impossible. A portable laser-heating system, first developed in Bayerisches Geoinstitut (BGI)¹², can be mounted directly on a goniometer stage and rotated along with the DAC providing the opportunity to collect SCXRD simultaneously during laser heating.

Here we describe the first dedicated SCXRD/dsLH setup consisting of a single-crystal X-ray diffractometer coupled with double-sided laser heating system. The setup was developed for beamline P02.2 the Extreme Conditions Beamline (ECB) at PETRA III and became available for the general users in 2017.

5.4.3 Setup overview

The SCXRD/dsLH setup is mounted on the General Purpose experiment of beamline P02.2¹³ (Figure 5.4-1). The major components of the setup (from the top to the bottom) are listed below and shown in Figure 5.4-2:

- *Sample holder* equipped with water cooling;
- *Two portable universal laser heating heads* (UniHeads, PrecitecTM) equipped with 4 mm-thick glassy carbon mirrors; one UniHead is mounted horizontally (the upstream h-UniHead), the other one – vertically (the downstream v-UniHead);
- *Multi-axis positioning systems* realized through combination of translation positioning stages:
 - motorized Newport X- and Y-stages and motorized Huber Z-stage for DAC alignment;
 - motorized Huber XY- and Huber Z-stages for upstream h-UniHead;
 - manual Standa Z-stage for downstream v-UniHead;
- *Stabilization elements* (aluminum frame with steel pillars and supporting corner elements, clamp for h-Unihead, counterbalance for the dsLH system, etc.) to decrease vibrations and improve the stability of heating during rotation;

- *4-axis positioning system* for alignment of dsLH system composed of following translation stages:
 - Huber motorized XY-stage;
 - Rotational positioning device, 2-circle (ω - 2θ) Huber goniometer;
 - Heavy-load Huber motorized Z-stage;
- *Heavy-load Huber motorized XY-stages* for the alignment of the ω rotation axis to the focus of the X-ray beam;
- *Aluminum base plate* (50 mm thick) integrating the entire setup, including an X-ray diode, and a beamstop;
- *Additional components of the setup*, which are not shown in Figure 5.4-2:
 - *Two SPI RedPower R4 fiber lasers* (50 W, excitation wavelength of 1070 nm);
 - *Two Ocean Optics QE65000 spectrometers* for collection of the thermal radiation;
 - *(Optional): 2θ -movable detector arm* mounted on ω -stage (for Lambda or Pilatus detectors).

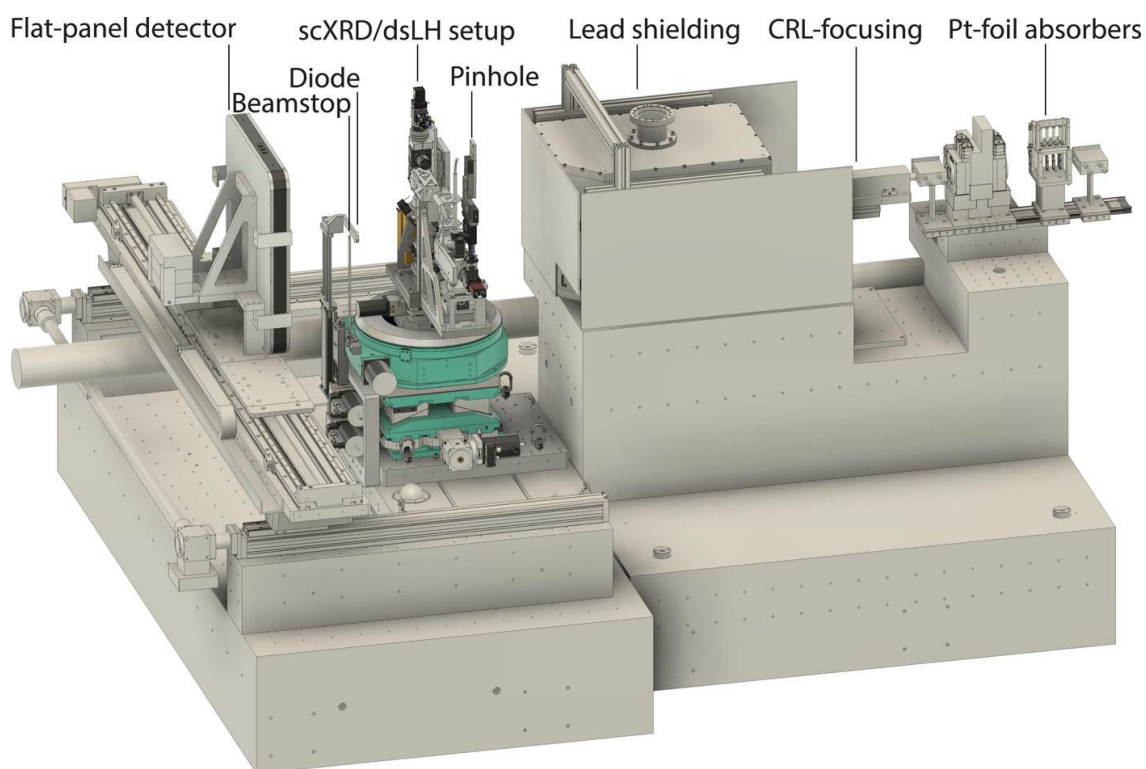


Figure 5.4-1. Overview of the SCXRD/dsLH setup mounted on the General Purpose experiment at PETRAIII beamline P02.2 (ECB). The primary X-ray beam passes through the set of Compound Refractive Lenses (CRLs) focusing the beam down to $\sim 5 \times 5 \mu\text{m}^2$. Lead shielding covers X-ray optics in order to reduce parasitic scattering. During rotation of the SCXRD/dsLH setup as a whole, diffraction data are collected using a Perkin Elmer XRD1621 flat panel detector. To allow rotation, the X-ray pinhole is located at a distance of about 80 mm from the sample. The intensity monitor (diode) and the beamstop are attached to the mounting plate of the SCXRD/dsLH setup. Pt-foil absorbers can be optionally used to attenuate the primary X-ray beam intensity.

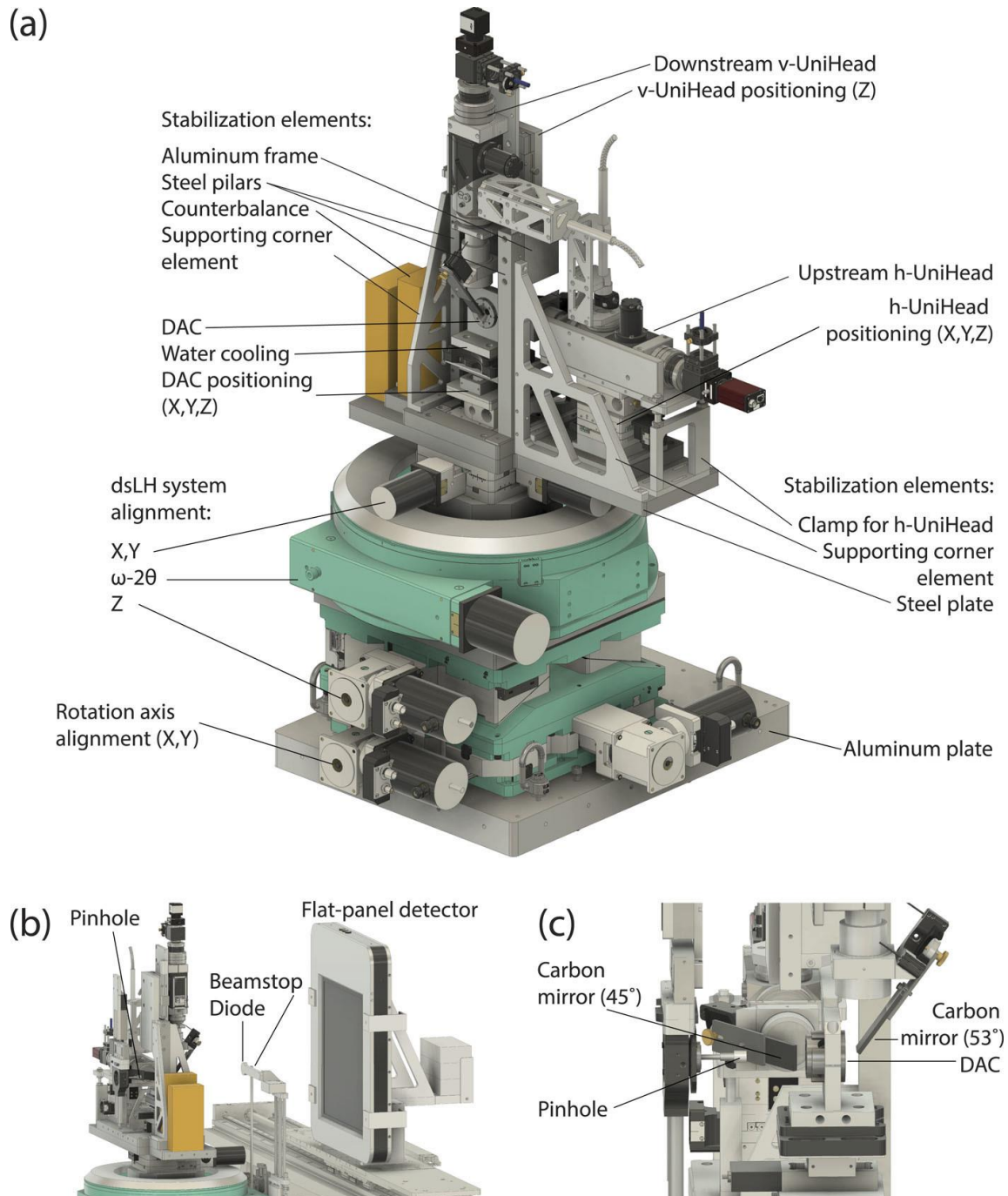


Figure 5.4-2. ScXRD/dsLH setup: view from the downstream side (a); from the upstream side (b) and perpendicular to the X-ray beam (c).

The scheme of the optical components in the dsLH system is adopted from Kuppenko et al.¹². It is shown in detail in Figure 5.4-3. Two UniHeads¹² are used to focus the laser beams on the sample from the both sides (Figure 5.4-2, Figure 5.4-3). Each of them includes a compact set of optical components. The 90° arrangement of the two UniHeads serves to minimize shadows cast on the detector by various components of the system, to reduce possible vibrations of the optical components, and to achieve the largest possible ω rotation range. The glassy carbon mirrors are mounted at an angle to the axes of the UniHeads (Figure 5.4-2 (c), Figure 5.4-3) and serve as a reflector of the laser light in order to direct it to the sample. The upstream

mirror is mounted precisely at 45°, which aligns the laser beam parallel (coaxial) to the X-rays that penetrate the mirror. The downstream mirror is placed at a larger angle, between 50 and 55°, to avoid primary X-ray beam interaction and prevent strong unwanted diffuse scattering. The both mirrors' holders are connected to Newport piezo mounts for the fine tuning of the final laser beam position.

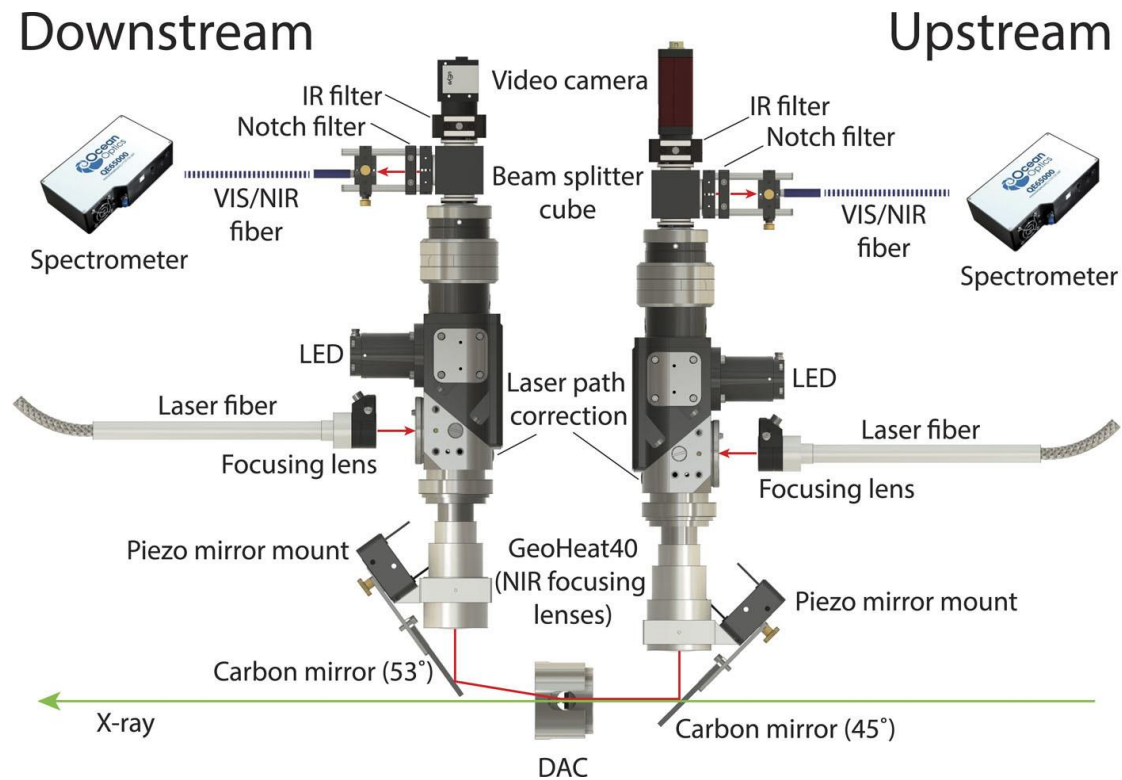


Figure 5.4-3. Schematic diagram of the optical components of the dsLH system (based on the system described in Ref. ¹²). The UniHeads are aligned mutually perpendicularly.

The SCXRD/dsLH setup contains all the components required for data collection and laser heating in one module. It can be mounted/unmounted on the General Purpose experiment at P02.2 (Figure 5.4-1) within a few hours.

5.4.4 Setup operation

5.4.4.1 Preparation of the beamline.

In comparison with the standard sample stack at the General Purpose experiment, the SCXRD/dsLH setup demands additional space between a sample and the lead shielding (which encapsulates X-ray optics) to allow its rotation (Figure 5.4-1). This requires a longer X-ray focusing distance. The focusing distance of 1477 mm is achieved by using 91 Compound Refractive Lenses (CRLs) at an X-ray energy of proximately 42.7 keV (Figure 5.4-1). The position of the X-ray focus is modified by moving either CRLs or the heavy-load Huber motorized X-stage along the beam direction. A standard tungsten round edge is used to estimate the focus size (typically $\sim 5 \times 5 \mu\text{m}^2$). A thin tungsten cross hair is used to calibrate the beam position and bring the rotation ω -axis to the beam by using the heavy-load Huber motorized Y-, Z- stages.

The sample-to-detector distance, coordinates of the beam center, tilt angle and tilt plane rotation angle of the detector images are calibrated using CeO₂ standard powder. In addition, a single crystal of orthoenstatite ((Mg_{1.93},Fe_{0.06})(Si_{1.93},Al_{0.06})O₆, *Pbca*, $a = 8.8117(2)$, $b = 5.18320(10)$, $c = 18.2391(3)$ Å) is used to calibrate instrument model of the CrysAlisPro[®] software (sample-to-detector distance, the detector's origin, offsets of the goniometer angles and rotation of the X-ray beam and the detector around the instrument axis).

5.4.4.2 Alignment of the lasers and temperature measurements.

The initial alignment of the lasers is accomplished via a piece of platinum foil by centering both guiding lasers on the observation area using adjusting screws on the UniHeads. The final adjustments are made using the Pt thermal glow appearing when a sufficient IR laser power is achieved.

Thermal radiation from both sides of the sample is collected using two optical fibers with core diameter of 400 μm, which are connected to Ocean Optics QE65000 spectrometers. Each optical fiber is aligned to the heating spot and focused on the image plane. To do so, the end of the optical fiber leading to the spectrometer is connected to a strong visible light source which illuminates the Pt foil. The position of the light spot on the foil is then adjusted by moving the screws which mount the optical fiber to the UniHead. In this way, due to the magnification of the system, the sample temperature is probed from an area of 20 μm diameter, centered at the heated spot.

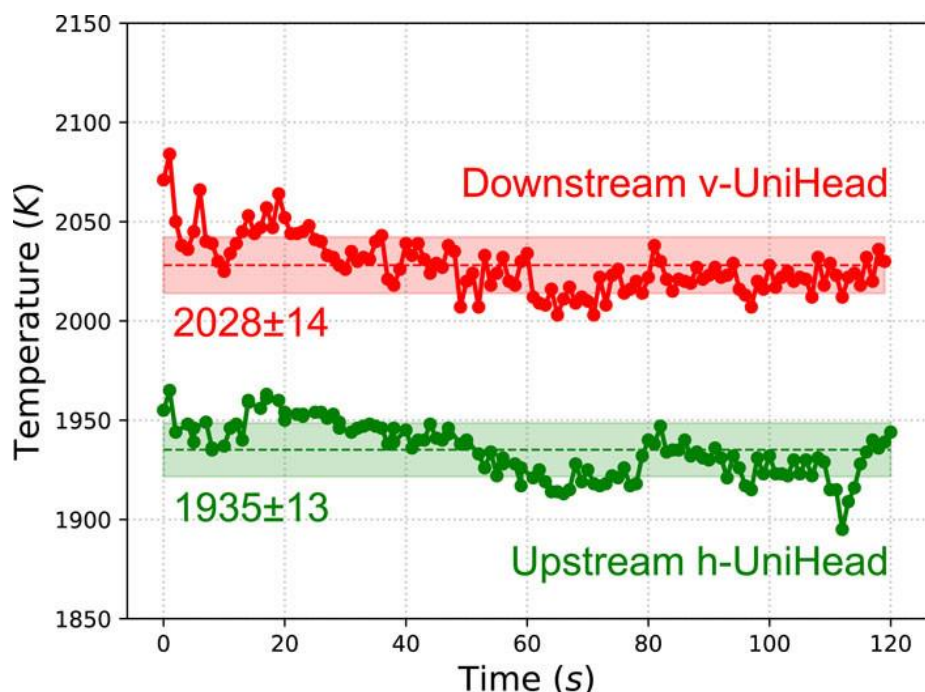


Figure 5.4-4. Example of the time-dependence of the temperature during laser heating and simultaneous SCXRD data collection (step-scan) recorded from both sides of the heated sample of CrN; green dots designate the upstream side temperature, red dots - the downstream side temperature. Thermal radiation is collected every second with exposure time of 800 ms. Solid lines connecting the dots are guides for the eye. Dashed lines show the mean temperature values for each side over the entire rotation. Shaded areas represent the margins of one standard deviation.

The thermal radiation spectra are analyzed using spectroradiometry¹⁴ and fitted using the gray body approximation of Planck's law in the wavelength range of 650–800 nm with software developed for this purpose. Temperatures are calibrated with tungsten halogen lamp (OPTEEMA Engineering GmbH, OL-245M-K3) tungsten bulbs placed on the sample stage and pre-calibrated at 2200, 2500 and 2900 K.

For temperature measurements during the ω rotation of the sample, thermal spectra are collected every second with exposure time of a few hundred of milliseconds. The stage rotation and the temperature data collection of the detector are synchronized manually. The setup allows maintaining the laser heated sample under stable temperature during the entire data collection with a temporal variation that is well below the typical temperature measurement uncertainty of ± 100 K (Figure 5.4-4).

5.4.4.3 Installation of a DAC.

After a DAC is placed in the holder, the sample alignment is accomplished in three steps. In the first step, the upstream and downstream lasers are aligned to the center of the gasket. Using a video camera and the motorized X-, Y-, Z- stages right below the DAC, the sample is first positioned from the downstream v-UniHead observation side. Then the upstream h-UniHead is moved into position using the motorized XY-, Z- stages below it. In the second step, using the motorized XY-stage, the heavy-load Z-stage and the ω -2 θ goniometer below the dsLH system, the DAC together with the aligned lasers is moved into the X-ray beam as well as to the center of the rotation axis using the standard procedure of the sample centering by X-ray absorption¹⁵. Finally, the exact point of interest on the sample can be chosen by moving the X-, Y-, Z-stages below the DAC while the sample is observed through the video camera. Currently, the motors allow the DAC movement by ± 25 μm with accuracy of 0.003 μm in horizontal (X and Y) directions, while in vertical (Z) direction it is possible to move by ± 15 μm with accuracy of 0.003 μm .

The SCXRD/ dsLH setup provides a possibility to work with various types of DACs. However, the appropriate thickness of a DAC (including a membrane cup, if used) is limited to 50 mm to enable correct positioning of the mirrors.

5.4.4.4 Data collection.

The SCXRD data collection is realized in an *oscillation (= narrow slicing) mode*, i.e. when the diffraction is recorded while rotating the sample about a single ω -axis in small steps of 0.5–1°. During the data collection combined with the laser heating it is possible to collect the frames in ranges of ω from -38 to +25°. Diffraction data are measured using a Perkin Elmer XRD1621 flat panel detector in a shutterless mode that reduces the data collection time to one or two minutes for the entire ω rotation range. Pt-foil absorbers of the beamline may be used to decrease intensity of the primary beam in order to avoid oversaturated diffraction peaks on the detector.

5.4.4.5 Known problems and limitations

At the moment, the SCXRD/dsLH setup for X-ray diffraction experiments provides an even power distribution within the laser beam with a diameter of 10 to 30 μm , since the size of the homogeneously heated area should be significantly larger than the diameter of the X-ray beam of $\sim 5 \times 5 \mu\text{m}^2$. Rotation of a DAC results in vibration of the sample around the aligned position with a magnitude of about 1-2 μm during the entire data collection (from -38 to $+25^\circ$). In experiments up to about 100 GPa, in which the size of a sample is of about 10 μm , such vibrations are acceptable, as the sample still remains irradiated. However, in experiments above 100 GPa, the size of a sample drastically decreases, and the size of the laser beam should be reduced down to 1-10 μm . This might require significant modifications of optical schemes and components, as well as mechanics of the system to improve stability further.

5.4.5 Examples of the setup application

We have conducted a number of experiments to demonstrate capabilities of the SCXRD/dsLH setup for *in situ* studies of materials, during which high pressures and high temperatures are applied simultaneously. Two examples are presented below.

5.4.5.1 High-pressure synthesis and crystal structure of FeN

Iron nitrides were discovered in the mid-19th century and have been studied intensively since then due to their refractory properties and potential applications as magnetic recording materials. Additionally, due to the abundance of nitrogen in deeper Earth's regions, assuming iron nitrides as components of the Earth's core can lead to an improved description of the core's elastic properties^{16,17}.

Until recently the iron-nitrogen system was only known for its iron-rich phases α' -Fe₁₆N₂, α' -Fe₈N, γ' -Fe₄N, ϵ -Fe₃N_{1-x}, β -Fe₇N₃ and ζ -Fe₂N¹⁸. Application of pressure leads to formation of nitrogen-rich compounds with potentially high hardness and high energy density¹⁹⁻²³. In particular, very recently Fe₃N₂, FeN, FeN₂ and FeN₄ were synthesized due to high-pressure high-temperature reactions between iron and nitrogen²⁴⁻²⁶.

In this study we have synthesized NiAs-type FeN^{24,25} and characterized its crystal structure at high-pressure and high-temperature conditions using the SCXRD/dsLH setup described above. Three pieces of Fe were placed into a BX90 DAC²⁷ equipped with 250- μm diamond anvils. The cell was then loaded with N₂ serving as both a pressure-transmitting medium and reaction agent. A small ruby ball was placed in the pressure chamber for pressure determination. The cell was pressurized to about 50 GPa. Laser heating at 1900(200) K provoked a chemical reaction between iron and nitrogen resulting in the synthesis of iron nitride FeN as single crystals.

The SCXRD data were collected both during and after laser heating. In each experiment, we managed to collect 36 unique reflections with intensities $I > 3\sigma(I)$, which enabled the refinement of anisotropic displacement parameters. As expected, the unit cell parameters

obtained during and after laser heating ($V = 29.853(7)$ and $28.86(4) \text{ \AA}^3$, respectively) differ due to the thermal expansion of the crystal. The thermal parameters acquired during laser heating are about twice as large as those at room temperature (Table 5.4-I, Figure 5.4-5). The difference in the quality of the structural refinements for the room- ($R_1 = 0.0594 / wR_2 = 0.0692$) and high-temperature data ($R_1 = 0.0772 / wR_2 = 0.0793$) is insignificant, proving the technical feasibility of SCXRD for *in-situ* studies of materials at high pressures and simultaneous high temperatures in laser-heated DACs.

5.4.5.2 High-pressure synthesis and crystal structure of CrN

Chromium nitrides are an attractive class of materials with a number of excellent physical and chemical properties. For example, chromium nitride CrN with a cubic rock salt structure plays a fundamental role in the steel hardening process²⁸ and is often used as a component in advanced coating systems²⁹.

Theoretically predicted nitrogen-rich chromium nitrides CrN₂ and CrN₄ were suggested to become thermodynamically stable at pressures above 7 and 15 GPa, respectively^{30,31}, and are expected to be superhard compounds^{30,31}. The high-pressure reaction between chromium and nitrogen, studied by Hasegawa and Yagi at 10 GPa and 1800 K in a laser-heated DAC, yielded CrN as the only product³². Here we studied the same reaction, but at pressure of 47 GPa in order to search for predicted nitrogen-rich chromium nitrides^{30,31}.

A piece of Cr was loaded into a BX90 DAC equipped with 250 μm Boehler-Almax type diamond anvils. The cell was loaded with N₂ as pressure-transmitting medium and reaction agent. Laser-heating of Cr in nitrogen to 1300 K at 47 GPa resulted in the formation of CrN, the same phase, which was observed in Ref. ³² (Table 5.4-I). The predicted CrN₂ and CrN₄ phases were not detected.

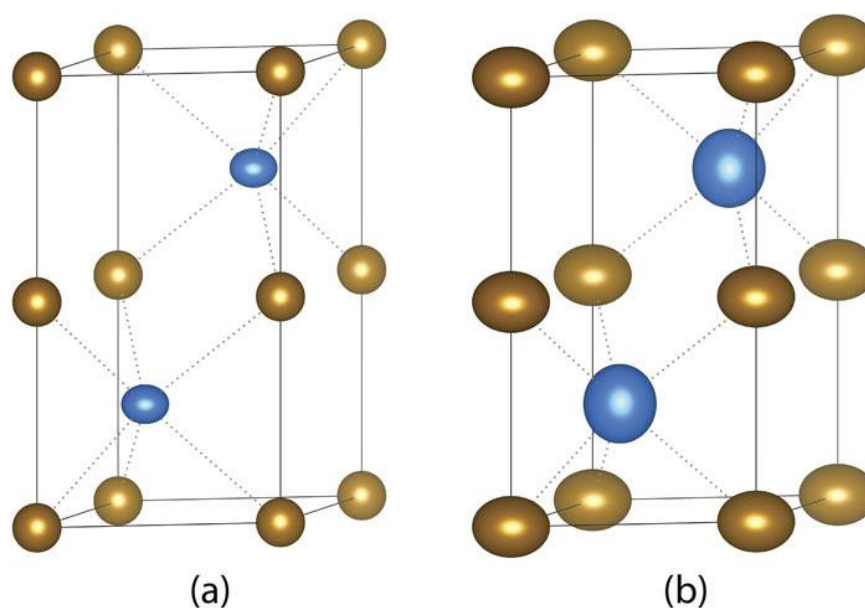


Figure 5.4-5. Crystal structure of FeN at 293K (a) and 1900K (b). Orange and blue balls show the positions of Fe and N atoms, respectively. Thermal ellipsoids are shown at the 90% probability level.

The CrN crystal showed thermal expansion upon laser heating (the unit cell volumes $V = 63.135(14)$ and $62.10(15) \text{ \AA}^3$ were obtained during and after laser heating, respectively). The thermal parameters acquired during laser heating are larger than those at ambient temperature (Table 5.4-I, Figure 5.4-6). As seen in Figure 5.4-7, no significant variations in temperature were observed during the entire data collection.

Table 5.4-I. Details of crystal structural refinements of FeN and CrN.

	FeN	FeN	CrN	CrN
Pressure, GPa	49.6	49.6	47	47
Temperature, K	293	1900(200)	293	1300(200)
Symmetry	P6 ₃ /mmc	P6 ₃ /mmc	Fm $\bar{3}$ m	Fm $\bar{3}$ m
Lattice parameters				
a = b, \AA	2.6299(11)	2.6689(4)	3.960(6)	3.9819(5)
c, \AA	4.819(7)	4.8394(6)	3.960(6)	3.9819(5)
V, \AA³	28.86(4)	29.853(7)	62.10(15)	63.135(14)
Z	2	2	4	4
Refinement				
No. of measured, independent and observed reflections	154/40/36	112/47/36	67/20/19	59/18/16
R₁/wR₂	0.0594/0.0692	0.0772/0.0840	0.0886/0.0870	0.0705/0.1061
U_{iso} (Metal), \AA²	0.0116(10)	0.0247(16)	0.0081(15)	0.036(7)
U_{iso} (N), \AA²	0.014(4)	0.026(4)	0.004(3)	0.030(6)

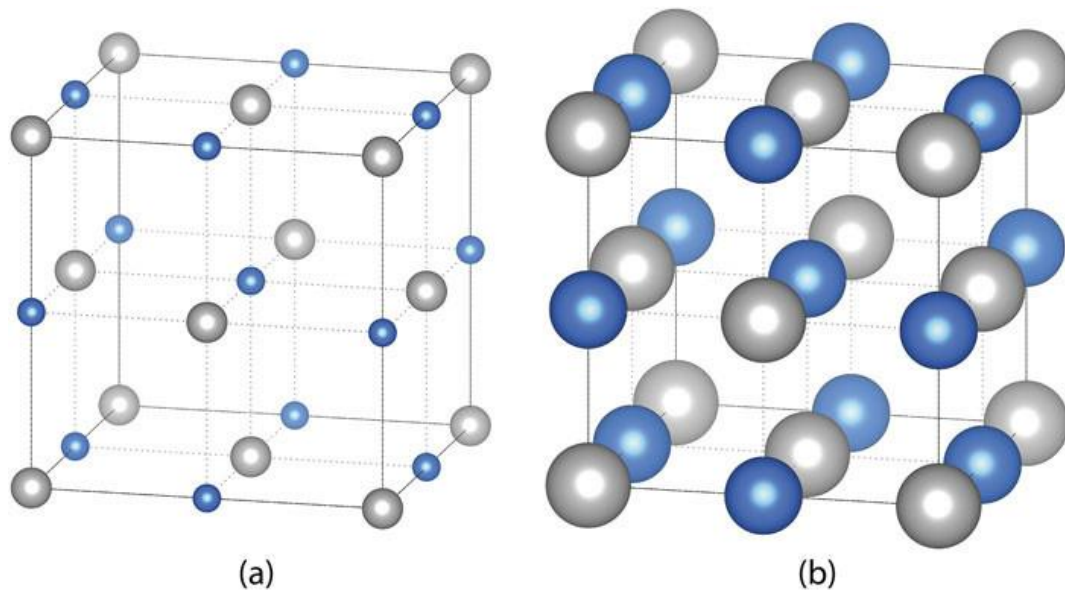


Figure 5.4-6. The crystal structure of CrN at 293 K (a) and 1300 K (b). Blue and grey balls show the positions of Cr and N atoms, respectively. Thermal ellipsoids are shown at the 90% probability level.

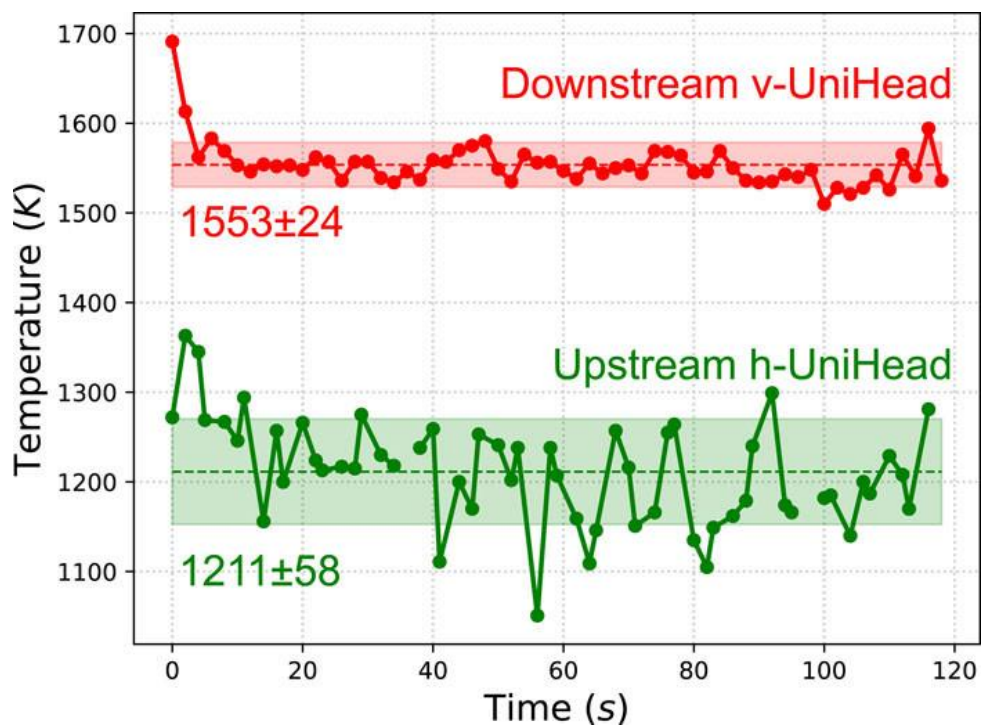


Figure 5.4-7. Time-dependence of the temperature during laser heating and simultaneous SCXRD data collection for CrN. Green dots designate the upstream side temperature, red dots - the downstream side temperature. Solid lines connecting the dots are guides for the eye. Dashed lines show the mean temperature values for each side over the entire rotation. Shaded areas represent the margins of one standard deviation.

5.4.6 Conclusions

We have developed the first dedicated single-crystal X-ray diffractometer coupled with double-sided laser heating system. The SCXRD/dsLH setup encompasses all the components required for SCXRD data collection and simultaneous double-sided laser heating in a single module, which can be mounted/unmounted on the General Purpose experiment of beamline P02.2 (ECB) at PETRA III within a few hours. The alignment of the optical components and preparation of the beamline takes approximately one working day. The setup has been tested in course of several high-pressure high-temperature experiments aimed at studying chemical reactions between nitrogen and two metals, iron and chromium. It enabled to obtain reliable results in the structure solution and refinement of iron and chromium nitrides.

5.4.7 Acknowledgments

N.D. and L.D. thank the Federal Ministry of Education and Research, Germany (BMBF, grant no. 5K16WC1) and the Deutsche Forschungsgemeinschaft (DFG projects DU 954-11/1, DU 393-9/2, and DU 393-13/1) for financial support. Portions of this research were carried out at the light source PETRA III at DESY, a member of the Helmholtz Association (HGF).

5.4.8 References

1. Mills, R. L., Liebenberg, D. H., Bronson, J. C. & Schmidt, L. C. Procedure for loading diamond cells with high-pressure gas. *Rev. Sci. Instrum.* **51**, 891–895 (1980).
2. Yagi, T., Yusa, H. & Yamakata, M. An apparatus to load gaseous materials to the diamond-anvil cell. *Rev. Sci. Instrum.* **67**, 2981–2984 (1996).
3. Kenichi, T., Sahu, P. C., Yoshiyasu, K. & Yasuo, T. Versatile gas-loading system for diamond-anvil cells. *Rev. Sci. Instrum.* **72**, 3873–3876 (2001).
4. Couzinet, B., Dahan, N., Hamel, G. & Chervin, J.-C. Optically monitored high-pressure gas loading apparatus for diamond anvil cells. *High Press. Res.* **23**, 409–415 (2003).
5. Rivers, M. *et al.* The COMPRES/GSECARS gas-loading system for diamond anvil cells at the Advanced Photon Source. *High Press. Res.* **28**, 273–292 (2008).
6. Kurnosov, A. *et al.* A novel gas-loading system for mechanically closing of various types of diamond anvil cells. *Rev. Sci. Instrum.* **79**, 045110 (2008).
7. Boehler, R. New diamond cell for single-crystal x-ray diffraction. *Rev. Sci. Instrum.* **77**, 115103 (2006).
8. Shen, G., Rivers, M. L., Wang, Y. & Sutton, S. R. Laser heated diamond cell system at the advanced photon source for in situ x-ray measurements at high pressure and temperature. *Rev. Sci. Instrum.* **72**, 1273–1282 (2001).
9. Schultz, E. *et al.* Double-sided laser heating system for in situ high pressure–high temperature monochromatic x-ray diffraction at the esrf. *High Press. Res.* **25**, 71–83

- (2005).
10. Prakapenka, V. B. *et al.* Advanced flat top laser heating system for high pressure research at GSECARS: application to the melting behavior of germanium. *High Press. Res.* **28**, 225–235 (2008).
 11. Boehler, R., Musshoff, H. G., Ditz, R., Aquilanti, G. & Trapananti, A. Portable laser-heating stand for synchrotron applications. *Rev. Sci. Instrum.* **80**, 045103 (2009).
 12. Kuppenko, I. *et al.* Portable double-sided laser-heating system for Mössbauer spectroscopy and X-ray diffraction experiments at synchrotron facilities with diamond anvil cells. *Rev. Sci. Instrum.* **83**, 124501 (2012).
 13. Liermann, H. P. *et al.* The Extreme Conditions Beamline P02.2 and the Extreme Conditions Science Infrastructure at PETRA III. *J. Synchrotron Radiat.* **22**, 908–924 (2015).
 14. Shen, G., Wang, L., Ferry, R., Mao, H. & Hemley, R. J. A portable laser heating microscope for high pressure research. *J. Phys. Conf. Ser.* **215**, 012191 (2010).
 15. Bykov, M. Structural aspects of pressure- and temperature-induced phase transitions in low-dimensional systems. (University of Bayreuth, 2015).
 16. Adler, J. F. A high-pressure X-ray diffraction study of iron nitrides: Implications for Earth's core. *J. Geophys. Res.* **110**, B01203 (2005).
 17. Minobe, S., Nakajima, Y., Hirose, K. & Ohishi, Y. Stability and compressibility of a new iron-nitride β -Fe₇N₃ to core pressures. *Geophys. Res. Lett.* **42**, 5206–5211 (2015).
 18. Höhn, P. & Niewa, R. Nitrides of Non-Main Group Elements. in *Handbook of Solid State Chemistry* 251–359 (Wiley-VCH Verlag GmbH & Co. KGaA, 2017). doi:10.1002/9783527691036.hsscvol1008
 19. Laniel, D., Weck, G., Gaiffe, G., Garbarino, G. & Loubeyre, P. High-Pressure Synthesized Lithium Pentazolate Compound Metastable under Ambient Conditions. *J. Phys. Chem. Lett.* **9**, 1600–1604 (2018).
 20. Steele, B. A. *et al.* High-Pressure Synthesis of a Pentazolate Salt. *Chem. Mater.* **29**, 735–741 (2017).
 21. Bykov, M. *et al.* High-Pressure Synthesis of a Nitrogen-Rich Inclusion Compound ReN₈ · x N₂ with Conjugated Polymeric Nitrogen Chains. *Angew. Chemie Int. Ed.* **57**, 9048–9053 (2018).
 22. Sun, W. *et al.* Thermodynamic Routes to Novel Metastable Nitrogen-Rich Nitrides. *Chem. Mater.* **29**, 6936–6946 (2017).
 23. Bykov, M. *et al.* High-pressure synthesis of ultraincompressible hard rhenium nitride pernitride Re₂(N₂)(N)₂ stable at ambient conditions. *Nat. Commun.* **10**, 2994 (2019).

24. Bykov, M. *et al.* Fe-N system at high pressure reveals a compound featuring polymeric nitrogen chains. *Nat. Commun.* **9**, (2018).
25. Clark, W. P. *et al.* High-Pressure NiAs-Type Modification of FeN. *Angew. Chemie Int. Ed.* **56**, 7302–7306 (2017).
26. Bykov, M. *et al.* Synthesis of FeN₄ at 180 GPa and its crystal structure from a submicron-sized grain. *Acta Crystallogr. Sect. E Crystallogr. Commun.* **74**, 1392–1395 (2018).
27. Kantor, I. *et al.* BX90: A new diamond anvil cell design for X-ray diffraction and optical measurements. *Rev. Sci. Instrum.* **83**, 125102 (2012).
28. Widenmeyer, M., Meissner, E., Senyshyn, A. & Niewa, R. On the Formation Mechanism of Chromium Nitrides: An in situ Study. *Zeitschrift für Anorg. und Allg. Chemie* **640**, 2801–2808 (2014).
29. Rivadulla, F. *et al.* Reduction of the bulk modulus at high pressure in CrN. *Nat. Mater.* **8**, 947–951 (2009).
30. Kvashnin, A. G., Oganov, A. R., Samtsevich, A. I. & Allahyari, Z. Computational Search for Novel Hard Chromium-Based Materials. *J. Phys. Chem. Lett.* **8**, 755–764 (2017).
31. Zhao, Z. *et al.* Potentially superhard hcp Cr N₂ compound studied at high pressure. *Phys. Rev. B* **93**, 214104 (2016).
32. Hasegawa, M. & Yagi, T. Systematic study of formation and crystal structure of 3d-transition metal nitrides synthesized in a supercritical nitrogen fluid under 10 GPa and 1800 K using diamond anvil cell and YAG laser heating. *J. Alloys Compd.* **403**, 131–142 (2005).

5.5 Fully time-resolved synchrotron Mössbauer spectroscopy for pulsed laser heating experiments in diamond anvil cell

Cornelius Strohm^{1,*}, [Georgios Aprilis](#)², Ilya Kupenko³, Denis M. Vasiukov², Valerio Cerantola^{4,5}, Aleksandr Chumakov⁵, Rudolf Rüffer⁵, Catherine McCammon⁶, and Leonid Dubrovinsky⁶.

¹ Deutsches Elektronen Synchrotron, Photon Science, 22607 Hamburg, Germany

² Materials Physics and Technology at Extreme Conditions, Laboratory of Crystallography, Universität Bayreuth, 95440 Bayreuth, Germany

³ Institut für Mineralogie, Universität Münster, 48149 Münster, Germany,

⁴ European X-ray Free Electron Laser GmbH, Holzkoppel 4, 22869 Schenefeld, Germany

⁵ ESRF - The European Synchrotron, 38043 Grenoble, France.

⁶ Bayerisches Geoinstitut, Universität Bayreuth, 95440 Bayreuth, Germany

* Correspondent author (e-mail: cornelius.strohm@desy.de)

Prepared for submission to Journal of Synchrotron Radiation

5.5.1 Abstract

Laser heated diamond anvil cells provide an ideal sample environment to investigate earth and planetary materials under relevant conditions of pressure and temperature. Mössbauer spectroscopy is particularly suited for the study of structural, dynamic, and magnetic properties of geomaterials. The combination of both methods for in situ experiments became possible through Mössbauer spectroscopy using a synchrotron source, which meets the requirement to approximately match the size of the x-ray focal spot with the area heated by an optical laser beam. Recently, pulsed laser heating has enabled high temperatures to be reached even in samples where prolonged continuous heating is not possible. We have developed an event-based detection scheme to combine pulsed laser heating with synchrotron Mössbauer spectroscopy. After completion of the experiment, the data can be explored and binned in the three dimensions of laser intensity, drive velocity (and thus energy), and acquisition time. We present first results from a series of heating experiments in Fe and Fe₂₅O₃₂ under pressure.

5.5.2 Introduction

The development of the diamond anvil cell (DAC) has significantly changed our knowledge of the Earth's interior, enabling static pressures up to the equivalent of the core mantle boundary to be reached in the laboratory¹. In addition, laser heating through the diamond anvils allowed the studies of compressed materials at temperatures high enough to reach the geotherm². Due to this, the laser heated diamond anvil cell (LHDAC) technique has become the main approach for simulating the pressure and temperature conditions of deep Earth and planetary

interiors, and for investigating chemical processes and physical phenomena at extreme conditions.

Alongside continuous-wave (CW) heating, pulsed lasers (PL) have also been used since the first attempts to laser heat samples in a DAC^{3,4}, with the advantage of achieving significantly higher temperatures due to the concentration of high laser power in a short impulse. Since the beginning of the 2000s, pulsed heating has been coupled with time-resolved measurements^{5,6}. The repetitive heating and cooling of the sample makes time an extra variable in addition to pressure and temperature, which is not possible with continuous-wave laser heating. An entirely new field of research has been introduced, allowing the determination of important material properties such as thermal conductivity, thermal diffusivity, and melting temperature^{7–11}.

At the same time, Mössbauer spectroscopy (MS) using ⁵⁷Fe has emerged as an ideal probe for the coordination, speciation, spin state, magnetic order, and dynamics of geophysically relevant materials because of its sensitivity and the generally high natural abundance of iron. However, conventional MS under pressure is difficult due to the lack of efficient focusing schemes, and in particular its combination with laser heating faces severe challenges, since usually only a small portion of the sample is heated. The high spectral flux of third generation synchrotron sources allows the excitation of Mössbauer transitions with an X-ray beam, their high brilliance permits focusing down to the micrometer scale, and the synchrotron Mössbauer source (SMS)¹² gives access to spectra in the energy domain. The determination of the second order Doppler shift from the spectra provides a measure of the temperature of the bulk sample¹³, which, in combination with spectroradiometry, makes SMS a powerful tool for experiments in laser heated diamond anvil cells^{14,15}.

The combination of Mössbauer spectroscopy with pulsed laser irradiation for samples at ambient pressure has already been demonstrated along with the possible applications of the method¹⁶. It was immediately clear that it is necessary to have time-resolved information of the Mössbauer absorption in order to take full advantage of the dynamic nature of pulsed laser heating in the DAC. Previous experimental schemes for high-pressure, high-temperature (HPHT) studies allowed only limited time-differentiated information¹⁷ in predetermined time windows. We have therefore developed a detection scheme to perform fully time-resolved SMS at high pressures, in combination with pulsed laser heating in DAC's which allows an arbitrary number and position of regions of interest and reprocessing of the data after completion of the experiment. The Mössbauer absorption of the sample can be fully tracked along the duration of the laser pulse, and its temperature can be estimated on both heated surfaces using spectroradiometry as well as in bulk from the center shift (CS) of the Mössbauer spectra. The method is demonstrated by heating iron in KCl at 32 GPa, iron in argon at 36 GPa, and Fe₂₅O₃₂ in Ne at 77 GPa.

5.5.3 Experiment

5.5.3.1 Beamline

The experiments were carried out using the synchrotron Mössbauer source¹⁴ at the nuclear resonance beamline ID18¹⁸ at the European Synchrotron Radiation Facility. A Si (1 1 1) high heat load monochromator, followed by a Si (12 2 2) channel cut crystal, and finally an electronically forbidden (1 1 1) pure nuclear reflection from an iron borate ($^{57}\text{FeBO}_3$) crystal successively reduce the broadband spectrum of the undulator source to a bandwidth on the order of a few times the natural linewidth of the 14.413 keV Mössbauer transition of ^{57}Fe . An additional deflector combining a Si (4 2 2) and Si (5 3 1) reflector upstream of the iron borate crystal keeps the outgoing beam nearly horizontal, and two mirrors in Kirkpatrick-Baez configuration focus the beam to a spot with size of about $8 \times 13 \mu\text{m}^2$ at the sample position. For the acquisition of the energy spectra, the incident beam is Doppler-tuned with respect to the absorber using a conventional Mössbauer transducer operated with a sinusoidal velocity profile at its mechanical resonance with the load of the holder, magnet, and furnace for the iron borate crystal.

5.5.3.2 Laser heating

For the heating of the sample, a portable double-sided pulsed laser heating setup was used¹⁹. The system is based on two electronically modulated SPI RedPower R4 fiber lasers with maximal power of 50 W each, operating at 1070 nm. The lasers are coupled to two universal laser cutting heads (Unihead by Precitec GmbH¹⁵) and two Focal- π Shapers (Focal- π Shaper_9_1064 by AdlOptica GmbH) that shape the laser beams into a flat-tops for more homogeneous heating²⁰. The Uniheads integrate the focusing optics, illuminators, filters, and dichroic beam-splitters to combine the infrared laser beam, the camera microscope for sample observation, and the port for the spectrometer into a single coaxial path to the diamond anvil cell. The optical access to the cell is realized using a pair of D-shaped, silver-coated glass mirrors at $\sim 42^\circ$ angles from the focusing optics in order to avoid x-ray absorption in the optical mirrors, while keeping the laser beam as close to the DAC compression axis as possible. The two lasers were triggered and synchronized using the trigger of the spectrometer detector (PI-MAX 1024i by Princeton Instruments, Inc.), or a Berkeley Nucleonics Model 555 pulse generator. This allows a common timing reference for the laser cycle and the spectrometer temperature collection¹⁹. The laser radiation is recorded by a pair of fast InGaAs detectors and observed using an oscilloscope.

5.5.3.3 Temperature determination

5.5.3.3.1 Spectroradiometry

The thermal radiation of the heated sample is collected from both sides through the same optical path that is used to focus the lasers, using the optics integrated in the UniHead modules. The temperature is estimated using the gray body approximation of Planck's law²¹. The light is guided through optical fibers into an IsoPlane SCT 320 spectrometer with a mounted PI-MAX 4 1024 \times 256 detector (Princeton Instruments). The gated mode of the

detector allows time-resolved temperature determination during pulsed laser heating. Using this technique, the temporal resolution of the temperature determination can be as short as 50 ns, depending on the experimental conditions. The detector can be gated with intervals as short as 4 ns but the sample emission intensity usually limits the minimum exposure time. The total collection time required to observe the temperature evolution of the sample over the duration of the laser pulse usually varies between a few tens of seconds up to a few minutes.

5.5.3.3.2 Mössbauer Spectroscopy

Apart from the temperature determination on both surfaces of the heated sample provided by spectroradiometry, Mössbauer spectroscopy also provides a measure of temperature: the relative energy resolution of $\sim 10^{-13}$ for ^{57}Fe allows the observation of the second order Doppler shift, i.e. a shift of the average transition frequency of the nuclei representing clocks moving at the speed of lattice vibrations^{22,23}. Assuming equipartition, a monoatomic lattice and a Debye-Model for the lattice phonon density of states, this center shift can be related to the sample temperature T_s as follows: for the case of α -iron $T_s = 1368.6034(13) \text{ Ks/mm} \cdot \Delta\nu + T_0$, where $\Delta\nu$ is the change of center shift in mm/s with respect to a spectrum acquired at the reference temperature T_0 . This assumes that the isomer shift and Debye temperature do not change upon heating, and that there is no sample movement. The line broadening arising from the velocity dispersion of the nuclei²⁴ is estimated to be about 10^{-4} mm/s for iron at 6000 K and therefore negligible for our experiments.

The temperature determination through the second order Doppler shift ideally complements spectroradiometry: it is bulk sensitive, it does not require calibration in order to account for the emissivity and optical transfer function, and it is applicable for temperatures below 1000 K, where the peak of the black-body radiation spectrum is shifted to the infrared, and the intensity in the bandwidth of typical spectrometer setups is low.

5.5.3.4 Detection

Pump probe experiments with SMS require the detection of the transmitted photons on two timescales. On the one side, there is the period of the velocity transducer, which is usually operated at its mechanical resonance frequency. On the other side, there is the repetition rate of the pulsed laser heating of the sample. In the experiments presented here, the mechanical resonance was at 12.75 Hz, the laser was operated in the range from 0.5 to 50 kHz, and the two frequencies were not synchronized.

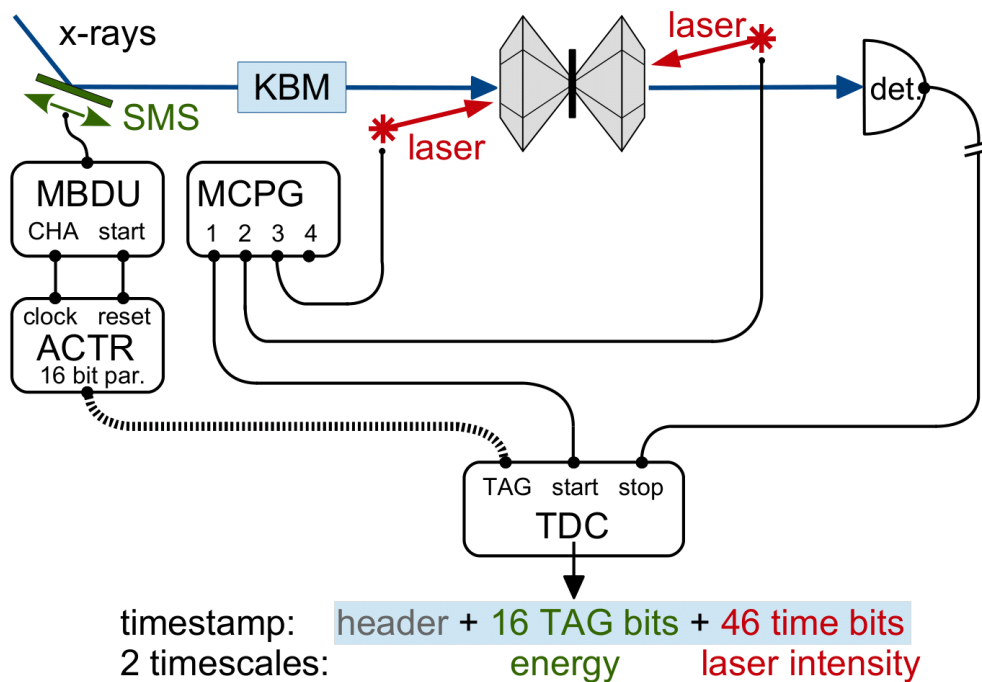


Figure 5.5-1. Experimental setup. KBM: focusing mirrors in Kirkpatrick Baez configuration. MBDU: Mössbauer drive unit. ACTR: auxiliary counter, MCPG: multi-channel pulse and delay generator, TDC: time to digital converter. Each laser trigger starts a TDC sweep. The phase of the transducer is encoded in a 16 bit tag which is inserted into the timestamp for each stop event from the detector.

The photons transmitted through the sample are detected with a scintillation detector. The detector signal is discriminated into fast NIM (Nuclear Instrumentation Module standard) pulses and these events are then recorded by a Fast Comtech 7889 multi-stop time to digital converter (TDC) with respect to the periodic laser trigger, serving as the start signal. This TDC generates a timestamp for each event. In addition, a parallel 16-bit TTL tag input is evaluated for each stop event and included in the timestamp. We used this tag input to encode the phase and thus the velocity of the transducer as a binary number. The number corresponds to the channel index of the multi-channel analyzer often used in conventional Mössbauer spectroscopy. This was implemented through a binary ripple counter using the 'channel advance' and 'start' signals from the Mössbauer drive unit (MDU) as clock and reset signals, respectively. As a result, each timestamp contains information on both, the excitation energy, and the time within the laser period. Figure 5.5-1 illustrates the setup and Figure 5.5-2 shows the two-dimensional histogram of the data constructed from the transducer and laser timescales. The timestamps of every detection from the TDC are written to a continuous list-file which can be explored not only in the two dimensions of transducer velocity and laser intensity, but also in the order of acquisition, i.e. representing different generations of the histogram (see Figure 5.5-2).

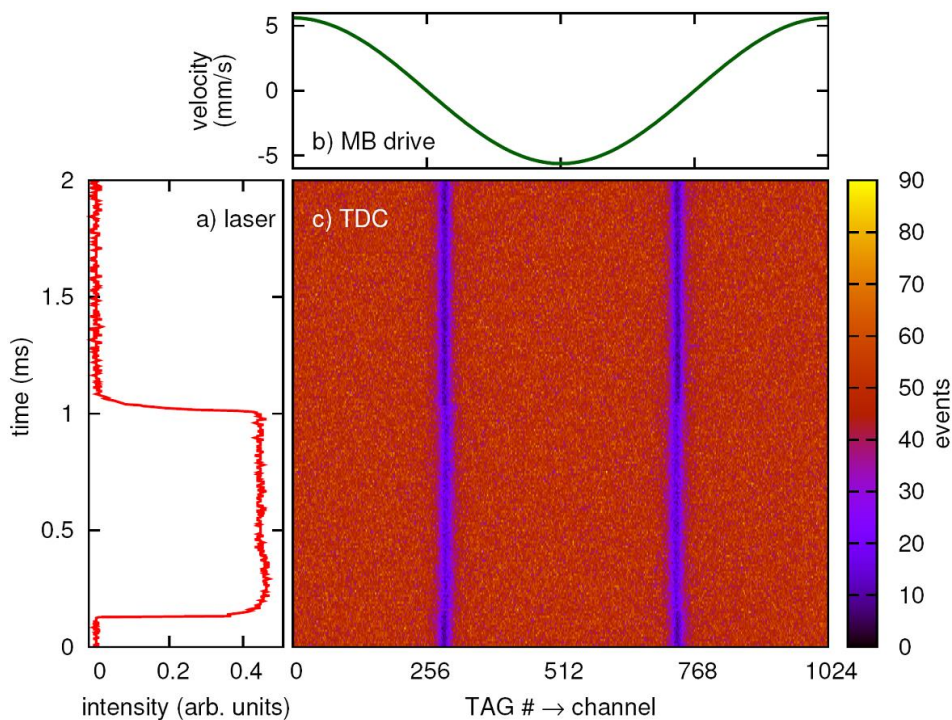


Figure 5.5-2. 2D histogram of the raw data, as a function of the transducer phase (encoded in the TAG bits) and laser time. The corresponding Doppler velocity and laser pulse shapes are shown in the top and left plots, respectively. The sample is Fe in KCl pressure medium at 32 GPa.

5.5.4 Pulsed Laser Heating of Metallic Iron

The study of metallic Fe is of paramount importance for the understanding of the Earth's core yet poses extreme challenges due to its high reactivity at high pressures and temperatures and the instability of the sample shape upon melting. In order to understand the capabilities using pulsed laser heating, we have performed a series of experiments.

5.5.4.1 Fe in KCl at 32 GPa

In the first experiment, a BX90-type²⁵ DAC that was equipped with diamond anvils of culet diameter 250 μm was prepared. A rhenium gasket was pre-indented from an initial thickness of 200 μm down to 25 – 35 μm and laser-drilled to create a circular pressure chamber of 100 – 200 μm in diameter. An ^{57}Fe -enriched iron foil was loaded in KCl as pressure transmitting medium and was pressurized to 32 GPa (transforming to $\epsilon\text{-Fe}$).

The data were collected while pulsed laser heating the sample with a low repetition rate of 0.5 kHz, using single-sided heating. Figure 5.5-2 (c) shows the two-dimensional histogram in the transducer and laser timescales over one transducer and one laser period. The transducer velocity and laser intensity are shown in Figure 5.5-2 (a) and (b) respectively. The entire dataset contains an integral of $5 \cdot 10^6$ events. In order to verify the stability of heating, as well as the chemical integrity of the sample and its relative alignment with the laser and x-ray spots during the experiment, we first selected two coarse regions of interest (with and without laser intensity, respectively) and extracted a time-series, i.e. different generations of the 2-dimensional histogram shown in Figure 5.5-2. Figure 5.5-3 (a) shows the folded spectra for

different ranges of integral counts and Figure 5.5-3 (b) shows the corresponding sample temperatures. After an initially warmer period, heating was stable from $1 \cdot 10^6$ to $4 \cdot 10^6$ integral counts, before the temperature increased again at the last part of the data collection. For the spectra in Figure 5.5-4 (a), the laser period was divided into 20 equal regions of interest of 100 μ s for the time when heating was stable. The temperature evolution throughout the laser pulse is plotted in Figure 5.5-4 (b). This data validates the acquisition scheme, demonstrates the determination of the sample temperature, and shows the advantage of the flexible binning scheme.

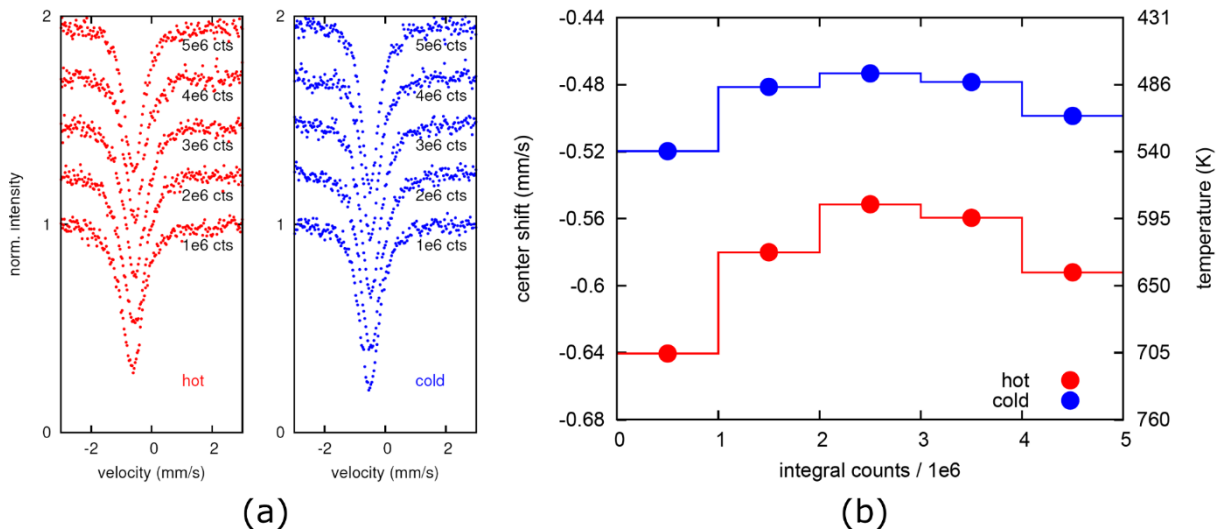


Figure 5.5-3. Time-resolved pulsed laser heating of an ^{57}Fe -enriched iron foil in KCl pressure medium at 32 GPa. SMS spectra corresponding to the hot and cold parts of the laser cycle (a) and temporal evolution (b) of the sample temperature in the hot and cold parts of the laser cycle for intervals of $1 \cdot 10^6$ counts.

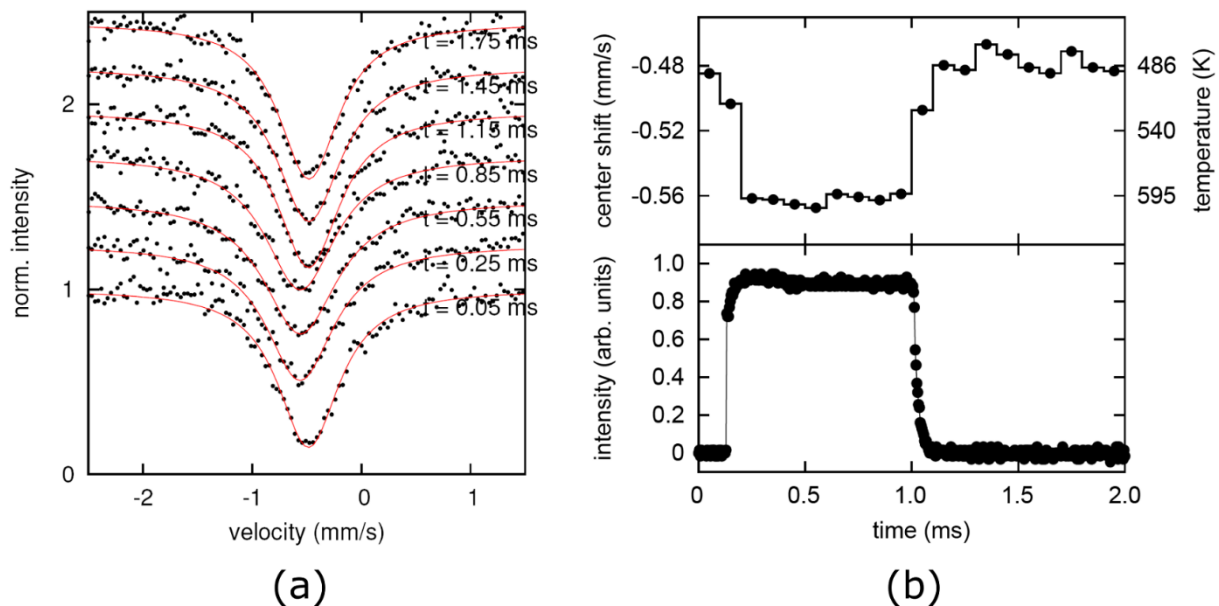


Figure 5.5-4. Time-resolved pulsed laser heating of an ^{57}Fe -enriched iron foil in KCl pressure medium at 32 GPa. SMS spectra corresponding to the indicated time within the laser period (a) and evolution of the sample center shift -due to temperature change- (b) within one laser period.

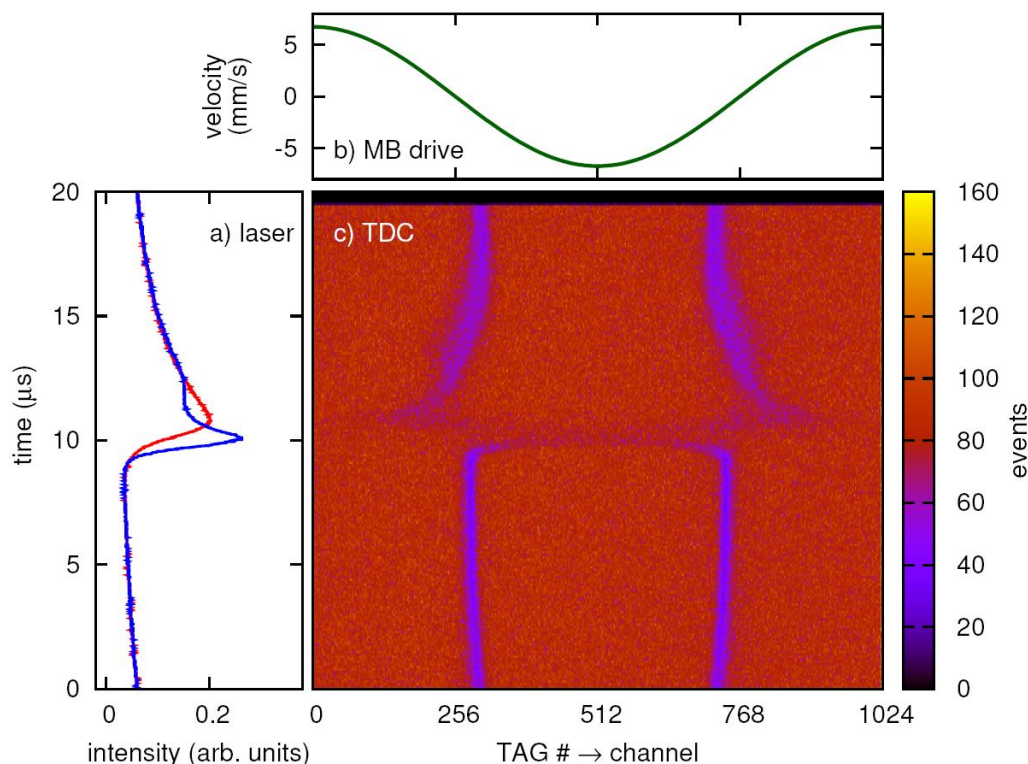


Figure 5.5-5. 2D histogram of the raw data, as a function of the transducer phase (tag) and laser time, with the corresponding laser pulse shapes (a) from both heating sides and Mössbauer drive velocity (b), of laser heated Fe in Ar pressure medium at 36 GPa.

5.5.4.2 Fe in Ar at 36 GPa

In the second experiment, a sample of Fe was gas-loaded in argon²⁶ and compressed to 36 GPa in a DAC and heated from both sides with a laser repetition rate of 50 kHz, i.e. ten times higher than in the previous experiment. A two-dimensional histogram with a total of $8.4 \cdot 10^6$ events is shown in Figure 5.5-5, along with the transducer velocity and intensity of the up and downstream lasers. With the beginning of the laser pulse and heating of the sample, the center of absorption first moves towards negative velocities, as expected. The most striking observation is, however, the apparent loss of resonant absorption when the laser intensity reaches its maximum. The absorption is recovered with a huge positive shift, which may possibly be attributed to mechanical motion from differential thermal expansion of the sample and the pressure medium during cooling, due to temperature differences between the up- and down-stream sides resulting from the different laser pulse shapes. Details on the fits of the data and scientific conclusions are beyond the scope of this methodology paper and will be reported elsewhere.

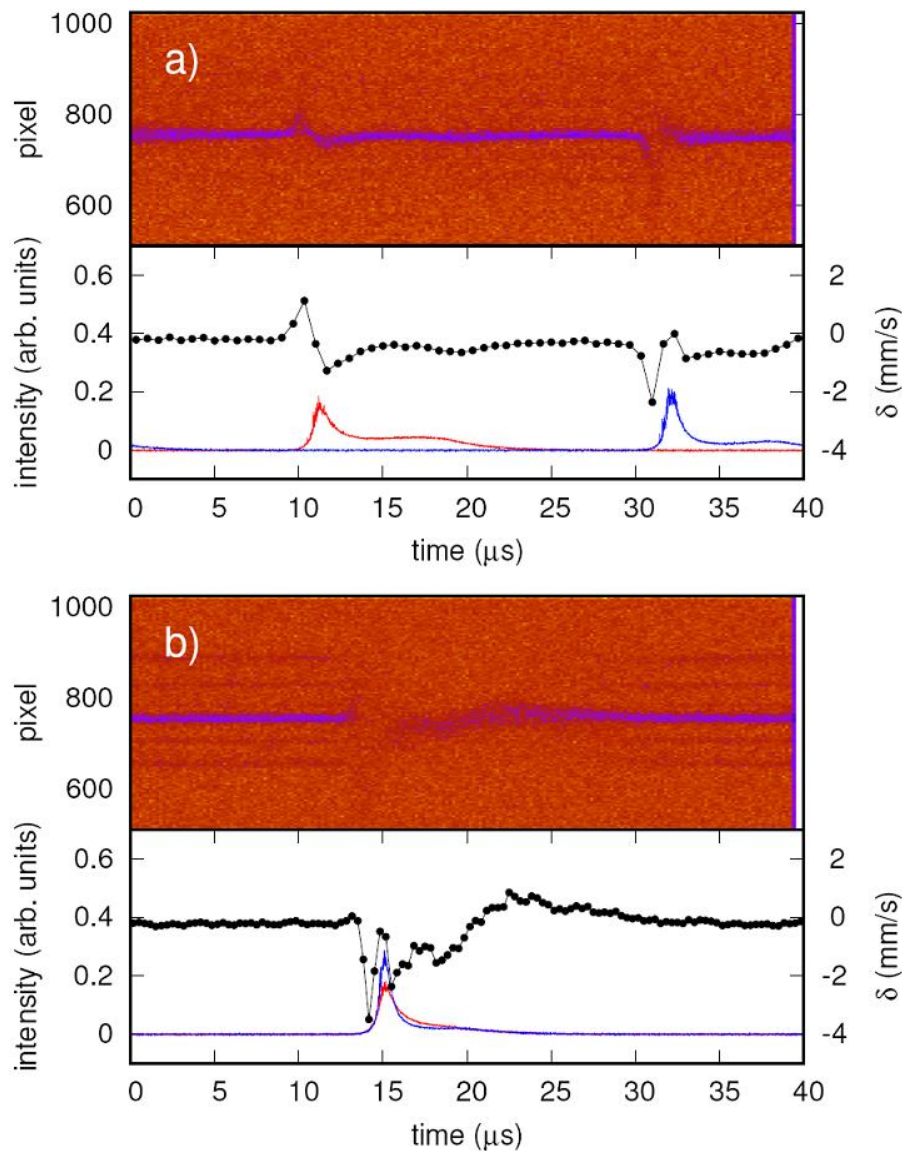


Figure 5.5-6. SMS for different relative timing of the up- and down-stream lasers. Top, 2D histogram of the raw data. Bottom, laser intensities (red and blue lines) and center shift (black dots). (a) the upstream laser pulse (red) precedes the downstream laser pulse (blue). (b) both laser pulses are matched temporally as closely as possible with the present setup.

5.5.4.3 Fe in Ar, different relative laser timing

In order to further investigate this observation of resonant absorption loss and dramatic energy shift, we repeated the experiment with different relative laser timing. As seen in Figure 5.5-6 (a), the two laser pulses were temporally separated, revealing that the response strongly depends on the side from which the sample is heated. Furthermore, the center shift has a derivative shape with respect to the main peak of the laser pulse. The second order Doppler shift is therefore ruled out as sole explanation. This point supports the conclusion that the large velocities are the results of actual displacements of the sample, consistent with previous reports¹⁶. From the data we conclude that the velocities are directed away from the respective laser for increasing and towards the laser for decreasing temperatures. Integrating the center shift yields maximum sample displacements on the order of nm.

5.5.5 Pulsed Laser Heating of $\text{Fe}_{25}\text{O}_{32}$

Understanding the magnetic properties of geomaterials is key to elucidating their possible role in the stabilization and reversal of the geo-dynamo. At the same time, paleo-magnetism of materials cooled in the Earth's magnetic field have helped to reveal the history of its orientation. Yet there is little data on the Curie and Neel temperatures at geophysically relevant pressures. The use of pulsed laser heating allows magnetic transitions to be crossed repeatedly during rising and decreasing temperatures, and the collection of statistics for spectra in the cold and hot phases simultaneously. In order to explore capabilities in this direction, a cell equipped with diamond anvils of culet diameter $80\ \mu\text{m}$ was loaded with $\text{Fe}_{0.94}\text{O}$ in Ne using a rhenium gasket and compressed to 77 GPa. Upon laser heating, the material quickly reacted in situ to form $\text{Fe}_{25}\text{O}_{32}$ based on x-ray diffraction performed after completion of the experiment. In order to observe the magnetic transition, the sample was heated from both sides with a repetition rate of 20 kHz. In this experiment, the pulse shapes were carefully matched to minimize effects of sample displacement, and the laser powers were balanced to 9 W and 7.5 W from the up- and down-stream side, respectively, to minimize mechanical excursions due to differential heating. Figure 5.5-7 shows the raw data for the part of the experiment where stable heating could be maintained, along with the monitor signals for the laser intensity. The collapse of the magnetic hyperfine splitting upon heating is clearly observed. Figure 5.5-8 shows selected spectra from the heating plateau, during cooling and in between the laser pulses. The location of the regions of interest are indicated by arrows in Figure 5.5-7. The lines represent the fits (red) and the individual components (colors) as obtained with MossA software²⁷ along with the data (open circles). The top panel shows the collapse of the hyperfine field at temperatures of 1740(250) K (determined by spectroradiometry). A possible small background of cold material apparent in the raw data is not resolved in the binned spectra. The middle panel shows partial recovery of magnetic order with a slightly reduced hyperfine field at 628 K (obtained from fits of the spectra), while the lower panel, showing data between the pulses at 328 K (obtained from fits of the spectra), is dominated by 91% of magnetic components. The temperature evolution on both, the up-stream and down-stream side of the sample during the laser pulse, as determined by spectroradiometry, is presented in Figure 5.5-9. While the present dataset demonstrates a proof of principle, pinpointing the magnetic transition temperatures requires precise control of the laser pulse shape in order to obtain ramp-profiles in the resulting sample temperatures. This procedure is technically possible, and the necessary developments are underway.

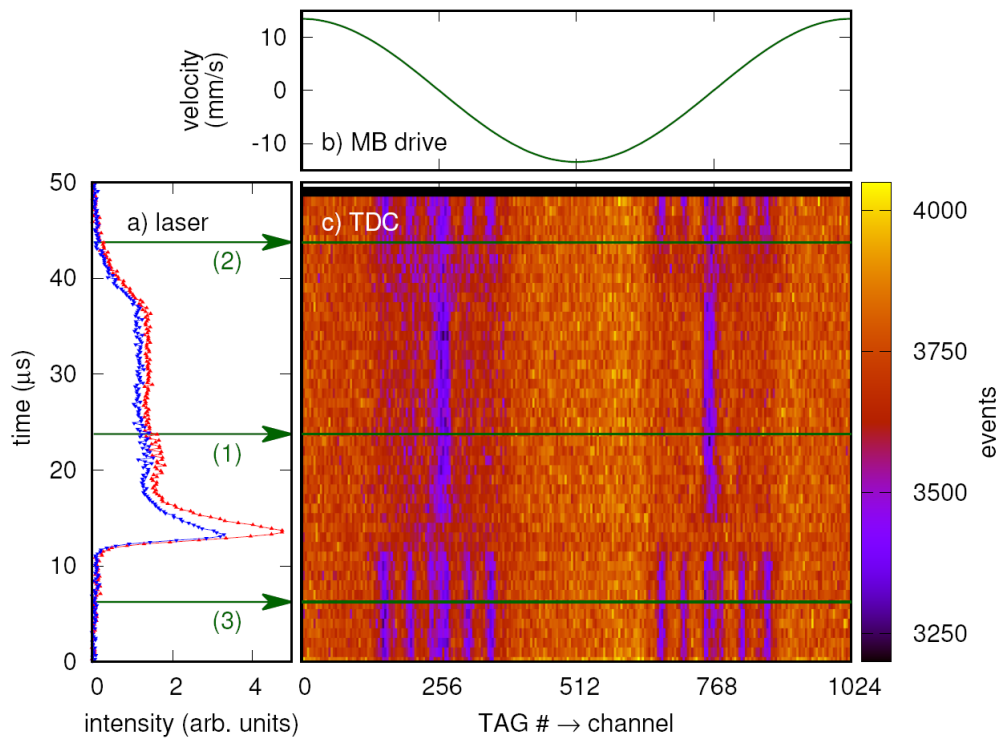


Figure 5.5-7. 2D histogram of the raw data, as a function of the transducer phase (tag) and laser time, with the corresponding laser pulse shapes (a) from both heating sides and Mössbauer drive velocity (b). The sample is $\text{Fe}_{25}\text{O}_{32}$ at 77 GPa in Ne pressure medium. The arrows indicate the position of the spectra shown in Figure 5.5-8.

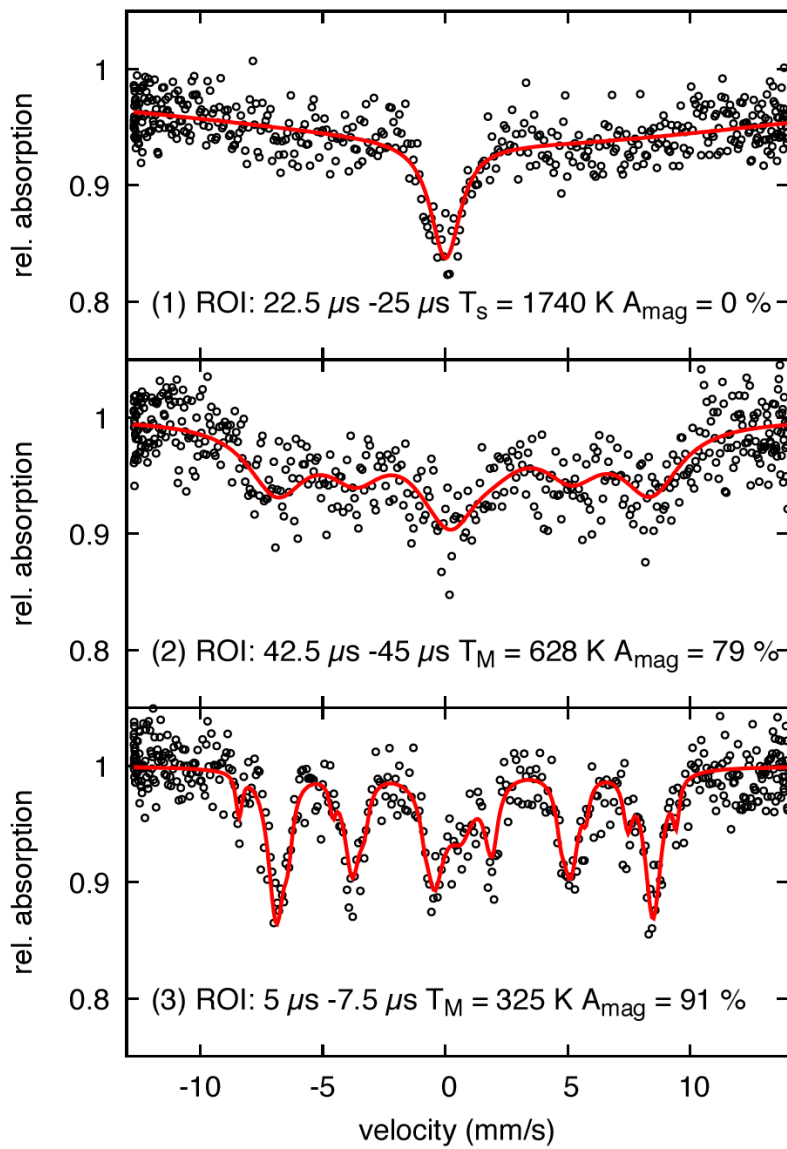


Figure 5.5-8. SMS spectra for $\text{Fe}_{25}\text{O}_{32}$ extracted from the raw data shown in Figure 5.5-7. Open circles show the data points and solid lines the theoretical fit. T_M : temperature determined from a fit of the Mössbauer spectra, T_s : temperature determined by spectroradiometry, A_{mag} : area of magnetic component in spectra.

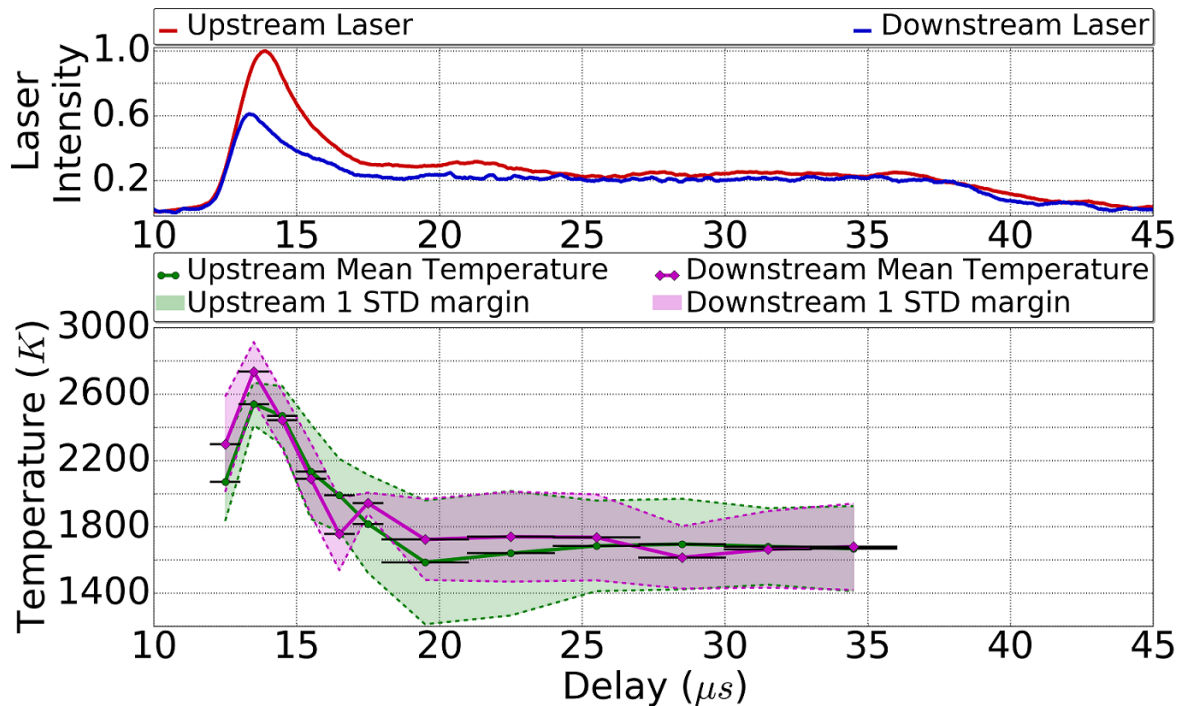


Figure 5.5-9. Temperature of $\text{Fe}_{25}\text{O}_{32}$ in Ne pressure medium during double-sided pulsed laser heating at 77 GPa. Red and blue solid lines represent the normalized laser pulse intensity for the lasers on the upstream and downstream side, respectively. Black horizontal lines show the sample temperature response at different moments during the laser pulse, collected with $1 \mu\text{s}$ exposure time for delays from 12 to $18 \mu\text{s}$ and $3 \mu\text{s}$ exposure time for delays from 18 to $36 \mu\text{s}$. Green and purple solid lines are guides for the eye for the temperatures on the upstream and downstream sides of the sample respectively. Green (upstream side) and purple (downstream side) areas indicate the margins of ± 1 standard deviation of each temperature over many collections during the same heating.

5.5.6 Conclusion and Outlook

We have developed a detection scheme to perform fully time resolved Synchrotron Mössbauer Source spectroscopy for experiments with pulsed laser heating in diamond anvil cells. We have demonstrated successful heating and data acquisition at pump frequencies from 0.5 to 50 kHz in samples of iron metal and $\text{Fe}_{25}\text{O}_{32}$, both enriched in ^{57}Fe .

The determination of melting, of structural, and of magnetic phase transitions directly benefits from the dynamics of pulsed laser heating in combination with the flexible binning scheme, because the transition lines are crossed twice, first during rising and then during falling temperatures, and with a well-defined velocity. In addition, the dataset for all temperatures is acquired simultaneously.

The extremely high spectral resolution of Mössbauer spectroscopy means that it is sensitive to both the second order Doppler shift, which can be exploited for temperature determination, and also minute transient displacements of the sample. We present the first evidence for thermal dilatation effects inside the sample chamber of the laser heated DAC, which will be investigated in further studies.

The temporal resolution of the present detection scheme is only limited by the nuclear lifetime (~ 98 ns for the transition of ^{57}Fe at 14.4 keV). Even shorter timescales are in principle accessible through synchronisation of the nuclear excitation and the laser pulse, similar to experiments in time-differential MS²⁸. In this case, the synchrotron timing would replace the detection of the 123 keV γ -decay populating the 14.4 keV level.

The detection scheme can be directly transferred to a setup with a conventional radioactive Mössbauer source. Furthermore, it is not limited to pulsed laser heating in a diamond anvil cell and can be easily applied to many other pump probe experiments including optical excitations, photo-chemistry, and experiments in time varying electromagnetic fields.

5.5.7 Acknowledgements

The authors would like to thank I. Kantor for support. We gratefully acknowledge the European Synchrotron Radiation Facility for provision of synchrotron radiation under proposal numbers HC-1427, ES-211 and ES-212.

5.5.8 References

1. Bassett, W. A. Diamond anvil cell, 50th birthday. *High Press. Res.* **29**, 163–186 (2009).
2. Bassett, W. A. The birth and development of laser heating in diamond anvil cells. *Rev. Sci. Instrum.* **72**, 1270 (2001).
3. Bassett, W. A. & Li-Chung Ming. Disproportionation of Fe_2SiO_4 to $2\text{FeO}+\text{SiO}_2$ at pressures up to 250kbar and temperatures up to 3000 °C. *Phys. Earth Planet. Inter.* **6**, 154–160 (1972).
4. Gold, J. S., Bassett, W. A., Weathers, M. S. & Bird, J. M. Melting of Diamond. *Science* (80-.). **225**, 921–922 (1984).
5. Funamori, N. & Sato, T. Heating in a diamond-anvil cell using relaxation oscillations of a Q-switched Nd:YAG laser. *Rev. Sci. Instrum.* **77**, 77–80 (2006).
6. Goncharov, A. F. & Crowhurst, J. C. Pulsed laser Raman spectroscopy in the laser-heated diamond anvil cell. *Rev. Sci. Instrum.* **76**, 063905 (2005).
7. Pangilinan, G. I., Ladouceur, H. D. & Russell, T. P. Temperature measurements of a thermal wave at static high pressures. *Appl. Phys. Lett.* **76**, 2460–2462 (2000).
8. McWilliams, R. S., Dalton, D. A., Konôpková, Z., Mahmood, M. F. & Goncharov, A. F. Opacity and conductivity measurements in noble gases at conditions of planetary and stellar interiors. *Proc. Natl. Acad. Sci.* **112**, 7925–7930 (2015).
9. Yang, L., Karandikar, A. & Boehler, R. Flash heating in the diamond cell: Melting curve of rhenium. *Rev. Sci. Instrum.* **83**, 1–6 (2012).
10. Goncharov, A. F. *et al.* Thermal conductivity of argon at high pressures and high

- temperatures. *J. Appl. Phys.* **111**, 112609 (2012).
11. Beck, P. *et al.* Measurement of thermal diffusivity at high pressure using a transient heating technique. *Appl. Phys. Lett.* **91**, 10–13 (2007).
 12. Smirnov, G. V. Synchrotron Mössbauer source of 57 Fe radiation. *HYPERFINE Interact.* **125**, 91–112 (2000).
 13. Maradudin, A. A., Flinn, P. A. & Ruby, S. Velocity Shift of the Mössbauer Resonance. *Phys. Rev.* **126**, 9–23 (1962).
 14. Potapkin, V. *et al.* The 57Fe Synchrotron Mössbauer Source at the ESRF. *J. Synchrotron Radiat.* **19**, 559–569 (2012).
 15. Kupenko, I. *et al.* Portable double-sided laser-heating system for Mössbauer spectroscopy and X-ray diffraction experiments at synchrotron facilities with diamond anvil cells. *Rev. Sci. Instrum.* **83**, 124501 (2012).
 16. Vagizov, F., Kolesov, R., Olariu, S., Rostovtsev, Y. & Kocharovskaya, O. Experimental observation of vibrations produced by pulsed laser beam in MgO:57Fe. *Hyperfine Interact.* **167**, 917–921 (2006).
 17. Kupenko, I. *et al.* Time differentiated nuclear resonance spectroscopy coupled with pulsed laser heating in diamond anvil cells. *Rev. Sci. Instrum.* **86**, 114501 (2015).
 18. Ruffer, R. & Chumakov, A. I. Nuclear Resonance Beamline at ESRF. *Hyperfine Interact.* **97–98**, 589–604 (1996).
 19. Aprilis, G. *et al.* Portable double-sided pulsed laser heating system for time-resolved geoscience and materials science applications. *Rev. Sci. Instrum.* **88**, 084501 (2017).
 20. Laskin, A. & Laskin, V. π Shaper – Refractive Beam Shaping Optics for Advanced Laser Technologies. *J. Phys. Conf. Ser.* **276**, 012171 (2011).
 21. Heinz, D. L. & Jeanloz, R. Temperature measurements in the laser-heated diamond cell. in *High pressure research in mineral physics: A Volume in Honor of Syun-iti Akimoto* (eds. Manghnani, M. H. & Syono, Y.) 113–127 (American Geophysical Union, 1987).
 22. Pound, R. V. & Rebka, G. A. Variation with Temperature of the Energy of Recoil-Free Gamma Rays from Solids. *Phys. Rev. Lett.* **4**, 274–275 (1960).
 23. Josephson, B. D. Temperature-Dependent Shift of γ -Rays Emitted by a Solid. *Phys. Rev. Lett.* **4**, 341–342 (1960).
 24. Kagan, Y. Theory of the temperature red shift and the broadening of the Mössbauer line. *Sov. Phys. JETP-USSR* **20**, 243 (1965).
 25. Kantor, I. *et al.* BX90: A new diamond anvil cell design for X-ray diffraction and optical measurements. *Rev. Sci. Instrum.* **83**, 125102 (2012).

26. Kurnosov, A. *et al.* A novel gas-loading system for mechanically closing of various types of diamond anvil cells. *Rev. Sci. Instrum.* **79**, 045110 (2008).
27. Prescher, C., McCammon, C. & Dubrovinsky, L. MossA : a program for analyzing energy-domain Mössbauer spectra from conventional and synchrotron sources. *J. Appl. Crystallogr.* **45**, 329–331 (2012).
28. Triftshäuser, W. & Craig, P. P. Time dependence of recoil-free resonance following electron capture in Co 57. *Phys. Rev.* **162**, 274–285 (1967).

Abbreviations

Acronym	Definition
APD	Avalanche Photodiode detector
BGI	Bayerisches Geoinstitut
CW	Continuous Wave
dsLH	double-sided Laser Heating
DAC	Diamond Anvil Cell
DESY	Deutsches Elektronen-Synchrotron
EoS	Equation of State
ESRF	European Synchrotron Radiation Facility
IR	Infrared Radiation
LHDAC	Laser-Heated Diamond Anvil Cell
NFS	Nuclear Forward Scattering
NIR	Near-Infrared Radiation
NIS	Nuclear Inelastic Scattering
PL	Pulsed Laser
PXRD	Powder X-ray Diffraction
SCXRD	Single-crystal X-ray Diffraction
VIS	Visible Spectrum
XANES	X-ray Absorption Near Edge Structure
XRD	X-ray Diffraction

(Eidesstattliche) Versicherungen und Erklärungen

(§ 9 Satz 2 Nr. 3 PromO BayNAT)

Hiermit versichere ich eidesstattlich, dass ich die Arbeit selbstständig verfasst und keine anderen als die von mir angegebenen Quellen und Hilfsmittel benutzt habe (vgl. Art. 64 Abs. 1 Satz 6 BayHSchG).

(§ 9 Satz 2 Nr. 3 PromO BayNAT)

Hiermit erkläre ich, dass ich die Dissertation nicht bereits zur Erlangung eines akademischen Grades eingereicht habe und dass ich nicht bereits diese oder eine gleichartige Doktorprüfung endgültig nicht bestanden habe.

(§ 9 Satz 2 Nr. 4 PromO BayNAT)

Hiermit erkläre ich, dass ich Hilfe von gewerblichen Promotionsberatern bzw. -vermittlern oder ähnlichen Dienstleistern weder bisher in Anspruch genommen habe noch künftig in Anspruch nehmen werde.

(§ 9 Satz 2 Nr. 7 PromO BayNAT)

Hiermit erkläre ich mein Einverständnis, dass die elektronische Fassung meiner Dissertation unter Wahrung meiner Urheberrechte und des Datenschutzes einer gesonderten Überprüfung unterzogen werden kann.

(§ 9 Satz 2 Nr. 8 PromO BayNAT)

Hiermit erkläre ich mein Einverständnis, dass bei Verdacht wissenschaftlichen Fehlverhaltens Ermittlungen durch universitätsinterne Organe der wissenschaftlichen Selbstkontrolle stattfinden können.

.....
Ort, Datum, Unterschrift